

DOCTORATE THESIS

Angular dynamics of small particles in fluids

JONAS EINARSSON

Department of Physics
University of Gothenburg
Göteborg, Sweden 2015

Angular dynamics of small particles in fluids

Jonas Einarsson

ISBN 978-91-628-9656-0 (PDF)

ISBN 978-91-628-9657-7 (Print)

This thesis is electronically published, available at

<http://hdl.handle.net/2077/40830>

Department of Physics

University of Gothenburg

SE-412 96 Göteborg

Sweden

Telephone: +46 (0)31-786 00 00

Parts I-II, pages 1–73, including all figures, are licensed under a Creative Commons Attribution 3.0 Unported License.



In Part IV,

Paper B is © 2015 American Physical Society, and is reprinted with permission.

Paper F is © 2015 AIP Publishing LLC, and is reprinted with permission.

Papers A & C-E are © 2015 their respective authors.

Front cover: Illustration of ellipsoidal particle tumbling in a shear flow.

Flipbooks: Ellipsoidal particles rotating in a simple shear flow.

Odd pages: Symmetric particle with major aspect ratio $\lambda = 7$ and minor aspect ratio

$\kappa = 1$. *Even pages:* Slightly asymmetric particle with $\lambda = 7$ and $\kappa = 1.2$. Their trajectories are qualitatively different despite the very slight asymmetry. See Section 3.5 for further explanation.

Printed by Kompendiet

Göteborg, Sweden 2015

ABSTRACT

This thesis concerns the angular motion of small particles suspended in fluid flows. A small particle experiences a hydrodynamic torque due to the local fluid velocity, and this torque leads to rotational motion. When inertial effects are negligible the torque on an ellipsoidal particle is given by Jeffery's theory [JEFFERY, G. B. *Proc. R. Soc. Lond. A* **102**, 161–179 (1922)]. In this thesis and the appended papers I describe three studies that all relate to this well-known result.

First, we derive an effective equation of motion for the orientation of a spheroid in a simple shear flow, valid for small values of the shear Reynolds number $\text{Re}_s = sa^2/\nu$, where s is the shear rate, a the particle size and ν the kinematic viscosity of the suspending fluid. In absence of inertia the equation of motion has infinitely many periodic solutions, the 'Jeffery orbits'. We show how this degeneracy is lifted by the effects of inertia.

Second, we describe experimental observations of the orientational dynamics of asymmetric particles advected in a microchannel. We record several trajectories with each particle by resetting the initial condition with an optical trap. We find that the dynamics depend sensitively on both particle shape and initial conditions. This confirms earlier theoretical results, which are also described in this thesis.

Third, we discuss the angular dynamics of axisymmetric particles in turbulent and random flow. In these flows the statistical averages of the angular dynamical quantities depend crucially on the intricate correlations between the particle orientation, angular velocity, and the flow vorticity relative to the principal straining directions of the fluid flow. We illustrate this by direct numerical simulation, experimental measurements and statistical model calculations.

Finally, this thesis contains an introduction to the field aimed at new students, as well as an accessible popular science introduction to low Reynolds particle dynamics.

LIST OF PAPERS

This thesis builds on the scientific work in the following papers:

Paper A

EINARSSON, J, CANDELIER, F, LUNDELL, F, ANGILELLA, J. R & MEHLIG, B 2015 Effect of weak fluid inertia upon Jeffery orbits. *Physical Review E* **91** (4), 041002.

Paper B

CANDELIER, F, EINARSSON, J, LUNDELL, F, MEHLIG, B & ANGILELLA, J. R 2015 Role of inertia for the rotation of a nearly spherical particle in a general linear flow. *Physical Review E* **91** (5), 053023.

Paper C

EINARSSON, J, CANDELIER, F, LUNDELL, F, ANGILELLA, J. R & MEHLIG, B 2015 Rotation of a spheroid in a simple shear at small Reynolds number. *Physics of Fluids* **27** (6), 063301.

Paper D

ROSEN T, EINARSSON, J, NORDMARK, A, AIDUN, C. K, LUNDELL, F & MEHLIG, B 2015 Numerical analysis of the angular motion of a neutrally buoyant spheroid in shear flow at small Reynolds numbers. *Physical Review E (in review)*. arXiv 1508.04976.

Paper E

EINARSSON, J, MIHIRETIE, B. M, LAAS, A, ANKARDAL, S, ANGILELLA, J. R, HANSTORP, D, & MEHLIG, B 2015 Tumbling of asymmetric microrods in a microchannel flow. *Physics of Fluids (in review)*. arXiv 1503.03023

Paper F

BYRON, M, EINARSSON, J, GUSTAVSSON, K, VOTH, G, MEHLIG, B & VARIANO, E 2015 Shape-dependence of particle rotation in isotropic turbulence. *Physics of Fluids* **27** (3), 035101.

MY CONTRIBUTIONS

My contributions to the appended publications are:

Papers A-D

I devised and performed the main calculation (presented in Paper C) valid for arbitrary aspect ratio. I performed the stability analysis in Paper D. I wrote Paper C in collaboration with BM, and I took active part in writing of Papers A, B and D.

Paper E

I took part in designing the experiment and the data analysis. I did the theory together with BM, in particular the reversal symmetry arguments and Eq. (2). I wrote Sections I & II, and took active part in editing of the entire manuscript.

Paper F

I computed the DNS results and took active part in interpreting the results of experiments, DNS and random models. I wrote most of Sec. IV and App. A, and took active part in writing the rest of the paper.

EARLIER WORK

The following publications were part of my Licentiate thesis [1]:

GUSTAVSSON, K, EINARSSON, J & MEHLIG, B 2014 Tumbling of small axisymmetric particles in random and turbulent flows. *Physical Review Letters* **112** (1), 014501.

EINARSSON, J, ANGILELLA, J. R & MEHLIG, B 2014 Orientational dynamics of weakly inertial axisymmetric particles in steady viscous flows. *Physica D: Nonlinear Phenomena* **278–279**, 79–85.

EINARSSON, J, JOHANSSON, A, MAHATO, S. K, MISHRA, Y. N, ANGILELLA, J. R, HANSTORP, D & MEHLIG, B 2013 Periodic and aperiodic tumbling of micro-rods advected in a microchannel flow. *Acta Mechanica* **224** (10), 2281–2289.

CONTENTS

Abstract

List of papers

My contributions

Earlier work

Contents

| | |
|--|-----------|
| I Introduction | 1 |
| 1 Motivation | 2 |
| 2 Background | 5 |
| 2.1 Our field of study: particles in flows | 5 |
| 3 Prerequisite concepts | 11 |
| 3.1 Fluid mechanics | 12 |
| 3.2 Effective equations of motion | 15 |
| 3.3 The Stokes approximation | 18 |
| 3.4 Simple shear flow | 20 |
| 3.5 The Jeffery equation and its solutions | 22 |
| II My work | 43 |
| 4 Effects of inertia | 43 |
| 4.1 History of problem | 44 |
| 4.2 Results | 46 |
| 5 Measurements of asymmetric rods | 51 |
| 5.1 Overview | 51 |

| | |
|--|-----------|
| 6 Rotation rates of particles in turbulence | 52 |
| 7 Closing words | 54 |
| 7.1 Discussion of results | 55 |
| 7.2 Outlook | 56 |
| A Triaxial particle in a linear flow | 69 |
| III Papers | 73 |

PART I

INTRODUCTION

This thesis is about *effective equations of motion* for solid particles suspended in fluid flows. In all but the simplest cases we are unable to directly compute the forces acting on a solid particle from first principles. The fundamental equations of fluid mechanics are too complicated, and even finding a numerical approximation with a computer is often too expensive.

But if we limit our scope to a particular physical situation, we may exploit its particular properties to simplify the calculations. With these simplifications we may find an effective equation governing the motion of the suspended particles. The effective equation is simpler, and therefore more useful, than the fundamental equations. The price for the simplicity is that they apply only within the limited scope. In this thesis we consider *small* particles. I will make a precise definition of what small means later. For now think of small as the plankton in the oceans, not the shark, or the mist droplets in the clouds, not an airplane.

The effective equations of motion are used as building blocks in higher-level modeling. For example the effective force on a small sphere becomes a building block in a model of the droplets in a rain cloud, and the effective torque on a spheroid is used to model the order of fibers in a paper-making machine.

The technical centerpiece of this thesis is the calculation of an effective equation of motion, starting from the fundamental equations. This effective equation describes the rotation of a spheroid which is small, but finite. The motion of a finite particle is affected by inertia, and so is the motion of the surrounding fluid. The inertia affects the forces and torques acting on the particle. These effects are captured in our calculation. It is described in detail in Section 4 in Part II, and the appended Papers A-D.

The new effective equation generalises aspects of an earlier effective equation: the Jeffery equation [2], which is valid for truly small particles that are not affected by inertia. In addition to this project I have also worked on two other projects which involve the Jeffery equation (Papers E & F).



Disposition of this thesis

The remainder of this thesis consists of an extended summary, and the appended papers.

You are now reading Part I, which continues in Section 1 with a motivation for our research. In Section 2 I attempt to introduce our research to a reader without a strong technical background. Perhaps the reader is a new student, or a curious uncle of mine. But I hope that also an experienced reader may enjoy the text. Section 3 is a technical introduction to the prerequisite concepts needed to understand this thesis. In particular I discuss the Jeffery equation and its solutions in some detail. Some material in Part I is adapted and revised from my Licentiate thesis [1].

Part II is where I present the original research contained in the appended papers. I give an “executive summary” of each project, including the context of the questions and the main results.

Part III consists of reprints of the Papers A-F.

1 Motivation

The motion of small particles suspended in fluid flows is a fundamental research topic of interest in many branches of science, as well as for technical applications. In some cases it is the actual motion of the particles that is of interest. For example, in the atmospheric sciences the collisions and aggregation of small drops are important to the formation of rain [3]. Similarly, in astronomy it is believed that the collisions of small dust grains lead eventually to the formation of planets in the accretion disk around a star [4]. Another example is in marine biology, where the dynamics of small planktonic organisms swirled around by the ocean is fundamental in understanding their feeding and mating patterns [5].

In other contexts the motion of the individual particle is of lesser interest. Instead its effects on the suspending fluid is the topic of study. The properties of so-called complex fluids, meaning fluids with suspended particles, are studied in the field of rheology. For instance, the “ketchup effect” (where ketchup is stuck in the bottle, and nothing happens, and then suddenly all the ketchup pours out at once, only to solidify again on the plate) exists because of how all the microscopic particles suspended in the liquid orient themselves



[6]. On a more serious note, the similarly sudden onset of landslides in clay soils is related to the complex fluid of water and clay particles [7]. A fundamental question in rheology is how to relate the microscopic motion of the suspended particles to the macroscopic behaviour of the complex fluid.

In many circumstances it is important to consider the non-spherical shape of particles, and how they are oriented. For instance, the ash clouds from volcanic eruptions play an important role in the radiation budget of our planet, and therefore its climate [8]. The ash particles are non-spherical [9], and their shapes and orientations influence how light and energy is absorbed in the volcanic cloud [10]. Similarly, the orientation of non-spherical plankton influences the light propagation through the upper layers of the oceans, determining to which depth life-supporting photosynthesis is possible [11].

Despite their diversity, all the above examples share a basis in a fundamental question. How do particles respond to a given flow, and how does the flow in return respond to the presence of particles? The underlying goal of our research is to find an answer to this fundamental question. But the mathematics of fluid dynamics have challenged physicists and mathematicians alike for several hundred years. Before moving on to the description of my work, I allow myself to digress into the story of a seemingly innocent question: what is the drag force on a perfect sphere moving with constant velocity through a still fluid?

Until the early 19th century the prevailing theory was the following: a moving sphere drags along some of the surrounding fluid in its motion, and the force upon the sphere is equal to the force required to drag along the extra weight. The force must then be dependent on the weight, or more precisely the density, of the fluid. But in 1829, Captain Sabine of the Royal Artillery performed detailed experiments with a pendulum in different gases [12]. By observing the attenuation of the pendulum motion in both hydrogen gas and in air, he concluded beyond doubt that the damping force on the pendulum is not proportional to the density of the surrounding gas - there has to be another force.

It was George Gabriel Stokes who first computed the force on a *slowly moving* sphere due to the internal friction of the fluid [13]. He found that the force depends on the “index of friction”, which we today know as the kinematic viscosity of a fluid. From his calculation, Stokes immediately concluded that “the apparent suspension of the clouds is mainly due to the internal friction of air” [13].



The *Stokes drag force* remains a great success, and it correctly predicts the forces for slowly moving particles. But the question of how to correctly amend the Stokes drag force to account for slightly faster motion turned out to be surprisingly hard. The correction took around a century of hard work, and the invention of a new branch of mathematics [14]. If we dare ask how to properly calculate the drag force on a particle moving quickly, in a curved path, and in a fluid which itself moves, the answer is still debated.

Meanwhile, the Stokes theory for slow motion has been extended to include both forces and torques on particles of any conceivable shape [2, 15, 16]. Much of modern research on particles in fluid flows still rely directly on these well-known results.

In general, the fundamental equations of fluid mechanics, the Navier-Stokes equations, seem to describe the motion of fluids. But applying them requires tremendous efforts due to their sheer complexity. Today, a modern supercomputer can produce an approximate solution for some simplified cases, like a cubic meter of moderately turbulent air without particles. But many interesting problems, such as a real rain cloud with drops, are far out of reach for any computer in any foreseeable future.

One aim of theoretical fluid mechanics is to derive new, simpler, equations of motion to use in place of the fundamental equations. This is in essence what Stokes did in 1851 for slowly moving spheres. But the price of simplification is the loss of generality. Every new physical situation potentially requires a new equation. And each new equation has to be tested against experiments and direct numerical solution of the general equations.

In this thesis I first present a derivation (Papers A-C) and validation (Paper D) of an effective equation of motion for the orientation of a spheroid in a simple shear flow. This equation of motion takes one step beyond the Stokes approximation of slow movements, at the expense of being valid precisely only for the simple shear flow. Why this trade-off is worthwhile is explained in this thesis. Secondly, the two remaining papers appended to this thesis involve the Stokes (Jeffery [2]) approximation for the angular motion of ellipsoids in linear flows. Paper E is an experimental verification of the predicted angular motions in shear flow. Paper F discusses the rotations of axisymmetric particles in turbulent flows.



2 Background

Every now and then I get the question “what is it you do, anyway?” Often enough the question is posed out of sheer politeness, and I can simply say “Physics! Tiny particles, like plankton, they tumble in the oceans, and stuff.” But sometimes the question is sincere, and I find it quite challenging to explain what I do. I may say that we calculate how non-spherical particles rotate in flows. But that is comparable to if I was designing a gearbox, and said that I work with cars. It is true, but not very helpful.

The following is an attempt at a description which is readable and not too complicated, but still complicated enough to get a glimpse of the physics.

2.1 Our field of study: particles in flows

Where do particles go when I put them into a flow? Which way do they face? How fast do they spin? These are all valid questions, but they are unspecific. Their answers depend on whether the particle is an aircraft or a grain of particulate carbon soot, and whether the fluid is air or water.

I will start with an elaboration on fluid physics, move to the question why we consider rigid particles specifically, then say something about the forces acting on the particles. This will naturally lead us to why we must consider “small” particles, which is not obvious from the outset. But let’s start from the beginning.

Fluids

Many physical systems around us are fluids. The air we breathe, the water we drink, the blood in our veins are all fluids. As a working definition we can think of a fluid as a system where the constituent molecules move around more or less freely. Sometimes they interact with each other and exchange some energy. These interactions give rise to what you perceive as friction. You know that syrup has more friction than water: if you pull a spoon through syrup, more of your energy is expended than if you were to pull the spoon through water. The *viscosity* of a fluid is a measure of how often and how violently the molecules interact, and we say that syrup has higher viscosity than water. Now, it gets interesting when something else, for example a drop



of oil or a particle, is added to the fluid. Consider dripping a drop of oil into water. Then what happens depends on how the water molecules interact with the oil molecules. As you probably have experienced, oil molecules prefer to stick together. Therefore the oil concentrates into a drop where as many oil molecules as possible may be neighbours with other oil molecules.

But so far, the above is a very qualitative, and you may rightly say naive, description of what happens. One could say that a fundamental problem of fluid physics is to figure out where all the different molecules go. From the detailed knowledge of every molecule we may proceed to deduce where the oil drop goes, and how fast, or if it perhaps breaks up, or maybe merges with another drop. However, making something useful out of this molecular picture is very difficult. Just consider that in one litre of water there are about 10^{25} molecules (that is a one followed by 25 zeroes). In fact, we are not even particularly interested in the specific details of every molecule. We are interested in the macroscopic, observable world that is built up from all these molecules. Therefore this thesis is not at all concerned with the detailed motion of molecules, but I still wanted to start with this picture because sometimes it becomes important to remember the microscopic origin of the macroscopic motion.

Fluid dynamics

Fluid dynamics is the discipline studying the macroscopic properties and motion of fluids. Some typical quantities studied there are the fluid velocity and pressure. We can think of the velocity at a certain position in the fluid as the average velocity of all the molecules at that point. The pressure is the force per area an object in contact with the fluid experiences, due to the constant bombardment of molecules. Think for example of the forces in a bottle of soda. There are well-known equations called the Navier-Stokes equations that tell us the velocity and pressure at every point in space and time, provided that we can solve them. You can see them in Eq. (3.7) on p. 13. We will soon return to how this helps us, but first we must restrict ourselves to avoid a difficult hurdle.

Recall our example of a drop of oil in water. The switch from a molecular view to a fluid dynamical view presents a new problem: if we do not keep track of every molecule, we instead have to keep track of which points in space contain oil and which contain water. A boundary surface separates



the two materials, and this boundary can deform over time as the oil drop changes shape. This sounds very complicated. Indeed, drop dynamics is a topic of its own, which this thesis does not intend to cover. Instead, this thesis concerns *rigid particles*.

Rigid bodies

A rigid body in physics is an object whose configuration can be described by the position of one point (usually the center-of-mass) and the rotation of the body around that point. Simply put: it cannot deform. The dynamics of a rigid body is described by Newton's laws. In particular, the center-of-mass motion is described by Newton's second law: the force F on a body equals its mass m times its acceleration α ,

$$F = m\alpha.$$

The above equation describes the movement of the center-of-mass, and there is a corresponding law for the rotation. Since this thesis concerns *orientational dynamics* of particles, here is Newton's law for the rotation of a rigid body:

$$T = \mathbb{I}\alpha.$$

It says that the torque T on a rigid body equals its moment of inertia \mathbb{I} (that's like the mass for rotations) times its angular acceleration α . The two equations above are deceptively simple-looking, but their solutions contain full knowledge of the motion of a rigid body. I state the equations here only to draw a conclusion: in order to extract all the information about the motion of a particle, we need to know both the force and the torque acting on the particle at all times.

There are many kinds of forces which can potentially act on a particle. For example there is gravity if the particle is heavy, or magnetic forces if the particle is magnetic. But for now we consider the forces on a particle due to the surrounding fluid, so called hydrodynamic forces. In everyday terms the hydrodynamic force is the drag, as experienced by the spoon you pull through syrup. Uneven drag over a body may also result in a hydrodynamic torque. For instance, turbulent air striking the wings of an aircraft will induce a torque which you feel as a rotational acceleration while the pilot compensates.



Hydrodynamic forces

In order to find out what the force on a particle is, we need to know how the fluid around the particle behaves. And for that, we need to solve the Navier-Stokes equations of fluid dynamics around the particle. We imagine the fluid in some environment (in lingo: “boundary conditions”), for example the air in a cloud, or liquid soap in a small pipe. A solution of the equations tells us the velocity and pressure of the fluid at any given point in space at any given time. If we have a solution, there is a mathematical recipe for how to extract the resulting forces and torques on a particle in the fluid.

The problem is that we cannot solve the equations. Not only are we unable to find solutions as mathematical formulas – in many cases we can not even find numerical solutions using a supercomputer. For example, computing the motion of the air in a cloud is utterly out of reach with any computer we can currently imagine. Before moving on to how we find the force on a particle, I’ll digress on the topic of numerical solutions.

From time to time I get the question why we struggle with difficult mathematical work, why not just “run it through the computer?” An answer to this question is that a numerical computer solution is like an experiment: it will give you the numbers for a particular case, but not necessarily any understanding of why. Conversely, we may extract physical understanding from the equations, even if we cannot solve them in general. It is the understanding of the underlying physics that enables us to simplify the equations until it is practical to solve them. This requires knowledge of which particular details may be neglected, and which details are crucial to keep track of. And indeed, the meteorologists now have methods of simulating the flows of air in the atmosphere, despite the fact that we cannot solve the exact equations. The trick is to ignore some parts of the equation dealing with very small motions, and spend the resources on describing the large eddies of the flow in so-called “Large Eddy Simulations”.

At any rate, we wish to figure out what the forces on a rigid body in a fluid flow are. It is clear that some type of simplification has to be made, because we cannot solve the Navier-Stokes equations. The great simplification is embodied in the word *small* in the title of this thesis. The particles we consider are small. But how small is a small particle? The answer I have to give right away is a rather unsatisfactory “it depends”. The smallness of the particle has to be relative to something else. This simple principle is



formalised by scientists, who discuss smallness in terms of *dimensionless numbers*. Because dimensionless numbers are very common in our work I will spend a few paragraphs to explain the basic idea.

Dimensionless numbers

In principle all physical quantities have some units. For example, the size of a particle has units of “length”, and the speed of the particle has units of “length per time”, which we write as length/time. Whenever we multiply or divide quantities with units, we also multiply or divide their units. For example dividing the length 20 m with the time 5 s gives the speed 4 m/s. Now suppose we divide the speed 4 m/s with the speed 2 m/s. The result is 2, without any units – they cancelled in the division.

The idea is that in order to determine if a quantity x_1 is “small” we have to divide it with another quantity x_2 of the same units. Then if the resulting dimensionless number x_1/x_2 is much smaller than 1, we say that x_1 is small, and implicitly mean *relative to* x_2 . This concept seems simple enough. Let’s apply it to particles moving in a fluid.

An example: the particle Reynolds number

Imagine stirring your cup of tea with a spoon. As you stir there is a wake behind the spoon, perhaps even a vortex is created if you are enthusiastic. When you stop stirring, the tea will splash about for a moment and then settle down because of its viscosity. If you stir vigorously, then stop suddenly and hold on to the spoon, you feel the force of the splashing fluid on the spoon. This continuing motion after you stopped forcing the fluid is due to the inertia of the fluid. Inertia means that things continue to move in their current direction, unless a force is applied. The inertia of the fluid is difficult to analyse mathematically, because the force on the spoon depends in a complicated fashion on how you stirred the tea in the past. To perform my calculation I want the inertia to be *small*. But small compared to what? How can I make a dimensionless number?

Imagine stirring with a spoon in syrup instead of tea. The wake behind the spoon relaxes quickly in the more viscous fluid. The viscous friction is the force which cancels the inertia. Viscous friction smears out any disturbances. Therefore we divide two times: the time it takes for viscosity to smear out



a disturbance over the size of the spoon (the *viscous time*), with the time it takes for the fluid to flow past the spoon:

$$\text{Re}_p = \frac{\text{Viscous time}}{\text{Time for fluid to flow past the spoon}}.$$

This number is called the particle Reynolds number. It is small when inertia is not important. If the viscous time is short, a disturbance is smeared out before it is allowed to flow past the particle. This is similar to stirring syrup. But if the fluid flows past the particle before the viscosity can smear out the disturbances, the particle Reynolds number is larger, like in your cup of tea.

The mathematical expression for the particle Reynolds number is

$$\text{Re}_p = \frac{u_0 a}{\nu},$$

where u_0 is the fluid velocity past the particle (units m/s), a is the particle size (units m), and ν is the viscosity (units m²/s). This gives us three options to keep the effects of inertia small: consider slower flows, or smaller particles, or fluids with higher viscosity.

Recall the story about the Stokes drag in the very beginning of this thesis. When Stokes in 1851 called a particle “slowly moving”, he meant exactly the condition that the particle is small, in the sense just described here. Among friends we often say “small particle”, or “slowly moving”, or “viscous flow”, when we mean “small value of the particle Reynolds number.” It is convenient, but less precise.

The reduction of three options into the value of a single number is an important insight. Instead of considering the effects of all three separate parameters, we can understand the physics by analysing a single dimensionless number. The dimensionless numbers tell us which physical quantities are important in relation to each other. In the example above, the actual size of the particle is not important – the size only matters in relation to the velocity and viscosity. All situations with the same particle Reynolds number are, in some sense, equivalent. This very fact is also what enables engineers to use scale models in wind tunnels. They know that to test a model of a suspension bridge in a wind tunnel, they must not use full-scale wind speeds, but instead a scaled down version of the wind. The dimensionless numbers reveal what scaling is appropriate to match the model bridge to real conditions.



Conclusion

We have discussed fluids, rigid particles, the Navier-Stokes equations and dimensionless numbers. If we add some mathematical rigor to the mix, you could soon have an undergraduate degree in fluid mechanics. But how does this connect to my research?

When we assume that there is no fluid inertia whatsoever, that is $Re_p = 0$, we enter the regime of the Stokes approximation. As explained in the introduction this approximation has been fantastically successful in predicting the forces and torques on particles in many situations. But for some special cases, the Stokes approximation does not lead to a definite answer. One of these cases is the rotation of a non-spherical particle in a so-called shear flow. Jeffery applied the Stokes approximation to this problem in 1922, and was disappointed to find that the answer is indeterminate. My contribution in this thesis is to amend the Stokes approximation for this particular case. The four Papers A-D explain the first effects of both fluid and particle inertia on the rotation of a non-spherical particle in shear flow.

During the course of this work, I have also worked with students and colleagues on related problems. How does the particle rotate if we throw it into a turbulent fluid? Can we tune an experiment to match the Stokes approximation? These and many more questions are ongoing work, and we published some results in the Papers E & F.

3 Prerequisite concepts

In this section I introduce some basic concepts needed to understand my work in Part II of this thesis, and the appended papers. My aim is to start at the beginning, and as quickly as possible arrive at the knowledge particular to the field of orientational dynamics of non-spherical particles. The scope is therefore narrow, but deep. For a wider presentation of low-Reynolds hydrodynamics I refer to the books by Kim & Karrila [16] and Happel & Brenner [17].



3.1 Fluid mechanics

3.1.1 Fluid flows

In this thesis we only encounter so-called Newtonian and incompressible fluids. The hydrodynamic state of such a fluid is described by a flow velocity vector field $\mathbf{u}(\mathbf{x}, t)$, and a scalar pressure field $p(\mathbf{x}, t)$. The incompressible nature of the fluid implies that $\nabla \cdot \mathbf{u} = 0$ everywhere. The fluid itself has two properties: its density ρ_f (kg/m^3), and its dynamic viscosity μ ($\text{kg}/\text{m}\cdot\text{s}$). Sometimes it is convenient to refer to the kinematic viscosity $\nu = \mu/\rho_f$ (m^2/s).

The work presented in this thesis involves the flow gradients, because it is the gradients in the flow that give rise to the torque on a small particle. The spatial derivatives of the flow field \mathbf{u} form a tensor $\mathbb{A} \equiv \nabla \mathbf{u}^T$, because there are three vector components defined in three coordinates. The components of \mathbb{A} in Cartesian coordinates are

$$A_{ij} = \frac{\partial u_i}{\partial x_j}. \quad (3.1)$$

In general the action of \mathbb{A} is defined as the directional derivative in the direction of the unit vector $\hat{\mathbf{y}}$:

$$\mathbb{A}\hat{\mathbf{y}} = \lim_{\epsilon \rightarrow 0} \frac{\mathbf{u}(x + \epsilon\hat{\mathbf{y}}, t) - \mathbf{u}(x, t)}{\epsilon}. \quad (3.2)$$

The incompressibility condition $\nabla \cdot \mathbf{u} = 0$ transfers directly to the condition $\text{Tr}\mathbb{A} = 0$.

It is often convenient to decompose the gradient tensor \mathbb{A} into its symmetric part \mathbb{S} and anti-symmetric part \mathbb{O} , because they have separate physical interpretations. We write

$$\mathbb{A} = \mathbb{S} + \mathbb{O}, \quad \mathbb{S} = \frac{1}{2}(\mathbb{A} + \mathbb{A}^T), \quad \mathbb{O} = \frac{1}{2}(\mathbb{A} - \mathbb{A}^T). \quad (3.3)$$

The symmetric part \mathbb{S} is called the rate-of-strain tensor, and it describes the local rate of deformation of the flow. The anti-symmetric part \mathbb{O} describes the local rotation of the flow and is related to the vorticity vector. The vorticity vector $\boldsymbol{\omega}_f$ of a flow \mathbf{u} is defined by the curl $\boldsymbol{\omega}_f = \nabla \times \mathbf{u}$. The matrix \mathbb{O} is related to the vorticity vector $\boldsymbol{\omega}_f$, because for any given vector \mathbf{x}

$$\mathbb{O}\mathbf{x} = \frac{1}{2}\boldsymbol{\omega}_f \times \mathbf{x} \equiv \boldsymbol{\Omega} \times \mathbf{x}. \quad (3.4)$$



The vector $\boldsymbol{\Omega} = \boldsymbol{\omega}_f/2$ is a common quantity in our calculations, and therefore is given its own symbol. For example, in absence of inertia the angular velocity of a sphere in a simple shear flow is exactly $\boldsymbol{\Omega}$. This is explained in detail in Section 3.5.

3.1.2 The Navier-Stokes equations

For a given physical situation the flow and pressure fields are determined by a Navier-Stokes problem. A Navier-Stokes problem for a Newtonian, incompressible fluid is fully specified by a momentum balance, the incompressibility condition and a set of boundary conditions.

Let us first derive the momentum equations. Consider the momentum balance in a volume \mathcal{V} bounded by surface \mathcal{S} . These equations are Newton's $m\boldsymbol{a} = \boldsymbol{F}$ over a volume:

$$\frac{\partial}{\partial t} \int_{\mathcal{V}} \rho_f \boldsymbol{u} d\mathcal{V} + \int_{\mathcal{S}} \rho_f \boldsymbol{u} (\boldsymbol{u} \cdot d\mathcal{S}) = \int_{\mathcal{S}} \boldsymbol{\sigma} \cdot d\mathcal{S} \quad (3.5)$$

The first term accounts for changing velocities in the bulk of the volume. The second term accounts for the momentum transfer across the boundary of the volume. The right hand side contains the forces acting on the surface of the volume. The stress tensor $\boldsymbol{\sigma}$ describes the force per unit area in the fluid, such that $\boldsymbol{\sigma} \cdot \boldsymbol{N}$ is the force per area on a surface with normal vector \boldsymbol{N} . A Newtonian fluid is modeled by $\boldsymbol{\sigma} = -p\mathbb{1} + 2\mu\mathbb{S}$, meaning that the forces arise in part from pressure, and in part from the viscous friction forces. This tensor is central in determining the forces on particle surfaces, too, as will be explained below.

We apply the divergence theorem to the surface integrals in Eq. (3.5) and find

$$\frac{\partial}{\partial t} \int_{\mathcal{V}} \rho_f \boldsymbol{u} d\mathcal{V} + \int_{\mathcal{V}} [(\nabla \cdot \rho_f \boldsymbol{u}) \boldsymbol{u} + (\rho_f \boldsymbol{u} \cdot \nabla) \boldsymbol{u}] d\mathcal{V} = \int_{\mathcal{V}} \nabla \cdot \boldsymbol{\sigma} d\mathcal{V}. \quad (3.6)$$

This equation holds point-wise, because the volume can be arbitrarily chosen. By using the incompressibility condition, we arrive at the Navier-Stokes equations for an incompressible fluid:

$$\rho_f \left(\frac{\partial}{\partial t} \boldsymbol{u} + (\boldsymbol{u} \cdot \nabla) \boldsymbol{u} \right) = \nabla \cdot \boldsymbol{\sigma}, \quad \nabla \cdot \boldsymbol{u} = 0, \quad \boldsymbol{\sigma} = -p\mathbb{1} + 2\mu\mathbb{S}. \quad (3.7)$$



The boundary condition where the fluid meets a solid surface is the *no-slip condition*. This means that the fluid at the boundary has the same velocity as the boundary itself. When considering problems with a solid particle suspended in a fluid, the typical boundary condition is no-slip on the particle surface and that the flow relaxes to a prescribed background flow as the distance to the particle goes to infinity.

3.1.3 Forces on particles

Consider a background flow $\mathbf{u}^\infty(\mathbf{x}, t)$ without any particle present. We introduce a particle into the flow through the no-slip boundary conditions at the particle surface S . The particle center-of-mass moves along the trajectory $\mathbf{y}(t)$ (velocity $\dot{\mathbf{y}}$), and its orientation $\mathbb{R}(t)$ changes with angular velocity $\boldsymbol{\omega}(t)$. Far away from the particle, “at infinity”, the fluid is not disturbed by the presence of the particle, and should be equal to $\mathbf{u}^\infty(\mathbf{x}, t)$:

$$\begin{aligned}\mathbf{u}(\mathbf{x}, t) &= \dot{\mathbf{y}} + \boldsymbol{\omega} \times (\mathbf{x} - \mathbf{y}), & \mathbf{x} \in S(\mathbf{y}, \mathbb{R}). \\ \mathbf{u}(\mathbf{x}, t) &= \mathbf{u}^\infty(\mathbf{x}, t), & |\mathbf{x} - \mathbf{y}| \rightarrow \infty.\end{aligned}\quad (3.8)$$

As explained above, the hydrodynamic force on a surface in the fluid is determined by integrating the fluid stress tensor σ over the surface. Therefore the forces and torques acting on the particle are

$$\begin{aligned}\mathbf{F} &= \int_S \sigma \cdot d\mathbf{S}, \\ \mathbf{T} &= \int_S (\mathbf{x} - \mathbf{y}) \times \sigma \cdot d\mathbf{S}.\end{aligned}\quad (3.9)$$

To complete the problem formulation, the particle trajectory is governed by Newton's equations

$$m\ddot{\mathbf{y}} = \mathbf{F}, \quad \frac{d}{dt}(\mathbb{I}\boldsymbol{\omega}) = \mathbf{T}. \quad (3.10)$$

Here dots denote the time derivative, m is the particle mass, and \mathbb{I} its moment-of-inertia tensor.

The coupled equations (3.7-3.10) describe the motion of both particle and fluid. However, they are incredibly complicated because of their nonlinearities: the so-called *convective term* $(\mathbf{u} \cdot \nabla)\mathbf{u}$ in Eq. (3.7), and the coupling through the moving boundary conditions (3.8).



We may understand that the problem is very hard just by imagining a particle in a fluid: as the particle moves and rotates, it stirs up a wake and vortices in its trail. These disturbances may linger and affect the particle at a later time. It seems that we are, in general, obliged to take into account the whole joint history of the particle and the fluid to predict the final state of the two. These complications raise the need for approximation, and *effective equations* for the particle motion.

3.2 Effective equations of motion

For the purposes of this thesis, the term *effective equations of motion* means a set of equations for the particle motion that does not involve the equations of fluid motion. The effective equations should be an approximation to the exact equations (3.7-3.10) in some limit.

In principle that means that the force on the particle is a functional of the particle trajectory and the background flow field \mathbf{u}^∞ :

$$\mathbf{F}_{\text{eff}} = \mathbf{g}(\mathbf{y}, \mathbb{R}, \mathbf{u}^\infty). \quad (3.11)$$

A concrete and well-known example is the Stokes force on a spherical particle of radius a

$$\mathbf{F}_{\text{Stokes}} = 6\pi\mu a(\mathbf{u}^\infty(\mathbf{y}, t) - \dot{\mathbf{y}}), \quad (3.12)$$

which we will discuss in detail shortly. Another example is the Stokes-Boussinesq force on a sphere accelerating in a still fluid:

$$\mathbf{F}_{\text{SB}} = -6\pi\mu a\dot{\mathbf{y}} - \frac{m}{2} \frac{\rho_f}{\rho_p} \ddot{\mathbf{y}} - 6a^2 \sqrt{\pi\rho_f\mu} \int_0^t \frac{\ddot{\mathbf{y}}(\tau)d\tau}{\sqrt{t-\tau}}. \quad (3.13)$$

This force depends on the history of the particle acceleration, and it is appropriate to describe rapidly accelerating particles. It is for example necessary to use Eq. (3.13) to describe the velocity of a particle in thermally agitated Brownian motion [18, 19].

The use of an effective equation is also called a *one-way coupling* approximation, because it explicitly gives the effect of the fluid on the particle, but not the other way around. We can therefore first compute, or choose, a flow



field \mathbf{u}^∞ in absence of any particles, and then use the effective equation to calculate the particle motion. This is a great simplification over solving the exact coupled system. It is a very common method to study for example the motion of particles in turbulence (for example, in Paper F).

But we have to be careful. In the derivation of the Stokes force, for example, it is assumed that the particle is alone in the fluid. If we use the Stokes force to consider several particles simultaneously and they happen to move close to each other, the approximation is no longer valid. In that case, we must create an effective equation for the particle pair instead. If the particle moves close to a wall, we have to make yet another equation for that. The price of simplicity is specialization.

3.2.1 The particle Reynolds number

My specialization is the the effective equations valid for “small” particles. The Stokes force in Eq. (3.12) was derived in 1851 [13] and is the first example of this specialization. Let me explain this limit more precisely.

As explained above, a particle moving through a fluid creates disturbances that may come back and affect the particle at a later time. We are aiming for the limit where the disturbances will be smeared out by the viscosity before they make any secondary impact. This happens if the time for viscosity to smoothen the flow field is much smaller than the time it takes for the flow field to transport the disturbance over the particle size. The condition is precisely that the dimensionless particle Reynolds number is small. As stated in Sec. 2.1,

$$\text{Re}_p = \frac{\text{Viscous time}}{\text{Time for fluid to flow one particle length}}. \quad (3.14)$$

More specifically,

$$\text{Re}_p = \frac{a^2/\nu}{a/u_0} = \frac{u_0 a}{\nu}. \quad (3.15)$$

Here u_0 is a typical flow speed relative to the particle surface, a is the size of the particle and ν is the kinematic viscosity of the fluid. We see that the limit I call “small particles” is actually that of either small particles, or large viscosity, or slow motions. The Reynolds number determines whether the inertia of the fluid is important compared to the viscosity.



In my work on rotating particles in shear flows, the typical flow speed is $u_0 = sa$, where s is the shear rate of units $1/\text{time}$ (the shear flow is explained in detail in Section 3.4.) The resulting dimensionless number is sometimes called the shear Reynolds number

$$\text{Re}_s = \frac{sa^2}{\nu}. \quad (3.16)$$

We introduce the dimensionless numbers in our equations by changing all variables into dimensionless variables using the available dimensions of the problem: length a and time $1/s$. In my case the change of variables is $\mathbf{u} = sa\mathbf{u}'$, $p = \mu s p'$, $\mathbf{x} = a\mathbf{x}'$, and $t = t'/s$. We make this change in Eq. (3.7), drop the primes, and find

$$\text{Re}_s \left(\frac{\partial}{\partial t} \mathbf{u} + (\mathbf{u} \cdot \nabla) \mathbf{u} \right) = \nabla \cdot \boldsymbol{\sigma}, \quad \nabla \cdot \mathbf{u} = 0, \quad \boldsymbol{\sigma} = -p \mathbf{1} + 2\mathbf{S}. \quad (3.17)$$

When $\text{Re}_s \ll 1$ we can hope to compute the force and torque on a particle by perturbation theory. The Stokes approximation is to set $\text{Re}_s = 0$, and solve $\nabla \cdot \boldsymbol{\sigma} = 0$. This important limit is the topic of Section 3.3.

Let me make a general remark about de-dimensionalisation and changes of variables. Mathematically, we assume nothing by just making a change of variables such as that from Eq. (3.7) to (3.17). If we solve Eq. (3.17) *exactly* and transform the result back to dimensionful variables, we find the exact solution to Eq. (3.7). However, if we solve Eq. (3.17) asymptotically as $\text{Re}_s \rightarrow 0$, the choice of variables determines the relative importance of the terms in Eq. (3.7), and therefore the resulting asymptotic solution. If we choose another change of variables, say $t = a^2 t' / \nu$, Eq. (3.17) is modified. In this case we find instead

$$\frac{\partial}{\partial t} \mathbf{u} + \text{Re}_s (\mathbf{u} \cdot \nabla) \mathbf{u} = \nabla \cdot \boldsymbol{\sigma}, \quad \nabla \cdot \mathbf{u} = 0, \quad \boldsymbol{\sigma} = -p \mathbf{1} + 2\mathbf{S}. \quad (3.18)$$

Again, if we solve Eq. (3.18) *exactly* and transform the result back to dimensionful variables we find the exact solution to Eq. (3.7). But the asymptotic solution of Eq. (3.18) as $\text{Re}_s \rightarrow 0$ is qualitatively different from that of Eq. (3.17). The choice of dimensionless variables embodies the physical assumptions that are effected by the perturbation theory. For the force on a translating sphere, this change in time scaling is responsible for the difference between the Stokes and the Stokes-Boussinesq forces in Eqs. (3.12) and (3.13).



3.2.2 The Stokes number

If we change the variables in the fluid equations, we must also make the corresponding changes in the coupled particle equations. The equation for the angular dynamics, for instance, becomes¹

$$\text{St} \frac{d}{dt}(\mathbb{I}\boldsymbol{\omega}) = \mathbf{T}, \quad \text{St} = \frac{\rho_p}{\rho_f} \text{Re}_s. \quad (3.19)$$

Another dimensionless number shows up: the Stokes number St . The Stokes number determines whether the particle inertia is important compared to the fluid forces. It is therefore not surprising that the Stokes number is related to the particle Reynolds number. They both compare inertial effects to the viscous forces. The only difference is through their relative densities. If the particle is heavier, its inertia is more important than the inertia of the fluid, and vice versa.

A neutrally buoyant particle has the same density as the fluid: $\rho_p = \rho_f$, and $\text{St} = \text{Re}_s$. This means that when we assume Re_s small, we also assume St small. If the densities are different, the particle will sink or float and we must consider its translation, unless $\text{Re}_s = \text{St} = 0$. In this thesis I consider only the orientation of the particle, and consequently I take $\text{St} = \text{Re}_s$.

3.3 The Stokes approximation

In the case when $\text{Re}_s = 0$, the Navier-Stokes equation (3.17) reduces to the linear Stokes equation $\nabla \cdot \boldsymbol{\sigma} = 0$:

$$\nabla^2 \mathbf{u} = \nabla p, \quad \nabla \cdot \mathbf{u} = 0. \quad (3.20)$$

This type of flow is called viscous flow, or creeping flow. Such flows are completely dominated by viscosity, and disturbances are assumed to disappear so quickly that they do not even exist in the equations: there is no time derivative in Eq. (3.20). Stokes equations are linear, and therefore many problems admit analytical solution. In particular, the force and torque on a particle in linear viscous flow has been worked out in quite some detail [16, 17, 20, 21].

¹I am sweeping some finer details under the carpet here. They are irrelevant for this argument, and you'll find it all in Sec. III in Paper C.



The fundamental result is that the force and torque on a small particle suspended in a flow is linearly related to the undisturbed flow. Given the particle velocity $\dot{\mathbf{y}}$ and angular velocity $\boldsymbol{\omega}$, we write the force \mathbf{F} and torque \mathbf{T} as

$$\begin{aligned}\mathbf{F} &= \mathcal{A}(\mathbf{u} - \dot{\mathbf{y}}) + \mathcal{B}(\boldsymbol{\Omega} - \boldsymbol{\omega}) + \mathcal{G} : \mathbb{S}, \\ \mathbf{T} &= \mathcal{B}^T(\mathbf{u} - \dot{\mathbf{y}}) + \mathcal{C}(\boldsymbol{\Omega} - \boldsymbol{\omega}) + \mathcal{H} : \mathbb{S}.\end{aligned}\quad (3.21)$$

Here \mathbb{S} and $\boldsymbol{\Omega}$ are the flow gradients as explained in Section 3.1.1. The resistance tensors \mathcal{A} , \mathcal{B} , \mathcal{C} , \mathcal{G} and \mathcal{H} depend only on the particle shape, and can be computed once and for all [16]. The tensors \mathcal{G} and \mathcal{H} are of rank three, and the double dot product $\mathcal{H} : \mathbb{S}$ is a contraction over two indices. In index notation it reads $(\mathcal{H} : \mathbb{S})_i = H_{ijk} S_{jk}$ (with implied summation over repeated indices).

The resistance tensors in the case of a sphere of radius a are $\mathcal{A} = 6\pi\mu a \mathbb{1}$, $\mathcal{B} = \mathcal{G} = \mathcal{H} = 0$ and $\mathcal{C} = 8\pi\mu a^3 \mathbb{1}$. In fact, for any particle that is mirror-symmetric in three orthogonal planes it holds that $\mathcal{B} = 0$ [20]. In such cases there is neither coupling between rotation and force, nor between translation and torque. An example of the contrary is a cork-screw-shaped particle. However, this thesis concerns particles with shapes such that the orientational dynamics decouple from the translational motion.

There is a hidden complication in Eq. (3.21): the flow is usually known in a fixed frame of reference, but the resistance tensors are known in the frame of reference of the particle. Expressing the resistance tensors in the fixed frame of reference entails a rotation dependent on the particle orientation. Thus, the torque is in general a non-linear function of particle orientation.

The Stokes resistance of a rotating ellipsoid was computed in a now famous paper by Jeffery in 1922 [2]. The result therein is of course not expressed in the subsequently invented tensor notation, but all the necessary calculations are there. The adaptation to current notation is found in *Microhydrodynamics* (Ref. 16 p. 56). Jeffery's result is the basis of all my work, so I dedicate Section 3.5 to discuss it in detail, but first we must discuss the anatomy of the simple shear flow in Section 3.4.



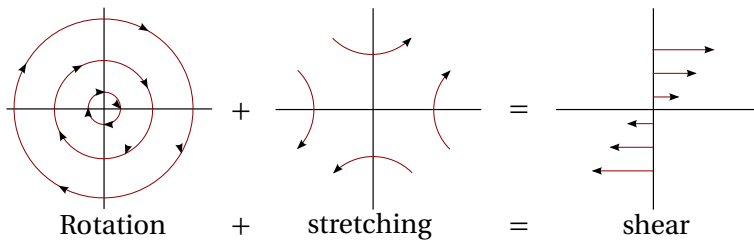


Figure 3.1: Decomposition of the simple shear flow into rotation and strain.

3.4 Simple shear flow

The simple shear flow is a uni-directional linear flow which varies in magnitude in only one transversal direction. It is shown in Fig. 3.1. The equation describing the shear flow is simply,

$$\mathbf{u}(y) = s y \hat{\mathbf{x}}. \quad (3.22)$$

Here s is a scalar called the shear strength, and y is the coordinate along the $\hat{\mathbf{y}}$ -axis. Fig. 3.2 shows the coordinate system we use for shear flows in this thesis and in the appended papers. The three principal directions are the flow direction $\hat{\mathbf{x}}$, the shear direction $\hat{\mathbf{y}}$ and the vorticity direction $\hat{\mathbf{z}}$. The vorticity direction $\hat{\mathbf{z}}$ is also the direction of $\boldsymbol{\Omega}$ introduced in Sec. 3.1.1.

The flow gradient of the simple shear flow is constant and in cartesian coordinates given by

$$\mathbf{A} = \begin{bmatrix} 0 & s & 0 \\ 0 & 0 & 0 \\ 0 & 0 & 0 \end{bmatrix}. \quad (3.23)$$

The shear flow is important for two reasons. First, it is one of the fundamental flows in rheology, the study of fluids. It is the flow inside an ideal Couette device, used for example to measure viscosity. Second, as far as particle dynamics go, the simple shear flow is relevant for *any* flow with parallel streamlines. Consider for example the laminar flow of a suspension through a pipe. The pipe is assumed to be large compared to the suspended particles, and the flow profile is most likely a complicated function of position y in the



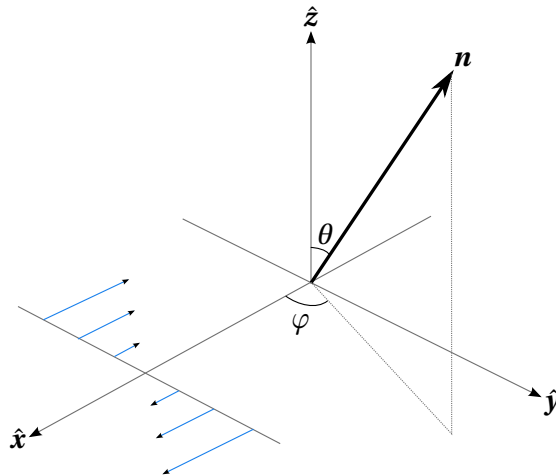


Figure 3.2: Coordinate system of simple shear flow in this thesis. The directions are the flow direction \hat{x} , the shear direction \hat{y} , and the vorticity direction \hat{z} . The angles (θ, φ) are the spherical coordinates of the particle direction \mathbf{n} .

pipe cross section²:

$$\mathbf{u}(y) = f(y)\hat{x}, \quad (3.24)$$

and the flow gradient is

$$\mathbb{A} = \begin{bmatrix} 0 & f'(y) & 0 \\ 0 & 0 & 0 \\ 0 & 0 & 0 \end{bmatrix}. \quad (3.25)$$

Thus, if the flow profile f varies slowly over the particle size, the particle experiences a simple shear flow of strength $f'(y)$. This is the case in the experiment described in Paper E.

Curiously, the dynamics of an ellipsoidal particle in a viscous shear flow offers a rich variety of behaviours. There is no stationary state, but a particle tumbles end-to-end indefinitely. If the particle is axisymmetric, the tumbling is periodic. The technical details and explanations of this are discussed in

²In principle the function should also depend on the position in the z -direction. In that case the result is also a simple shear flow, although rotated.



Sec. 3.5, but we can understand the underlying reason from the composition of the shear flow. Fig. 3.1 illustrates schematically how the shear is a superposition of two flows. One is a pure rotation, corresponding to the antisymmetric part \mathbb{O} of the flow gradient. The other is a pure strain, the symmetric part \mathbb{S} of the flow gradient. Now imagine a rod-shaped particle in these flows. The pure rotation, the vorticity, will rotate the rod with a constant angular velocity, regardless of the rod's orientation. The strain, on the other hand, has a preferred direction to which it will attract the long axis of the rod. Sometimes the vorticity and strain will cooperate to turn the rod onto the strain eigendirection, and sometimes the vorticity will struggle to rotate the rod out of the attracting direction. The result is that the rod will always rotate, but sometimes faster and sometimes slower. When the difference between the fast and the slow rotations is large, we perceive this as intermittent tumbling.

3.5 The Jeffery equation and its solutions

The main result of Jeffery [2] is the hydrodynamic torque \mathbf{T} on a general ellipsoid rotating in a viscous shear flow (his Eq. (36)). In other words, he computed the elements of the resistance tensors in Eq. (3.21). Some elements were known to Jeffery from earlier work by Oberbeck [22] and Edwardes [23]. However, Jeffery completed what is arguably the hardest part of the calculation, and has received the most credit for this work.

The viscous torque is calculated neglecting the effects of fluid inertia, $\text{Re}_s = 0$. To be consistent (see Section 3.2.2) we also neglect the effects of particle inertia, $\text{St} = 0$. This is the overdamped limit where the equation of motion is determined by a static force and torque balance. Jeffery [2] found the angular velocity of the particle by solving $\mathbf{T} = 0$. Here I give the result in my notation, the details are available in Appendix A.

We represent the shape and orientation of an ellipsoid by the lengths (a_1, a_2, a_3) and directions $(\mathbf{n}_1, \mathbf{n}_2, \mathbf{n}_3)$ of the three half-axes. Then \mathbf{n}_1 gives the direction of the axis with length a_1 , and so on. The angular velocity of the particle depends on the flow gradients, the particle orientation and the aspect ratios of the particle as

$$\boldsymbol{\omega} = \boldsymbol{\Omega} + \frac{\Lambda - K}{K\Lambda - 1} (\mathbf{n}_2^T \mathbb{S} \mathbf{n}_3) \mathbf{n}_1 + \Lambda (\mathbf{n}_3^T \mathbb{S} \mathbf{n}_1) \mathbf{n}_2 - K (\mathbf{n}_1^T \mathbb{S} \mathbf{n}_2) \mathbf{n}_3, \quad (3.26)$$



where

$$K = \frac{\kappa^2 - 1}{\kappa^2 + 1}, \quad \Lambda = \frac{\lambda^2 - 1}{\lambda^2 + 1}, \quad \lambda = a_3/a_1, \quad \kappa = a_2/a_1. \quad (3.27)$$

Here Ω and S are the flow rotation and strain as defined in Section 3.1.1. The coefficients Λ and K are the *shape parameters*, and for an ellipsoid $-1 < \Lambda, K < 1$. A sphere is described by $\Lambda = K = 0$. If either Λ or K is zero, the particle is an axisymmetric spheroid. Eq. (3.26) is valid for most particles with the same mirror symmetries as an ellipsoid, with a suitable redefinition of Λ and K [16, 17, 24]. More precisely, there are other particle shapes described by resistance tensors of the same *form*, but different numerical values of the elements.

We rename $\mathbf{n} = \mathbf{n}_3$ and $\mathbf{p} = \mathbf{n}_2$, and compute their equation of motion by $\dot{\mathbf{n}}_i = \boldsymbol{\omega} \times \mathbf{n}_i$ (details in Appendix A):

$$\begin{aligned} \dot{\mathbf{n}} &= \mathbb{O}\mathbf{n} + \Lambda(S\mathbf{n} - (\mathbf{n}^T S\mathbf{n})\mathbf{n}) + \frac{K(1-\Lambda^2)}{K\Lambda-1}(\mathbf{n}^T S\mathbf{p})\mathbf{p}, \\ \dot{\mathbf{p}} &= \mathbb{O}\mathbf{p} + K(S\mathbf{p} - (\mathbf{p}^T S\mathbf{p})\mathbf{p}) + \frac{\Lambda(1-K^2)}{K\Lambda-1}(\mathbf{n}^T S\mathbf{p})\mathbf{n}. \end{aligned} \quad (3.28)$$

Eq. (3.28) is the Jeffery equation of motion for the axes of a triaxial ellipsoid. Recall that $\mathbb{O}\mathbf{n} = \boldsymbol{\Omega} \times \mathbf{n}$. The motion of the third axis is fully determined by $\mathbf{n}_3 = \mathbf{n} \times \mathbf{p}$. The equations are symmetric under the simultaneous exchange of $\Lambda \leftrightarrow K$ and $\mathbf{n} \leftrightarrow \mathbf{p}$, because the new equations describe the same physical situation with the axes permuted.

For a simple shear flow Eq. (3.28) is *reversible* in the general sense [25]: the equations are symmetric under $(t, n_x, p_x) \rightarrow (-t, -n_x, -p_x)$, with \hat{x} the flow direction of the shear flow. A reversible dynamical system shares many properties with conservative ('Hamiltonian') systems [25]. In particular, around any elliptic fixed point there must exist a family of periodic orbits. In Section 3.5.2 we will see that this is exactly the case for the solutions of Eq. (3.28) for a triaxial particle in shear flow.

In the following we will study the solutions to Eq. (3.28) in some detail. But it is helpful to first inspect the meaning of the different terms in the equation of motion:

The first term means that the particle is rotated by the local flow vorticity, and that this rotation is independent of the particle shape.



The second term means that the local rate-of-strain attracts the particle axis to the strongest eigendirection of \mathbb{S} . The strength of the attraction is affected by the particle shape. The more elongated an axis is, the stronger the attraction becomes. The non-linear part $-(\mathbf{n}^T \mathbb{S} \mathbf{n}) \mathbf{n}$ simply preserves the unit magnitude of the vector \mathbf{n} , and it has no physical meaning. This fact is explained in detail in Section 3.5.1.

The third and last term couples the motion of \mathbf{n} and \mathbf{p} . This is because the local rate-of-strain will try to align all elongated axes. But since the particle is a rigid body, this is not possible. Instead there is competition, and the outcome depends on the relative elongation of the axes. If the particle is axisymmetric, say $K = 0$, there is only one elongated axis and therefore no competition. This case is described in detail in Section 3.5.1. The general case of a triaxial ellipsoid in a simple shear flow is discussed in Section 3.5.2.

3.5.1 Axisymmetric particles

In this section we consider axisymmetric particles: particles which are rotationally symmetric around an axis of symmetry. For such particles the shape factor $K = 0$, and Eq. (3.28) reduces to

$$\dot{\mathbf{n}} = \mathcal{O}\mathbf{n} + \Lambda(\mathbb{S}\mathbf{n} - (\mathbf{n}^T \mathbb{S} \mathbf{n}) \mathbf{n}), \quad (3.29)$$

$$\dot{\mathbf{p}} = \mathcal{O}\mathbf{p} - \Lambda(\mathbf{n}^T \mathbb{S} \mathbf{p}) \mathbf{n}. \quad (3.30)$$

The vector \mathbf{n} describes the direction of the symmetry axis of the particle, see Fig. 3.3. The vector \mathbf{p} describes the rotation around the symmetry axis. The equations for \mathbf{n} and \mathbf{p} are decoupled: we may first solve Eq. (3.29) for $\mathbf{n}(t)$, then Eq. (3.30) is a linear equation for $\mathbf{p}(t)$. In this Section we will neglect the dynamics of \mathbf{p} , it is discussed in Section 3.5.2.

Eq. (3.29) is a non-linear vector equation, and as such it is seemingly hard to solve. However, the non-linearity is only apparent: it is due to the geometric constraint that \mathbf{n} is a unit vector. The underlying dynamics is in fact linear. I will now explain two ways to understand this fact.

The vorticity \mathcal{O} rotates \mathbf{n} , and the strain \mathbb{S} aligns and stretches \mathbf{n} towards its strongest eigendirection. The non-linear term $\mathbf{n} \mathbf{n}^T \mathbb{S} \mathbf{n}$ is simply the stretching component of the strain, which is subtracted in order to prevent elongation of \mathbf{n} . Bretherton (Sec. 6 in Ref. 24) realised that we may instead model the orientation of the particle with any vector \mathbf{q} which obeys the same



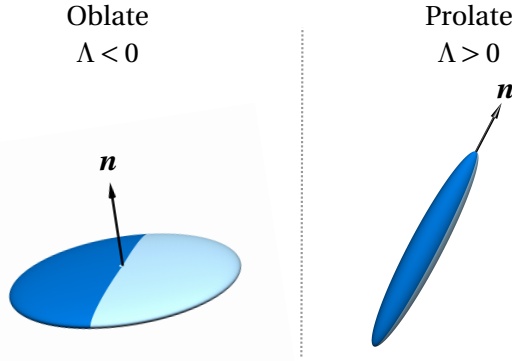


Figure 3.3: Illustration of axisymmetric particles and the definition of the vector n . *Left:* Oblate, disk-shaped particle. *Right:* Prolate, rod-shaped particle.

linear terms, but without compensating for any elongation:

$$\dot{\mathbf{q}} = (\mathbb{O} + \Lambda \mathbb{S}) \mathbf{q}. \quad (3.31)$$

Owing to the common linear terms in Eq. (3.29) and Eq. (3.31), the vector \mathbf{q} will have the same angular dynamics as \mathbf{n} . In addition, \mathbf{q} may be stretched and compressed by the strain \mathbb{S} . But since we are only interested in the angular degrees of freedom, we can at any instant recover \mathbf{n} by normalising \mathbf{q} to unit length. Thus, the general solution of the Jeffery equation is given by solving Eq. (3.31) for $\mathbf{q}(t)$, then the solution to Eq. (3.29) is given by normalising $\mathbf{q}(t)$ to unit length:

$$\mathbf{n}(t) = \frac{\mathbf{q}(t)}{|\mathbf{q}(t)|}. \quad (3.32)$$

Another, more mathematical, way of understanding how the linear companion equation (3.31) arises is the following. Like above, we choose to represent the particle orientation by a vector \mathbf{q} which is parallel to \mathbf{n} . Define $\mathbf{q} = \alpha(t)\mathbf{n}$, with $\alpha(t)$ an arbitrary function of time. We know from this definition that we may always recover \mathbf{n} by normalising \mathbf{q} to unit length. Now, we can calculate the equation of motion for \mathbf{q} :

$$\frac{d\mathbf{q}}{dt} = \frac{d}{dt}(\alpha\mathbf{n}) = \dot{\alpha}\mathbf{n} + \alpha(\mathbb{O}\mathbf{n} + \Lambda(\mathbb{S}\mathbf{n} - \mathbf{n}\mathbf{n}^T\mathbb{S}\mathbf{n})). \quad (3.33)$$



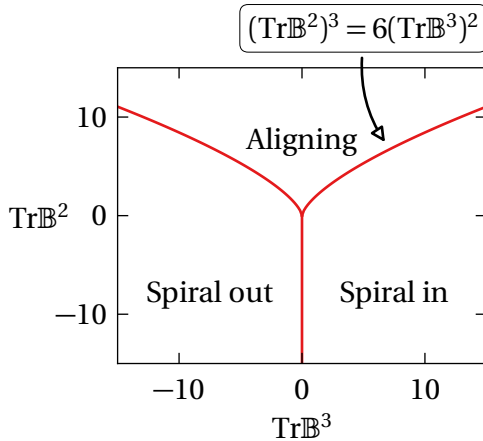


Figure 3.4: Map of the three possible types of particle motion, as determined by the eigensystem of $\mathbb{B} = \mathbb{O} + \Lambda \mathbb{S}$. On the red line between “Spiral out” and “Spiral in” the motion is on a closed orbit.

But $\alpha(t)$ is an arbitrary function which we may choose. In particular we can choose $\alpha(t)$ to be a function satisfying

$$\dot{\alpha} = \alpha \Lambda \mathbf{n}^T \mathbb{S} \mathbf{n}. \quad (3.34)$$

By inserting this choice of $\alpha(t)$ into Eq. (3.33), we again arrive at Eq. (3.31).

We now consider the solutions of Jeffery's equation in a time-independent linear flow. This case includes for example the simple shear flow. It is also a useful model when the flow changes only slowly in time, compared to the time it takes for the gradients to affect the particle orientation. First, I will describe the possible solutions of Eq. (3.29) in linear flows. Second, I will discuss the solutions of Jeffery's equation in a simple shear flow. These solutions are called the Jeffery orbits, and they play an important role in Papers A-E.

When \mathbb{O} and \mathbb{S} are time-independent the linear companion equation (3.31) is solved by the matrix exponential:

$$\mathbf{q}(t) = e^{(\mathbb{O} + \Lambda \mathbb{S})t} \mathbf{q}(0). \quad (3.35)$$



This solution implies that the long-time dynamics of \mathbf{q} , and therefore \mathbf{n} , is determined by the eigenvalues and eigenvectors of the matrix $\mathbb{B} = \mathbb{O} + \Lambda \mathbb{S}$. For an incompressible flow $\text{Tr}\mathbb{B} = 0$, because $\text{Tr}\mathbb{A} = 0$. In three spatial dimensions, the three eigenvalues of \mathbb{B} must sum to zero. Thus, as noted by Bretherton [24], there are four distinct possibilities for the eigensystem of \mathbb{B} :

1. Three real eigenvalues, then

\mathbf{q} aligns with the eigenvector corresponding to the largest eigenvalue.

2. One real eigenvalue $a > 0$, and a complex pair $-a/2 \pm i\omega$, then

\mathbf{q} spirals into alignment with the eigenvector corresponding to the real eigenvalue.

3. One real eigenvalue $a < 0$, and a complex pair $-a/2 \pm i\omega$, then

\mathbf{q} spirals out towards infinity in the plane that contains the origin and is spanned by the real and imaginary parts of the complex eigenvector.

4. One real eigenvalue $a = 0$, and an imaginary pair $\pm i\omega$, then

\mathbf{q} rotates indefinitely in a closed elliptic orbit in a plane that contains the initial condition and is spanned by the real and imaginary parts of the complex eigenvector.

The characteristic equation for the eigenvalues b of a 3×3 -matrix \mathbb{B} is

$$-b^3 + b^2 \text{Tr}\mathbb{B} + \frac{b}{2} (\text{Tr}\mathbb{B}^2 - (\text{Tr}\mathbb{B})^2) + \det\mathbb{B} = 0. \quad (3.36)$$

But for a traceless matrix $\text{Tr}\mathbb{B} = 0$ and $\det\mathbb{B} = \text{Tr}\mathbb{B}^3/3$, because

$$\text{Tr}\mathbb{B} = b_1 + b_2 + b_3 = 0 \implies b_3 = -(b_1 + b_2), \quad (3.37)$$

therefore

$$\text{Tr}\mathbb{B}^3 = b_1^3 + b_2^3 + b_3^3 = -3(b_1^2 b_2 + b_1 b_2^2), \quad (3.38)$$

$$\det\mathbb{B} = b_1 b_2 b_3 = -(b_1^2 b_2 + b_1 b_2^2). \quad (3.39)$$



Thus the characteristic equation simplifies to

$$-b^3 + \frac{b}{2} \text{Tr}\mathbb{B}^2 + \frac{1}{3} \text{Tr}\mathbb{B}^3 = 0. \quad (3.40)$$

It is possible to solve Eq. (3.40) exactly for the eigenvalues, but the important observation is that they are determined by only two parameters: $\text{Tr}\mathbb{B}^2$ and $\text{Tr}\mathbb{B}^3$. In Fig. 3.4 I illustrate how the three cases outlined above correspond to different values of $\text{Tr}\mathbb{B}^2$ and $\text{Tr}\mathbb{B}^3$. The boundary curve of the region of three real eigenvalues is where the discriminant Δ of the characteristic equation is zero:

$$\Delta = (\text{Tr}\mathbb{B}^2)^3 - 6(\text{Tr}\mathbb{B}^3)^2 = 0. \quad (3.41)$$

In the region where there is a pair of complex eigenvalues, the two cases of spiral in or out are separated by $\text{Tr}\mathbb{B}^3 = 0$. For any given flow gradient, changing the particle from rod-like to disk-shaped (or vice versa) transforms $\text{Tr}\mathbb{B}^3 \rightarrow -\text{Tr}\mathbb{B}^3$ and therefore change the qualitative dynamics from aligning to rotating (or vice versa). This transformation may be understood because

$$\text{Tr}\mathbb{B}^3 = 3\Lambda \text{Tr}\mathbb{O}\mathbb{O}\mathbb{S} + \Lambda^3 \text{Tr}\mathbb{S}\mathbb{S}\mathbb{S}. \quad (3.42)$$

The other combinations of \mathbb{S} and \mathbb{O} which could be expected to contribute, such as $\text{Tr}\mathbb{O}\mathbb{O}\mathbb{O}$, vanish identically because of symmetries of \mathbb{O} and \mathbb{S} . As explained above, changing a particle from rod-like to disk-shaped implies a change of sign of the shape factor Λ . We discussed the implications of this observation for the tumbling of particles in turbulent and random flows in an earlier paper [26].

Jeffery Orbits

The remainder of this section concerns the case of simple shear flow. This case is characterised by $\text{Tr}\mathbb{B}^3 = 0$ and $\text{Tr}\mathbb{B}^2 < 0$. The simple shear has a special position among flows, and we understand the significance of the condition $\text{Tr}\mathbb{B}^3 = 0$ from the above discussion: First, a change of particle shape does not change the qualitative dynamics. Both disk-shaped particles and rod-like particles rotate in a shear flow. Second, \mathbb{B} has a zero eigenvalue, as seen from the characteristic equation (3.40). The zero eigenvalue is important, because it implies that the particle dynamics never forgets its initial condition.



The eigenvector of the zero eigenvalue is the vorticity direction³, thus the component of \mathbf{q} in the vorticity direction is constant in a shear flow. The other two eigenvalues form an imaginary pair, resulting in a periodic rotation of \mathbf{q} .

In summary, the dynamics of \mathbf{q} in a simple shear flow is a periodic rotation in a plane. The plane is normal to the vorticity direction, and determined by the initial condition of \mathbf{q} .

When the trajectories $\mathbf{q}(t)$ are projected onto the unit sphere, the result $\mathbf{n}(t)$ are the Jeffery orbits. I visualise this in Fig. 3.5 where the trajectories $\mathbf{q}(t)$ and $\mathbf{n}(t)$ are shown for three different initial conditions.

The orbits on the north and south hemispheres are the same, because of the particle inversion symmetry: changing $\mathbf{n} \rightarrow -\mathbf{n}$ implies $\dot{\mathbf{n}} \rightarrow -\dot{\mathbf{n}}$. The orbits are also symmetric under a 180 degree rotation around the vorticity, $\mathbf{n} \rightarrow \mathbb{R}_\pi \mathbf{n}$ implies $\dot{\mathbf{n}} \rightarrow \mathbb{R}_\pi \dot{\mathbf{n}}$, because of the symmetry of the shear flow. These two symmetries together enforce that no orbit may cross the equator of the sphere, because on the equator the two symmetries coincide but have different sign. The Jeffery orbit which is exactly on the equator of the sphere is called the *tumbling orbit*, because the vector \mathbf{n} tumbles in the flow-shear plane. The orbit at a pole of the sphere, where \mathbf{n} is aligned with the vorticity direction, is called the *log-rolling* orbit. The name refers to the motion of a rod which rolls around its axis of symmetry, but the name is used for both prolate and oblate particles. Log-rolling for an oblate particle means that it spins like a frisbee. These particular orbits are depicted in Fig. 3.6.

The solutions to Jeffery's equation in a simple shear flow are degenerate: the orientational trajectory depends on the initial condition indefinitely. The degeneracy is a result of the assumptions made in the course deriving the Jeffery orbits. The Jeffery equation neglects the effects of both fluid and particle inertia. In fact, Jeffery suggested that inertia should dissolve the degeneracy and lead to a determinate prediction. My work in the Papers A-D resolves this question. Although Jeffery was right in principle, it did not turn out exactly like he envisaged it. This is described in detail in Section 4.

One might expect that the degeneracy of the Jeffery orbits is lifted for a particle that is not perfectly axisymmetric. This is not the case. However, the trajectories are much more intricate. This is the topic of Section 3.5.2.

³See Fig. 3.2 and Sec. 3.4 for the definition of the coordinate system and the terminology of its directions in a simple shear flow.



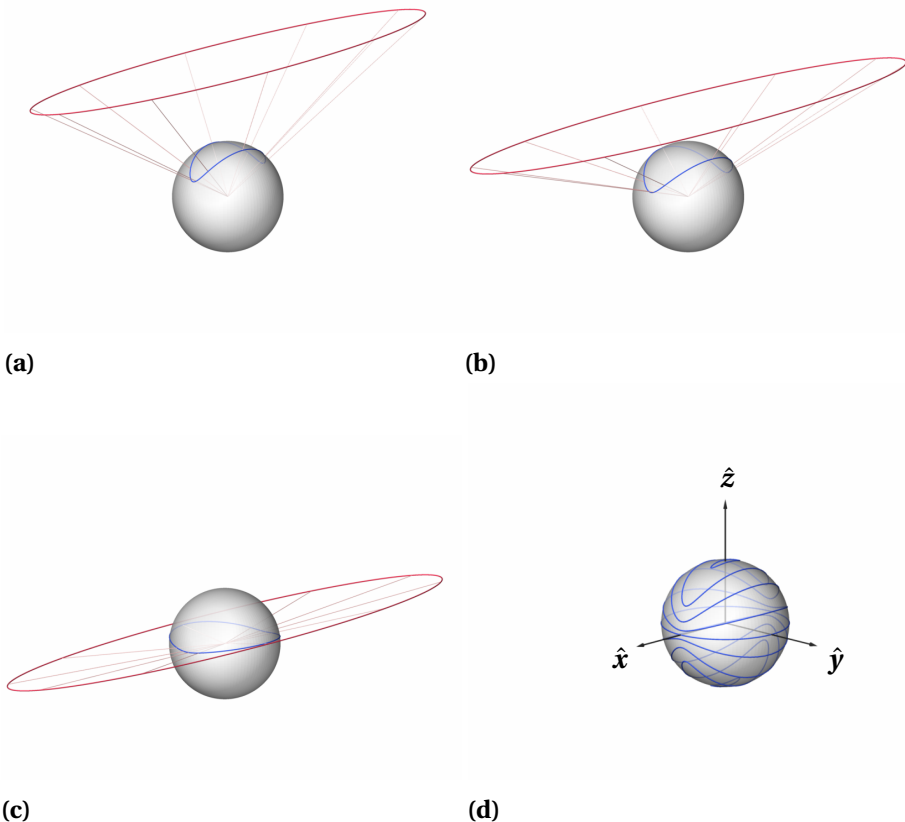


Figure 3.5: (a-c) Illustrations of how the trajectories $\mathbf{q}(t)$ (red) produces the Jeffery orbits $\mathbf{n}(t)$ (blue) upon projection onto the unit sphere. (d) Sample of resulting Jeffery orbits with coordinate system. All trajectories correspond to a particle of aspect ratio $\lambda = 5$ in a simple shear flow.



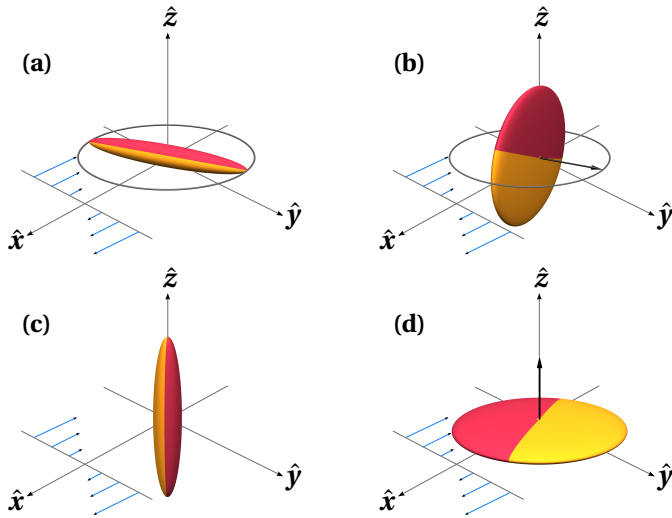
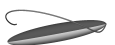


Figure 3.6: Illustration of the tumbling and log-rolling orbits it a simple shear flow. **(a)** prolate tumbling, **(b)** oblate tumbling, **(c)** prolate log-rolling, **(d)** oblate log-rolling.

3.5.2 Non-axisymmetric particles

In this Section I describe the solutions to the Jeffery equation (3.28) for a triaxial particle in a simple shear flow. It turns out that a triaxial particle also tumbles, but in a much more complicated fashion than the Jeffery orbits for an axisymmetric particle [27–29]. In general no closed form solutions are known, therefore we rely on numerical solutions in this section.

A rotation in three dimensions has three degrees of freedom, but in general it is complicated to represent rotations because there is no simple set of three coordinates which covers all rotations without singularities. The vectors \mathbf{n} and \mathbf{p} in Eq. (3.28) are physically intuitive, but mathematically their six components are strongly redundant because of the constraints $|\mathbf{n}| = |\mathbf{p}| = 1$ and $\mathbf{n} \cdot \mathbf{p} = 0$. For the purpose of visualisations, we use Euler angle coordinates in the Goldstein z - x' - z'' convention [30]: Start from $\mathbf{n}_i = \mathbf{e}_i$, with \mathbf{e}_i a fixed frame of reference. First rotate the \mathbf{n}_i by φ around \mathbf{n}_3 , then by θ around the resulting \mathbf{n}_1 and finally by ψ around the resulting \mathbf{n}_3 . With the shorthand



$c x = \cos x$ and $s x = \sin x$ the elements of the rotation matrix are

$$\mathbb{R} = \begin{pmatrix} c\varphi c\psi - c\theta s\varphi s\psi & c\psi s\varphi + c\theta c\varphi s\psi & s\theta s\psi \\ -c\theta c\psi s\varphi - c\varphi s\psi & c\theta c\varphi c\psi - s\varphi s\psi & c\psi s\theta \\ s\theta s\varphi & -c\varphi s\theta & c\theta \end{pmatrix}. \quad (3.43)$$

The rows of this matrix are the components of \mathbf{n}_i along the coordinate axes \mathbf{e}_i . In particular the second and third rows are the elements of \mathbf{p} and \mathbf{n} . Hinch & Leal [28] showed that in the absence of noise $\dot{\varphi} < 0$. This means that the tumbling of a triaxial particle shares one property with the Jeffery orbits: the vector \mathbf{n} monotonically rotates around the vorticity. It is therefore natural to regard the orientation space as a torus, in which the deterministic trajectories go around, see Fig. 3.7. Each transversal slice of constant φ of this torus is a *Poincaré surface-of-section* [31] which intersects all trajectories, schematically shown in Fig. 3.7.

We follow Hinch & Leal [28] and choose the surface-of-section $\varphi = 2n\pi$. This corresponds to $n_x = 0, n_y < 0$. We solve Eq. (3.28) numerically for many different initial conditions. Every time a trajectory passes through the surface-of-section we plot a point at the corresponding value of $n_z = \cos \theta$ and ψ , see Fig. 3.8. Four examples for $\lambda = 5$ and increasing values of κ are shown in Figs. 3.9-3.12.

Fig. 3.9 shows the surface-of-section for an axisymmetric particle. The horizontal lines are the Jeffery orbits of an axisymmetric particle. Every time a trajectory reaches the surface-of-section, the value of n_z is the same, because the Jeffery orbits are strictly periodic in \mathbf{n} . However, it turns out that the value of ψ is in general not periodic. This means that the vector \mathbf{p} does not, in general, make one revolution around \mathbf{n} for every Jeffery orbit. The strict periodicity of the Jeffery orbits really only applies to the motion of the symmetry axis. This detail has no physical implications for the motion. But if we were to paint a pattern on a particle, and observe the motion experimentally, this aperiodicity would be apparent.

For the trajectory of a nearly axisymmetric particle neither n_z , nor ψ is constant. The structure of trajectories on the surface-of-section is more complicated, with closed ellipses near $n_z \approx 0$, and curved lines towards $n_z \approx \pm 1$, shown in Fig. 3.10. The point $(0, 0)$ on the surface-of-section is an elliptic fixed point. As explained in Section 3.5 the dynamical system (3.28) is reversible, and consequently the dynamics around the fixed point is described by a one-parameter family of closed orbits [25].



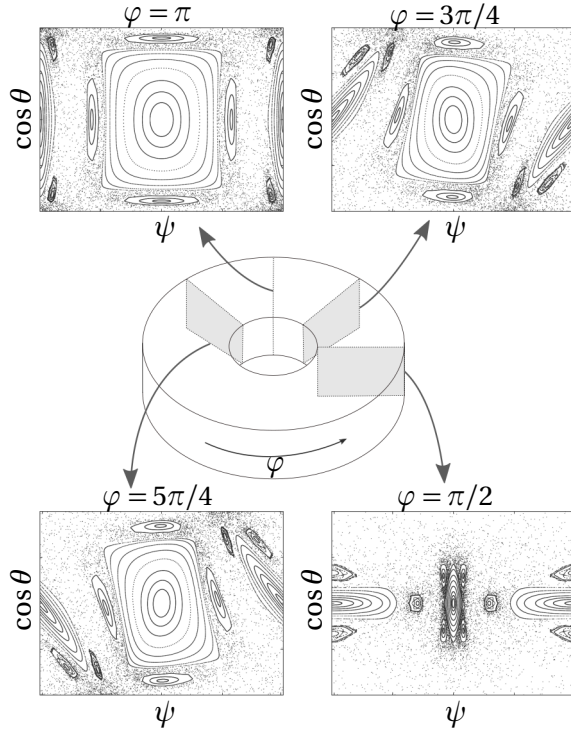


Figure 3.7: Schematic explanation of the surfaces-of-section for the orientational dynamics of triaxial ellipsoids in shear flow. The torus depicts the three-dimensional orientational space for an ellipsoid. The major axis of the ellipsoid rotates monotonously around the vorticity [28], depicted by the azimuthal angle φ along the torus. The surfaces-of-sections shown correspond to the major axis pointing the direction along the flow, along the extensional strain, perpendicular to the flow, and along the compressing strain. The surfaces-of-section at $\varphi \rightarrow \varphi + \pi$ are equal, because the flow is symmetric under this rotation. Surfaces-of-section computed by G. Almondo.



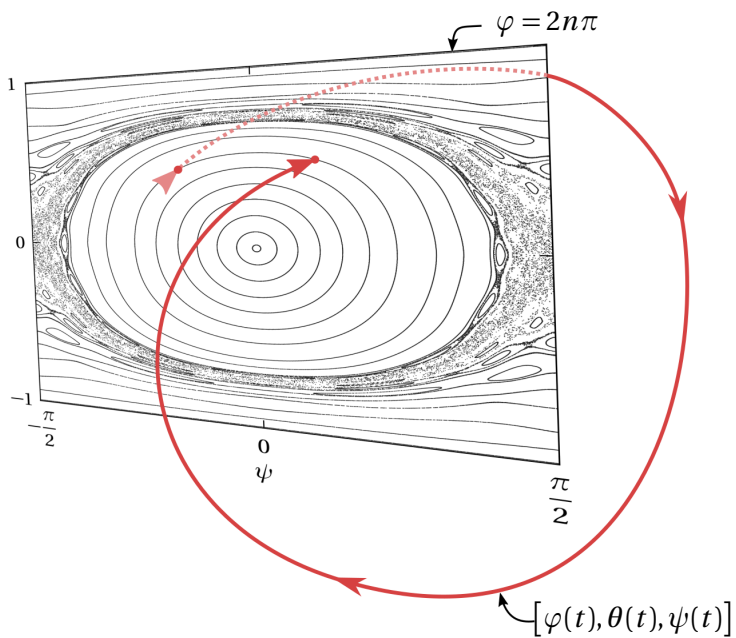


Figure 3.8: Illustration of the surface-of-section $\varphi = 2n\pi$. The trajectory (in red) starts at a point in the surface-of-section, makes one revolution of φ in phase-space, and returns to another point on the same curve in the surface-of-section. We create a picture of the surface-of-section by computing many trajectories with many different initial condition and plotting a point at each hit.



A trajectory is always confined to the curve on which it started. In this sense the orientational dynamics of a triaxial particle is degenerate, just like the Jeffery orbits for an axisymmetric particle. No orbit is physically preferred over any other, but the dynamics are determined by the initial condition.

The degeneracy of these solutions may be broken by the effect of particle and fluid inertia, like in the case of axisymmetric particles. Lundell [32] show numerical simulations for $Re_s = 0$ but $St > 0$ which support this expectation. The method used in Papers A-D and Refs. [33, 34] can in principle be extended to the case of ellipsoids. However, that calculation will involve rather large amounts of algebra.

When we consider a significantly non-axisymmetric particle, the trajectories on the surface-of-section look very different, like in Fig. 3.11 and Fig. 3.12. Many initial conditions lead to deterministic chaos, which shows up as areas full of gray dots without apparent structure. A trajectory starting in this chaotic layer can go anywhere else inside it.

In Paper E we describe experimental observations of micro-sized glass rods in a microfluidic channel flow. We argue that their orientational motion is consistent with the solutions presented in this Section although the analysis is complicated by the fact that we can not resolve the angle ψ in the experiment. This is further described in Section 5 and Paper E.



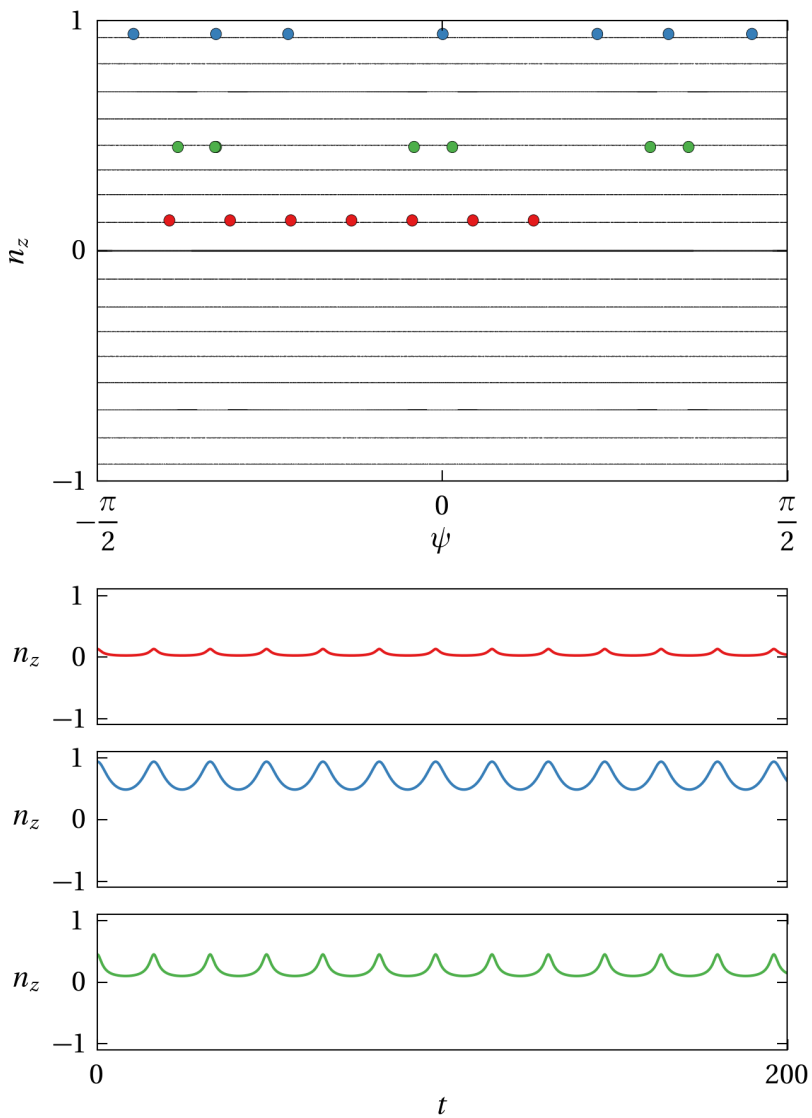


Figure 3.9: Top: Poincaré surface-of-section of an axisymmetric particle with aspect ratios $\lambda = 5$, $\kappa = 1$. Bottom: Examples of what $n_z(t)$ looks like, given the trajectory indicated by the color coded markers on the surface-of-section.



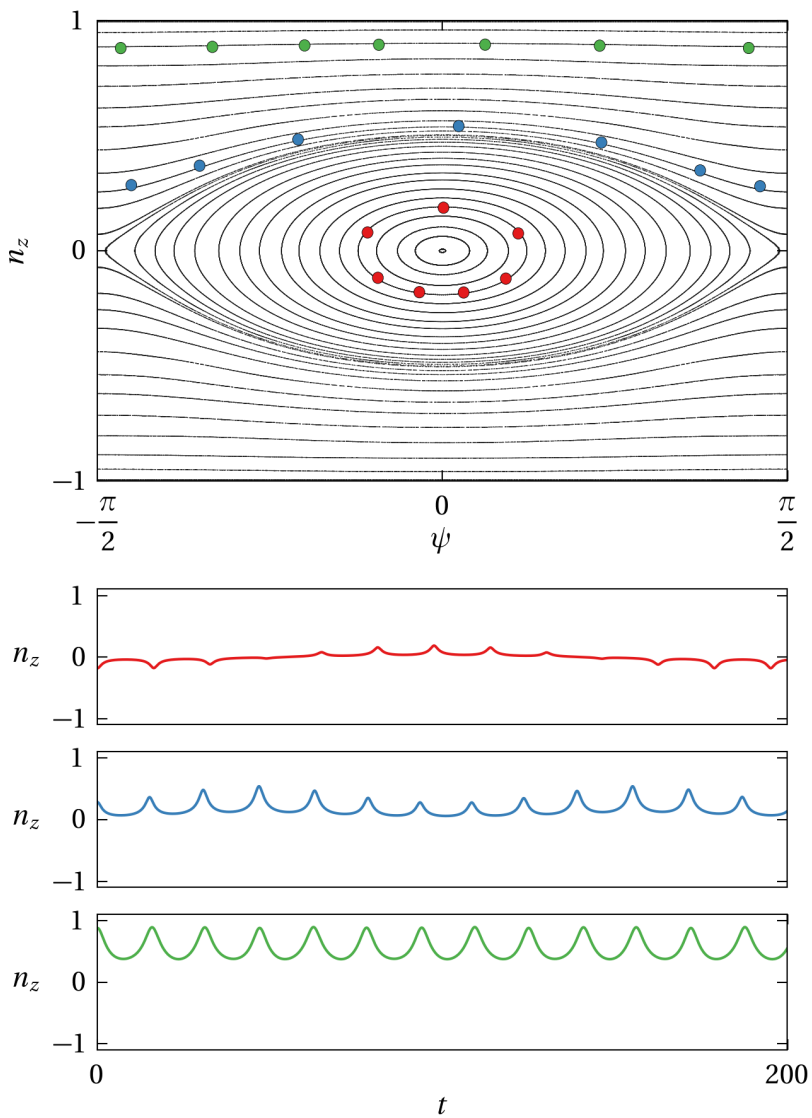


Figure 3.10: Top: Poincaré surface-of-section of an asymmetric particle with aspect ratios $\lambda = 5$, $\kappa = 1.1$. Bottom: Examples of what $n_z(t)$ looks like, given the trajectory indicated by the color coded markers on the surface-of-section.



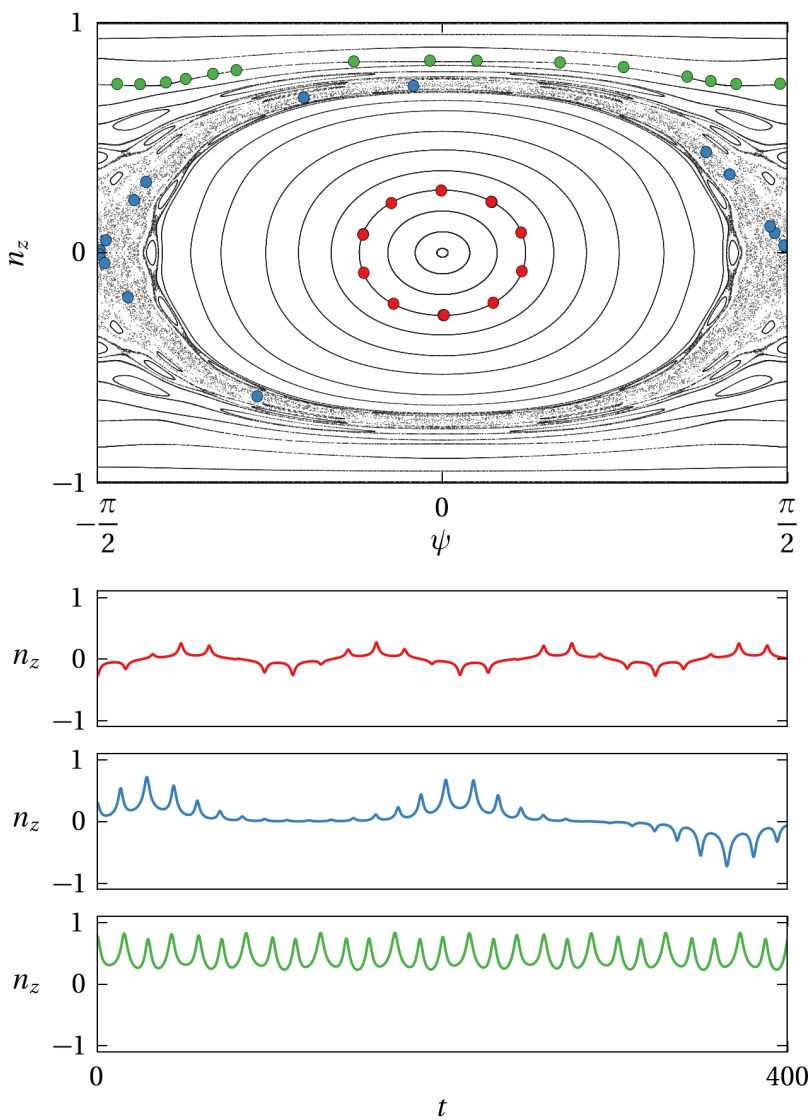


Figure 3.11: Top: Poincaré surface-of-section of an axisymmetric particle with aspect ratios $\lambda = 5$, $\kappa = 1.3$. Bottom: Examples of what $n_z(t)$ looks like, given the trajectory indicated by the color coded markers on the surface-of-section.



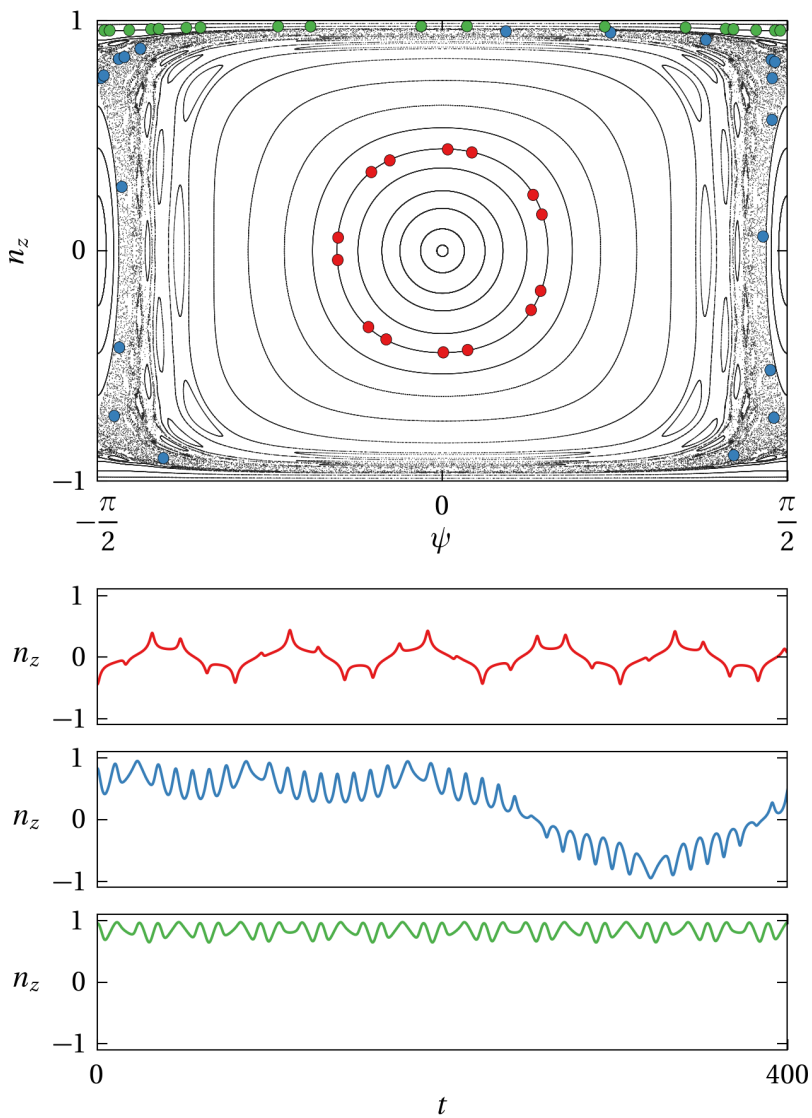


Figure 3.12: Top: Poincaré surface-of-section of an axisymmetric particle with aspect ratios $\lambda = 5$, $\kappa = 2$. Bottom: Examples of what $n_z(t)$ looks like, given the trajectory indicated by the color coded markers on the surface-of-section.



S

*Men då mitt skarpsinne visade sig otillräckligt
även för detta, slungade jag schackbrädet ut
genom fönstret i huvudet på en gammal man
med träben, för vilken döden endast var en
välgärning, och kastade mig därefter ut i
världsvimlet, föraktande mig själv.*

ur *Spleen*, av Hjalmar Söderberg



S

PART II

MY WORK

In the following three Sections I give the context and main results of my recent work.

In Section 4 I describe the development of an effective equation of motion for the orientation of a neutrally buoyant spheroid suspended in a simple shear flow, valid when inertial effects are weak but not vanishing. In short, we calculate what happens to the Jeffery orbits when the particle Reynolds number is non-zero. The results are contained in the appended Papers A-D.

The other two studies also relate to the orientational motion of non-spherical particles, and their common denominator is that they involve Jeffery's theory for ellipsoidal particles. The first, in Section 5, is a microfluidic experiment aiming to validate Jeffery's theory for the rotation of triaxial particles in shear flow (Paper E). The second, in Section 6, is a description of the rotational modes of small disks and rods in isotropic turbulence, combining data from experiments, direct numerical simulations and random flow theory (Paper F).

4 Effects of inertia on the Jeffery orbits

This project is a collaboration with colleagues in Cherbourg and Marseille (France), and Stockholm (Sweden). J.R. Angilella (Cherbourg) and F. Candelier (Marseille) have many years of experience in dynamical systems, fluid mechanics and perturbation theory, without which this project would not have landed. T. Rosén and F. Lundell in Stockholm are experts in direct numerical simulation of particulate flows by the lattice Boltzmann method, by which we could validate our calculations. I also attribute the initial idea to perform stability analysis on the log-rolling motion under inertial perturbation, however vague at the time, to F. Lundell at a COST meeting in Udine, Italy.



Paper A is a brief summary of the calculation and result in letter form, while the Papers B & C contain all details. Paper D describes the direct numerical simulations that validate our theoretical calculation, and show in detail when the effective equations break down due to finite domain size and increasing importance of inertial effects.

4.1 History of problem

The Jeffery equations for an axisymmetric particle in simple shear flow are interesting because their solutions are degenerate, as explained in Section 3.5.1. Their solutions form a one-parameter family of periodic orbits. No orbit is preferred over another, so that the initial condition determines the dynamics indefinitely. Jeffery was very aware of this fact, he writes "It is obviously undesirable to leave a problem, which is physically quite determinate, in this indeterminate form." He further conjectures that "this failure is due to the limitations of the theory of the slow motion of a viscous fluid." In other words, he believed that inertial corrections were necessary to break the degeneracy. He concludes, referring to inertial corrections, "[...] a more complete investigation would reveal the fact that the particles do tend to adopt special orientations..." In connection with this discussion Jeffery hypothesized that this preferred orientation would be such that the energy dissipated by viscosity is minimized: a prolate particle ends up log-rolling (long axis along the vorticity), and an oblate particle tumbles (with a diameter along vorticity.)

Saffman [35] made the first attempt to include the non-linear inertial terms. It seems, although details are sparse, that he used an early form of asymptotic matching. For this he acknowledges I. Proudman, who a year later co-authored a paper [36] on the inertial correction to the drag on a translating sphere, pioneering the use of asymptotic matching in viscous fluid mechanics. But Saffman did not have the proper solution to the outer "Oseen problem" for matching, instead he invented a plausible but ad-hoc boundary condition to match the inner expansion. With this method, applied for nearly spherical particles, he found agreement with Jeffery's minimum dissipation hypothesis.

Harper & Chang [37] analyzed the rotation of two spheres rigidly constrained by an invisible rod, a so-called dumbbell. In the purely viscous regime a dumbbell is equivalent to a prolate spheroid when its aspect ratio



approaches infinity. They assumed that both spheres experienced lift forces (calculated by Saffman [38]) independently of each other. By this method they found the opposite of Jeffery's minimum dissipation hypothesis: a slender rod ends up tumbling end-to-end in the flow-shear plane.

More recently Subramanian & Koch [33, 34] re-examined the slender rod and nearly-spherical limiting cases using a reciprocal theorem [16, 39]. Their method is less controversial than those employed by the earlier attempts. However, they found, like Harper & Chang [37], that for small values of the Reynolds number a slender rod tumbles end-to-end in the flow-shear plane. For larger values of the Reynolds number the tumbling orbit is destroyed and replaced by fixed points, which means that the particle stops rotating and aligns, a phenomenon observed in numerical studies [40] (see below). Subramanian & Koch [34] found that a nearly spherical prolate particle aligns its long axis along the vorticity, and a nearly spherical oblate particle tumbles, in agreement with Saffman [35]. They remark that the different types of motions for nearly spherical prolate particles, and slender prolate particles "suggests a possible bifurcation [...] at an intermediate aspect ratio."

Meanwhile, several groups began studies of this problem using direct numerical solution of the Navier-Stokes equations, via lattice Boltzmann simulations [40–48]. These studies reveal a rich structure of dynamical modes for moderate to large values of the Reynolds number. Not only log-rolling or tumbling is possible, but also intermediate limit cycles and alignment with new fixed points. The studies are limited to a few particle shapes, typically $\lambda = 1/4$, $\lambda = 1/2$, $\lambda = 2$ and $\lambda = 4$. Instead they focus on the effects of increasing Reynolds numbers, confinement and particle buoyancy.

I enter this chronology sometime in 2013, after submitting a paper [49] in which we describe the effects of particle inertia alone, neglecting the fluid inertia. We were intrigued by the results of Subramanian & Koch [33, 34] outlined above, and the fact that no numerical results had shown the predicted log-rolling mode for nearly spherical prolate particles. For example, Qi & Luo [42] simulated both oblate ($\lambda = 1/2$) and prolate ($\lambda = 2$) spheroids, and found for that the oblate particle log-rolls while the prolate particle tumbles, opposite to the existing theoretical prediction. But, as Subramanian & Koch [34] points out, there were several possible explanations for this discrepancy. First, the simulations were performed at moderately small Reynolds numbers, but not much smaller than unity, where a perturbation theory should be valid. Second, they were performed in a finite computational domain,



whereas the theory is valid for an unbounded shear flow. Third, the particle aspect ratio $\lambda = 2$ is not close to unity, whereas the theory assumed $\lambda \approx 1$. The parameter ranges where the existing theory should be valid is also where the numerical simulations become computationally impractical. More precisely, small values of the Reynolds number, large distance to the boundaries, and extreme particle shape all add to the computational cost. Therefore any comparisons to existing theory were qualitative.

These facts convinced us to attempt relaxing the assumption of $\lambda \approx 1$, and find the exact value of λ for the cross-over from log-rolling to tumbling.

During my work several more numerical studies have appeared [45–48]. Despite improved methods and more raw computer power, there was still no evidence of log-rolling prolate spheroids at small values of the Reynolds number. The clearest example is in Fig. 12 of Mao & Alexeev [46], where they find that the dynamics of a nearly spherical particle ($\lambda = 1.2$ and $\lambda = 0.8$) also contradicts the theoretical prediction. Their belief is that this "may be caused by the influence of the higher-order effects...", implying that the value of the Reynolds number in their simulation was out-of-range for the perturbation theory.

4.2 Results

We initially set out to calculate only the linear stability exponents of the log-rolling position. But it turned out that we could compute an explicit correction to Jeffery's equation of motion, which is more useful. Let \mathbf{n} be the unit vector along the symmetry axis of the particle, and \mathbb{O} and \mathbb{S} the antisymmetric and symmetric parts of the shear flow gradient (see Section 3.1.1 for details.) Then the result is

$$\begin{aligned} \dot{\mathbf{n}} = & \mathbb{P}[\mathbb{O}\mathbf{n} + \Lambda\mathbb{S}\mathbf{n}] \\ & + \text{Re}_s \mathbb{P}[b_1(\mathbf{n} \cdot \mathbb{S}\mathbf{n})\mathbb{S}\mathbf{n} + b_2(\mathbf{n} \cdot \mathbb{S}\mathbf{n})\mathbb{O}\mathbf{n} + b_3\mathbb{O}\mathbf{S}\mathbf{n} + b_4\mathbb{S}\mathbf{S}\mathbf{n}]. \end{aligned} \quad (4.1)$$

Here the first row is the result of Jeffery [2]. The projection matrix $\mathbb{P} = \mathbb{1} - \mathbf{n}\mathbf{n}^T$ removes any component of the vector field which is not tangent to the unit sphere (see also Section 3.5.) The scalar parameters Λ and b_α depend only on the particle aspect ratio λ . The shape factor $\Lambda = (\lambda^2 - 1)/(\lambda^2 + 1)$ was computed by Jeffery. Our main accomplishment is the calculation of $b_\alpha(\lambda)$.



The result (4.1) resolves the inconsistencies between earlier theories, and between theory and numerical simulations. It also conclusively refutes Jeffery's minimum dissipation hypothesis with respect to inertia. I summarise the main conclusions in the following.

Linear stability analysis

The solution to Jeffery's equation, Eq. (4.1) with $\text{Re}_s = 0$, are the degenerate periodic Jeffery orbits. In terms of the dynamical system (4.1) the phase space S^2 is covered by a continuous family of marginally stable periodic orbits. But just as Jeffery conjectured, an arbitrarily small amount of inertia breaks this degeneracy. The periodic orbits in phase space are replaced by a set of limit cycles and fixed points. The stable limit cycles and fixed points of (4.1) represent the preferred motions of the particle. The form of Eq. (4.1) reveals that the vorticity direction $n_i \sim \varepsilon_{ijk} O_{jk}$ is a fixed point, whatever the values of $\beta_\alpha(\lambda)$. This fixed point is called *log-rolling*. Similarly, no trajectory of Eq. (4.1) can cross the flow-shear plane, and therefore the phase space in that plane must contain either a limit cycle, or a set of fixed points. If it is a limit cycle, the dynamics is called *tumbling*. These general features are due to the symmetries of the shear flow and the axisymmetric particle.

First effects of inertia

For an arbitrarily small value of $\text{Re}_s > 0$ the phase space looks almost like the Jeffery orbits, but with a slow *drift* between the orbits. This drift is bounded by the log-rolling and tumbling orbits, and the direction of the drift is determined by the particle shape. We determine the drift by linear stability analysis of Eq. (4.1) to order $O(\text{Re}_s)$, and find

- $1 < \lambda < \infty$ (prolate): The particle drifts to the stable tumbling limit cycle, whatever the initial condition.
- $1/7.3 \approx \lambda_c < \lambda < 1$ (thick oblate): The particle drifts to the stable log-rolling fixed point, whatever the initial condition.
- $0 < \lambda < \lambda_c$ (thin oblate): Both the log-rolling fixed point and the tumbling limit cycle are stable. Their basins of attraction are separated by one of the intermediate Jeffery orbits which have turned into an



unstable limit cycle. The position of the unstable limit cycle depends on the particle shape, shown in Fig. 4 of Paper C.

Our result (4.1) agrees with those of Subramanian & Koch [33] in the limit $\lambda \rightarrow \infty$ (up to a factor of 8π). However, we find that the earlier results for nearly spherical particles [34, 35] are mistaken. We have checked this in two ways. First, with F. Candelier we analysed the case of nearly spherical particles by a simultaneous perturbation around $Re_s = 0$ and $\lambda = 1$. We regard this complementary calculation as technically independent, because the flow solutions are expressed in spherical harmonics instead of a singularity system, and it does not use the symmetry arguments we put forward for the general case. This calculation, due mostly to F. Candelier, is described in Paper B. We knew that my general solution must match this special solution for nearly spherical particles exactly, as $\lambda \rightarrow 1$. Once we established this equivalence we compared my solution to Subramanian & Koch [33] as $\lambda \rightarrow \infty$, and found agreement up to a numerical factor of 8π . We have not identified exactly where in their calculation this factor appears, but the likely culprit is in the definition of Green's functions for the Stokes flow (see App. A.2 in Paper C.) With these comparisons we were confident enough to submit our calculations for review and publication. The second check of our result is the direct numerical stability analysis by T. Rosén and F. Lundell. Our effective equation (4.1) agrees very well with the full numerical solution as $Re_s \rightarrow 0$ and the computational box size becomes large. This comparison is in Paper D (in particular Fig. 2). We conclude that our effective equation is correct. But we also see that the orientational dynamics of a non-spherical particle in shear flow is sensitive to both confinement (wall-effects), and to higher-order corrections in the shear Reynolds number.

Dynamics of oblate particles at finite values of Re_s

In the previous Section I discussed the effects of inertia when Re_s is arbitrarily small, but not zero. In this limit we expect the perturbative effective equation (4.1) to be valid. For larger values of Re_s we cannot be certain that the dynamics of the effective equation reflects the dynamics of the exact equations. For example, the effective equation can in general not predict at which value of Re_s a disk-shaped particle with $\lambda = 1/12$ will cease rotating. Nevertheless, we may construct a bifurcation diagram of the effective equation in the parameter space (λ, Re_s) . We know that any bifurcation line



that extends to $\text{Re}_s = 0$ in the parameter space of the effective equation must *connect* to a corresponding bifurcation line in the parameter space of the exact dynamics. This constrains the possible bifurcation topologies for the exact equations, and may serve as a guide for further numerical analysis.

Three bifurcation lines in the parameter space of the effective equation extend to $\text{Re}_s = 0$. Two of them describe the value of Re_s where the tumbling orbit ceases to exist and is replaced by a pair of fixed points. Those reach $\text{Re}_s = 0$ only asymptotically as $\lambda \rightarrow 0$ and $\lambda \rightarrow \infty$, corresponding to infinitely thin disks or rods. The slender-body limit was described by Subramanian & Koch [33]. The third bifurcation line separates the regions of stable and unstable tumbling for oblate particles, referred to in the previous Section. It connects to $\text{Re}_s = 0$ at $\lambda = \lambda_c \approx 1/7.3$. In Paper D there is numerical evidence that this happens also in the exact equations. This raises the question: where does this bifurcation line go as Re_s increase in the effective equation? To answer this question I show the bifurcation diagram for oblate particles in Fig. 4.1. The interesting feature of this diagram is the fate of the tumbling orbit bifurcation. It meets several other bifurcation lines in a “critical point” (marked by a red circle in Fig. 4.1). For even larger values of Re_s there may exist more bifurcations (not shown), but I expect them to be less relevant.

Numerical simulation of the exact equations reveals many different modes of rotation, depending on parameters such as particle aspect ratio, Reynolds number, confinement ratio and particle buoyancy. One may hope that the effective equation is qualitatively correct in predicting what the first bifurcation is as Re_s increases. The data of Rosén *et al.* [48] and Paper D indicate that the “critical point”, where several bifurcation lines merge, does exist also in the exact dynamics. However, the bifurcation lines seem to be sensitive to the confinement ratio in the numerical simulations and as of now we do not have enough data to confirm nor refute any claims on equivalence.



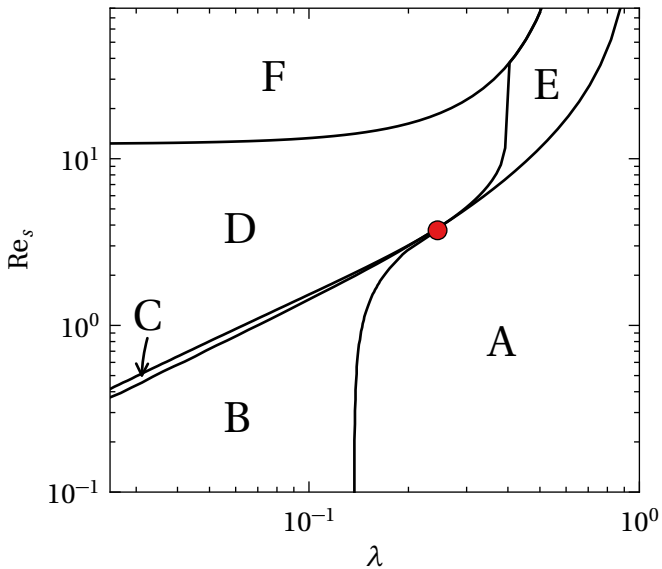


Figure 4.1: Bifurcation diagram for oblate particles ($\lambda < 1$) in the effective equations (4.1). Log-rolling is stable everywhere in this phase diagram. Regions:

- A - Tumbling orbit unstable,
 - No additional fixed points/orbits exist.
- B - Tumbling orbit stable,
 - Limit cycle separates basins of attraction of log rolling and tumbling.
- C - Fixed points replace tumbling orbit: one saddle, one stable node,
 - Limit cycle separates basins of attraction of log rolling and tumbling.
- D - Fixed points replace tumbling orbit: one unstable node, one stable node,
 - Saddle point exists in interior near tumbling fixed points.
- E - Fixed points replace tumbling orbit: one unstable node, one saddle,
 - No additional fixed points/orbits exist.
- F - Two new fixed points are created, in total four fixed points exist in place of the tumbling orbit.

For larger values of Re_s there may exist more bifurcations (not shown).



5 Measurements of asymmetric rods tumbling in microchannel flow

5.1 Overview

This project is a collaboration with our experimentalist colleagues in Gothenburg, Sweden. Roughly the division of work is that they build and perform the experiment, and we design the specifications and perform the analysis.

The project was initiated with an intention of observing the scattering between Jeffery orbits due to thermal noise. But first we needed to observe plain Jeffery orbits, as a baseline. With hindsight that was naive, given the long list of skilled experimentalists before us who struggled with this: Sec. II in Paper E gives a more or less exhaustive list.

Our focus has shifted away from thermal noise, to the sensitive dependence on particle shape and initial condition. In Section 3.5.2 in Part I, I explained how Jeffery's result implies complicated dynamics for triaxial particles, even if the deviation from axisymmetry very small [28, 29]. We want to observe this effect in experiment.

We previously published two papers [50, 51] describing our methods and some initial observations. In Paper E we describe our most recent measurements. We are still using pressure-driven flow in a microchannel molded in PDMS plastic (Fig. 5.1), but there are two main technical improvements from earlier work. First, we employ an optical trap to arrange particles for the experimental runs. This allows us to use the same particle several times, and to control its initial condition. Second, we have particles made from glass rods which have a very symmetric cross-section (see Fig. 2 in Paper E).

In Paper E we claim to observe both quasi-periodic and chaotic trajectories, for the same particle. Thus we confirm the predictions of Hinch & Leal [28] and Yarin *et al.* [29]. We claim that the observed trajectories are due to the triaxial particle shape for two reasons.

First, we reverse the pressure over the channel at the end of each particle trajectory. In the Stokes approximation the particle must then retrace its trajectory backwards, in line with the time-reversal symmetry of the Jeffery equations discussed in Section 3.5. If the particle trajectory does not reverse we discard the data. These reversals exclude any non-reversible effects, in





Figure 5.1: Photograph of a microchannel of the type used in our experiment. The channel is molded in a block of PDMS plastic. In the picture the channel is filled with dye. To the left and right are inlet/outlet tubes. The channel is approximately 5 cm long.

particular effects of inertia or thermal noise.

Second, with each particle we record several distinct trajectories with different initial conditions. This enables comparison with theory despite the fact that we cannot determine the particle shape accurately, because we know that all trajectories for the same particle must be consistent with the same surface-of-section of the Jeffery dynamics (see Section 3.5.2). A complication is that we cannot measure the rotation of the rod around its long axis, that is the angle ψ in the surface-of-section. However, the elliptic-island structure of the surface-of-section makes a comparison with the measured values of n_z meaningful, because the dynamics are strongly influenced by the initial condition and the size of the island bounds the oscillations of n_z for any trajectory.

6 Rotation rates of particles in turbulence

Paper F started as the synthesis of discussions during a workshop at NORDITA in Stockholm. For those I am grateful especially to E. Variano and G. Voth. The paper is a discussion of the rotations of axisymmetric particles in isotropic turbulence. I think the strength of this paper is it's breadth, as it contains pieces of experimental results, numerical results and analytical model calculations.



From what I remember, the discussions started because of confusion between the *rotation rate* and the *tumbling rate* of a particle. In this context rotation rate means magnitude of the angular velocity: $|\boldsymbol{\omega}|$. The tumbling rate is the rate at which the symmetry axis of the particle turns: $|\dot{\mathbf{n}}| = |\boldsymbol{\omega} \times \mathbf{n}|$. The two are kinematically related, because

$$|\boldsymbol{\omega}|^2 = |\dot{\mathbf{n}}|^2 + |\boldsymbol{\omega} \cdot \mathbf{n}|^2. \quad (6.1)$$

The difference $|\boldsymbol{\omega} \cdot \mathbf{n}|$ is called the *spinning rate*, because it is the rate at which the particle spins around its symmetry axis.

In the paper we make two main observations. First, that the average rotation rate is roughly independent of particle shape. This is true in numerical simulations (Fig. 3 in Paper F), and in experimental measurements (Fig. 5 in Paper F). This shape independence is unexpected, in particular because the average tumbling rate has a strong shape dependence [26, 52]. Therefore it turns out that the shape dependence of the average spinning rate almost exactly cancels the shape dependence of the average tumbling rate, as to make the total rotation rate shape independent. The reasons for this cancellation are still not known. However, in the paper we show that the average rotation rate of a particle in a random flow field is *not* shape independent. This implies that the cancellation is due to the properties of the turbulent flow, and not inherent in the equations of motion.

The second main observation is on the *instantaneous* rotation rates of particles. Although the average rotation rates for a thin disk and a slender rod are almost the same, their trajectories are qualitatively very different.

A key feature of turbulence is the existence of *vortex tubes* [53]. They are regions of strong vorticity, created by stretching of a large vortex into a thinner but more intensive vortex. These regions typically are long-lived, compared to the average rate of change in the flow. In these vortex tubes rod-shaped particles tend to rotate such that they keep aligned with the direction of the vorticity. The vorticity makes them spin around their own symmetry axis. But disks instead align perpendicularly to the vorticity, and the vorticity makes them tumble. But as a disk tumbles, the tumbling rate alternates between being faster and slower than vorticity, because of the flow strain. An example of this is shown in the first panel of Fig. 1 in Paper F. The rotation rate of the rod varies smoothly, and is very close to the strength of the vorticity. The rotation rate of the disk oscillates strongly, but is on average close to the strength of the vorticity.



We may partly understand these observations by a simplified picture. The effect of a rotational flow $\mathbf{u}_R = \boldsymbol{\Omega} \times \mathbf{r}$ is to rotate a particle around $\boldsymbol{\Omega}$. The effect of a strain flow $\mathbf{u}_S = \mathbb{S}\mathbf{r}$ is to align a long axis of a particle with the strongest eigendirection of \mathbb{S} . The simple picture is that the same strain that stretches and intensifies a vortex to a vortex tube along $\boldsymbol{\Omega}$, will also align the axes of any nearby particles with $\boldsymbol{\Omega}$. Therefore long axes of rods, and diameters of disks tend to align with $\boldsymbol{\Omega}$ in these regions. With this alignment it follows that rods spin and disks tumble because of the strong vorticity.

This simple argument cannot explain why the rotation rate of the disk happens to average to the same value as that of the rod. The details of the tumbling rate depends on how the vorticity $\boldsymbol{\Omega}$, and the particle direction \mathbf{n} , are aligned relative to the eigensystem of \mathbb{S} . The details and implications of these alignments are important open questions. In the random-flow model these alignments are very weak, and that is the underlying reason for the shape-dependence of the average rotation rate.

7 Closing words

The past five years have been an immense learning experience for me. I was fortunate to come to Bernhard Mehlig's group around 2010. They had been working on the dynamics of particles in random flows for some time, and were increasingly interested in the theory of fluid mechanics underlying the equations of motion. I got the job as a Ph.D student, and my new job was to learn, which is a fantastic job description.

Five years later I can say that I surely learned some fluid mechanics and mathematics, but more importantly I learned about intellectual independence. I learned that independent thought requires *knowing what you don't know*. It seems trivial that we should not accept, or worse, repeat, arguments that we do not understand. In my experience I am nevertheless tempted to accept an argument because I find the conclusion attractive. The most important skill I learned is to recognize and fight this temptation within myself.

During this time we also made some scientific progress, documented in Part II of this thesis and the appended papers. I end this thesis with a brief discussion of those results, and their possible future extension.



7.1 Discussion of results

Personally, the most satisfying result of my work is the description of the effect of inertia on the Jeffery orbits (Papers A-D). First, it resolves a rather long-standing problem in theoretical fluid mechanics. The degeneracy of the Jeffery orbits is well-known, and anyone in the field immediately understands the question. Second, the result offered a couple of surprises. While the established asymptotic results for nearly spherical particles motivated us to attempt the calculation (see Section 4), they turned out to be mistaken, and there is no bifurcation of the log-rolling orbit for rod-shaped particles. On the other hand we found a non-trivial bifurcation for oblate particles of intermediate aspect ratio that I believe no-one anticipated. The original assertion that the effects of inertia breaks the degeneracy is somewhat thwarted, as the dynamics of a thin oblate particle is determined by which basin of attraction it starts in. The fact that this theoretical prediction seems to agree with new direct numerical simulations is of course very satisfying.

The experiment described in Paper E has been a catalyst for me to dig into the dynamics of triaxial particles in shear flow. Our group has roots in research on dynamical systems, so from first sight Bernhard asked why the surfaces-of-section (Section 3.5.2) look like those of the Hamiltonian ‘standard map’? Eventually, with help from S. Östlund, we realized that the reversal symmetry we invoke in the analysis of the experiment must also imply a combined time-reversal and mirror symmetry in the equations of motion. This symmetry is not obvious in the Euler angle coordinates, because they cannot describe a mirror operation. But in the vector equations for \mathbf{n} and \mathbf{p} the symmetry is easily checked. In fact, I believe the symmetry should hold for any particle shape, because it is a consequence of Stokes equation.

Paper F is different because it concerns random and turbulent flows instead of a simple shear flow. For me it was a lot of fun discussing and writing this paper, as well as our earlier paper on the same topic [26], because I had to learn about the statistics of turbulent flow. The main complication with angular dynamics is that the torque on a particle depends on the orientation of the particle relative to the gradients. Several groups are at work measuring, simulating and understanding these correlations between the particle orientation and the fluid gradients in turbulence. This research will contribute to our understanding of both the particle dynamics and the dynamics of the turbulent gradients, and I like to think I made a contribution towards this.



7.2 Outlook

Experimental observations of angular dynamics in shear flow

There are two obvious extensions to this work, one theoretical and one experimental.

Experimentally the next step is to measure the complete three-dimensional orientation of the particle. This is very difficult with microrods, and therefore we investigate alternative particle shapes. For example it is possible to measure the orientation of a triangular platelet using only one camera, except for some degenerate orientations which have to be determined by continuity.

The theoretical question concerns how the surface-of-section is modified for asymmetric particles. The Jeffery equation is valid for any particle with three orthogonal mirror symmetries [20]. But the real particles in this experiment are not perfectly symmetric. The trajectories are sensitive to the transition from axisymmetric to triaxial, and the question is whether they are equally sensitive to breaking the mirror symmetries as well.

The effects of fluid inertia

The reason that the calculation described in Papers A-C is conceptually straightforward is that the Stokes flow works as the zeroth order flow field in the reciprocal theorem integral. Perturbation theory for small values of the Reynolds number is infamous, because the Stokes flow field is not a uniformly valid approximation of the flow field as $\text{Re}_s \rightarrow 0$. This generally leads to a erroneous or divergent result in perturbation theory. In our case this did not matter, because the erroneous contribution to the volume integral of the reciprocal theorem is small. But in cases involving translational motion the volume integral diverges. We may not, for example, reproduce the Saffman lift force on a sphere translating in simple shear with just the Stokes flow field and the reciprocal theorem.

In order to solve most problems, it is necessary to construct uniformly valid flow fields to lowest order. This usually requires singular perturbation theory, of which asymptotic matching is perhaps the most common technique in fluid dynamics. Learning these methods is a necessary next step.

An interesting extension is to solve the coupled spatial and angular dy-



namics of a non-spherical particle in shear flow. To lowest order it makes sense to consider the rotation separately, because the Reynolds number based on the particle slip velocity is small compared to the shear Reynolds number. But at the next order of perturbation the rotation and translation are probably not decoupled. Such a calculation would be the analogue of the Saffman lift for non-spherical particles, and could make our results more relevant to inertial microfluidics.

Another effect neglected in our calculation is the effect of confinement of the particle by nearby walls. The nearby boundaries affect the nature of the inertial correction. Likely this effect can be computed similarly to the result in Paper C, with the method of images for the multipole expansion.

Finally, in my view, a long-term goal of this research is to understand how to derive an effective equation of motion for the translational and orientational dynamics of a neutrally buoyant particle in turbulence. The Stokes drag is a good approximation for very small particles, or for finite particles if they are much heavier than the fluid. But for a neutrally buoyant particle in turbulence I expect both particle inertia and fluid inertia to contribute to an effective equation of motion.



Dr. J. C. R. Licklider

*Blåsten visslar i fönsterspringorna, och regnet
porlar i takrännan, och nu är sagan slut. Den
som icke har förstått den kan trösta sig med
att det blir vackert väder imorgon.*

ur *Duggregnet*, av Hjalmar Söderberg





ACKNOWLEDGEMENTS

Although written by my hand, this thesis is by no means conceived by me alone. I am most grateful for the enthusiastic guidance from my supervisor Bernhard Mehlig. It is a privilege to work with someone with the physical insight, unquenchable enthusiasm and sheer perseverance it takes to get things right.

Further, I am indebted to all our collaborators for their work. Fabien Candelier and Jean-Régis Angilella in France for teaching me fluid dynamics. Greg Voth and Evan Variano in the US for the wonderful experiments and discussions, and our experimental colleagues in Dag Hanstorp's lab for hunting the Jeffery orbits with us.

I also want to thank my present and former collegues for the open scientific environment at the department. In particular I appreciate the company of my fellow students Kristian Gustafsson, Marina Rafajlović and Erik Werner (who all graduated before me), and I welcome our new students Johan Fries and Jan Meibohm to this group. An extra thank you to Erik and Jan who improved this thesis with their helpful comments. Any remaining mistakes are mine alone.

Finally, I am fortunate to have my wonderful family. Thank you Freja and Tora for giving meaning to it all ♡.





Bibliography

- [1] EINARSSON, J 2013 *Orientational dynamics of small non-spherical particles in fluid flows*. Gothenburg University, ISBN: 978-91-637-4473-0, <https://gupea.ub.gu.se/handle/2077/34320>.
- [2] JEFFERY, G. B 1922 The motion of ellipsoidal particles immersed in a viscous fluid. *Proceedings of the Royal Society of London. Series A* **102** (715), 161–179.
- [3] DEVENISH, B. J, BARTELLO, P, BRENGUIER, J. L, COLLINS, L. R, GRABOWSKI, W. W, IJZERMANS, R. H. A, MALINOWSKI, S. P, REEKS, M. W, VASSILICOS, J. C, WANG, L. P & WARHAFT, Z 2012 Droplet growth in warm turbulent clouds. *Quarterly Journal of the Royal Meteorological Society* **138** (667), 1401–1429.
- [4] WILKINSON, M, MEHLIG, B & USKI, V 2008 Stokes trapping and planet formation. *The Astrophysical Journal Supplement Series* **176** (2), 484–496.
- [5] GUASTO, J. S, RUSCONI, R & STOCKER, R 2012 Fluid mechanics of planktonic microorganisms. *Annual Review of Fluid Mechanics* **44** (1), 373–400.
- [6] BAYOD, E, WILLERS, E. P & TORNBERG, E 2008 Rheological and structural characterization of tomato paste and its influence on the quality of ketchup. *LWT - Food Science and Technology* **41** (7), 1289–1300.
- [7] COUSSOT, P, NGUYEN, Q. D, HUYNH, H. T & BONN, D 2002 Avalanche behavior in yield stress fluids. *Physical Review Letters* **88** (17), 175501.
- [8] MATHER, T, PYLE, D & OPPENHEIMER, C 2003 Tropospheric volcanic aerosol. In *Volcanism and the Earth's Atmosphere* (ed. A Robock & C Oppenheimer), p. 189–212. American Geophysical Union.
- [9] GASTEIGER, J, GROSS, S, FREUDENTHALER, V & WIEGNER, M 2011 Volcanic ash from Iceland over Munich: mass concentration retrieved from ground-based remote sensing measurements. *Atmos. Chem. Phys.* **11** (5), 2209–2223.



- [10] DUBOVIK, O, HOLBEN, B. N, LAPYONOK, T, SINYUK, A, MISHCHENKO, M. I, YANG, P & SLUTSKER, I 2002 Non-spherical aerosol retrieval method employing light scattering by spheroids. *Geophysical Research Letters* **29** (10), 54–1.
- [11] MARCOS, SEYMOUR, J. R, LUHAR, M, DURHAM, W. M, MITCHELL, J. G, MACKE, A & STOCKER, R 2011 Microbial alignment in flow changes ocean light climate. *Proceedings of the National Academy of Sciences* PMID: 21368125.
- [12] SABINE, E 1829 On the reduction to a vacuum of Captain Kater's convertible pendulum. *Philosophical Transactions of the Royal Society of London* **119**, 331–338.
- [13] STOKES, G. G 1851 On the effect of the internal friction of fluids on the motion of pendulums. *Transactions of the Cambridge Philosophical Society* **IX**, 8, reprinted in Cambridge Library Collection: Mathematical and Physical Papers Vol. 3. ISBN 9780511702266.
- [14] VEYSEY, J & GOLDENFELD, N 2007 Simple viscous flows: From boundary layers to the renormalization group. *Reviews of Modern Physics* **79** (3), 883–927.
- [15] BRENNER, H 1974 Rheology of a dilute suspension of axisymmetric Brownian particles. *International Journal of Multiphase Flow* **1** (2), 195–341.
- [16] KIM, S & KARRILA, S. J 1991 *Microhydrodynamics: principles and selected applications*. Boston: Butterworth-Heinemann.
- [17] HAPPEL, J. R & BRENNER, H 1965 *Low Reynolds Number Hydrodynamics: With Special Applications to Particulate Media*. Springer.
- [18] CLERCX, H. J. H & SCHRAM, P. P. J. M 1992 Brownian particles in shear flow and harmonic potentials: A study of long-time tails. *Physical Review A* **46** (4), 1942–1950.
- [19] KHEIFETS, S, SIMHA, A, MELIN, K, LI, T & RAIZEN, M. G 2014 Observation of Brownian Motion in Liquids at Short Times: Instantaneous Velocity and Memory Loss. *Science* **343** (6178), 1493–1496.



- [20] BRENNER, H 1964 The Stokes resistance of an arbitrary particle—II. *Chemical Engineering Science* **19** (9), 599–629.
- [21] BRENNER, H & O'NEILL, M. E 1972 On the Stokes resistance of multiparticle systems in a linear shear field. *Chemical Engineering Science* **27** (7), 1421–1439.
- [22] OBERBECK, A 1876 Über stationäre flüssigkeitsbewegungen mit berücksichtigung der inneren reibung. *Journal für die reine und angewandte Mathematik* **81**, 62–80.
- [23] EDWARDES, D 1893 Steady motion of a viscous liquid in which an ellipsoid is constrained to rotate about a principal axis. *The quarterly journal of pure and applied mathematics* **26**, 70–78.
- [24] BRETHERTON, F. P 1962 The motion of rigid particles in a shear flow at low reynolds number. *Journal of Fluid Mechanics* **14** (02), 284–304.
- [25] LAMB, J. S. W & ROBERTS, J. A. G 1998 Time-reversal symmetry in dynamical systems: A survey. *Physica D: Nonlinear Phenomena* **112** (1–2), 1–39.
- [26] GUSTAVSSON, K, EINARSSON, J & MEHLIG, B 2014 Tumbling of small axisymmetric particles in random and turbulent flows. *Physical Review Letters* **112** (1), 014501.
- [27] GIERSZEWSKI, P. J & CHAFFEY, C. E 1978 Rotation of an isolated triaxial ellipsoid suspended in slow viscous flow. *Canadian Journal of Physics* **56** (1), 6–11.
- [28] HINCH, E. J & LEAL, L. G 1979 Rotation of small non-axisymmetric particles in a simple shear flow. *Journal of Fluid Mechanics* **92** (03), 591–607.
- [29] YARIN, A. L, GOTTLIEB, O & ROISMAN, I. V 1997 Chaotic rotation of triaxial ellipsoids in simple shear flow. *Journal of Fluid Mechanics* **340**, 83–100.
- [30] GOLDSTEIN, H 1980 *Classical Mechanics*. Reading, Massachusetts: Addison-Wesley.
- [31] STROGATZ, S. H 1994 *Nonlinear dynamics and Chaos*. Westview Press.



- [32] LUNDELL, F 2011 The effect of particle inertia on triaxial ellipsoids in creeping shear: From drift toward chaos to a single periodic solution. *Physics of Fluids* **23** (1), 011704.
- [33] SUBRAMANIAN, G & KOCH, D. L 2005 Inertial effects on fibre motion in simple shear flow. *Journal of Fluid Mechanics* **535**, 383–414.
- [34] SUBRAMANIAN, G & KOCH, D. L 2006 Inertial effects on the orientation of nearly spherical particles in simple shear flow. *Journal of Fluid Mechanics* **557**, 257–296.
- [35] SAFFMAN, P. G 1956 On the motion of small spheroidal particles in a viscous liquid. *Journal of Fluid Mechanics* **1** (05), 540–553.
- [36] PROUDMAN, I & PEARSON, J. R. A 1957 Expansions at small Reynolds numbers for the flow past a sphere and a circular cylinder. *Journal of Fluid Mechanics* **2** (03), 237–262.
- [37] HARPER, E. Y & CHANG, I.-D 1968 Maximum dissipation resulting from lift in a slow viscous shear flow. *Journal of Fluid Mechanics* **33** (02), 209–225.
- [38] SAFFMAN, P. G 1965 The lift on a small sphere in a slow shear flow. *Journal of Fluid Mechanics* **22** (02), 385–400.
- [39] LOVALENTI, P. M & BRADY, J. F 1993 The hydrodynamic force on a rigid particle undergoing arbitrary time-dependent motion at small Reynolds number. *Journal of Fluid Mechanics* **256**, 561–605.
- [40] DING, E.-J & AIDUN, C. K 2000 The dynamics and scaling law for particles suspended in shear flow with inertia. *Journal of Fluid Mechanics* **423**, 317–344.
- [41] FENG, J & JOSEPH, D. D 1995 The unsteady motion of solid bodies in creeping flows. *Journal of Fluid Mechanics* **303**, 83–102.
- [42] QI, D & LUO, L.-S 2003 Rotational and orientational behaviour of three-dimensional spheroidal particles in couette flows. *Journal of Fluid Mechanics* **477**, 201–213.



- [43] YU, Z, PHAN-THIEN, N & TANNER, R. I 2007 Rotation of a spheroid in a couette flow at moderate reynolds numbers. *Physical Review E* **76** (2), 026310.
- [44] HUANG, H, YANG, X, KRAFCZYK, M & LU, X.-Y 2012 Rotation of spheroidal particles in couette flows. *Journal of Fluid Mechanics* **692**, 369–394.
- [45] ROSÉN, T, LUNDELL, F & AIDUN, C. K 2014 Effect of fluid inertia on the dynamics and scaling of neutrally buoyant particles in shear flow. *Journal of Fluid Mechanics* **738**, 563–590.
- [46] MAO, W & ALEXEEV, A 2014 Motion of spheroid particles in shear flow with inertia. *Journal of Fluid Mechanics* **749**, 145–166.
- [47] ROSÉN, T, DO-QUANG, M, AIDUN, C. K & LUNDELL, F 2015 The dynamical states of a prolate spheroidal particle suspended in shear flow as a consequence of particle and fluid inertia. *Journal of Fluid Mechanics* **771**, 115–158.
- [48] ROSÉN, T, DO-QUANG, M, AIDUN, C. K & LUNDELL, F 2015 Effect of fluid and particle inertia on the rotation of an oblate spheroidal particle suspended in linear shear flow. *Physical Review E* **91** (5).
- [49] EINARSSON, J, ANGILELLA, J. R & MEHLIG, B 2014 Orientational dynamics of weakly inertial axisymmetric particles in steady viscous flows. *Physica D: Nonlinear Phenomena* **278–279**, 79–85.
- [50] MISHRA, Y. N, EINARSSON, J, JOHN, O. A, ANDERSSON, P, MEHLIG, B & HANSTORP, D 2012 A microfluidic device for studies of the orientational dynamics of microrods. In *Proc. SPIE*, , vol. 8251, pp. 825109–825109–11.
- [51] EINARSSON, J, JOHANSSON, A, MAHATO, S. K, MISHRA, Y. N, ANGILELLA, J. R, HANSTORP, D & MEHLIG, B 2013 Periodic and aperiodic tumbling of microrods advected in a microchannel flow. *Acta Mechanica* **224** (10), 2281–2289.
- [52] PARSA, S, CALZAVARINI, E, TOSCHI, F & VOTH, G. A 2012 Rotation rate of rods in turbulent fluid flow. *Physical Review Letters* **109** (13), 134501.
- [53] SHE, Z.-S, JACKSON, E & ORSZAG, S. A 1990 Intermittent vortex structures in homogeneous isotropic turbulence. *Nature* **344** (6263), 226–228.





APPENDIX

A Triaxial particle in a linear flow

In this Appendix I derive the torque-free equation of motion for an triaxial ellipsoidal particle in a general linear flow. It is the generalisation of the Jeffery equation to triaxial particles.

We represent the orientation of the particle with a rotation matrix $\mathbb{R}(t)$, which transforms the world-fixed cartesian coordinate frame $(\mathbf{e}_1, \mathbf{e}_2, \mathbf{e}_3)$ to the particle-fixed coordinate frame $(\mathbf{n}_1, \mathbf{n}_2, \mathbf{n}_3)$. The ellipsoid is defined by the lengths of its three half-axes, we denote them a_1, a_2 and a_3 . Each a_i is the length along the corresponding particle axis \mathbf{n}_i .

The end result of this calculation is an equation of motion for \mathbf{n}_1 and \mathbf{n}_2 . The two orthogonal vectors describe fully the orientation of the rigid body.

The kinematic equation of motion for a rotating vector is

$$\dot{\mathbf{n}}_i = \boldsymbol{\omega} \times \mathbf{n}_i, \quad (\text{A.1})$$

where $\boldsymbol{\omega}$ is the angular velocity of the particle. Jeffery [2] computed the components of the angular velocity vector in the particle frame of reference. Updated to the present notation, his Eq. (37) reads

$$\begin{aligned} (\mathbf{n}_1 \cdot \boldsymbol{\omega}) &= \mathbf{n}_1 \cdot \boldsymbol{\Omega} + \frac{a_2^2 - a_3^2}{a_2^2 + a_3^2} (\mathbf{n}_2^T \mathbb{S} \mathbf{n}_3), \\ (\mathbf{n}_2 \cdot \boldsymbol{\omega}) &= \mathbf{n}_2 \cdot \boldsymbol{\Omega} + \frac{a_3^2 - a_1^2}{a_3^2 + a_1^2} (\mathbf{n}_3^T \mathbb{S} \mathbf{n}_1), \\ (\mathbf{n}_3 \cdot \boldsymbol{\omega}) &= \mathbf{n}_3 \cdot \boldsymbol{\Omega} + \frac{a_1^2 - a_2^2}{a_1^2 + a_2^2} (\mathbf{n}_1^T \mathbb{S} \mathbf{n}_2). \end{aligned}$$

Here $\boldsymbol{\Omega}$ is such that $\boldsymbol{\Omega} \times \mathbf{x} = \mathbb{O}\mathbf{x}$, where \mathbb{S} and \mathbb{O} are the symmetric and anti-symmetric parts of the flow gradient:

$$\mathbb{O} = \frac{1}{2}(\mathbb{A} - \mathbb{A}^T), \quad \mathbb{S} = \frac{1}{2}(\mathbb{A} + \mathbb{A}^T), \quad \mathbb{A} = \nabla \mathbf{u} = \mathbb{O} + \mathbb{S}.$$



We can put Jeffery's expression into a single vector expression

$$\boldsymbol{\omega} = \boldsymbol{\Omega} + \frac{a_2^2 - a_3^2}{a_2^2 + a_3^2} (\mathbf{n}_2^T \mathbb{S} \mathbf{n}_3) \mathbf{n}_1 + \frac{a_3^2 - a_1^2}{a_3^2 + a_1^2} (\mathbf{n}_3^T \mathbb{S} \mathbf{n}_1) \mathbf{n}_2 + \frac{a_1^2 - a_2^2}{a_1^2 + a_2^2} (\mathbf{n}_1^T \mathbb{S} \mathbf{n}_2) \mathbf{n}_3.$$

In order to ease the notation we introduce the two aspect ratios $\lambda = a_3/a_1$ and $\kappa = a_2/a_1$:

$$\boldsymbol{\omega} = \boldsymbol{\Omega} + \frac{\Lambda - K}{K\Lambda - 1} (\mathbf{n}_2^T \mathbb{S} \mathbf{n}_3) \mathbf{n}_1 + \Lambda (\mathbf{n}_3^T \mathbb{S} \mathbf{n}_1) \mathbf{n}_2 - K (\mathbf{n}_1^T \mathbb{S} \mathbf{n}_2) \mathbf{n}_3,$$

where

$$K = \frac{\kappa^2 - 1}{\kappa^2 + 1}, \quad \Lambda = \frac{\lambda^2 - 1}{\lambda^2 + 1}.$$

Now, take the equations of motion for \mathbf{n}_2 and \mathbf{n}_3 ,

$$\begin{aligned} \dot{\mathbf{n}}_2 &= \boldsymbol{\omega} \times \mathbf{n}_2 \\ &= \boldsymbol{\Omega} \times \mathbf{n}_2 + K (\mathbf{n}_1^T \mathbb{S} \mathbf{n}_2) \mathbf{n}_1 + \frac{\Lambda - K}{K\Lambda - 1} (\mathbf{n}_2^T \mathbb{S} \mathbf{n}_3) \mathbf{n}_3, \\ \dot{\mathbf{n}}_3 &= \boldsymbol{\omega} \times \mathbf{n}_3 \\ &= \boldsymbol{\Omega} \times \mathbf{n}_3 + \Lambda (\mathbf{n}_3^T \mathbb{S} \mathbf{n}_1) \mathbf{n}_1 - \frac{\Lambda - K}{K\Lambda - 1} (\mathbf{n}_2^T \mathbb{S} \mathbf{n}_3) \mathbf{n}_2. \end{aligned}$$

The final step is to eliminate \mathbf{n}_1 from the equations. This elimination is accomplished by noting that

$$\mathbb{S} \mathbf{x} = (\mathbf{n}_1^T \mathbb{S} \mathbf{x}) \mathbf{n}_1 + (\mathbf{n}_2^T \mathbb{S} \mathbf{x}) \mathbf{n}_2 + (\mathbf{n}_3^T \mathbb{S} \mathbf{x}) \mathbf{n}_3,$$

implying

$$(\mathbf{n}_1^T \mathbb{S} \mathbf{x}) \mathbf{n}_1 = \mathbb{S} \mathbf{x} - (\mathbf{n}_3^T \mathbb{S} \mathbf{x}) \mathbf{n}_3 - (\mathbf{n}_2^T \mathbb{S} \mathbf{x}) \mathbf{n}_2.$$

Take the equation for $\dot{\mathbf{n}}_3$,

$$\begin{aligned} \dot{\mathbf{n}}_3 &= \boldsymbol{\Omega} \times \mathbf{n}_3 + \Lambda (\mathbf{n}_3^T \mathbb{S} \mathbf{n}_1) \mathbf{n}_1 - \frac{\Lambda - K}{K\Lambda - 1} (\mathbf{n}_2^T \mathbb{S} \mathbf{n}_3) \mathbf{n}_2 \\ &= \boldsymbol{\Omega} \times \mathbf{n}_3 + \Lambda (\mathbb{S} \mathbf{n}_3 - (\mathbf{n}_3^T \mathbb{S} \mathbf{n}_3) \mathbf{n}_3 - (\mathbf{n}_2^T \mathbb{S} \mathbf{n}_3) \mathbf{n}_2) - \frac{\Lambda - K}{K\Lambda - 1} (\mathbf{n}_2^T \mathbb{S} \mathbf{n}_3) \mathbf{n}_2 \\ &= \boldsymbol{\Omega} \times \mathbf{n}_3 + \Lambda (\mathbb{S} \mathbf{n}_3 - (\mathbf{n}_3^T \mathbb{S} \mathbf{n}_3) \mathbf{n}_3) + \frac{K(1 - \Lambda^2)}{K\Lambda - 1} (\mathbf{n}_2^T \mathbb{S} \mathbf{n}_3) \mathbf{n}_2. \end{aligned}$$



In the same fashion, we find for $\dot{\mathbf{n}}_2$,

$$\dot{\mathbf{n}}_2 = \boldsymbol{\Omega} \times \mathbf{n}_2 + K (\mathbb{S} \mathbf{n}_2 - (\mathbf{n}_2^T \mathbb{S} \mathbf{n}_2) \mathbf{n}_2) + \frac{\Lambda(1-K^2)}{K\Lambda-1} (\mathbf{n}_2^T \mathbb{S} \mathbf{n}_3) \mathbf{n}_3.$$

In most places in this thesis, I write the cross product with $\boldsymbol{\Omega}$ as the matrix product with \mathbb{O} instead. We also rename $\mathbf{n} = \mathbf{n}_3$ and $\mathbf{p} = \mathbf{n}_2$:

$$\begin{aligned}\dot{\mathbf{n}} &= \mathbb{O} \mathbf{n} + \Lambda (\mathbb{S} \mathbf{n} - (\mathbf{n}^T \mathbb{S} \mathbf{n}) \mathbf{n}) + \frac{K(1-\Lambda^2)}{K\Lambda-1} (\mathbf{n}^T \mathbb{S} \mathbf{p}) \mathbf{p}, \\ \dot{\mathbf{p}} &= \mathbb{O} \mathbf{p} + K (\mathbb{S} \mathbf{p} - (\mathbf{p}^T \mathbb{S} \mathbf{p}) \mathbf{p}) + \frac{\Lambda(1-K^2)}{K\Lambda-1} (\mathbf{n}^T \mathbb{S} \mathbf{p}) \mathbf{n}\end{aligned}$$

In terms of the aspect ratios λ and κ the equations read

$$\begin{aligned}\dot{\mathbf{n}} &= \mathbb{O} \mathbf{n} + \frac{\lambda^2-1}{\lambda^2+1} (\mathbb{S} \mathbf{n} - \mathbf{n}^T \mathbb{S} \mathbf{n}) \mathbf{n} + \frac{2\lambda^2(1-\kappa^2)}{(\lambda^2+\kappa^2)(\lambda^2+1)} (\mathbf{n}^T \mathbb{S} \mathbf{p}) \mathbf{p}, \\ \dot{\mathbf{p}} &= \mathbb{O} \mathbf{p} + \frac{\kappa^2-1}{\kappa^2+1} (\mathbb{S} \mathbf{p} - \mathbf{p}^T \mathbb{S} \mathbf{p}) \mathbf{p} + \frac{2\kappa^2(1-\lambda^2)}{(\kappa^2+\lambda^2)(\kappa^2+1)} (\mathbf{n}^T \mathbb{S} \mathbf{p}) \mathbf{n}.\end{aligned}$$





PART III
PAPERS





Paper A

Open Access (CC BY 3.0) at <http://dx.doi.org/10.1103/PhysRevE.91.041002>





Effect of weak fluid inertia upon Jeffery orbits

J. Einarsson,¹ F. Candelier,² F. Lundell,³ J. R. Angilella,⁴ and B. Mehlig¹

¹*Department of Physics, Gothenburg University, SE-41296 Gothenburg, Sweden*

²*University of Aix-Marseille, CNRS, IUSTI UMR 7343, 13 013 Marseille, Cedex 13, France*

³*KTH Royal Institute of Technology, SE-100 44 Stockholm, Sweden*

⁴*Department of Mathematics and Mechanics, LUSAC-ESIX 50130 Cherbourg, University of Caen, France*

(Received 27 January 2015; published 28 April 2015)

We consider the rotation of small neutrally buoyant axisymmetric particles in a viscous steady shear flow. When inertial effects are negligible the problem exhibits infinitely many periodic solutions, the “Jeffery orbits.” We compute how inertial effects lift their degeneracy by perturbatively solving the coupled particle-flow equations. We obtain an equation of motion valid at small shear Reynolds numbers, for spheroidal particles with arbitrary aspect ratios. We analyze how the linear stability of the “log-rolling” orbit depends on particle shape and find it to be unstable for prolate spheroids. This resolves a puzzle in the interpretation of direct numerical simulations of the problem. In general, both unsteady and nonlinear terms in the Navier-Stokes equations are important.

DOI: 10.1103/PhysRevE.91.041002

PACS number(s): 47.55.Kf, 47.10.-g, 47.15.G-, 83.10.Pp

Consider a small neutrally buoyant axisymmetric particle rotating in a steady viscous shear flow. This problem was solved by Jeffery [1]. He found that the particle tumbles periodically: it aligns with the flow direction for a long time and then rapidly changes orientation by 180 degrees. There are infinitely many marginally stable periodic orbits, the “Jeffery orbits.” This degeneracy means that small perturbations may have substantial consequences. It is thus necessary to consider perturbations due to physical effects neglected in Jeffery’s theory.

For very small particles rotational diffusion must be taken into account [2]. The resulting orientational dynamics forms the basis for the theoretical understanding of the rheology of dilute suspensions [3,4]. A second important perturbation is breaking of axisymmetry. It is known that the rotation of small particles in a simple shear depends very sensitively on their shape [5–7]. Third, for larger particles inertial effects must become important. This is the question we address here. To compute the effect of particle inertia is straightforward [8,9]. But to determine the effect of fluid inertia on the tumbling is much more difficult. Despite the significance of the question there are few theoretical results, we discuss them in connection with our results below.

To understand the effect of fluid inertia on the motion of particles suspended in a fluid is a question of fundamental importance. But in general it is impractical to solve the coupled particle-flow problem, and there is a long history of deriving approximate equations of motion for the particles, taking into account the unsteady and nonlinear convective terms in the Navier-Stokes equations [10]. The translational motion of a sphere in nonuniform flows at low Reynolds numbers, for example, is approximately described allowing for unsteadiness of the disturbance flow but neglecting convective fluid inertia [11,12]. There are many examples where convective

fluid inertia must be taken into account, leading to drag and lift effects [13–16]. In most cases either the unsteady or the nonlinear term in the Navier-Stokes equations are considered (but see Refs. [17] and [18]). In our problem both unsteady and nonlinear convective effects matter.

We have derived an equation of motion for the orientation of a neutrally buoyant spheroid in a steady shear when inertial effects are weak but essential. We show how the unsteady and convective terms in the Navier-Stokes equations determine the dynamics. Our results explain how the degeneracy of the Jeffery orbits is lifted by weak inertia. We concentrate on four examples that have been discussed in the literature [19–24]: tumbling and log rolling of prolate and oblate particles (Fig. 1).

In this Rapid Communication we give only a brief account of the formulation of the problem and its perturbative solution (Secs. 1 and 2). We focus on the main results, Eqs. (6), (7), and (8), and explain their implications. Details of our calculation are given in Ref. [25].

1. Formulation of the problem. Tumbling of a spheroid in a simple shear is governed by the shear Reynolds number $Re_s = sa^2 \rho_f / \mu$ (fluid inertia), the Stokes number $St = (\rho_p / \rho_f) Re_s$ (particle inertia), and the particle aspect ratio λ . Here s denotes the shear rate, ρ_f and ρ_p are fluid- and particle-mass densities, and μ is the dynamic viscosity of the fluid. We reserve a for the major axis length of the particle (used in the definitions of Re_s and St). The aspect ratio is defined as the ratio of lengths along and perpendicular to the symmetry axis. Thus, $\lambda = a/b > 1$ (prolate particle) and $\lambda = b/a < 1$ (oblate particle), where b is the minor particle-axis length. We dedimensionalize the problem by using the inverse shear rate s^{-1} as time scale, particle size a as length scale, and μs as pressure scale. For a neutrally buoyant particle $Re_s = St$. To distinguish the contributions from particle and fluid inertia we keep these two parameters separate. In dimensionless variables the angular equations of motion for an axisymmetric particle read

$$\dot{\boldsymbol{n}} = \boldsymbol{\omega} \times \boldsymbol{n}, \quad (1a)$$

$$St \dot{\boldsymbol{L}} = St(\mathbb{I}\dot{\boldsymbol{\omega}} + \dot{\mathbb{I}}\boldsymbol{\omega}) = \boldsymbol{T}. \quad (1b)$$

Here \boldsymbol{n} is the unit vector along the particle symmetry axis. Dots denote time derivatives, \boldsymbol{L} is the particle angular

Published by the American Physical Society under the terms of the Creative Commons Attribution 3.0 License. Further distribution of this work must maintain attribution to the author(s) and the published article’s title, journal citation, and DOI.



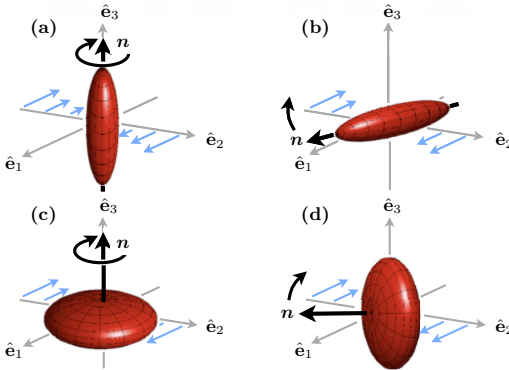


FIG. 1. (Color online) Spheroid in a simple shear. The flow direction is $\hat{\mathbf{e}}_1$, shear direction $\hat{\mathbf{e}}_2$, and the vorticity points in the negative $\hat{\mathbf{e}}_3$ -direction. (a) Log-rolling of a prolate particle, \mathbf{n} is a unit vector along the symmetry axis of the particle. (b) Tumbling in the shear plane of a prolate particle. (c) Log-rolling of an oblate particle. (d) Tumbling of an oblate particle.

momentum, \mathbb{I} is the moment-of-inertia matrix of the particle. The particle angular velocity is $\boldsymbol{\omega}$, and \mathbf{T} is the torque that the fluid exerts on the particle. To find the torque one must solve the Navier-Stokes equations for the flow velocity \mathbf{u} and pressure p subject to no-slip boundary conditions on the particle surface \mathcal{S} :

$$\text{Re}_s(\partial_t \mathbf{u} + \mathbf{u} \cdot \nabla \mathbf{u}) = -\nabla p + \nabla^2 \mathbf{u}, \quad \nabla \cdot \mathbf{u} = 0, \quad (2a)$$

$$\mathbf{u} = \boldsymbol{\omega} \times \mathbf{r} \quad \text{for } \mathbf{r} \in \mathcal{S}, \quad \text{and } \mathbf{u} = \mathbf{u}^\infty \text{ as } |\mathbf{r}| \rightarrow \infty. \quad (2b)$$

Here \mathbf{r} is a spatial coordinate vector with components (r_1, r_2, r_3) in the Cartesian coordinate system $\hat{\mathbf{e}}_1, \hat{\mathbf{e}}_2, \hat{\mathbf{e}}_3$ shown in Fig. 1. The undisturbed flow field, \mathbf{u}^∞ , is a simple shear flow. We write it as $\mathbf{u}^\infty = r_2 \hat{\mathbf{e}}_1$, so that its gradient matrix \mathbb{A} has only one nonzero element, $A_{ij} = \delta_{i1}\delta_{j2}$. We decompose \mathbb{A} into its symmetric part $\mathbb{S} = (\mathbb{A} + \mathbb{A}^T)/2$, and its antisymmetric part $\mathbb{O} = (\mathbb{A} - \mathbb{A}^T)/2$.

2. *Perturbation theory.* The hydrodynamic torque in Eq. (1b) derives from the solutions of Eq. (2). The boundary conditions Eq. (2b) in turn depend on both particle orientation \mathbf{n} and particle angular velocity $\boldsymbol{\omega}$. Thus, Eqs. (1) and (2) are coupled and present a difficult problem. To proceed we use a reciprocal theorem [17,20,26] to calculate the torque. Following Ref. [17] we find for the particular case of a simple shear flow:

$$\mathbf{T} = \mathbf{T}^{(0)} - \text{Re}_s \int_{\mathcal{V}} d\mathbf{v} \tilde{\mathbb{U}} \left(\underbrace{\partial_t \mathbf{u}}_{\substack{\text{unsteady} \\ \text{fluid inertia}}} + \underbrace{\mathbf{u} \cdot \nabla \mathbf{u}}_{\substack{\text{convective} \\ \text{fluid inertia}}} \right). \quad (3)$$

The first term $\mathbf{T}^{(0)}$ in Eq. (3) is the viscous torque computed by Jeffery [1]. The volume integral is the $O(\text{Re}_s)$ -correction to the hydrodynamic torque. The integral is taken over the entire fluid volume \mathcal{V} outside the particle. The elements of the matrix $\tilde{\mathbb{U}}$ are obtained by solving an auxiliary Stokes problem. Details are given in Ref. [25].

Equation (3) is exact. The difficulty is that the integrand depends on the sought solution \mathbf{u} of Eq. (2). Therefore, we follow Refs. [17] and [20] and evaluate Eq. (3) to order $O(\text{Re}_s)$, the integrand is then only needed to $O(1)$. More precisely, we assume that St and Re_s are small and of the same order, so that $\text{Re}_s \text{St}$ is negligible. This allows us to use the known $\text{Re}_s = \text{St} = 0$ solutions of Eq. (2) in Eq. (3). The two terms in the integrand in Eq. (3) have the interpretations given in the equation, to linear order in Re_s .

To obtain an equation of motion for \mathbf{n} we substitute the hydrodynamic torque Eq. (3) into Eq. (1b) and expand:

$$\boldsymbol{\omega} = \boldsymbol{\omega}^{(0)} + \text{St} \boldsymbol{\omega}^{(\text{St})} + \text{Re}_s \boldsymbol{\omega}^{(\text{Re}_s)} + \dots \quad (4)$$

Each order in St and Re_s must satisfy Eqs. (1b) and (3), determining the contributions on the right-hand side of Eq. (4). To lowest order we find the condition $\mathbf{T}^{(0)} = 0$. It gives

$$\boldsymbol{\omega}^{(0)} = \boldsymbol{\Omega} + \Lambda \mathbf{n} \times \mathbb{S} \mathbf{n}, \quad (5)$$

where $\Lambda = (\lambda^2 - 1)/(\lambda^2 + 1)$ and $\boldsymbol{\Omega} = (\nabla \times \mathbf{u}^\infty)/2$, so that $\mathbb{O} \mathbf{n} = \boldsymbol{\Omega} \times \mathbf{n}$. Equation (5) is Jeffery's result [1] for the angular velocity of a spheroid in a simple shear, in the absence of inertial effects. The second term in Eq. (4), the St correction, is found to be equivalent to a result given by Einarsson *et al.* [9]. We do not reproduce the details here because the expression for $\boldsymbol{\omega}^{(\text{St})}$ is lengthy. The third term, the $O(\text{Re}_s)$ correction, involves the integral in Eq. (3). But even in perturbation theory [evaluating the integrand to order $O(1)$] it is difficult to perform the integral for arbitrary orientations \mathbf{n} .

3. *Symmetries.* Exploiting the symmetries of the problem we can show that it is enough to evaluate the integral for only four directions \mathbf{n} . The corresponding four integrals suffice to determine the orientational equation of motion for \mathbf{n} . Here we discuss the idea and give the resulting equation of motion. Details are found in Ref. [25].

The small-St and - Re_s corrections to Jeffery's equation of motion are quadratic in $\mathbb{A} = \mathbb{O} + \mathbb{S}$. The symmetries listed in Table I constrain the form of these contributions. The resulting equation of motion has only four degrees of freedom, which we denote β_1, \dots, β_4 :

$$\dot{\mathbf{n}} = \mathbb{O} \mathbf{n} + \Lambda [\mathbb{S} \mathbf{n} - (\mathbf{n} \cdot \mathbb{S} \mathbf{n}) \mathbf{n}] \quad (6)$$

$$+ \beta_1 (\mathbf{n} \cdot \mathbb{S} \mathbf{n}) \mathbb{P} \mathbb{S} \mathbf{n} + \beta_2 (\mathbf{n} \cdot \mathbb{S} \mathbf{n}) \mathbb{O} \mathbf{n}$$

$$+ \beta_3 \mathbb{P} \mathbb{O} \mathbb{S} \mathbf{n} + \beta_4 \mathbb{P} \mathbb{S} \mathbf{S} \mathbf{n}.$$

The right-hand side of the first row is Jeffery's equation, it follows from Eqs. (1a) and (5). The remaining terms are all the terms quadratic in $\mathbb{A} = \mathbb{O} + \mathbb{S}$ that are allowed by the symmetries listed in Table I. The projection \mathbb{P} projects out components in the \mathbf{n} direction: $\mathbb{P} \mathbf{x} = \mathbf{x} - (\mathbf{n} \cdot \mathbf{x}) \mathbf{n}$. The four

TABLE I. Symmetries constraining the form of Eq. (6).

| | |
|---------------------------------|---|
| Incompressibility: | $\text{Tr } \mathbb{S} = 0$ |
| Symmetry of \mathbb{S} : | $\mathbb{S}^T = \mathbb{S}$ |
| Antisymmetry of \mathbb{O} : | $\mathbb{O}^T = -\mathbb{O}$ |
| Steady shear: | $\mathbb{O} \mathbb{O} = -\mathbb{S} \mathbb{S}, \mathbb{O} \mathbb{S} = -\mathbb{S} \mathbb{O}$ |
| Normalization of \mathbf{n} : | $\mathbf{n} \cdot \mathbf{n} = 0$ |
| Inversion symmetry: | invariance under $\mathbf{n} \rightarrow -\mathbf{n}, \dot{\mathbf{n}} \rightarrow -\dot{\mathbf{n}}$ |

scalar coefficients β_α are linear in St and Re_s , and functions of the particle aspect ratio: $\beta_\alpha = St\beta_\alpha^{(St)}(\lambda) + Re_s\beta_\alpha^{(Re_s)}(\lambda)$. To obtain these functions we evaluate Eq. (4) directly for four suitably chosen directions \mathbf{n} . Comparison with Eq. (6) gives a linear system of equations that can be solved for the β_α .

4. Results for the coefficients β_α . In two important limiting cases, the integrand in Eq. (3) simplifies so that we can derive explicit formulas for the coefficients β_α . Details are given in Ref. [25].

First, in the limit of large aspect ratios we find that particle inertia does not contribute, $\beta_\alpha^{(St)}(\lambda) = 0$, and we obtain that the β_α coefficients are asymptotic to

$$\beta_1 = \frac{7Re_s}{30\log(2\lambda) - 45}, \quad \beta_2 = \frac{3\beta_1}{7}, \quad \beta_3 = \beta_4 = 0, \quad (7)$$

for large values of λ . The large- λ asymptote of Eq. (7) agrees with the slender-body limit obtained in Ref. [20], up to a factor of 8π . We cannot explain this factor but have verified our results by comparing with an independent calculation (Ref. [27], see below).

Second, we can evaluate the limit of nearly spherical particles. We set $\lambda = 1/(1-\epsilon)$ and find to $O(\epsilon)$:

$$\begin{aligned} \beta_1 &= 0, & \beta_2 &= \epsilon(St/15 + Re_s/35), \\ \beta_3 &= \epsilon(St/15 - 37Re_s/105), & \beta_4 &= \epsilon(St/15 + 11Re_s/35). \end{aligned} \quad (8)$$

In this case particle inertia contributes, and this contribution is consistent with the results of Ref. [9] and also with Eqs. (3.15) and (3.16) in Ref. [21].

But the correction due to fluid inertia differs from the earlier results, Eq. (7) in Ref. [19] and Eq. (4.22) in Ref. [21]. In Ref. [19], the Navier-Stokes equations (2) were solved iteratively with approximate boundary conditions. Only the final result is given, thus we cannot determine whether the problem lies in the method or in the algebra. We note that Saffman's assertion that particle inertia can be neglected is incorrect, as Eq. (8) and the results of Ref. [9] show. We have also verified Eq. (8) by an independent calculation, based on a joint perturbation theory in ϵ and Re_s using a basis expansion in spherical harmonics. The results are summarized in Ref. [27] and agree with Eq. (8). We also note that Eq. (4.22) of Ref. [21] violates the particle inversion symmetry (Table I).

It follows from Eq. (3) that the unsteady and convective fluid-inertia terms contribute linearly to $\beta_\alpha^{(Re_s)}$. This enables us to separate their effects to order Re_s . For large values of the aspect ratio λ we find that unsteady fluid inertia contributes $(8\log 2\lambda - 12)^{-1}$ to $\beta_1^{(Re_s)}$ and $\beta_2^{(Re_s)}$. Comparison with Eq. (7) shows that the contribution from convective fluid inertia is of the same order. For nearly spherical particles, by contrast, we find that convective inertia dominates (order ϵ), while the contribution from unsteady fluid inertia is smaller, of order ϵ^2 .

5. Angular dynamics and linear stability analysis. The inertial corrections in Eq. (6) are small in magnitude when $Re_s = St$ is small, but they are important because they destroy the degeneracy of the Jeffery orbits. We illustrate this effect by analyzing four cases: log-rolling along the vorticity axis and tumbling in the flow-shear plane, for prolate and oblate particles (Fig. 1). In the absence of inertial effects these orbits are neutrally stable, as all Jeffery orbits in this limit.

Our analysis is motivated by the fact that recent direct numerical simulation (DNS) results [22–24] of the problem at small but finite Re_s have resulted in a debate as to whether log rolling is stable for prolate particles, or not. We rewrite Eq. (6) in spherical coordinates, $n_1 = \sin\theta \cos\varphi$, $n_2 = \sin\theta \sin\varphi$, $n_3 = \cos\theta$ (the Cartesian coordinates are defined in Fig. 1):

$$\begin{aligned} \dot{\varphi} &\equiv f(\varphi, \theta) = (\Lambda \cos 2\varphi - 1)/2 + (\beta_1/8) \sin^2 \theta \sin 4\varphi \\ &\quad - \sin 2\varphi (\beta_2 \sin^2 \theta + \beta_3)/4, \end{aligned} \quad (9a)$$

$$\begin{aligned} \dot{\theta} &\equiv g(\varphi, \theta) = \Lambda \sin \theta \cos \theta \sin \varphi \cos \varphi \\ &\quad + \sin \theta \cos \theta (\beta_1 \sin^2 \theta \sin^2 2\varphi + \beta_3 \cos 2\varphi + \beta_4)/4. \end{aligned} \quad (9b)$$

Equation (9) admit two equilibria for θ , log rolling ($\theta = 0$), and tumbling in the shear plane ($\theta = \pi/2$); see Fig. 1.

Consider first the linear stability of the tumbling orbit. The angle φ is a monotonously decreasing function of time for infinitesimal values of $Re_s = St$. We can thus parametrize the orbit by φ instead of time, noting that φ changes from 0 to -2π during the period time $T_p = 4\pi/\sqrt{1 - \Lambda^2}$. We obtain a one-dimensional periodically driven dynamical system $d\theta/d\varphi = g(\varphi, \theta)/f(\varphi, \theta)$. We define the stability exponent as the rate of separation in one period:

$$\gamma_T = T_p^{-1} \lim_{\delta\theta_0 \rightarrow 0} \log |\delta\theta_{-2\pi}/\delta\theta_0|. \quad (10)$$

Here $\delta\theta_0$ is a small initial separation from $\pi/2$ at $\varphi = 0$, and $\delta\theta_{-2\pi}$ is the value of this separation at $\varphi = -2\pi$, after one period. Linearization of the θ dynamics gives

$$\gamma_T = T_p^{-1} \int_0^{-2\pi} d\varphi \frac{\partial}{\partial \theta} \frac{g(\varphi, \pi/2)}{f(\varphi, \pi/2)}. \quad (11)$$

Evaluating the integral Eq. (11) to order Re_s yields an expression for the exponent γ_T , linear in β_α :

$$\gamma_T = -\frac{\beta_4}{4} + \frac{1 - \sqrt{1 - \Lambda^2}}{4\Lambda^2} (\Lambda\beta_2 - \beta_1). \quad (12)$$

Log-rolling is a fixed point of the dynamics Eq. (6), not a periodic orbit. But its stability exponent can be calculated as outlined above since the φ -dynamics decouples from that of θ ; see also Ref. [9]. We find

$$\gamma_{LR} = \beta_4/4. \quad (13)$$

Using Eqs. (7) and (8) we obtain in the nearly spherical limit [$\epsilon = (\lambda - 1)/\lambda \rightarrow 0$]

$$\frac{\gamma_T}{Re_s} \sim -2\epsilon/21, \quad \frac{\gamma_{LR}}{Re_s} \sim 2\epsilon/21. \quad (14)$$

Thus, log-rolling is unstable for nearly spherical prolate particles ($\epsilon > 0$), and tumbling is stable. For nearly spherical oblate particles the stabilities are reversed. An earlier approximate theory by Saffman [19] predicts that log-rolling is stable for neutrally buoyant, near-spherical prolate spheroids at small Re_s ; see also Ref. [21]. But stable log rolling has not been observed in DNS for nearly spherical prolate spheroids [22–24], and it has been debated how to reconcile this fact with Saffman's prediction. We have corrected Saffman's equation of motion. As Eq. (14) shows, it follows that log-rolling is unstable for prolate spheroids at small Re_s , consistent with the DNS results [23].



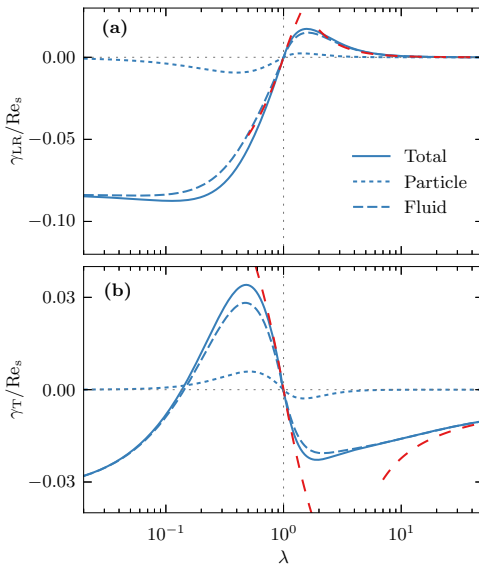


FIG. 2. (Color online) (a) Stability exponent of log-rolling (solid line). Separately shown are particle-inertia (dotted) and fluid-inertia contributions (dashed). Data computed using Eqs. (12) and (13) and numerical results for β_α (details are given in Ref. [25]). Also shown are the asymptote Eqs. (14) and (15), red dashed lines. (b) Same for tumbling in the shear plane.

In the limit of large aspect ratios we find that the exponents are asymptotic to

$$\frac{\gamma_T}{Re_s} \sim (45 - 30 \log 2\lambda)^{-1}, \quad \frac{\gamma_{LR}}{Re_s} \sim (15\lambda^2)^{-1}. \quad (15)$$

We see that tumbling is stable in this limit, and log rolling is unstable.

To determine the stability of the tumbling and log-rolling orbits for arbitrary values of λ we have computed the β_α by numerically integrating Eq. (3) for four directions \mathbf{n} , as outlined above. Figures 2(a) and 2(b) show the resulting exponents. The asymptote Eqs. (14) and (15) are also shown in Fig. 2. Figure 2(a) demonstrates that log rolling is unstable for prolate particles of any aspect ratio. Figures 2(a) and 2(b) also show the separate contributions from fluid and particle inertia to the stability exponents. We see that the contribution of fluid inertia is in general significantly larger than that of particle inertia.

6. Concluding remarks. It would be of great interest to study by DNS how the stability exponents change as Re_s is increased and to determine how the results described here connect to those of Ref. [24] valid at larger Re_s . Second, we plan to generalize the calculation summarized here to describe wall effects at small Re_s , by the method of reflection [28]. Third, to describe sedimenting particles it is necessary to generalize our results to $\rho_p \neq \rho_f$. Fourth, both the unsteady term and the nonlinear term in the Navier-Stokes equations matter in our problem. This raises the question under which circumstances both effects matter for the tumbling of small particles in unsteady flows, and in particular in turbulence. Finally, we remark that Jeffery orbits are commonly used as benchmarks for DNS, despite being valid only in the limit $Re_s = 0$. Our solutions provide a new reference when fluid inertia is essential but weak.

This work was supported by grants from Vetenskapsrådet and the Göran Gustafsson Foundation for Research in Natural Sciences and Medicine. Support from the MPNS COST Action MP1305 Flowing matter is gratefully acknowledged.

-
- [1] G. B. Jeffery, *Proc. R. Soc. A* **102**, 161 (1922).
[2] E. J. Hinch and L. G. Leal, *J. Fluid Mech.* **52**, 683 (1972).
[3] C. J. Petrie, *J. Non-Newton. Fluid* **87**, 369 (1999).
[4] F. Lundell, D. Soderberg, and H. Alfredsson, *Annu. Rev. Fluid Mech.* **43**, 195 (2011).
[5] E. J. Hinch and L. G. Leal, *J. Fluid Mech.* **92**, 591 (1979).
[6] A. Yarin, O. Gottlieb, and I. Roisman, *J. Fluid Mech.* **340**, 83 (1997).
[7] J. Einarsson, B. Mihiretie, A. Laas, S. Ankardal, J.R. Angilella, D. Hanstorp, and B. Mehlig, [arXiv:1503.03023](#).
[8] F. Lundell and A. Carlsson, *Phys. Rev. E* **81**, 016323 (2010).
[9] J. Einarsson, J. R. Angilella, and B. Mehlig, *Physica D* **278**, 79 (2014).
[10] L. G. Leal, *Annu. Rev. Fluid Mech.* **12**, 435 (1980).
[11] M. R. Maxey and J. J. Riley, *Phys. Fluids* **26**, 883 (1983).
[12] R. Gatignol, *J. Méc. Théor. Appl.* **2**, 143 (1983).
[13] I. Proudman and J. R. A. Pearson, *J. Fluid Mech.* **2**, 237 (1957).
[14] P. G. Saffman, *J. Fluid Mech.* **22**, 385 (1965).
[15] J. McLaughlin, *J. Fluid Mech.* **224**, 261 (1991).
[16] J. Magnaudet, *J. Fluid Mech.* **485**, 115 (2003).
[17] P. Lovalenti and J. Brady, *J. Fluid Mech.* **256**, 561 (1993).
[18] F. Candelier and J.R. Angilella, *Phys. Rev. E* **73**, 047301 (2006).
[19] P. G. Saffman, *J. Fluid Mech.* **1**, 540 (1956).
[20] G. Subramanian and D. L. Koch, *J. Fluid Mech.* **535**, 383 (2005).
[21] G. Subramanian and D. L. Koch, *J. Fluid Mech.* **557**, 257 (2006).
[22] D. Qi and L. Luo, *J. Fluid Mech.* **477**, 201 (2003).
[23] W. Mao and W. Alexeev, *J. Fluid Mech.* **749**, 145 (2014).
[24] T. Rosén, F. Lundell, and C. K. Aidun, *J. Fluid Mech.* **738**, 563 (2014).
[25] J. Einarsson, F. Candelier, F. Lundell, J. R. Angilella, and B. Mehlig, [arXiv:1504.02309](#).
[26] S. Kim, *Microhydrodynamics: Principles and Selected Applications* (Butterworth-Heinemann, Boston, 1991).
[27] F. Candelier, J. Einarsson, F. Lundell, B. Mehlig, and J. R. Angilella (unpublished).
[28] J. R. Blake and A. T. Chwang, *J. Eng. Math.* **8**, 23 (1974).



Paper B

arXiv preprint available at <http://arxiv.org/abs/1505.02661>





Role of inertia for the rotation of a nearly spherical particle in a general linear flow

F. Candelier,¹ J. Einarsson,² F. Lundell,³ B. Mehlig,² and J.-R. Angilella⁴

¹*University of Aix-Marseille, CNRS, IUSTI UMR 7343, 13 013 Marseille, Cedex 13, France*

²*Department of Physics, Gothenburg University, SE-41296 Gothenburg, Sweden*

³*KTH Royal Institute of Technology, SE-100 44 Stockholm, Sweden*

⁴*Department of Mathematics and Mechanics, LUSAC-ESIX, University of Caen, 50130 Cherbourg, France*

(Received 20 February 2015; published 27 May 2015)

We analyze the angular dynamics of a neutrally buoyant, nearly spherical particle immersed in a steady general linear flow. The hydrodynamic torque acting on the particle is obtained by means of a reciprocal theorem, a regular perturbation theory exploiting the small eccentricity of the nearly spherical particle, and by assuming that inertial effects are small but finite.

DOI: 10.1103/PhysRevE.91.053023

PACS number(s): 47.15.G-, 83.10.Pp, 47.55.Kf, 47.10.-g

I. INTRODUCTION

In this article we derive an effective equation of motion for the orientational dynamics of a neutrally buoyant, nearly spherical axisymmetric particle suspended in a time-independent linear flow. Our result is valid to leading order in the shear Reynolds number Re_s and the particle eccentricity ϵ . Terms of order Re_s^2 , ϵ^3 , and $\epsilon^2 Re_s$ are neglected.

Our motivation was twofold. First, we recently computed the stability of log-rolling and tumbling orbits of a neutrally buoyant spheroid in a simple shear at weak fluid and particle inertia [1,2]. The calculations leading to these results are quite involved. We therefore decided to check our calculations by an alternative method, which is summarized below. We refer to Ref. [2] for a summary of the background of the problem, and for a discussion of the implications of the results. Second, the results described in the present article are valid for general linear flows while those given in Refs. [1,2] pertain to the particular (and important) case of a simple shear flow. We believe that it is of interest to obtain results for general linear flows because this can be a first step towards describing the effect of a time-dependent but slowly varying perturbation of the flow.

II. FORMULATION OF THE PROBLEM

We consider a nearly spherical particle corresponding to an ellipsoid of revolution (around the axis \mathbf{t}_1) of low eccentricity, as depicted in Fig. 1. The surface of the particle is parametrized as

$$r(\vartheta) = 1 - \epsilon \sin^2(\vartheta) - \frac{3}{2}\epsilon^2 \sin^2(\vartheta) \cos^2(\vartheta) + O(\epsilon^3). \quad (1)$$

Here ϑ denotes the polar angle made by any vector \mathbf{r} with the orientation of the axis of revolution \mathbf{t}_1 . The eccentricity ϵ is a small parameter. Lengths are normalized by the semi-axis length a along the direction \mathbf{t}_1 (Fig. 1).

Suppose that the particle is immersed in a steady general linear flow. In this case the angular dynamics of the particle is governed by three dimensionless parameters: the shear Reynolds number $Re_s = sa^2 \rho_f / \mu$ which measures the effect of fluid inertia, the Stokes number $St = (\rho_p / \rho_f)Re_s$ measuring the importance of particle inertia, and the particle eccentricity ϵ . Here ρ_f and ρ_p denote, respectively, the densities of the fluid

and of the particle, s denotes the shear rate of the linear flow, and μ is the dynamic viscosity of the fluid.

Using the inverse shear rate as the timescale, the semi-axis length a as the length scale, and μs as the pressure scale, the equations governing the angular dynamics of a neutrally buoyant particle in the laboratory frame of reference read

$$\frac{d\mathbf{t}_1}{dt} = \boldsymbol{\omega} \times \mathbf{t}_1, \quad (2)$$

$$St \frac{d}{dt} (\mathbf{J} \cdot \boldsymbol{\omega}) = \boldsymbol{\tau}_h. \quad (3)$$

In Eq. (3), \mathbf{J} denotes the moment-of-inertia tensor of the particle, $\boldsymbol{\omega}$ is its angular velocity, and $\boldsymbol{\tau}_h$ is the hydrodynamic torque acting on the particle. Throughout this paper the centered dot (\cdot) defines a simply contracted tensor product, uppercase letters are used to denote matrix-tensors, and lowercase letters are used for simple vectors.

For a neutrally buoyant particle we have $St = Re_s$. Making this substitution only at the end of the calculation allows us to separate the effects of particle and fluid inertia.

The hydrodynamic torque is given by

$$\boldsymbol{\tau}_h = \int_{\mathcal{S}} \mathbf{r} \times (\boldsymbol{\Sigma} \cdot \mathbf{n}) dS.$$

The integral is over the particle surface \mathcal{S} , and \mathbf{n} is the outward surface normal. For an incompressible Newtonian fluid the stress tensor reads $\boldsymbol{\Sigma} = -p\mathbf{I} + 2\mathbf{S}$, where p is the pressure, \mathbf{I} is the identity tensor, and \mathbf{S} is the symmetric part of the fluid-velocity gradient tensor. To determine the hydrodynamic torque acting on the spheroid, we use a reciprocal theorem [3–7].

III. METHOD

We consider a general steady linear ambient flow. In the laboratory frame, it takes the form

$$\mathbf{u}^\infty = \mathbf{A}^\infty \cdot \mathbf{x},$$

where \mathbf{A}^∞ is a constant tensor. We decompose the gradient matrix \mathbf{A}^∞ into its symmetric (\mathbf{S}^∞) and antisymmetric (\mathbf{O}^∞) parts:

$$\mathbf{A}^\infty = \mathbf{O}^\infty + \mathbf{S}^\infty.$$



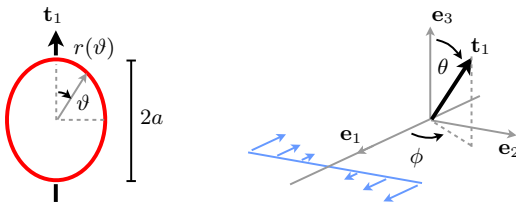


FIG. 1. (Color online) (left) The surface of a nearly spherical particle is constructed as the surface of revolution of the curve Eq. (3). (right) Simple shear. The flow-shear plane is spanned by \mathbf{e}_1 and \mathbf{e}_2 , and vorticity points in the negative \mathbf{e}_3 direction. The orientation of the vector \mathbf{t}_1 pointing along the symmetry axis of the particle is expressed in spherical coordinates (θ, ϕ) .

The antisymmetric tensor \mathbf{O}^∞ is linked to the vorticity of the unperturbed flow through

$$\mathbf{O}^\infty \cdot \mathbf{x} = \boldsymbol{\omega}^\infty \times \mathbf{x}, \quad \text{where} \quad \boldsymbol{\omega}^\infty = \frac{1}{2} \nabla \times \mathbf{u}^\infty.$$

The vectors \mathbf{x}_p and \mathbf{u}_p denote the position and the velocity of the center-of-mass of the particle. As the spheroid is assumed to be neutrally buoyant, we consider it to be advected along streamlines with a vanishing slip velocity

$$\mathbf{u}_p = \mathbf{A}^\infty \cdot \mathbf{x}_p.$$

We consider the equations governing the fluid motion in a translating frame of reference centered on the particle. This frame being noninertial, the pseudoforce $-\text{Re}_s d\mathbf{u}_p/dt$ appears in the force balance acting on the particle. However, it does not appear in the equations below of the perturbation flow. In the moving frame of reference the Navier-Stokes equations for the fluid velocity \mathbf{u} read

$$\begin{aligned} \nabla \cdot \mathbf{u} &= 0, \\ \text{Re}_s \left[\frac{\partial \mathbf{u}}{\partial t} + (\mathbf{u} \cdot \nabla) \mathbf{u} \right] &= \nabla \cdot \Sigma - \text{Re}_s \frac{d\mathbf{u}_p}{dt}, \end{aligned} \quad (4)$$

with boundary conditions

$$\mathbf{u} = \boldsymbol{\omega} \times \mathbf{r}, \quad \mathbf{r} \in \mathcal{S} \quad \text{and} \quad \mathbf{u} \rightarrow \mathbf{A}^\infty \cdot \mathbf{r}, \quad r \rightarrow \infty,$$

with $\mathbf{r} = \mathbf{x} - \mathbf{x}_p$.

We use the reciprocal theorem to determine the torque acting on the spheroid. The reciprocal theorem relates integrals of the velocity and stress fields of two incompressible Newtonian fluids:

$$\begin{aligned} \int_{\mathcal{S}} [(\tilde{\Sigma} \cdot \mathbf{n}) \cdot \mathbf{u} - (\Sigma \cdot \mathbf{n}) \cdot \tilde{\mathbf{u}}] dS \\ = \int_{\mathcal{V}} [\tilde{\mathbf{u}} \cdot (\nabla \cdot \Sigma) - \mathbf{u} \cdot (\nabla \cdot \tilde{\Sigma})] dV, \end{aligned} \quad (5)$$

where the integral on the right-hand side (r.h.s.) is over the entire volume \mathcal{V} outside the particle. In Eq. (5) the set (\mathbf{u}, Σ) represents the solutions of the problem of interest and $(\tilde{\mathbf{u}}, \tilde{\Sigma})$ are the solutions of a suitable auxiliary problem describing the creeping flow produced by a particle moving with angular velocity $\tilde{\boldsymbol{\omega}}$ in an otherwise quiescent fluid.

We also introduce the decompositions

$$\mathbf{u} = \mathbf{A}^\infty \cdot \mathbf{r} + \mathbf{u}' \quad \text{and} \quad \Sigma = \Sigma^\infty + \Sigma',$$

where \mathbf{u}' and Σ' correspond to the perturbation flow and the perturbation stress tensor induced by the spheroid. By using these decompositions it follows from the boundary conditions for \mathbf{u}' both on the particle surface and at infinity that

$$\begin{aligned} \omega_s \cdot \tilde{\tau}_h - \int_{\mathcal{S}} (\tilde{\Sigma} \cdot \mathbf{n}) \cdot (\mathbf{S}^\infty \cdot \mathbf{r}) dS \\ = \tilde{\boldsymbol{\omega}} \cdot \boldsymbol{\tau}_h + \text{Re}_s \int_{\mathcal{V}} \mathbf{f}(\mathbf{u}') \cdot \tilde{\mathbf{u}} dV. \end{aligned} \quad (6)$$

In this equation we introduced the slip angular velocity

$$\omega_s = \boldsymbol{\omega} - \boldsymbol{\omega}^\infty,$$

and the function $\mathbf{f}(\mathbf{u}')$ in Eq. (6) is given by

$$\mathbf{f}(\mathbf{u}') = \frac{\partial \mathbf{u}'}{\partial t} + \mathbf{A}^\infty \cdot \mathbf{u}' + [(\mathbf{A}^\infty \cdot \mathbf{r}) \cdot \nabla] \mathbf{u}' + \mathbf{u}' \cdot \nabla \mathbf{u}'.$$

To derive Eq. (6) we also used the fact that the torque τ_h^∞ due to the unperturbed stress vanishes. To see this recall that, in the laboratory frame of reference, the unperturbed flow field satisfies the Navier-Stokes equations $(\mathbf{A}^\infty)^2 \cdot \mathbf{x} = \nabla \cdot \Sigma^\infty$. By using Stokes integration theorem it follows that the torque due to the unperturbed stress tensor is given by

$$\tau_h^\infty = \int_{\mathcal{V}_p} \mathbf{r} \times [(\mathbf{A}^\infty)^2 \cdot \mathbf{x}_p] dV + \int_{\mathcal{V}_p} \mathbf{r} \times [(\mathbf{A}^\infty)^2 \cdot \mathbf{r}] dV, \quad (7)$$

where the integral is over the volume \mathcal{V}_p inside the particle. The symmetrical shape of the particle implies that the first integral on the r.h.s. of Eq. (7) is zero. Incompressibility and the vorticity equation for a steady flow

$$\text{Tr}(\mathbf{S}^\infty) = 0 \quad \text{and} \quad \mathbf{S}^\infty \cdot \boldsymbol{\omega}^\infty = 0 \quad (8)$$

imply that the second integral also vanishes.

Equation (6) allows us to compute the hydrodynamic torque $\boldsymbol{\tau}_h$ provided that we can determine the contribution of the integral over the entire volume \mathcal{V} outside the particle. To leading order [2,7] one can replace the actual perturbation flow \mathbf{u}' in the integral by its limit of vanishingly small Re_s . In other words, \mathbf{u}' can be replaced by the solution of

$$0 = \nabla \cdot \mathbf{u}', \quad 0 = -\nabla p' + \Delta \mathbf{u}', \quad (9)$$

with boundary conditions

$$\begin{aligned} \mathbf{u}' &= (\boldsymbol{\omega} - \boldsymbol{\omega}^\infty) \times \mathbf{r} - \mathbf{S}^\infty \cdot \mathbf{r} \quad \text{for } \mathbf{r} \in \mathcal{S}, \\ \mathbf{u}' &\rightarrow \mathbf{0} \quad \text{as } r \rightarrow \infty. \end{aligned} \quad (10)$$

To determine \mathbf{u}' we follow Refs. [8,9] and use a perturbation method that assumes that the particle eccentricity ϵ is small. Our approach is based on the general Lamb solution [10] of the Stokes problem (9) and (10) derived in terms of spherical harmonics. Details are given in the Appendix.

IV. RESULTS FOR GENERAL LINEAR FLOWS

Equation (6) makes it possible to derive the torque acting on a neutrally buoyant spheroid immersed in a general linear



flow. For the auxiliary torque—the first term on the left-hand side (l.h.s.) of Eq. (6)—we find

$$\begin{aligned}\boldsymbol{\tau}_h = & -8\pi\left(1-\frac{9}{5}\epsilon+\frac{459}{350}\epsilon^2\right)\tilde{\boldsymbol{\omega}} \\ & +8\pi\left(\frac{3}{5}\epsilon-\frac{177}{350}\epsilon^2\right)(\tilde{\boldsymbol{\omega}} \cdot \mathbf{t}_1)\mathbf{t}_1+O(\epsilon^3).\end{aligned}$$

The second term on the l.h.s. of Eq. (6) evaluates to

$$\begin{aligned}\int_S(\tilde{\boldsymbol{\Sigma}} \cdot \mathbf{n}) \cdot (\mathbf{S}^\infty \cdot \mathbf{r})dS \\ =8\pi\left(\epsilon-\frac{13}{10}\epsilon^2\right)[(\mathbf{S}^\infty \cdot \mathbf{t}_1) \times \mathbf{t}_1] \cdot \tilde{\boldsymbol{\omega}}+O(\epsilon^3).\end{aligned}$$

In order to determine the second term on the r.h.s. of Eq. (6), which is, as already said, the most difficult part of this

$$\begin{aligned}\text{Re}_s \int_V \mathbf{f}(\mathbf{u}') \cdot \tilde{\mathbf{u}} dV = & -8\pi \text{Re}_s \left(-\frac{1}{3} \frac{d\boldsymbol{\omega}_s}{dt} + \frac{1}{8} \mathbf{S}^\infty \cdot \boldsymbol{\omega}_s \right) \cdot \tilde{\boldsymbol{\omega}} \\ & -8\pi\epsilon \text{Re}_s \left\{ -\frac{32}{105}[(\mathbf{S}^\infty \cdot \mathbf{t}_1) \cdot \mathbf{t}_1]\boldsymbol{\omega}^\infty + (\mathbf{M} \cdot \mathbf{t}_1) \times \mathbf{t}_1 \right\} \cdot \tilde{\boldsymbol{\omega}} + O(\epsilon^2 \text{Re}_s),\end{aligned}$$

where

$$\mathbf{M} = -\frac{3}{5}\mathbf{S}^\infty \cdot \mathbf{O}^\infty + \frac{3}{35}\mathbf{O}^\infty \cdot \mathbf{S}^\infty - \frac{123}{280}\mathbf{S}^\infty \cdot \mathbf{S}^\infty. \quad (11)$$

So far the hydrodynamic torque acting on the spheroid in a general linear flow is given in a form involving the scalar product with the angular velocity $\tilde{\boldsymbol{\omega}}$ of the auxiliary problem. Since these results are valid for arbitrary $\tilde{\boldsymbol{\omega}}$ we conclude

$$\begin{aligned}\boldsymbol{\tau}_h = & -8\pi\left(1-\frac{9}{5}\epsilon+\frac{459}{350}\epsilon^2\right)\boldsymbol{\omega}_s+8\pi\left(\frac{3}{5}\epsilon-\frac{177}{350}\epsilon^2\right)(\boldsymbol{\omega}_s \cdot \mathbf{t}_1)\mathbf{t}_1-8\pi\left(\epsilon-\frac{13}{10}\epsilon^2\right)[(\mathbf{S}^\infty \cdot \mathbf{t}_1) \times \mathbf{t}_1] \\ & +8\pi\text{Re}_s\left(-\frac{1}{3} \frac{d\boldsymbol{\omega}_s}{dt} + \frac{1}{8} \mathbf{S}^\infty \cdot \boldsymbol{\omega}_s\right)+8\pi\epsilon\text{Re}_s\left\{-\frac{32}{105}[(\mathbf{S}^\infty \cdot \mathbf{t}_1) \cdot \mathbf{t}_1]\boldsymbol{\omega}^\infty + (\mathbf{M} \cdot \mathbf{t}_1) \times \mathbf{t}_1\right\}+O(\epsilon^2 \text{Re}_s). \quad (12)\end{aligned}$$

This equation constitutes one of the main results of this paper. Note that the terms in the first row of the r.h.s. of Eq. (12) correspond to the creeping-flow limit ($\text{Re}_s = 0$). The terms in the second row account for fluid-inertia effects. Since the slip angular velocity scales as $O(\epsilon)$ we infer that these effects scale as $O(\epsilon \text{Re}_s)$ for any linear flow.

In what follows, an approximate dynamical equation for the angular dynamics of the particle is derived. To do so, we need to return to Eq. (3) which governs the orientational dynamics of the spheroid. The moment-of-inertia tensor of the nearly spherical particle reads

$$\mathbf{J} = A^I \mathbf{t}_1 \otimes \mathbf{t}_1 + B^I (\mathbf{t}_2 \otimes \mathbf{t}_2 + \mathbf{t}_3 \otimes \mathbf{t}_3),$$

where

$$A^I = \frac{8\pi}{15}(1-4\epsilon+6\epsilon^2)+O(\epsilon^3), \quad B^I = \frac{8\pi}{15}\left(1-3\epsilon+\frac{7}{2}\epsilon^2\right)+O(\epsilon^3).$$

Expanding the time derivative in Eq. (3) yields

$$\text{St} \frac{d}{dt}(\mathbf{J} \cdot \boldsymbol{\omega}) = \text{St} \left[\mathbf{J} \cdot \frac{d\boldsymbol{\omega}}{dt} + (A^I - B^I)(\boldsymbol{\omega} \times \mathbf{t}_1)(\boldsymbol{\omega} \cdot \mathbf{t}_1) \right].$$

Writing this equation in terms of the slip angular velocity, and making use of the fact that $d\boldsymbol{\omega}^\infty/dt = 0$, we are led to

$$\text{St} \frac{d}{dt}(\mathbf{J} \cdot \boldsymbol{\omega}) = 8\pi \text{St} \left(\frac{1}{15} \frac{d\boldsymbol{\omega}_s}{dt} \right) - 8\pi\epsilon \text{St} \left[\frac{1}{15}(\boldsymbol{\omega}^\infty \cdot \mathbf{t}_1)(\boldsymbol{\omega}^\infty \times \mathbf{t}_1) \right] + O(\epsilon^2 \text{St}). \quad (13)$$

From Eqs. (3), (12), and (13) we obtain

$$\begin{aligned}\mathbf{0} = & \left(1-\frac{9}{5}\epsilon+\frac{459}{350}\epsilon^2\right)\boldsymbol{\omega}_s - \left(\frac{3}{5}\epsilon-\frac{177}{350}\epsilon^2\right)(\boldsymbol{\omega}_s \cdot \mathbf{t}_1)\mathbf{t}_1 + \left(\epsilon-\frac{13}{10}\epsilon^2\right)[(\mathbf{S}^\infty \cdot \mathbf{t}_1) \times \mathbf{t}_1] + \text{St} \left(\frac{1}{15} \frac{d\boldsymbol{\omega}_s}{dt} \right) \\ & + \text{Re}_s \left(\frac{1}{3} \frac{d\boldsymbol{\omega}_s}{dt} - \frac{1}{8} \mathbf{S}^\infty \cdot \boldsymbol{\omega}_s \right) - \epsilon \text{St} \left[\frac{1}{15}(\boldsymbol{\omega}^\infty \cdot \mathbf{t}_1)(\boldsymbol{\omega}^\infty \times \mathbf{t}_1) \right] + \epsilon \text{Re}_s \left\{ \frac{32}{105}[(\mathbf{S}^\infty \cdot \mathbf{t}_1) \cdot \mathbf{t}_1]\boldsymbol{\omega}^\infty - (\mathbf{M} \cdot \mathbf{t}_1) \times \mathbf{t}_1 \right\} \\ & + O(\epsilon^2 \text{St}, \epsilon^2 \text{Re}_s).\end{aligned} \quad (14)$$



From this equation we compute the particle angular velocity order by order. To this end we insert the ansatz

$$\begin{aligned}\boldsymbol{\omega}_s &= \boldsymbol{\omega}_s^{(0)} + \epsilon \boldsymbol{\omega}_s^{(\epsilon)} + St \boldsymbol{\omega}_s^{(St)} + Re_s \boldsymbol{\omega}_s^{(Re_s)} + \epsilon^2 \boldsymbol{\omega}_s^{(\epsilon^2)} \\ &\quad + \epsilon St \boldsymbol{\omega}_s^{(\epsilon St)} + \epsilon Re_s \boldsymbol{\omega}_s^{(\epsilon Re_s)} + O(\epsilon^3, \epsilon^2 St, \epsilon^2 Re_s)\end{aligned}\quad (15)$$

into Eq. (14). To order $O(1)$ this gives

$$\boldsymbol{\omega}_s^{(0)} = \mathbf{0}.$$

This means that, to leading order, the angular velocity of the particle is governed by the vorticity of the unperturbed flow ($\boldsymbol{\omega}^{(0)} = \boldsymbol{\omega}^\infty$). To order $O(\epsilon)$ we find

$$\boldsymbol{\omega}_s^{(\epsilon)} = \mathbf{t}_1 \times (\mathbf{S}^\infty \cdot \mathbf{t}_1). \quad (16)$$

This term is the leading-order term of Jeffery's angular velocity. It combines with the order- ϵ^2 term,

$$\boldsymbol{\omega}_s^{(\epsilon^2)} = \frac{1}{2} \mathbf{t}_1 \times (\mathbf{S}^\infty \cdot \mathbf{t}_1), \quad (17)$$

to give Jeffery's angular velocity $\Delta \mathbf{t}_1 \times (\mathbf{S}^\infty \cdot \mathbf{t}_1)$ to order $O(\epsilon^3)$. To orders $O(St)$ and $O(Re_s)$ we find

$$\boldsymbol{\omega}_s^{(St)} = \mathbf{0}, \quad \boldsymbol{\omega}_s^{(Re_s)} = \mathbf{0}.$$

These results suggest that, for any linear flow and up to first order, neither particle inertia nor fluid inertia modify the orientation of the angular velocity of a sphere, as expected from symmetry arguments. Finally, to orders $O(\epsilon St)$ and $O(\epsilon Re_s)$ we find

$$\begin{aligned}\boldsymbol{\omega}_s^{(\epsilon St)} &= -\frac{1}{15} [(\mathbf{O}^\infty \cdot \mathbf{t}_1) \times (\mathbf{S}^\infty \cdot \mathbf{t}_1) + \mathbf{t}_1 \times (\mathbf{S}^\infty \cdot \mathbf{O}^\infty \cdot \mathbf{t}_1) \\ &\quad - (\boldsymbol{\omega}^\infty \cdot \mathbf{t}_1) \mathbf{O}^\infty \cdot \mathbf{t}_1],\end{aligned}\quad (18)$$

and

$$\begin{aligned}\boldsymbol{\omega}_s^{(\epsilon Re_s)} &= -\frac{1}{3} (\mathbf{O}^\infty \cdot \mathbf{t}_1) \times (\mathbf{S}^\infty \cdot \mathbf{t}_1) - \frac{1}{3} \mathbf{t}_1 \times (\mathbf{S}^\infty \cdot \mathbf{O}^\infty \cdot \mathbf{t}_1) \\ &\quad + \frac{1}{8} \mathbf{S}^\infty \cdot [\mathbf{t}_1 \times (\mathbf{S}^\infty \cdot \mathbf{t}_1)] - \frac{32}{105} [(\mathbf{S}^\infty \cdot \mathbf{t}_1) \cdot \mathbf{t}_1] \boldsymbol{\omega}^\infty \\ &\quad - [(\frac{3}{5} \mathbf{S}^\infty \cdot \mathbf{O}^\infty - \frac{3}{35} \mathbf{O}^\infty \cdot \mathbf{S}^\infty + \frac{123}{280} \mathbf{S}^\infty \cdot \mathbf{S}^\infty) \cdot \mathbf{t}_1] \times \mathbf{t}_1.\end{aligned}\quad (19)$$

These correction terms account for particle-inertia and fluid-inertia effects. The particle-inertia contribution to the particle angular velocity was calculated in Ref. [12] for a spheroid immersed in a general linear flow. Expanding Eq. (8) in Ref. [12] to first order in ϵ results in an expression consistent with Eq. (18).

From Eqs. (18) and (19) we see that both correction terms are quadratic in the ambient flow-gradient tensors \mathbf{A}^∞ . We also observe that the orientation vector \mathbf{t}_1 occurs twice in each part composing these corrections. This implies that the slip angular velocity remains unchanged upon replacing \mathbf{t}_1 by $-\mathbf{t}_1$ (particle inversion symmetry).

The above results for the angular velocity of the particle give rise to an effective equation of motion that allows us to examine the role played by inertial effects on the rotation of a nearly spherical particle in general linear flows. To this end we parametrize the orientation of the particle by using the polar angle θ and the azimuthal angle ϕ , see Fig. 1. In the laboratory basis \mathbf{e}_i the orientation vector \mathbf{t}_1 reads

$$\mathbf{t}_1 = \sin \theta \cos \phi \mathbf{e}_1 + \sin \theta \sin \phi \mathbf{e}_2 + \cos \theta \mathbf{e}_3. \quad (20)$$

Equations (2) and (15)–(20) result in a nonlinear dynamical system of the form

$$\dot{\phi} = f(\theta, \phi), \quad \dot{\theta} = g(\theta, \phi). \quad (21)$$

In the following section we discuss the explicit forms of this equation for three different linear flows.

V. EXAMPLES

Pure shear flow. For a pure shear flow the matrix \mathbf{A}^∞ in the laboratory basis reads

$$\mathbf{A}^\infty = \begin{pmatrix} 0 & 1 & 0 \\ 0 & 0 & 0 \\ 0 & 0 & 0 \end{pmatrix}$$

(see Fig. 1). Equation (21) takes the form

$$\begin{aligned}\dot{\phi} &= \frac{1}{2} (\epsilon \cos 2\phi - 1) - \frac{\sin 2\phi}{4} \left[\left(\frac{\epsilon St}{15} + \frac{\epsilon Re_s}{35} \right) \sin^2 \theta \right. \\ &\quad \left. + \frac{\epsilon St}{15} - \frac{37\epsilon Re_s}{105} \right],\end{aligned}\quad (22a)$$

$$\begin{aligned}\dot{\theta} &= \epsilon \frac{\sin 2\theta \sin 2\phi}{4} + \frac{\sin \theta \cos \theta}{4} \left[\left(\frac{\epsilon St}{15} - \frac{37\epsilon Re_s}{105} \right) \cos 2\phi \right. \\ &\quad \left. + \frac{\epsilon St}{15} + \frac{11\epsilon Re_s}{35} \right].\end{aligned}\quad (22b)$$

This equation is equivalent to the near-spherical limit of Eq. (9) in Ref. [1]. The derivation outlined in the present article differs from the calculations in Refs. [1,2] in that the method summarized here relies on a basis expansion in spherical harmonics, and a joint expansion in the particle eccentricity ϵ and the shear Reynolds number Re_s . The calculations in Refs. [1,2], in contrast, make use of a multipole expansion, valid for arbitrary aspect ratios. The fact that the calculations agree lends support to the result; i.e., to Eq. (22) as well as to Eq. (9) in Ref. [1]. We refer the reader to Refs. [1,2] for a further discussion of the implications of these results.

Purely rotational flow. In the case of a purely rotational flow the matrix \mathbf{A}^∞ reads

$$\mathbf{A}^\infty = \mathbf{O}^\infty = \begin{pmatrix} 0 & -1 & 0 \\ 1 & 0 & 0 \\ 0 & 0 & 0 \end{pmatrix}, \text{ so that } \mathbf{S}^\infty = \mathbf{0}.$$

In this case, Jeffery's slip angular velocity vanishes and fluid-inertia effects vanish for small Re_s . Only particle inertia affects the angular velocity of the spheroid, and we find

$$\dot{\phi} = 1, \quad (23a)$$

$$\dot{\theta} = \frac{\epsilon St}{30} \sin 2\theta. \quad (23b)$$

In a rotational flow the evolutions of the Euler angles are thus decoupled. Equation (23a) indicates that the spheroid rotates with the same angular velocity as the fluid. Equation (23b) admits two equilibrium orientations (*modulo* π) for the angle θ . The first is $\theta = 0$ (alignment with vorticity), and the second is $\theta = \pi/2$ (the particle rotates in the flow plane). Alignment with vorticity is unstable for prolate particles ($\epsilon > 0$). For oblate nearly spherical particles we find that the stabilities are reversed.

Purely elongational flow. In the case of a purely elongational flow, the matrix \mathbf{A}^∞ reads

$$\mathbf{A}^\infty = \mathbf{S}^\infty = \begin{pmatrix} 1 & 0 & 0 \\ 0 & -1 & 0 \\ 0 & 0 & 0 \end{pmatrix}, \quad \text{so that } \mathbf{O}^\infty = \mathbf{0}.$$

In this case particle-inertia effects vanish so that only fluid-inertia effects remain:

$$\dot{\phi} = -\epsilon \sin 2\phi, \quad (24a)$$

$$\dot{\theta} = \frac{\epsilon}{2} \sin 2\theta \cos 2\phi + \frac{11\epsilon \text{Re}_s}{70} \sin 2\theta. \quad (24b)$$

As in the rotational flow, the temporal evolution of the azimuthal angle ϕ decouples from that of the polar angle θ . Two equilibrium positions are found for the azimuthal angle: $\phi = 0$ which is stable for a prolate particle ($\epsilon > 0$) and unstable for an oblate one ($\epsilon < 0$), and $\phi = \pi/2$ for which the stability is reversed. The equilibrium positions found for θ are similar to those obtained for ϕ ; that is, $\theta = 0$ and $\theta = \pi/2$. From the stability analysis of the ϕ dynamics it follows that $\epsilon \cos(2\phi)/2$ remains positive for both prolate and oblate particles, so that only the polar angle $\theta = \pi/2$ is found to be stable. As a result, prolate and oblate particles orient their axes of symmetry in the flow plane and finally reach fixed orientation, respectively, along $\pm \mathbf{e}_1$ (prolate) or along $\pm \mathbf{e}_2$ (oblate). As Re_s is a small parameter, fluid-inertia effects cannot modify these equilibrium positions. They simply speed up alignment of prolate particles and slow down alignment of oblate particles.

VI. CONCLUSIONS

In this paper, an equation of motion is derived for the orientational dynamics of a neutrally buoyant and nearly spherical particle, immersed in a general steady linear flow. It would be of interest to extend the results to time-dependent linear flows of the form $\mathbf{u}^\infty = \mathbf{A}^\infty(t) \cdot \mathbf{x}$. In this case the second part of Eq. (8) no longer holds and consequently the torque due to unperturbed flow does not vanish. Correction terms scaling as $O(\text{Re}_s)$ and $O(\text{St})$ arise. These additional terms are expected to render the orientational dynamics of the spheroid more complex, but it remains to be seen in detail how these terms affect the orientational dynamics of a neutrally buoyant particle in an unsteady flow.

APPENDIX: STOKES FLOW AROUND A SPHEROID IN A GENERAL LINEAR AMBIENT FLOW

In this appendix we describe how to determine the Stokes flow around a spheroid immersed in a general linear ambient flow. To this end, Eqs. (9) and (10) must be solved. This task is difficult because of the nonspherical shape of the particle. This is the reason why we have used a perturbation method, briefly described in the following.

The surface of the particle is parametrized by

$$r(\vartheta) = 1 + \epsilon h(\vartheta) + \epsilon^2 g(\vartheta)$$

[see Eq. (1) for the actual definition of the spheroid considered in this study]. We introduce the slip angular velocity tensor

$$\boldsymbol{\Omega}_s = \boldsymbol{\Omega} - \mathbf{O}^\infty, \quad \text{where } \boldsymbol{\Omega} \cdot \mathbf{r} = \boldsymbol{\omega} \times \mathbf{r}.$$

Performing an expansion to order $O(\epsilon^3)$ of the fluid velocity in the boundary equation (10) yields

$$\begin{aligned} \mathbf{u}' + [\epsilon h(\vartheta) + \epsilon^2 g(\vartheta)] \frac{\partial \mathbf{u}'}{\partial r} \Big|_{r=1} + \frac{1}{2} [\epsilon h(\vartheta) + \epsilon^2 g(\vartheta)]^2 \frac{\partial^2 \mathbf{u}'}{\partial r^2} \Big|_{r=1} \\ = [1 + \epsilon h(\vartheta) + \epsilon^2 g(\vartheta)] (\boldsymbol{\Omega}_s - \mathbf{S}^\infty) \cdot \mathbf{e}_r, \end{aligned}$$

where $\mathbf{e}_r \equiv \mathbf{r}/|\mathbf{r}|$ is the unit radial vector. We seek a solution of Eqs. (9) and (10) in the form

$$\mathbf{u}' = \mathbf{u}'_0 + \epsilon \mathbf{u}'_1 + \epsilon^2 \mathbf{u}'_2 + O(\epsilon^3).$$

Identifying terms of the same order in ϵ results in a set of three subproblems to solve, associated with the boundary conditions

$$\mathbf{u}'_0|_{r=1} = (\boldsymbol{\Omega}_s - \mathbf{S}^\infty) \cdot \mathbf{e}_r, \quad (A1)$$

$$\mathbf{u}'_1|_{r=1} = (\boldsymbol{\Omega}_s - \mathbf{S}^\infty) \cdot h(\vartheta) \mathbf{e}_r - h(\vartheta) \frac{\partial \mathbf{u}'_0}{\partial r} \Big|_{r=1}, \quad (A2)$$

$$\begin{aligned} \mathbf{u}'_2|_{r=1} = (\boldsymbol{\Omega}_s - \mathbf{S}^\infty) \cdot g(\vartheta) \mathbf{e}_r - g(\vartheta) \frac{\partial \mathbf{u}'_0}{\partial r} \Big|_{r=1} \\ - h(\vartheta) \frac{\partial \mathbf{u}'_1}{\partial r} \Big|_{r=1} - \frac{h(\vartheta)^2}{2} \frac{\partial^2 \mathbf{u}'_0}{\partial r^2} \Big|_{r=1}. \end{aligned} \quad (A3)$$

Lamb solutions. To determine the solutions of Eqs. (A1) to (A3), we use general Lamb solutions which exploit the fact that any flow solution of the Stokes equations can be written in terms of linear combinations of spherical harmonics. According to Lamb [10] (see also Happel and Brenner [4]) the general solution for a velocity field that vanishes at infinity can be cast in the form

$$\begin{aligned} \mathbf{u}' = \sum_{n=1}^{\infty} \left[\nabla \times (r \mathbf{e}_r \chi_{-(n+1)}) + \nabla \Phi_{-(n+1)} - \frac{(n-2)}{2n(2n-1)} \right. \\ \times r^2 \nabla \mathcal{P}_{-(n+1)} + \left. \frac{(n+1)}{n(2n-1)} r \mathbf{e}_r \mathcal{P}_{-(n+1)} \right]. \end{aligned}$$

Here $\mathcal{P}_{-(n+1)}$, $\chi_{-(n+1)}$, and $\Phi_{-(n+1)}$ are spherical harmonics [13]. These three spherical harmonics involve coefficients that remain to be determined using the boundary conditions satisfied by the fluid velocity on the surface of the particle. Happel and Brenner [4] proposed an efficient method to determine these coefficients that consists of writing the three spherical harmonic functions in the form

$$\begin{aligned} \mathcal{P}_{-(n+1)} &= \frac{(2n-1)}{(n+1)} \left(\frac{1}{r} \right)^{n+1} [(n+2)X_n + Y_n], \\ \Phi_{-(n+1)} &= \frac{1}{2(n+1)} \left(\frac{1}{r} \right)^{n+1} [nX_n + Y_n], \\ \chi_{-(n+1)} &= \frac{1}{n(n+1)} \left(\frac{1}{r} \right)^{n+1} Z_n. \end{aligned}$$

Here X_n , Y_n , and Z_n are surface harmonics [14]. To give an example, the surface harmonics X_n read

$$\begin{aligned} X_n &= A_n P_n [\cos(\vartheta)] + \sum_{m=1}^n [B_{nm} \cos(m\varphi) + C_{nm} \sin(m\varphi)] \\ &\times P_n^m [\cos(\vartheta)]. \end{aligned} \quad (A4)$$



Here A_n , B_{nm} , and C_{nm} are constants to be determined, and P_n and P_n^m are the Legendre polynomials and their associated functions [14]. The surface harmonics Y_n and Z_n have expansions similar to X_n but with different constants. The constants are determined by using the relations

$$\mathbf{e}_r \cdot \mathbf{V}(\vartheta, \varphi) = \sum_{n=1}^{\infty} X_n(\vartheta, \varphi), \quad (\text{A5})$$

$$-r\nabla \cdot \mathbf{V}(\vartheta, \varphi) = \sum_{n=1}^{\infty} Y_n(\vartheta, \varphi), \quad (\text{A6})$$

$$r\mathbf{e}_r \cdot \nabla \times \mathbf{V}(\vartheta, \varphi) = \sum_{n=1}^{\infty} Z_n(\vartheta, \varphi), \quad (\text{A7})$$

where by definition

$$\mathbf{u}'|_{r=1} = \mathbf{V}(\vartheta, \varphi).$$

Now the coefficients in X_n , Y_n , and Z_n are determined as follows: Let N be the finite number of harmonics in the solution. The value of N does not exceed $p + 2$ where p is the maximal power of $\cos(\vartheta)$ or $\sin(\vartheta)$ in the boundary condition. The idea here is to fix first the value of m of the associated Legendre polynomials by exploiting the orthogonality of the trigonometric functions $\cos(m\varphi)$ and $\sin(m\varphi)$ and then to exploit the orthogonality of the Legendre polynomials:

$$\int_{-1}^1 P_n(x)P_m(x)dx = \frac{2}{2n+1}\delta_{nm},$$

and their associated functions (for a given m):

$$\int_{-1}^1 P_n^m(x)P_{n'}^m(x)dx = \frac{2}{2n+1}\frac{(n+m)!}{(n-m)!}\delta_{nn'}.$$

As an example, let us show how we determine the coefficients A_n , B_{nm} , and C_{nm} involved in the surface harmonic X_n in Eq. (A4) from Eq. (A5). Consider first the case $m = 0$. Then

$$T_1 = \frac{1}{2\pi} \int_0^{2\pi} [\mathbf{e}_r \cdot \mathbf{V}(\vartheta, \varphi)]d\varphi,$$

and we find for n from 0 to N :

$$A_n = \frac{2n+1}{2} \int_0^\pi \sin(\vartheta)P_n[\cos(\vartheta)]T_1 d\vartheta.$$

Now consider $m > 0$. Let

$$T_{1m} = \frac{1}{\pi} \int_0^{2\pi} [\mathbf{e}_r \cdot \mathbf{V}(\vartheta, \varphi)] \cos(m\varphi)d\varphi,$$

and

$$T_{2m} = \frac{1}{\pi} \int_0^{2\pi} [\mathbf{e}_r \cdot \mathbf{V}(\vartheta, \varphi)] \sin(m\varphi)d\varphi.$$

Then we find for n from m to N :

$$B_{nm} = \frac{2n+1}{2} \frac{(n-m)!}{(n+m)!} \int_0^\pi \sin(\vartheta)P_n^m[\cos(\vartheta)]T_{1m} d\vartheta,$$

and

$$C_{nm} = \frac{2n+1}{2} \frac{(n-m)!}{(n+m)!} \int_0^\pi \sin(\vartheta)P_n^m[\cos(\vartheta)]T_{2m} d\vartheta.$$

We implemented this method to determine the solutions of the three subproblems associated with the boundary conditions (A1)–(A3) in MAPLE®.

-
- [1] J. Einarsson, F. Candelier, F. Lundell, J. R. Angilella, and B. Mehlig, *Phys. Rev. E* **91**, 041002 (2015).
 - [2] J. Einarsson, F. Candelier, F. Lundell, J. R. Angilella, and B. Mehlig, [arXiv:1504.02309](https://arxiv.org/abs/1504.02309).
 - [3] H. Lorentz, Versl. Kon. Akad. Wetensch. Amsterdam **4**, 176 (1896).
 - [4] J. Happel and H. Brenner, *Low Reynolds Number Hydrodynamics* (Kluwer Academic Publisher, Dordrecht, The Netherlands, 1983).
 - [5] S. Kim and S. J. Karrila, *Microhydrodynamics: Principles and Selected Applications* (Butterworth-Heinemann, Boston, 1991).
 - [6] G. Subramanian and D. L. Koch, *J. Fluid Mech.* **535**, 383 (2005).
 - [7] G. Subramanian and D. L. Koch, *J. Fluid Mech.* **557**, 257 (2006).
 - [8] H. Brenner, *Chem. Eng. Sci.* **19**, 519 (1964).
 - [9] E. J. Hinch, *Perturbation Methods* (Cambridge University Press, Cambridge, 1991).
 - [10] H. Lamb, *Hydrodynamics*, 6th ed. (Dover, New York, 1945).
 - [11] G. B. Jeffery, *Proc. R. Soc. London, Ser. A* **102**, 161 (1922).
 - [12] J. Einarsson, J. R. Angilella, and B. Mehlig, *Phys. D* **278–279**, 79 (2014).
 - [13] W. E. Byerly, *An Elementary Treatise on Fourier Series and Spherical, Cylindrical, and Ellipsoidal Harmonics, with Applications to Problems in Mathematical Physics* (Dover, New York, 1959).
 - [14] M. Abramowitz and A. Stegun, *Handbook of Mathematical Functions*, 9th ed. (Dover, New York, 1972).



Erratum: Role of inertia for the rotation of a nearly spherical particle in a general linear flow
[Phys. Rev. E 91, 053023 (2015)]

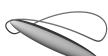
F. Candelier, J. Einarsson, F. Lundell, B. Mehlig, and J.-R. Angilella

(Received 23 October 2015; published xxxxxx)

DOI: [10.1103/PhysRevE.00.009900](https://doi.org/10.1103/PhysRevE.00.009900) PACS number(s): 47.15.G-, 83.10.Pp, 47.55.Kf, 47.10.-g, 99.10.Cd

In this paper we investigated the role of inertia for the rotation of a nearly spherical particle in a general linear time-independent flow. As we continued to work on related questions we realized that the argument used in this paper to show that Eq. (7) evaluates to zero is valid for a constant shear flow, but not in general. This implies that our results for the shear flow [Eq. (22)] are correct and consistent with the results of Refs. [1–3]. But for other linear flows Eq. (7) may give rise to additional contributions to the angular particle velocity [Eq. (19)]. As a consequence, Eq. (23b) for the case of a purely rotational flow is replaced by $\dot{\theta} = (\epsilon/30)[St - Re_s] \sin 2\theta$. The right-hand side of this equation evaluates to zero for neutrally buoyant particles ($St = Re_s$). This means that a neutrally buoyant particle rotates precisely like the surrounding fluid as it must since the fluid rotates as a rigid body. For an elongational flow the factor 11/70 in Eq. (24b) is replaced by 8/42. The conclusions for a nearly spherical particle in an elongational flow do not change.

- [1] J. Einarsson, F. Candelier, F. Lundell, J. R. Angilella, and B. Mehlig, *Phys. Fluids* **27**, 063301 (2015).
- [2] J. Einarsson, F. Candelier, F. Lundell, J. R. Angilella, and B. Mehlig, *Phys. Rev. E* **91**, 041002(R) (2015).
- [3] T. Rosen, J. Einarsson, A. Nordmark, C. Aidun, F. Lundell, and B. Mehlig, [arXiv:1508.04976](https://arxiv.org/abs/1508.04976).





Paper C

Open Access (CC BY 3.0) at <http://dx.doi.org/10.1063/1.4921543>





Rotation of a spheroid in a simple shear at small Reynolds number

J. Einarsson,¹ F. Candelier,² F. Lundell,³ J. R. Angilella,⁴ and B. Mehlig¹

¹*Department of Physics, Gothenburg University, 41296 Gothenburg, Sweden*

²*University of Aix-Marseille, CNRS, IUSTI UMR 7343, 13 013 Marseille Cedex 13, France*

³*KTH Royal Institute of Technology, SE-100 44 Stockholm, Sweden*

⁴*Department of Mathematics and Mechanics, LUSAC-ESIX, University of Caen, 50130 Cherbourg, France*

(Received 5 February 2015; accepted 6 May 2015; published online 1 June 2015)

We derive an effective equation of motion for the orientational dynamics of a neutrally buoyant spheroid suspended in a simple shear flow, valid for arbitrary particle aspect ratios and to linear order in the shear Reynolds number. We show how inertial effects lift the degeneracy of the Jeffery orbits and determine the stabilities of the log-rolling and tumbling orbits at infinitesimal shear Reynolds numbers. For prolate spheroids, we find stable tumbling in the shear plane and log-rolling is unstable. For oblate spheroids, by contrast, log-rolling is stable and tumbling is unstable provided that the particle is not too disk-like (moderate asphericity). For very flat oblate spheroids, both log-rolling and tumbling are stable, separated by an unstable limit cycle. © 2015 Author(s). All article content, except where otherwise noted, is licensed under a Creative Commons Attribution 3.0 Unported License. [http://dx.doi.org/10.1063/1.4921543]

I. INTRODUCTION

In this article, we describe the effect of weak inertia upon the orientational dynamics of a neutrally buoyant spheroid in a simple shear flow using perturbation theory. In the absence of inertial effects, the rotation of a neutrally buoyant spheroid in a simple shear was determined by Jeffery who found that there are infinitely many degenerate periodic orbits,¹ the so-called “Jeffery orbits.” In this limit, the initial orientation determines in which way the particle rotates. Fluid and particle inertias lift this degeneracy, but little is known about how this comes about. A notable exception is the work by Subramanian and Koch who have solved the problem for rod-shaped particles in the slender-body approximation.² We discuss other theoretical results below in Sec. II.

The question is currently of great interest: several recent papers have reported results of direct numerical simulations (DNSs) of the problem, using “lattice Boltzmann” methods.^{3–6} These studies reveal that fluid and particle inertias affect the orientational dynamics of a neutrally buoyant spheroid in a simple shear in intricate ways. The DNSs are performed at moderate and large shear Reynolds numbers, defined as $Re_s = sa^2/\nu$, where a is the largest particle dimension, s is the shear strength, and ν the kinematic viscosity of the suspending fluid. DNSs at very small Reynolds numbers are difficult to perform. But this limit (Re_s of order unity and smaller) is of particular interest. There is a long-standing question whether or not a nearly spherical prolate spheroid exhibits stable “log-rolling” in this limit, so that its symmetry axis aligns with the vorticity axis. It was first suggested by Saffman that this is the case,⁷ in an attempt to explain Jeffery’s hypothesis¹ that spheroids rotate in orbits that minimise energy dissipation. But stable log-rolling of prolate spheroids has not been found in DNS, and it has been suggested that higher Re_s -corrections may explain this discrepancy.⁶ The small- Re_s limit is of interest also because it provides stringent tests for DNS. These reasons motivated us to derive an equation of motion that takes into account the effect of weak fluid and particle inertia. Our main result is an approximate dynamical equation for the rotation of a neutrally buoyant spheroid suspended in a simple shear flow, valid for arbitrary aspect ratios and to first order in Re_s (Eq. (42) in Sec. IV). In the slender-body limit, this equation



is of the same form as the one derived in Ref. 2. In the completely inertia-free case, our results reduce to Jeffery's equation.¹ We find that corrections to this limit arise from both particle inertia (centrifugal and gyroscopic forces) and fluid inertia (modifying the hydrodynamic torque on the particle). The particle-inertia corrections we report here are consistent with earlier numerical and analytical results.^{8,9}

Fluid-inertia corrections are taken into account to first order in Re_s using a reciprocal theorem.¹⁰ Our approach is similar to the one adopted in Ref. 2 in the slender-body limit, but our equation of motion is valid for spheroids with arbitrary aspect ratios. By linear stability analysis, we determine the stabilities of the periodic orbits of this equation at infinitesimal Re_s as a function of the particle aspect ratio. The stability calculation details how the degeneracy of the Jeffery orbits for a neutrally buoyant spheroid in a simple shear is lifted by weak inertia.

We find that the log-rolling orbit is unstable for prolate particles. This explains why stable log-rolling is not observed in DNS^{3–6} at the smallest shear Reynolds numbers accessible in the simulations. Moreover, we find that tumbling in the flow-shear plane is stable for prolate particles. As the aspect ratio tends to unity, there is a bifurcation: for nearly spherical oblate particles, log-rolling is stable and tumbling in the flow-shear plane is unstable. There is a second bifurcation for oblate particles. At a critical aspect ratio $\lambda_c \approx 1/7.3$, tumbling becomes stable and an unstable limit cycle is born. This means that the behaviour of a very flat disk depends on its initial orientation for $\lambda < \lambda_c$. We discuss how the shape of the limit cycle changes as the aspect ratio tends to zero.

The remainder of this article is organised as follows. In Sec. II, we give an overview over the background of the problem. Section III summarises the method employed in this article, based on a reciprocal theorem.¹⁰ We demonstrate how to calculate the effect of particle and fluid inertias to first order and how we use the symmetries of the problem to make it tractable. Section IV summarises our results: the equation of motion and its stability analysis. We discuss the results in Sec. V and conclude with Sec. VI.

A brief account of the main results described in this article was given in Ref. 11. Here we describe the complete derivation. We also present additional results and discussion that could not be included in the shorter format: we quote precise asymptotic formulae for small and large aspect ratios, as well as for aspect ratios close to unity. We also characterise the limit cycle that arises for $\lambda < \lambda_c$, and compute its linear stability.

II. BACKGROUND

The question of describing the rotation of a neutrally buoyant particle in a simple shear flow has a long history. Jeffery derived an expression for the torque on an ellipsoidal (tri-axial) particle neglecting inertial effects.¹ To obtain an equation of motion for small particles, he assumed that the dynamics is overdamped and that the particle rotates so as to instantaneously achieve zero torque. This gives rise to Jeffery's equation that is commonly quoted for the special case of spheroidal (axisymmetric) particles. From this equation, it follows that spheroids suspended in a simple shear tumble: they stay aligned with the flow direction for some time, and then switch orientation by 180°. The dynamics is degenerate in that there are infinitely many different periodic orbits, the so-called "Jeffery orbits." The initial orientation determines which particular orbit is selected. The goal of Jeffery's calculation was to compute the viscosity of a dilute suspension of spheroids, and Jeffery hypothesised that the particles select orbits that minimise energy dissipation.

Saffman⁷ pointed out that inertial effects lift the degeneracy of the Jeffery orbits, and he described the orientational dynamics of a nearly spherical particle in a simple shear taking into account the fluid inertia. For prolate particles, he concluded that log-rolling is stable, that tumbling in the shear plane is unstable, and that the stabilities are reversed for oblate particles. These results are stated in terms of an effective drift for the particle orientation (towards the vorticity axis for prolate particles). This conclusion supports Jeffery's hypothesis. Saffman did not take into account the particle inertia. His method of calculation rests on a joint expansion in small eccentricity and Re_s .



Harper and Chang¹² addressed the problem in a different way, modeling the dynamics of a rod in a simple shear in terms a dumb-bell, that is, two spheres connected by an invisible rigid rod. The spheres are subjected to Stokes drag and hydrodynamic lift forces.¹³ This approximation neglects hydrodynamic interactions between the two spheres, as well as the unsteady term in the Navier-Stokes equations. Harper and Chang arrive at the opposite conclusion, namely, that log-rolling is unstable. Since their result pertains to the slender-body limit, the question is how the stability of the log-rolling orbit depends on the particle aspect ratio.

It was subsequently shown by Hinch and Leal¹⁴ how weak rotational diffusion breaks the degeneracy of the Jeffery orbits, and their results form the basis for a large part of the work during the last decades on the rheology of dilute suspensions, see Refs. 15 and 16 for reviews.

Recently, there has been a surge of interest in determining the effect of weak inertia upon a spheroid tumbling in a simple shear flow in the absence of rotational diffusion. Subramanian and Koch² derived an effective equation of motion for a neutrally buoyant rod in the slender-body limit to first order in fluid and particle inertias. Their calculation uses a reciprocal theorem¹⁰ and takes into account the unsteady term in the Navier Stokes equation as well as particle inertia. The authors arrive at qualitatively the same conclusion as Harper and Chang, namely, that the orientation of the rod eventually drifts towards the flow-shear plane.

In a second paper, Subramanian and Koch¹⁷ repeated Saffman's calculation for a neutrally buoyant nearly spherical particle. They used a different method, similar to the one used in Ref. 2, and came to the same conclusion as Saffman that log-rolling is stable for nearly spherical prolate particles.

Recent DNSs^{3–6} have explored the stability of log-rolling and tumbling orbits, mostly at moderate and large Reynolds numbers and only for a small number of aspect ratios. The simulations show unstable log-rolling for prolate particles at the smallest Reynolds numbers studied. We note that Yu, Phan-Thien and Tanner¹⁸ misquote Saffman when they describe their numerical results on the rotation of a spheroid in a Couette flow at Reynolds numbers of the order of 10 and larger. In the Introduction of Ref. 18, it is implied that Saffman's theory⁷ predicts that nearly spherical prolate particles tend to the flow-shear plane.

III. METHOD

In this section, we give a brief but complete summary of our calculation. The most technical details and tabulations are deferred to appendices. We start with notation and the relevant dimensionless parameters determining the physics. Then, we give the governing equations and explain how to express the hydrodynamic torque through a reciprocal theorem.^{2,10,19,20} Finally, we explain the perturbation scheme and list the symmetries that severely constrain the form of the solution.

A. Notation

The calculations described in this paper involve vectors and tensors in three spatial dimensions. We employ index notation with the implicit summation convention for repeated indices and we use the Kronecker (δ_{ij}) and Levi-Civita (ε_{ijk}) tensors.

B. Units and dimensionless numbers

The physics of the problem is governed by three dimensionless numbers: the shear Reynolds number Re_s (measuring fluid inertia), the Stokes number St (measuring particle inertia), and the particle aspect ratio λ .

We work with dimensionless variables. The length scale is given by the particle major axis a . The velocity scale is taken to be sa , where s is the shear rate. The explicit time dependence of the flow (the time scale for the unsteady fluid inertia) scales as $\sim 1/s$ since it is determined by the particle angular velocity because to the lowest order, the unsteadiness arises from the particle motion. The corresponding scale for pressure is μs , and force and torque are measured in units of μsa^2 and μsa^3 , respectively.



From these scales, the dimensionless parameters are formed. As mentioned in the Introduction, the shear Reynolds number is defined as

$$\text{Re}_s = \frac{sa^2\rho_f}{\mu}. \quad (1)$$

Here, ρ_f is the density and $\mu = \rho_f v$ is the dynamic viscosity of the surrounding fluid (v is the kinematic viscosity).

The Stokes number, measuring the particle inertia, is given by the ratio of the typical rate of change of angular momentum and the typical torque,

$$\text{St} = \frac{\rho_p sa^2}{\mu} = \frac{\rho_p}{\rho_f} \text{Re}_s. \quad (2)$$

Here, ρ_p is the particle density. For a neutrally buoyant particle, $\rho_p = \rho_f$, we have $\text{St} = \text{Re}_s$.

We define the particle aspect ratio λ as the ratio between the length along the symmetry axis and the length transverse to the symmetry axis (Fig. 1). That is, $\lambda > 1$ denotes prolate particles, while $\lambda < 1$ denotes oblate particles. Because we measure length in units of the major particle axis a , the aspect ratio λ of a prolate particle is a/b , while the aspect ratio of an oblate particle is b/a , where b denotes the length of the minor axis of the particle (see Fig. 1).

C. Equations of motion

Let n_i denote the components of the unit vector \mathbf{n} pointing in the direction of the particle symmetry axis (Fig. 1) and ω_i the components of the angular velocity of the particle. Newton's second law for the orientational degrees of freedom for an axisymmetric particle reads

$$\dot{n}_i = \varepsilon_{ijk}\omega_j n_k, \quad \text{St} [\dot{I}_{ij}\omega_j + I_{ij}\dot{\omega}_j] = T_i. \quad (3)$$

Dots denote time derivatives, and I_{ij} are the elements of the moment-of-inertia tensor of the particle and T_i are the components of the torque exerted on the particle. The elements of the moment-of-inertia tensor of an axisymmetric particle with axis of symmetry \mathbf{n} take the form

$$I_{ij} = A^I n_i n_j + B^I (\delta_{ij} - n_i n_j), \quad (4)$$

where A^I and B^I correspond to the moments-of-inertia around and transverse to the symmetry axis. Using the dimensionless variables introduced in Sec. III B, we have for a prolate spheroid ($\lambda > 1$),

$$A^I = \frac{8\pi}{15} \frac{1}{\lambda^4}, \quad B^I = \frac{4\pi}{15} \frac{1}{\lambda^2} \left(1 + \frac{1}{\lambda^2}\right) \quad (5)$$

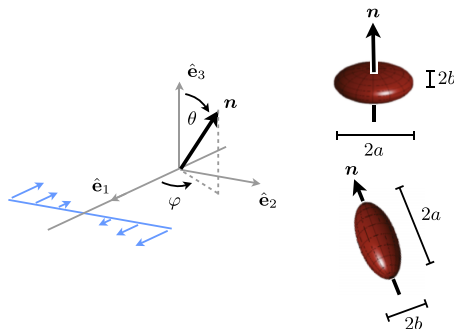


FIG. 1. Spheroid rotating in a simple shear (schematic). Drawing shows the Cartesian coordinate system $\hat{\mathbf{e}}_j$, $j = 1, \dots, 3$. Vorticity points in the negative $\hat{\mathbf{e}}_3$ -direction. The flow-shear plane is spanned by $\hat{\mathbf{e}}_1$ and $\hat{\mathbf{e}}_2$. The unit vector \mathbf{n} points along the symmetry axis of the spheroid. Its polar angle is denoted by θ and the azimuthal angle by φ . The major axis length of the spheroid is denoted by a and the minor length by b . For prolate particles, the aspect ratio is defined as $\lambda = a/b$, and for oblate particles as $\lambda = b/a$.



and for an oblate spheroid ($\lambda < 1$),

$$A^I = \frac{8\pi}{15}\lambda, \quad B^I = \frac{4\pi}{15}\lambda(1 + \lambda^2). \quad (6)$$

We rewrite equation of motion (3) as

$$\dot{\omega}_i = -I_{ij}^{-1}\dot{l}_{jk}\omega_k + \frac{1}{St}I_{ij}^{-1}T_j = -\frac{A^I - B^I}{B^I}\varepsilon_{ijk}\omega_j n_k n_l \omega_l + \frac{1}{St}I_{ij}^{-1}T_j. \quad (7)$$

In the final step, we used definition (4) of I_{ij} and equation of motion (3) for \dot{n}_i . In this paper, T_i are the components of the hydrodynamic torque exerted on the particle by the fluid. In Sec. III D, we formulate the hydrodynamic torque to $O(\text{Re}_s)$ via the reciprocal theorem. In Sec. III E, we perturbatively compute the resulting angular velocity to orders $O(\text{Re}_s)$ and $O(\text{St})$.

D. Calculation of the hydrodynamic torque to order Re_s

The straightforward approach to determine the torque on a particle in a fluid is to solve Navier-Stokes equations for the velocity and pressure fields, to compute the stress tensor, and finally to integrate the stress tensor over the surface of the particle. The reciprocal theorem^{2,10,19} offers an alternative, and often more convenient, route to the hydrodynamic forces. In particular, we may avoid solving for the complete flow field. In this section, we specify the Navier-Stokes problem that we need to solve and explain how we use the reciprocal theorem to simplify the calculations.

1. Navier-Stokes problem for the disturbance flow

We consider a particle with boundary \mathcal{S} immersed in a linear ambient flow $(\mathbf{u}^\infty, p^\infty)$. Throughout this paper, we express the components of the ambient flow as

$$u_i^\infty = A_{ij}^\infty r_j = \varepsilon_{ikj}\Omega_k^\infty r_j + S_{ij}^\infty r_j, \quad (8)$$

or equivalently with $\varepsilon_{ikj}\Omega_k^\infty = O_{ij}^\infty$,

$$u_i^\infty = O_{ij}^\infty r_j + S_{ij}^\infty r_j. \quad (9)$$

Here, S^∞ and O^∞ are the symmetric and antisymmetric parts of the flow gradient with elements

$$S_{ij}^\infty = \frac{1}{2}(A_{ij}^\infty + A_{ji}^\infty), \quad O_{ij}^\infty = \frac{1}{2}(A_{ij}^\infty - A_{ji}^\infty). \quad (10)$$

In dimensionless variables (Sec. III B), the Navier-Stokes equations read

$$\text{Re}_s (\partial_t u_i + u_j \partial_j u_i) = -\partial_i p + \partial_j \partial_j u_i, \quad \partial_i u_i = 0. \quad (11)$$

Note that the unsteady and convective inertia terms come with the same prefactor in this problem. This happens because the time scale of the particle motion is the same as the time scale of the flow. The boundary condition is no-slip on the surface of the particle

$$u_i = \varepsilon_{ijk}\omega_j r_k \quad \text{for } \mathbf{r} \in \mathcal{S}, \quad u_i = u_i^\infty \text{ as } |\mathbf{r}| \rightarrow \infty. \quad (12)$$

We introduce the disturbance field (\mathbf{u}', p') from the particle, defined by

$$u_i = u_i^\infty + u'_i, \quad p = p^\infty + p'. \quad (13)$$

If we assume that $(\mathbf{u}^\infty, p^\infty)$ satisfies the Navier-Stokes equations, we have the disturbance problem

$$\text{Re}_s (\partial_t u'_i + u_j^\infty \partial_j u'_i + u'_j \partial_j u_i^\infty + u'_j \partial_j u_i) = -\partial_i p' + \partial_j \partial_j u'_i, \quad (14)$$

and the boundary conditions are expressed in the slip angular velocity $\Omega_i = \Omega_i^\infty - \omega_i$ as

$$u'_i = -\varepsilon_{ijk}\Omega_j r_k - S_{ij}^\infty r_j, \quad \mathbf{r} \in \mathcal{S}, \\ u'_i = 0, \quad |\mathbf{r}| \rightarrow \infty. \quad (15)$$



Finally, when applying the reciprocal theorem, we shall use that, by definition, the divergence of the stress tensor satisfies the following equalities:

$$\begin{aligned}\partial_j \sigma'_{ij} &= -\partial_i p' + \partial_j \partial_j u'_i \\ &= \text{Re}_s (\partial_t u'_i + u_j^\infty \partial_j u'_i + u'_j \partial_j u_i^\infty + u'_j \partial_j u'_i) \\ &\equiv \text{Re}_s f_i(\mathbf{u}').\end{aligned}\quad (16)$$

2. The Stokes solution

This paper concerns a spheroidal particle suspended in a linear flow. We thus need explicit solutions to Eq. (14) at $\text{Re}_s = 0$ in this geometry. We use a finite multipole expansion^{10,21} (see Appendix A). In our notation, the solutions read

$$\begin{aligned}u'_i &= Q_{ij,k}^R \varepsilon_{jkl} [(A^R n_l n_m + B^R (\delta_{lm} - n_l n_m)) \Omega_m + C^R \varepsilon_{lmn} n_m S_{no}^\infty n_o] \\ &+ (Q_{ij,k}^S + \alpha Q_{ij,llk}^O) \\ &\times [(A^S n_{jklm}^A + B^S n_{jklm}^B + C^S n_{jklm}^C) S_{lm}^\infty - C^R (\varepsilon_{jlm} n_k n_m + \varepsilon_{klm} n_j n_m) \Omega_l],\end{aligned}\quad (17)$$

where

$$\begin{aligned}n_{jklm}^A &= (n_j n_k - \frac{1}{3} \delta_{jk})(n_l n_m - \frac{1}{3} \delta_{lm}), \\ n_{jklm}^B &= n_j \delta_{kl} n_m + n_k \delta_{jl} n_m + n_j \delta_{km} n_l + n_k \delta_{jm} n_l - 4 n_j n_k n_l n_m, \\ n_{jklm}^C &= -\delta_{jk} \delta_{lm} + \delta_{jl} \delta_{km} + \delta_{kl} \delta_{jm} \\ &+ \delta_{jk} n_l n_m + \delta_{lm} n_j n_k - n_j \delta_{kl} n_m - n_k \delta_{jl} n_m \\ &- n_j \delta_{km} n_l - n_k \delta_{jm} n_l + n_j n_k n_l n_m.\end{aligned}$$

Here, A^R , B^R , C^R , A^S , B^S , C^S , and α are known constants that depend on the particle aspect ratio λ . The exact definition of the spheroidal multipoles Q and the values of all constants are given in Appendix A, see in particular Table III.

3. The reciprocal theorem

This theorem^{2,10,19,20} relates integrals of the velocity and stress fields of two incompressible and Newtonian fluids. The idea is the following. Let one set of fields represent the actual problem of interest, the *primary problem*. Then, choose the second set of fields to be an *auxiliary problem* with known solution, such that an integral in the theorem relates to hydrodynamic torque of the primary problem. Provided that all integrals in the theorem converge and can be evaluated, we can solve the resulting equations for the hydrodynamic torque.

The reciprocal theorem for the two sets $(\tilde{u}_i, \tilde{\sigma}_{ij})$ and (u'_i, σ'_{ij}) can be stated as

$$\int_S d\tilde{F}_i u'_i + \int_V dV u'_i \partial_j \tilde{\sigma}_{ij} = \int_S dF'_i \tilde{u}_i + \int_V dV \tilde{u}_i \partial_j \sigma'_{ij}. \quad (18)$$

Here, $dF_i = \sigma_{ij} \xi_j dS$ is the differential force from the fluid on the surface element with normal vector $\xi_j dS$. The volume integrals are to be taken over the entire fluid volume outside the particle, and the surface integrals over all surfaces bounding the fluid volume, with surface normals pointing out of the fluid volume.

In the following, we apply the reciprocal theorem to the calculation of the hydrodynamic torque on a particle.

4. Calculation of the torque

We choose the auxiliary problem $(\tilde{u}_i, \tilde{\sigma}_{ij})$ to be the Stokes flow around an identical particle rotating with an angular velocity $\tilde{\omega}_i$ in an otherwise quiescent fluid. Its solution is given by Eq. (17)



with $\mathbf{u}^\infty = 0$. The primary problem is the disturbance problem defined in Eq. (14). Inserting the boundary conditions into the reciprocal theorem yields

$$\int_S d\tilde{F}_i(\varepsilon_{ijk}(\omega_j - \Omega_j^\infty)r_k - S_{ij}^\infty r_j) = \int_S dF'_i \varepsilon_{ijk} \tilde{\omega}_j r_k + \text{Re}_s \int_V dV \tilde{u}_i f_i(\mathbf{u}'). \quad (19)$$

Here, $f_i(\mathbf{u}')$ is defined in Eq. (16). We also used that $\partial_j \tilde{\sigma}_{ij} = 0$. This equality holds because \tilde{u}_i is a Stokes flow. Both primary and auxiliary velocity fields vanish as $|\mathbf{r}| \rightarrow \infty$; therefore, both integration surfaces are only the particle surface S . Note that the surface integrals are to be taken with surface normals out of the fluid domain, so that dF_i is the differential force exerted on the particle by the fluid. In the integrals, we identify the hydrodynamic torque on the particle. Its components are given by

$$T_j = \int_S dF_i \varepsilon_{ijk} r_k. \quad (20)$$

It follows

$$(\omega_j - \Omega_j^\infty) \tilde{T}_j - \int_S d\tilde{F}_i S_{ij}^\infty r_j = \tilde{\omega}_j (T_j - T_j^\infty) + \text{Re}_s \int_V dV \tilde{u}_i f_i(\mathbf{u}'). \quad (21)$$

The auxiliary torque \tilde{T}_j together with the surface integral adds up to the Jeffery torque¹ $T_j^{(0)}$,

$$T_j^{(0)} = c_\xi [(A^R n_j n_k + B^R (\delta_{jk} - n_j n_k)) (\Omega_k^\infty - \omega_k) + C^R \varepsilon_{jkm} n_k n_l S_{ml}^\infty]. \quad (22)$$

The constant c_ξ is given in Table III in Appendix A. The contribution

$$T_j^\infty \equiv \int_S dS \sigma_{il}^\infty \xi_l \varepsilon_{ijk} \tilde{\omega}_j r_k \quad (23)$$

evaluates to zero for any time-independent linear flow u_i^∞ . It follows that Eq. (21) becomes

$$\tilde{\omega}_j T_j = \tilde{\omega}_j T_j^{(0)} - \text{Re}_s \int_V dV \tilde{u}_i f_i(\mathbf{u}'). \quad (24)$$

Since \tilde{u}_i is linear in $\tilde{\omega}_j$, this variable can be eliminated. We finally obtain

$$T_j = T_j^{(0)} - \text{Re}_s \int_V dV \tilde{U}_{ij} f_i(\mathbf{u}'), \quad (25)$$

where

$$\begin{aligned} \tilde{U}_{ip} &= -Q_{ij,k}^R \varepsilon_{jkl} [(A^R n_l n_p + B^R (\delta_{lp} - n_l n_p))] \\ &\quad + (Q_{ij,k}^S + \alpha Q_{ij,llk}^O) [C^R (\varepsilon_{jpm} n_k n_m + \varepsilon_{kpm} n_j n_m)]. \end{aligned} \quad (26)$$

Thus, so far we have made no approximation, and Eq. (25) is exact, the difficulty lies in evaluating the Navier-Stokes disturbance flow \mathbf{u}' . This is a complicated non-linear problem since $T_j^{(0)}$, \tilde{U}_{ij} , and $f_i(\mathbf{u}')$ all depend on the direction \mathbf{n} and upon the angular velocity $\boldsymbol{\omega}$ of the particle. The flow equations thus couple non-linearly to the rigid body equations of motion for the particle. In the following, we solve this system of equations in perturbation theory valid to first order in St and Re_s .

E. Perturbative calculation of the particle angular velocity

In this section, we determine the angular velocity $\boldsymbol{\omega}$ of the particle to the lowest order in St and Re_s , assuming that both St and Re_s are small, so that $\text{Re}_s \text{St}$ is negligible. We recall equation of motion (7) for the particle orientation and insert the expression for the hydrodynamic torque obtained in Sec. III D,

$$\begin{aligned} \dot{n}_i &= \varepsilon_{ijk} \omega_j n_k, \\ \text{St} \dot{\omega}_i &= -\text{St} \frac{A^I - B^I}{B^I} \varepsilon_{ijk} \omega_j n_k n_l \omega_l + I_{ij}^{-1} T_j^{(0)} - \text{Re}_s I_{ij}^{-1} \int_V dV \tilde{U}_{kj} f_k(\mathbf{u}'). \end{aligned} \quad (27)$$

Now, we expand the angular velocity as

$$\omega_i = \omega_i^{(0)} + \text{St} \omega_i^{(\text{St})} + \text{Re}_s \omega_i^{(\text{Re}_s)} + o(\text{Re}_s, \text{St}). \quad (28)$$



Next, we insert these expansions into equation of motion (7) and collect terms of equal order in St and Re_s ,

$$\begin{aligned} 0 &= T_j^{(0)}, \\ \omega_i^{(0)} &= -\frac{A^I - B^I}{B^I} \varepsilon_{ijk} \omega_j^{(0)} n_k n_l \omega_l^{(0)} - I_{ij}^{-1} c_\xi (A^R n_j n_k + B^R (\delta_{jk} - n_j n_k)) \omega_i^{(\text{St})}, \\ 0 &= c_\xi (A^R n_j n_k + B^R (\delta_{jk} - n_j n_k)) \omega_i^{(\text{Res})} + \int_V dV \tilde{U}_{kj} f_k(\mathbf{u}'). \end{aligned} \quad (29)$$

In the last term, it is understood that the volume integral need only be evaluated to $O(1)$, so that we may use the Stokes flow solutions for \mathbf{u}' . The first equation gives the Jeffery angular velocity $\omega_i^{(0)}$,

$$\omega_i^{(0)} = \Omega_i^\infty + \frac{C^R}{B^R} \varepsilon_{ikm} n_k n_l S_{ml}^\infty. \quad (30)$$

The dynamics of \mathbf{n} is to the lowest order given by

$$\dot{n}_i^{(0)} = \varepsilon_{ipq} \omega_p^{(0)} n_q = \varepsilon_{ipq} \Omega_p^\infty n_q + \frac{C^R}{B^R} (S_{ip}^\infty n_p - n_i n_p n_q S_{pq}^\infty). \quad (31)$$

From Table III in Appendix A, we infer that for both prolate and oblate spheroids,

$$\frac{C^R}{B^R} = \Lambda = \frac{\lambda^2 - 1}{\lambda^2 + 1}. \quad (32)$$

This shows that Eq. (31) is Jeffery's equation¹ for the orientational dynamics of a spheroid in a simple shear.

The two remaining equations in (29) may be inverted to

$$\begin{aligned} \omega_i^{(\text{St})} &= \frac{1}{c_\xi} \left(\frac{1}{A^R} n_i n_j + \frac{1}{B^R} (\delta_{ij} - n_i n_j) \right) \left[-I_{jk} \dot{\omega}_k^{(0)} - \frac{A^I - B^I}{B^I} I_{jk} \varepsilon_{klm} \omega_l^{(0)} n_m n_p \omega_p^{(0)} \right], \\ \omega_i^{(\text{Res})} &= -\frac{1}{c_\xi} \left(\frac{1}{A^R} n_i n_j + \frac{1}{B^R} (\delta_{ij} - n_i n_j) \right) \int_V dV \tilde{U}_{kj} f_k(\mathbf{u}'). \end{aligned} \quad (33)$$

Equation (28) together with Eqs. (30) and (33) yields the effective angular velocity under the effect of weak particle and fluid inertia. From equation of motion (7), we define the effective vector field

$$\dot{n}_i = \varepsilon_{ijk} \omega_j n_k \equiv \dot{n}_i^{(0)} + \text{St} \dot{n}_i^{(\text{St})} + \text{Re}_s \dot{n}_i^{(\text{Res})}. \quad (34)$$

This vector field describes the time evolution of \mathbf{n} . The first term is Jeffery vector field (31). The two new terms represent the effects of particle inertia and fluid inertia. The terms due to particle inertia are straightforward to evaluate directly, but the volume integral in Eq. (33) is very tedious to evaluate. To make the calculation feasible, we exploit the symmetries of the problem.

F. Symmetries of the effective equation of motion

Both correction terms in Eq. (34) are quadratic in the ambient flow gradient tensor A_{ij}^∞ . In other words, they are on the form

$$\dot{n}_i = C_{ijklm}^{(1)} O_{jk}^\infty O_{lm}^\infty + C_{ijklm}^{(2)} O_{jk}^\infty S_{lm}^\infty + C_{ijklm}^{(3)} S_{jk}^\infty S_{lm}^\infty, \quad (35)$$

where the tensorial coefficients $C_{ijklm}^{(i)}$ are composed of the remaining available tensor quantities: n_p and δ_{pq} (ε_{ijk} is already used in O_{ij}^∞). We make an exhaustive enumeration of all possible combinations and then use the symmetries listed in Table I to remove or combine items in the list. For example, we start by letting

$$C_{ijklm}^{(1)} = \sum_P [\eta_1^{(P)} n_{p_1} \delta_{p_2 p_3} \delta_{p_4 p_5} + \eta_2^{(P)} n_{p_1} n_{p_2} n_{p_3} \delta_{p_4 p_5} + \eta_3^{(P)} n_{p_1} n_{p_2} n_{p_3} n_{p_4} n_{p_5}], \quad (36)$$

where the sum is over all $5!$ permutations P of (i, j, k, l, m) and $\eta_i^{(P)}$ are unique coefficients for each term. We include only odd powers of n_i as any even terms would break the particle inversion symmetry. We then insert this enumeration into the first term of Eq. (35) and contract and apply



TABLE I. Symmetries constraining the form of the effective equation of motion, Eq. (34).

| | |
|--|------------------------------|
| $S_{ii}^\infty = 0$ | Incompressible flow |
| $S_{ij}^\infty = S_{ji}^\infty$ | S^∞ symmetric |
| $O_{ij}^\infty = -O_{ji}^\infty$ | O^∞ anti-symmetric |
| $n_i \dot{n}_i = 0$ | Dynamics preserves magnitude |
| $n_i \rightarrow -n_i \implies \dot{n}_i \rightarrow -\dot{n}_i$ | Particle inversion symmetry |

the first three symmetries in Table I until we reach a list of unique candidate terms. In this case, the only two unique terms turn out to be $O_{ij}O_{jk}n_k$ and $n_i n_j O_{jk}O_{ki}n_l$. Finally, we use the fact that the equation of motion may not change the magnitude of the unit vector \mathbf{n} . This constraint forces the coefficients of the two unique terms to be the same magnitude but opposite signs. Upon renaming the coefficients $\pm\alpha_1$, we get the first term in Eq. (37). The other terms are derived similarly by inserting (36) into the other terms in Eq. (35). The result contains only six independent terms

$$\begin{aligned} \dot{n}_i &= \alpha_1(\delta_{ij} - n_i n_j) O_{jk}^\infty O_{kl}^\infty n_l + \alpha_2(\delta_{ij} - n_i n_j) S_{jk}^\infty O_{kl}^\infty n_l + \alpha_3(\delta_{ij} - n_i n_j) O_{jk}^\infty S_{kl}^\infty n_l \\ &\quad + \alpha_4(\delta_{ij} - n_i n_j) S_{jk}^\infty S_{kl}^\infty n_l + \alpha_5(n_p S_{pq}^\infty n_q) O_{ij}^\infty n_j + \alpha_6(n_p S_{pq}^\infty n_q)(\delta_{ij} - n_i n_j) S_{jk}^\infty n_k. \end{aligned} \quad (37)$$

Here, the scalar functions $\alpha_1, \dots, \alpha_6$ are linear in St and Re_s and depend on the aspect ratio λ in a non-linear (and unknown) way. These coefficients are determined by evaluating the vector field in Eq. (34) for six independent directions of \mathbf{n} and solving the resulting system of linear equations for $\alpha_1, \dots, \alpha_6$.

In the particular case of a simple shear flow, we have explicitly (see Fig. 1 for the geometry)

$$O_{ij}^\infty = \frac{1}{2}(\delta_{i1}\delta_{j2} - \delta_{i2}\delta_{j1}), \quad S_{ij}^\infty = \frac{1}{2}(\delta_{i1}\delta_{j2} + \delta_{i2}\delta_{j1}). \quad (38)$$

We observe that for the simple shear, $O_{ij}^\infty O_{jk}^\infty = -S_{ij}^\infty S_{jk}^\infty$ and $S_{ij}^\infty O_{jk}^\infty = -O_{ij}^\infty S_{jk}^\infty$. Then, the form of the equation of motion simplifies to

$$\begin{aligned} \dot{n}_i &= \beta_1(n_p S_{pq}^\infty n_q)(\delta_{ij} - n_i n_j) S_{jk}^\infty n_k + \beta_2(n_p S_{pq}^\infty n_q) O_{ij}^\infty n_j \\ &\quad + \beta_3(\delta_{ij} - n_i n_j) O_{jk}^\infty S_{kl}^\infty n_l + \beta_4(\delta_{ij} - n_i n_j) S_{jk}^\infty S_{kl}^\infty n_l, \end{aligned} \quad (39)$$

with

$$\beta_1 = \alpha_6, \quad \beta_2 = \alpha_5, \quad \beta_3 = \alpha_3 - \alpha_2, \quad \beta_4 = \alpha_4 - \alpha_1. \quad (40)$$

Thus, for the case of the simple shear flow, it suffices to evaluate the effective vector field in Eq. (34), in particular the volume integral in Eq. (33), with four independent values of \mathbf{n} in order to solve for the unknown scalar coefficients β_1, \dots, β_4 .

G. Evaluation of the volume integral in Eq. (33)

The volume integral in Eq. (33) contains four distinct terms: $\partial_t u'_i$ represents unsteady fluid inertia and the three terms $u_j^\infty \partial_j u'_i + u'_j \partial_j u_i^\infty + u'_j \partial_j u'_i$ represent convective fluid inertia. We compute these four terms using explicit Stokes-flow solutions (17). While the Stokes flow has no explicit time dependence, both particle direction \mathbf{n} and angular velocity $\boldsymbol{\omega}$ do. Thus, each occurrence of n_k and ω_k has to be differentiated to compute the contribution due to unsteady fluid inertia. The differentiation and tensor contractions are implemented by a custom set of pattern matching rules in Mathematica®. The calculation is both long and error prone. We have therefore automated every possible step, including solving the Stokes-flow equations.

We demonstrate the remainder of the procedure by a small example. Consider the contribution in the $\hat{\mathbf{e}}_3$ -direction of Eq. (33) due to unsteady fluid inertia

$$-\delta_{i3} \frac{1}{c_\xi} \left(\frac{1}{A^R} n_i n_j + \frac{1}{B^R} (\delta_{ij} - n_i n_j) \right) \int_V dV \tilde{U}_{kj} \partial_t u'_k. \quad (41)$$



We first perform the time derivatives in (17) in the manner explained above. Then, we insert the components of \mathbf{n} and the explicit form of shear flow (38). At this point, we can explicitly perform the sum over all repeated indices. The result in this example consists of 858 terms, after collecting terms with same spatial dependence. The terms have a prefactor that stems from the Stokes-flow coefficients (see Appendix A) and a spatial dependence coming from r_i and the spheroidal integrals J_m^n and K_m^n (see Appendix B). For $\mathbf{n} = [1/2, \sqrt{3}/2, 0]$, a typical term looks like the following:

$$\frac{1575\alpha^2 C^R (A^S - 3C^S)(2B^R + C^R)r^2 r_2^3 K_7^0 K_9^1}{16(B^R)^2 c_\xi}.$$

We note that the only spatial dependence on the azimuthal angle around the symmetry axis of the body comes from factors of r_i . We introduce a rotated coordinate system in which $r_i = R_{ji}r'_j$, such that r'_1 is along the particle symmetry axis (see Appendix B). This change of basis enables integration of one spatial coordinate.

After this operation, 260 terms still remain which we program Mathematica to express in spheroidal coordinates (Appendix C) and integrate over the remaining two spatial coordinates. As a consistency check, we have also evaluated the volume integral numerically over all three spatial dimensions by converting to spheroidal coordinates and choosing a specific value of λ . For extreme values of λ , the numerics are difficult; nevertheless, they serve as a check for a wide range of aspect ratios (see markers in Fig. 2).

IV. RESULTS

A. Effective equation of motion

We parametrize the vector \mathbf{n} in a spherical coordinate system (θ, φ) with θ the polar angle and φ the azimuthal angle (Fig. 1),

$$n_1 = \sin \theta \cos \varphi, \quad n_2 = \sin \theta \sin \varphi, \quad n_3 = \cos \theta.$$

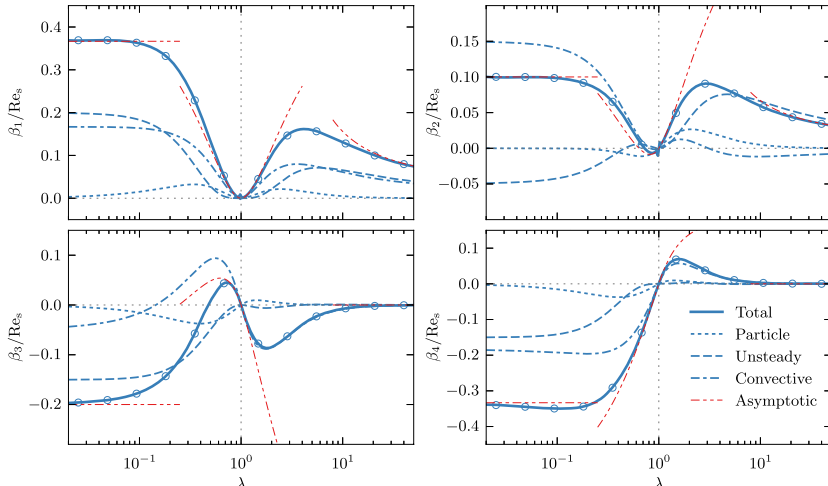


FIG. 2. Coefficients β_α in Eq. (42), $\alpha = 1, \dots, 4$ as a function of particle aspect ratio λ for $Re_s = St$. Solid line shows the sum of all contributions. The other curves show the partial contributions from particle inertia (dotted), unsteady fluid inertia (dashed), and convective inertia (dash-dotted). The thin red lines (dashed-dotted) show the asymptotic solutions from Table II (second column labeled “total”). Circular markers show result of numerical integration of Eq. (33) for certain values of λ .



In these coordinates, Eq. (39) is expressed as

$$\dot{\varphi}(\theta, \varphi) = \frac{1}{2} (\Lambda \cos 2\varphi - 1) + \frac{1}{8} \beta_1 \sin^2 \theta \sin 4\varphi - \frac{1}{4} \sin 2\varphi (\beta_2 \sin^2 \theta + \beta_3), \quad (42a)$$

$$\dot{\theta}(\theta, \varphi) = \Lambda \sin \theta \cos \theta \sin \varphi \cos \varphi + \frac{1}{4} \sin \theta \cos \theta (\beta_1 \sin^2 \theta \sin^2 2\varphi + \beta_3 \cos 2\varphi + \beta_4). \quad (42b)$$

We compute the contributions to β_α from three sources: particle inertia, unsteady fluid inertia, and convective fluid inertia. Although the result is only valid for neutrally buoyant particles ($\text{Re}_s = \text{St}$), it is interesting to consider the contributions separately,

$$\beta_\alpha = \text{St}\beta_\alpha^{(P)} + \text{Re}_s\beta_\alpha^{(U)} + \text{Re}_s\beta_\alpha^{(C)}. \quad (43)$$

The contribution from particle inertia is straightforward to compute and can be expressed in closed form as

$$\begin{aligned} \beta_1^{(P)} &= \frac{2B^I(C^R)^2}{(B^R)^3 c_\xi}, \\ \beta_2^{(P)} &= -\frac{C^R(A^I - 2B^I)}{(B^R)^2 c_\xi}, \\ \beta_3^{(P)} &= \frac{A^I C^R}{(B^R)^2 c_\xi}, \\ \beta_4^{(P)} &= -\frac{(A^I - B^I)(B^R)^2 + B^I(C^R)^2}{(B^R)^3 c_\xi}. \end{aligned} \quad (44)$$

The coefficients on the r.h.s. of these equations are tabulated for both prolate and oblate spheroids in Table III in Appendix A. The coefficients in Eq. (44) are shown as dotted lines in Fig. 2.

The expressions for the contributions from unsteady and convective fluid inertias ($\beta_\alpha^{(U)}$ and $\beta_\alpha^{(C)}$) are very lengthy and not particularly instructive. We therefore present the full result graphically as function of aspect ratio λ in Fig. 2. In addition, we give the asymptotic behaviors of all contributions to β_α in three limiting cases: thin oblate particles ($\lambda \rightarrow 0$), thin prolate particles ($\lambda \rightarrow \infty$), and nearly spherical particles. For nearly spherical particles, we define a small parameter ϵ as follows:

$$\begin{aligned} \lambda &= \frac{1}{1 - \epsilon} && \text{for prolate spheroids } (\epsilon > 0), \\ \lambda &= 1 + \epsilon && \text{for oblate spheroids } (\epsilon < 0). \end{aligned}$$

The asymptotic results for β_α in the limits $\lambda \rightarrow 0$, $\lambda \rightarrow \infty$, and $|\epsilon| \rightarrow 0$ are summarised in Table II and are shown as red lines (dashed-dotted) in Fig. 2.

B. Linear stability analysis at infinitesimal Re_s

The effective equations of motion (42) have two special polar angles θ across which no orbit may pass, regardless of the values of β_α . These angles are $\theta = 0$ (the vorticity direction) and at $\theta = \pi/2$ (the flow-shear plane). In the Jeffery dynamics ($\text{Re}_s = \text{St} = 0$), the two orbits are called “log-rolling” and “tumbling,” and they are both marginally stable, just like all other Jeffery orbits. When the β_α are non-zero but infinitesimal, the log-rolling and tumbling Jeffery orbits still exist for any finite aspect ratio, but their stabilities change.

We quantify how particle and fluid inertias lift the degeneracy of the Jeffery orbits by computing the stability exponents γ for the log-rolling (γ_{LR}) and tumbling (γ_T) orbits. The stability exponent is the exponential growth rate over one period of the orbit

$$\gamma = T_p^{-1} \lim_{\delta\theta_0 \rightarrow 0} \log |\delta\theta(T_p)/\delta\theta_0| = T_p^{-1} \int_0^{-2\pi} \frac{d\varphi}{\dot{\varphi}} \frac{\partial \dot{\theta}}{\partial \theta}, \quad (45)$$



TABLE II. Asymptotic results for β_α . Contributions from particle inertia, unsteady fluid inertia, and convective fluid inertia are shown separately. Factors of Re_s and St are omitted.

| Thin oblate particles ($\lambda \rightarrow 0$) | | | | |
|---|--|----------------------------------|--|--|
| | Total | Unsteady | Convective | Particle |
| β_1 | $\frac{11}{30}$ | $\frac{1}{5}$ | $\frac{1}{6}$ | 0 |
| β_2 | $\frac{1}{10}$ | $-\frac{1}{20}$ | $\frac{3}{20}$ | 0 |
| β_3 | $-\frac{1}{5}$ | $-\frac{3}{20}$ | $-\frac{1}{20}$ | 0 |
| β_4 | $-\frac{1}{3}$ | $-\frac{3}{20}$ | $-\frac{11}{60}$ | 0 |
| Nearly spherical particles ($ \epsilon \ll 1$) | | | | |
| | Total | Unsteady | Convective | Particle |
| β_1 | $\frac{137\epsilon^2}{294}$ | 0 | $\frac{163\epsilon^2}{490}$ | $\frac{2\epsilon^2}{15}$ |
| β_2 | $\frac{2\epsilon}{21} + \frac{81\epsilon^2}{245}$ | $\frac{62\epsilon^2}{525}$ | $\frac{\epsilon}{35} + \frac{37\epsilon^2}{294}$ | $\frac{\epsilon}{15} + \frac{13\epsilon^2}{150}$ |
| β_3 | $-\frac{2\epsilon}{7} - \frac{229\epsilon^2}{735}$ | $-\frac{58\epsilon^2}{525}$ | $-\frac{37\epsilon}{105} - \frac{227\epsilon^2}{1470}$ | $\frac{\epsilon}{15} - \frac{7\epsilon^2}{150}$ |
| β_4 | $\frac{8\epsilon}{21} - \frac{103\epsilon^2}{735}$ | 0 | $\frac{11\epsilon}{35} - \frac{229\epsilon^2}{2450}$ | $\frac{\epsilon}{15} - \frac{7\epsilon^2}{150}$ |
| Thin prolate particles ($\lambda \rightarrow \infty$) | | | | |
| | Total | Unsteady | Convective | Particle |
| β_1 | $\frac{7}{30 \log 2\lambda - 45}$ | $\frac{1}{8 \log 2\lambda - 12}$ | $\frac{13}{120 \log 2\lambda - 180}$ | 0 |
| β_2 | $\frac{1}{10 \log 2\lambda - 15}$ | $\frac{1}{8 \log 2\lambda - 12}$ | $\frac{1}{20 \log 2\lambda - 60}$ | 0 |
| β_3 | 0 | 0 | 0 | 0 |
| β_4 | 0 | 0 | 0 | 0 |

where $T_p = 4\pi/\sqrt{1-\Lambda^2}$ is the Jeffery period. As $\text{Re}_s \rightarrow 0$, we find

$$\gamma_T = -\frac{\beta_4}{4} + \frac{1-\sqrt{1-\Lambda^2}}{4\Lambda^2}(\Lambda\beta_2 - \beta_1), \quad \gamma_{LR} = \frac{\beta_4}{4}. \quad (46)$$

For $\text{Re}_s = \text{St}$, these two exponents are shown as function of particle aspect ratio in Fig. 3. Also shown are their limiting behaviours in the thin oblate limit ($\lambda \rightarrow 0$),

$$\begin{aligned} \frac{\gamma_T}{\text{Re}_s} &\sim -\frac{1}{30} + \left(\frac{7}{30} - \frac{34}{45\pi} + \frac{7\pi}{80} \right) \lambda \\ &+ \frac{(-53\,248 + 19\,200\pi - 1728\pi^2 - 1728\pi^3 + 567\pi^4)\lambda^2}{8640\pi^2}, \\ \frac{\gamma_{LR}}{\text{Re}_s} &\sim -\frac{1}{12} + \left(\frac{\pi}{80} - \frac{16}{45\pi} \right) \lambda + \left(\frac{5}{12} - \frac{256}{135\pi^2} + \frac{3\pi^2}{320} \right) \lambda^2, \end{aligned} \quad (47)$$

in the nearly spherical limit ($\epsilon \rightarrow 0$),

$$\frac{\gamma_T}{\text{Re}_s} \sim -\frac{2\epsilon}{21} - \frac{59\epsilon^2}{1680}, \quad \frac{\gamma_{LR}}{\text{Re}_s} \sim \frac{2\epsilon}{21} - \frac{103\epsilon^2}{2940}, \quad (48)$$

and in the thin prolate limit ($\lambda \rightarrow \infty$),

$$\frac{\gamma_T}{\text{Re}_s} \sim \frac{1}{45 - 30 \log 2\lambda}, \quad \frac{\gamma_{LR}}{\text{Re}_s} \sim \frac{1}{15\lambda^2}. \quad (49)$$

Fig. 3 shows that prolate spheroids of all aspect ratios are unstable at the log-rolling position and stable at the tumbling orbit. For nearly spherical particles, there is a bifurcation: log-rolling and tumbling switch stabilities. For oblate spheroids, the log-rolling position is stable for any aspect ratio.



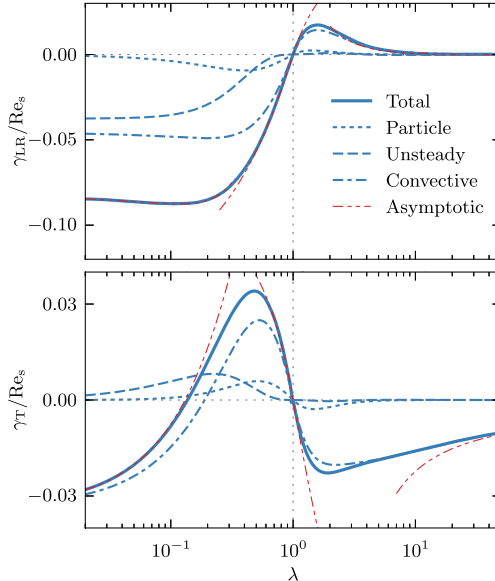


FIG. 3. Stability exponents of log-rolling (top panel) and tumbling (bottom panel) as a function of particle aspect ratio λ for infinitesimal $Re_s = St$. Solid line shows the sum of all contributions. The other curves show the partial contributions from particle inertia (dotted), unsteady fluid inertia (dashed), and convective inertia (dashed-dotted). Thin red lines (dashed-dotted) show asymptotic results which are given by Eqs. (47)–(49).

For oblate particles, there is a second bifurcation at $\lambda_c \approx 1/7.3$ where the tumbling orbit becomes stable. Clearly, this behavior is caused by the convective inertia of the fluid (see the dashed-dotted line in Fig. 3). For sufficiently oblate particles, both log-rolling and tumbling orbits are stable and the long-time dynamics depend on the initial orientation of the particle. Between the two now stable orbits, a new unstable limit cycle is born, separating the two basins of attraction.

Fig. 4 shows how the shape of this limit cycle depends upon the particle aspect ratio. Close to the bifurcation, the limit cycle lies in the neighbourhood of the tumbling orbit. But as $\lambda \rightarrow 0$, the

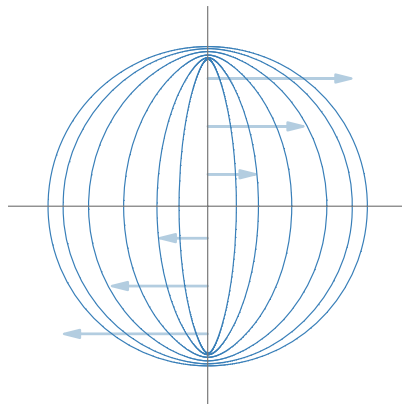


FIG. 4. The shape of the limit cycle for different aspect ratios $\lambda < \lambda_c = 1/7.3$. Trajectories are projected onto the unit disk by $[X, Y] = \sqrt{1/(1-n_3)}[n_1, n_2]$ (equal area projection). The tumbling orbit is the unit circle and log-rolling is the center point. The flow-shear directions are indicated in the background. Parameters are, starting from the outermost (tumbling) orbit: $\lambda = 1/7.2, 1/7.4, 1/8, 1/10, 1/15$, and $1/25$. Data created by numerically integrating Eq. (42) with $Re_s = 10^{-2}$.



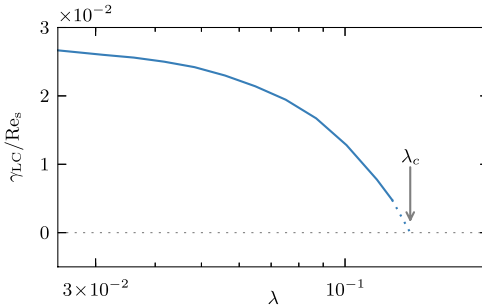


FIG. 5. Stability exponent γ_{LC} of the unstable limit cycle as a function of aspect ratio. Computed by numerically integrating Eq. (42) for $Re_s = 0.05$ (solid line). The limit cycle bifurcates at λ_c , indicated by an arrow and the dotted continuation of the numerical result.

limit cycle approaches the log-rolling orbit. We have computed the stability exponent of the limit cycle at infinitesimal Re_s by numerically integrating Eqs. (42). The result is shown in Fig. 5. We see that $\gamma_{LC} > 0$ and its magnitude is of the same order as that of γ_T .

V. DISCUSSION

A. Effective equation of motion

Equation (42) is an effective equation of motion for the orientational dynamics of a neutrally buoyant spheroid in a simple shear flow. How the dynamics depends upon the particle aspect ratio is determined by four coefficients β_1, \dots, β_4 . Fig. 2 shows the four functions $\beta_\alpha(\lambda)$. Limiting behaviours of the β_α are tabulated in Table II. We see that the β -coefficients tend to zero as $\lambda \rightarrow \infty$, but they approach constants as $\lambda \rightarrow 0$. In both limits, the contribution from particle inertia must tend to zero because the volume of the particle does. The effects of fluid inertia vanish as $\lambda \rightarrow \infty$ because the particle effectively disappears in the slender-body limit and the perturbation caused by the particle decreases as $\sim 1/\log \lambda$ as the asymptotic form in Table II shows. We remark that the leading-order term in this asymptotic form makes a substantial correction to the slender-body theory for aspect ratios of order 30.

An oblate particle, on the other hand, always presents no-slip boundaries to the fluid, with an area of the order of $\sim a^2$ as $\lambda \rightarrow 0$. Therefore, the contribution of fluid inertia approaches a constant. We note that the asymptotic forms of the coefficients β_α listed in Table II yield accurate values for $\lambda < 1/30$ and $\lambda > 30$, as shown in Fig. 2.

We see in Fig. 2 that the particle-inertia contribution to the coefficients β_α is always much smaller than the fluid-inertia contributions. In general, both unsteady and convective fluid inertias contribute, and it would be qualitatively wrong to neglect one of these terms. This is due to the fact that the time scale of the particle motion is the same as the time scale of the flow, and it raises the question under which circumstances both effects may matter for the tumbling of small particles in unsteady flows and, in particular, in turbulence.

B. Linear stability analysis at infinitesimal Re_s

The stability exponents of tumbling and log-rolling orbits are shown in Fig. 3. We find that the log-rolling orbit is unstable for prolate spheroids of any aspect ratio, tumbling is stable for prolate spheroids, and no other orbit exists at infinitesimal Re_s . For moderately oblate particles with aspect ratios $\lambda > \lambda_c \approx 1/7.3$, the stabilities are reversed: log-rolling is stable, tumbling is unstable, and no other periodic orbits exist for infinitesimal Re_s . At $\lambda = \lambda_c$, there is a bifurcation where an unstable periodic orbit is born close to the tumbling orbit, which in turn becomes stable. As λ becomes even smaller, the unstable orbit moves closer to the log-rolling orbit (Fig. 4). We remark that the



asymptotic forms (47) and (49) of the stability exponents yield very accurate approximations for the log-rolling exponent, except for aspect ratios close to unity. For the tumbling exponent, the asymptotes do not work equally well.

Our results are in agreement with results of recent DNS studies^{3–6,18} determining the orientational dynamics of a neutrally buoyant spheroid in a simple shear flow. These studies are conducted for a number of different aspect ratios with shear Reynolds numbers ranging from moderate to large. At the smallest values of Re_s accessible in the DNS, no stable log-rolling is found for prolate spheroids of any aspect ratio. For oblate particles with aspect ratio $\lambda = 1/5$, DNSs show stable log-rolling and unstable tumbling at the smallest Re_s that were simulated,⁶ also in agreement with our results. There are no simulations for particles for $\lambda < \lambda_c$ at small Re_s .

Saffman⁷ predicted that log-rolling is stable for nearly spherical prolate particles, at variance with the behaviour described above. We do not know why the original calculation fails to give the correct stability of log-rolling. Since no details of the calculation are given, it is difficult to figure out the precise origin of this discrepancy. Subramanian and Koch¹⁷ also computed the stability of the log-rolling orbit for nearly spherical particles and came to the same conclusion as Saffman, different from ours. We have compared the small- ϵ limit of our calculation to the results of Ref. 17 and found that the particle-inertia correction to the equation of motion agrees, Eqs. (3.15) and (3.16) in Ref. 17. But the fluid-inertia correction does not satisfy the symmetries of the problem. We believe that this explains the discrepancy.

We have independently calculated the stability of log-rolling for nearly spherical particles by expanding the particle-angular velocity jointly in ϵ and Re_s , using spherical harmonics as a basis set.²² The results of this calculation agree to order ϵ with the results presented above. Further, we have checked that the particle-inertia correction in Eq. (42) is consistent with the results obtained in Ref. 9. We also compared the slender-body limit of our results to the prediction of Subramanian and Koch for the dynamics of slender fibres² and found that the fluid-inertia corrections agree (up to a factor of 8π).

These observations indicate that the results presented in this paper are correct, explain the results of DNS, and resolve the puzzle concerning the stability of log-rolling of spheroids in a simple shear at small Re_s .

C. A new benchmark for DNS at small Re_s

Recently, a number of groups have developed DNS codes based on the lattice Boltzmann method to simulate the dynamics of particles in flows.^{3–6} Much effort is spent on validating the model and studying for instance the effects changing grid size, time step, size of the simulation box, and so forth. The benchmark adopted is often the question whether Jeffery orbits are seen for a neutrally buoyant spheroid in a simple shear at small Reynolds numbers. But the limit $Re_s = 0$ can never be strictly reached in the simulations. DNSs at small values of Re_s (specifically: in the linear regime), by contrast, allow precise comparisons with the results obtained in this paper. One could for instance compare trajectories, stability exponents, and period times. We thus expect that our results can serve as benchmarks for present and future DNS codes.

VI. CONCLUSIONS

In this paper, we have derived an effective equation of motion for the orientational dynamics of a neutrally buoyant spheroid suspended in a simple shear flow. The equation is valid for arbitrary aspect ratios and to linear order in Re_s , at small but finite shear Reynolds numbers. The effective equation of motion allows us to determine how the degeneracy of the Jeffery orbits is lifted by weak inertial effects. We have determined the bifurcations that occur at infinitesimal Re_s as the particle aspect ratio changes. For prolate spheroids, log-rolling is unstable and for oblate spheroids, it is stable. Tumbling in the shear plane is stable for prolate particles and unstable for nearly spherical oblate particles. For thin disks with aspect ratios $\lambda < 1/7.3$, both log-rolling and tumbling are stable. An unstable limit cycle separates the basins of attraction of the periodic orbits.



Our results imply that the tumbling and log-rolling orbits survive a finite perturbation whose magnitude depends on the aspect ratio λ . It would be of interest to derive a bifurcation diagram in the λ - Re_s -plane for small Re_s . We plan to determine how the small- Re_s region of this diagram connects to the intricate bifurcation patterns that were found by Rosén, Lundell and Aidun⁵ at larger shear Reynolds numbers. We expect that the results summarised here can guide numerical computations with the lattice Boltzmann method that become difficult at small Re_s and large aspect ratios.

ACKNOWLEDGMENTS

This work was supported by grants from Vetenskapsrådet and the Göran Gustafsson Foundation for Research in Natural Sciences and Medicine. Support from the MPNS COST Action MP1305 “Flowing matter” is gratefully acknowledged.

APPENDIX A: SOLUTIONS TO STOKES' EQUATION

In this appendix, we solve the steady Stokes' equation for an arbitrarily aligned spheroid in a general linear flow $\mathbf{u}^\infty = \mathbf{A}^\infty \mathbf{r}$. The calculation is a special case of the calculation by Jeffery.¹ However, instead of the ellipsoidal harmonics that Jeffery used, we employ a finite multipole expansion, following Chwang and Wu.²¹ The purpose of this appendix is to derive an explicit closed form expression for the Stokes flow field, suitable for evaluation in the reciprocal theorem. For a more general description of the method, we refer to the book by Kim and Karrila.¹⁰

1. Formulation of the problem

Stokes' equation reads:

$$\partial_j \partial_j u_i = \partial_i p, \quad \partial_i u_i = 0, \quad (\text{A1})$$

with no-slip boundary conditions on the surface S of the particle

$$u_i = \varepsilon_{ijk} \omega_j r_k \quad \text{for } \mathbf{r} \in S. \quad (\text{A2})$$

Here, ω_j is the angular velocity of the particle. Furthermore, it is assumed that the flow remains unperturbed at infinitely far away from the particle

$$u_i = u_i^\infty \quad \text{as } |\mathbf{r}| \rightarrow \infty. \quad (\text{A3})$$

We solve for the disturbance flow $u'_i = u_i - u_i^\infty$ that satisfies Stokes' equation (A1) with boundary conditions,

$$u'_i = \varepsilon_{ijk} \omega_j r_k - u_i^\infty \quad \text{for } \mathbf{r} \in S, \quad u'_i = 0 \quad \text{as } |\mathbf{r}| \rightarrow \infty. \quad (\text{A4})$$

We decompose the linear background flow u_i^∞ into its symmetric and antisymmetric parts, defining the vector Ω_i^∞ and strain S_{ij}^∞ by

$$u_i^\infty = A_{ij}^\infty r_j = \varepsilon_{ijk} \Omega_j^\infty r_k + S_{ij}^\infty r_j. \quad (\text{A5})$$

Finally, in terms of the “slip angular velocity” $\Omega_i = \Omega_i^\infty - \omega_i$, the problem to be solved reads

$$\begin{aligned} \partial_j \partial_j u'_i &= \partial_i p', \quad \partial_i u'_i = 0, \\ u'_i &= -\varepsilon_{ijk} \Omega_j r_k - S_{ij}^\infty r_j \quad \text{for } \mathbf{r} \in S, \\ u'_i &= 0 \quad \text{as } |\mathbf{r}| \rightarrow \infty. \end{aligned} \quad (\text{A6})$$

2. Multipoles

We solve Eq. (A6) by a finite multipole expansion.^{10,21} The multipoles are the Green's function for the Stokes' equation and its derivatives. In this appendix, we use the shorthand notation



$\mathcal{G}_{ij,k} \equiv \partial_k \mathcal{G}_{ij}$. The multipoles needed to solve for the fluid velocity field around particles in a linear flow are

$$\begin{aligned}\mathcal{G}_{ij} &= \frac{\delta_{ij}}{r} + \frac{x_i x_j}{r^3}, \\ \mathcal{G}_{ij,k} &= -\frac{\delta_{ij} x_k}{r^3} + \frac{\delta_{ik} x_j}{r^3} + \frac{\delta_{jk} x_i}{r^3} - \frac{3x_i x_j x_k}{r^5}, \\ \mathcal{G}_{ij,ll} &= \nabla^2 \mathcal{G}_{ij} = \frac{2\delta_{ij}}{r^3} - \frac{6x_i x_j}{r^5}, \\ \mathcal{G}_{ij,llk} &= \nabla^2 \mathcal{G}_{ij,k} = -\frac{6}{r^5} (\delta_{ij} x_k + \delta_{jk} x_i + \delta_{ik} x_j) + \frac{30x_i x_j x_k}{r^7}.\end{aligned}\quad (\text{A7})$$

The following two higher-order multipoles are required in the reciprocal theorem. We include them for reference,

$$\begin{aligned}\mathcal{G}_{ij,km} &= \frac{\delta_{im} \delta_{jk}}{r^3} + \frac{\delta_{ik} \delta_{jm}}{r^3} - \frac{\delta_{ij} \delta_{km}}{r^3} - \frac{3x_i x_j \delta_{km}}{r^5} \\ &\quad - \frac{3x_j x_k \delta_{im}}{r^5} - \frac{3x_j x_m \delta_{ik}}{r^5} + \frac{3x_k x_m \delta_{ij}}{r^5} \\ &\quad - \frac{3x_i x_k \delta_{jm}}{r^5} - \frac{3x_i x_m \delta_{jk}}{r^5} + \frac{15x_i x_j x_k x_m}{r^7}, \\ \mathcal{G}_{ij,llkm} &= \frac{30x_i x_m \delta_{jk}}{r^7} + \frac{30x_i x_j \delta_{km}}{r^7} + \frac{30x_i x_k \delta_{jm}}{r^7} \\ &\quad + \frac{30x_j x_k \delta_{im}}{r^7} + \frac{30x_j x_m \delta_{ik}}{r^7} + \frac{30x_k x_m \delta_{ij}}{r^7} \\ &\quad - \frac{6\delta_{im} \delta_{jk}}{r^5} - \frac{6\delta_{ik} \delta_{jm}}{r^5} - \frac{6\delta_{ij} \delta_{km}}{r^5} \\ &\quad - \frac{210x_i x_j x_k x_m}{r^9}.\end{aligned}\quad (\text{A8})$$

Note that we use the “Oseen tensor” notation. The Green’s function for the Stokes’ equation is in fact $G_{ij} = \mathcal{G}_{ij}/8\pi$. It is convenient to split the dipole contribution $\mathcal{G}_{ij,k}$ into its antisymmetric (“rotlet”) and symmetric (“stresslet”) parts. They are

$$\begin{aligned}\mathcal{G}_{ij,k}^R &= \frac{1}{2} (\mathcal{G}_{ij,k} - \mathcal{G}_{ik,j}) = \frac{1}{r^3} (\delta_{ik} x_j - \delta_{ij} x_k), \\ \mathcal{G}_{ij,k}^S &= \frac{1}{2} (\mathcal{G}_{ij,k} + \mathcal{G}_{ik,j}) = \frac{\delta_{kj} x_i}{r^3} - \frac{3x_i x_j x_k}{r^5}.\end{aligned}\quad (\text{A9})$$

3. Spheroidal multipoles

Whereas the flow around a spherical particle may be represented by multipoles anchored at a single point, representing the flow around a spheroidal particle requires a weighted line distribution of multipoles.^{10,21} We therefore define the “spheroidal multipoles” as the following distributions, note especially the different weights for higher-order multipoles:

$$\begin{aligned}Q_{ij,k}^R(\mathbf{r}, \mathbf{n}) &= \int_{-c}^c d\xi (c^2 - \xi^2) \mathcal{G}_{ij,k}^R(\mathbf{r} - \xi \mathbf{n}), \\ Q_{ij,k}^S(\mathbf{r}, \mathbf{n}) &= \int_{-c}^c d\xi (c^2 - \xi^2) \mathcal{G}_{ij,k}^S(\mathbf{r} - \xi \mathbf{n}), \\ Q_{ij,ll}^Q(\mathbf{r}, \mathbf{n}) &= \int_{-c}^c d\xi (c^2 - \xi^2)^2 \mathcal{G}_{ij,ll}(\mathbf{r} - \xi \mathbf{n}).\end{aligned}\quad (\text{A10})$$

The constant c is related to the spheroidal geometry. Prolate and oblate coordinates are obtained by rotating an ellipse around its major or minor axis. We call the distance between the foci of the underlying ellipse d , then $c = d/2$ for prolate coordinates, and $c = id/2$ for oblate coordinates (see definition of coordinate systems in Appendix C).



In order to write down explicit tensor expressions for the spheroidal multipoles, we introduce the integrals I_m^n , J_m^n , and K_m^n by

$$\begin{aligned} I_m^n &= \int_{-c}^c d\xi \frac{\xi^n}{|\mathbf{r} - \xi \mathbf{n}|^m}, \\ J_m^n &= c^2 I_m^n - I_m^{n+2}, \\ K_m^n &= c^2 J_m^n - J_m^{n+2} = c^4 I_m^n - 2c^2 I_m^{n+2} + I_m^{n+4}. \end{aligned} \quad (\text{A11})$$

The spatial variation of the functions I_m^n depends upon $|\mathbf{r}|^2$ and $\mathbf{r} \cdot \mathbf{n}$ only. Further properties and evaluation of the integrals are discussed in Appendix B. With J_m^n and K_m^n , we express the spheroidal multipoles explicitly, for example, the spheroidal rotlet,

$$\begin{aligned} Q_{ij,k}^R(\mathbf{r}, \mathbf{n}) &= \int_{-c}^c d\xi \frac{c^2 - \xi^2}{|\mathbf{r} - \xi \mathbf{n}|^3} [\delta_{ik}(r_j - \xi n_j) - \delta_{ij}(r_k - \xi n_k)] \\ &= (\delta_{ik}r_j - \delta_{ij}r_k)J_3^0 + (\delta_{ij}n_k - \delta_{ik}n_j)J_3^1. \end{aligned}$$

The integrals I_m^n play the same part in spheroidal geometry as do $1/r^m$ in spherical geometry. The spheroidal stresslet and quadrupole are given by

$$\begin{aligned} Q_{ij,k}^S(\mathbf{r}, \mathbf{n}) &= \delta_{kj}x_i J_3^0 - \delta_{kj}n_i J_3^1 - 3r_i r_j r_k J_5^0 - \delta_{jk}n_i J_3^1 \\ &\quad + 3(n_i r_j r_k + n_j r_i r_k + n_k r_i r_j) J_5^1 \\ &\quad - 3(r_i n_j n_k + r_j n_i n_k + r_k n_i n_j) J_5^2 \\ &\quad + 3n_i n_j n_k J_5^3, \end{aligned} \quad (\text{A12})$$

$$\begin{aligned} Q_{ij,llk}^Q(\mathbf{r}, \mathbf{n}) &= -6(\delta_{jk}r_i + \delta_{ik}r_j + \delta_{ij}r_k)K_5^0 + 30r_i r_j r_k K_7^0 \\ &\quad + 6(\delta_{jk}n_i + \delta_{ik}n_j + \delta_{ij}n_k)K_5^1 \\ &\quad - 30(r_i r_j n_k + r_i r_k n_j + r_j r_k n_i)K_7^1 \\ &\quad + 30(n_i n_j r_k + n_i n_k r_j + n_j n_k r_i)K_7^2 \\ &\quad - 30n_i n_j n_k K_7^3. \end{aligned} \quad (\text{A13})$$

4. Solution by a finite multipole expansion

The spheroidal multipoles are functions that satisfy Stokes' equation, and a suitable linear combination of them also satisfies the no-slip boundary condition on the surface of a spheroid with symmetry axis \mathbf{n} . The remaining problem is to determine the coefficients for this linear combination.

Following Kim and Karrila,¹⁰ we use the following ansatz for the disturbance flow field:

$$\begin{aligned} u'_i &= Q_{ij,k}^R \varepsilon_{jkl} [(A^R n_l n_m + B^R (\delta_{lm} - n_l n_m)) \Omega_m + C^R \varepsilon_{lmn} n_m S_{no} n_o] \\ &\quad + (Q_{ij,k}^S + \alpha Q_{ij,llk}^Q) \\ &\quad \times [(A^S n_{jklm}^A + B^S n_{jklm}^B + C^S n_{jklm}^C) S_{lm}^\infty - C^R (\varepsilon_{jlm} n_k n_m + \varepsilon_{klm} n_j n_m) \Omega_l], \end{aligned} \quad (\text{A14})$$

where

$$\begin{aligned} n_{jklm}^A &= (n_j n_k - \frac{1}{3} \delta_{jk})(n_l n_m - \frac{1}{3} \delta_{lm}), \\ n_{jklm}^B &= n_j \delta_{kl} n_m + n_k \delta_{jl} n_m + n_j \delta_{km} n_l + n_k \delta_{jm} n_l - 4n_j n_k n_l n_m, \\ n_{jklm}^C &= -\delta_{jk} \delta_{lm} + \delta_{jl} \delta_{km} + \delta_{kl} \delta_{jm} \\ &\quad + \delta_{jk} n_l n_m + \delta_{lm} n_j n_k - n_j \delta_{kl} n_m - n_k \delta_{jl} n_m \\ &\quad - n_j \delta_{km} n_l - n_k \delta_{jm} n_l + n_j n_k n_l n_m. \end{aligned} \quad (\text{A15})$$

Given the ambient strain S_{ij}^∞ and angular slip velocity $\Omega_i = \Omega_i^f - \omega_i^p$, we must determine seven unknown scalars, which may depend upon the particle shape: A^R , B^R , C^R , A^S , B^S , C^S , and α . When the coefficients are known, Eq. (A14) is the sought Stokes solution.



In order to match linear boundary condition Eq. (A4), we need the combinations of J_m^n and K_m^n in the ansatz to be constant on the particle surface, much like the scalar function $1/r^m$ is in spherical geometry.

Upon examination, the functions J_3^0 and K_5^0 are constant on the spheroidal surface. Further, the functions J_3^1 and K_5^1 can be written as $J_3^1 = n_j r_j J_3'^1$ and $K_5^1 = n_j r_j K_5'^1$, where $J_3'^1$ and $K_5'^1$ are constant on the spheroidal surface. The remaining spheroidal functions J_5^n and K_7^n which appear in ansatz (A14) are more complicated. However, it turns out that they appear only in the combinations $J_5^n - 10\alpha K_7^n$. We therefore choose

$$\alpha = \frac{J_5^0}{10K_7^0} \Big|_{\text{surface}} = \frac{1}{8(\lambda^2 - 1)}. \quad (\text{A16})$$

With this choice of α , it holds that, on the surface of the spheroid,

$$\begin{aligned} J_5^0 - 10\alpha K_7^0 &= 0, \\ J_5^1 - 10\alpha K_7^1 &= 0, \\ J_5^2 - 10\alpha K_7^2 &= \frac{1}{3} J_3'^1 - 2\alpha K_5'^1, \\ J_5^3 - 10\alpha K_7^3 &= \frac{5}{3} J_3^1 - \frac{42}{3} \alpha K_5^1, \end{aligned} \quad (\text{A17})$$

both for prolate and oblate spheroids.

In order to extract the six independent equations for the six remaining coefficients, we exploit that the boundary condition must be satisfied for any choice of n_j , Ω_j , and S_{jk}^∞ . First, with $S_{jk}^\infty = 0$, we contract Eq. (A4) with n_i , $\varepsilon_{ijk} n_j \Omega_k$, and $\varepsilon_{ipq} n_q \varepsilon_{pjk} n_j \Omega_k$. Second, with $\Omega_j = 0$, we contract Eq. (A4) with n_i , $S_{ij}^\infty n_j$, and finally $\varepsilon_{ijk} n_j S_{kl}^\infty n_l$. These six equations together have only one solution. We tabulate the resulting expressions for both oblate and prolate spheroids in Table III.

TABLE III. Coefficients for Stokes-flow solutions and moments of inertia for prolate and oblate spheroids. These coefficients are collected in the book by Kim and Karrila.¹⁰ We tabulate them here for convenience as our conventions differ slightly from those adopted in Ref. 10. We remark that some of the coefficients tabulated here assume imaginary values. All physical quantities come out to be real-valued.

| Expressions common to both prolate and oblate spheroids | | |
|---|---|---|
| $\alpha = \frac{1}{8(\lambda^2 - 1)}$ | $A^R = \frac{\sqrt{\lambda^2 - 1}}{4(C - \lambda^3 + \lambda)}$ | $B^R = \frac{\sqrt{\lambda^2 - 1}(\lambda^2 + 1)}{4(-2C\lambda^2 + C + \lambda^3 - \lambda)}$ |
| $C^R = \frac{(\lambda^2 - 1)^{3/2}}{4(-2C\lambda^2 + C + \lambda^3 - \lambda)}$ | $A^S = \frac{(\lambda^2 - 1)^{3/2}}{4(2C\lambda^2 + C - 3\lambda^3 + 3\lambda)}$ | $C^S = \frac{(\lambda^2 - 1)^{3/2}}{2(3C + 2\lambda^3 - 7\lambda^2 + 5\lambda)}$ |
| | $B^S = -\frac{(\lambda^2 - 1)^{3/2}(C\lambda + \lambda^4 - 3\lambda^2 + 2)}{8(-2C\lambda^2 + C + \lambda^3 - \lambda)(-3C\lambda + \lambda^4 + \lambda^2 - 2)}$ | |
| Expressions particular to prolate and oblate spheroids | | |
| Oblate ($\lambda < 1$) | | |
| C | $-\sqrt{1 - \lambda^2} \cot^{-1} \left(\frac{\lambda}{\sqrt{1 - \lambda^2}} \right)$ | $\sqrt{\lambda^2 - 1} \coth^{-1} \left(\frac{\lambda}{\sqrt{\lambda^2 - 1}} \right)$ |
| d | $2\sqrt{1 - \lambda^2}$ | $\frac{2\sqrt{\lambda^2 - 1}}{\lambda}$ |
| c | $\frac{id}{2}$ | $\frac{d}{2}$ |
| c_ξ | $\frac{64}{3} i \pi (1 - \lambda^2)^{3/2}$ | $-\frac{64\pi(\lambda^2 - 1)^{3/2}}{3\lambda^3}$ |
| A^I | $\frac{8\pi\lambda}{15}$ | $\frac{8\pi}{15\lambda^4}$ |
| B^I | $\frac{4\pi}{15} \lambda (\lambda^2 + 1)$ | $\frac{4\pi(\lambda^2 + 1)}{15\lambda^4}$ |



Computing the torque on a body due to this flow is straightforward, because by construction²¹ the torque on a body due to the rotlet flow $u_i = G_{ij,k}^R \varepsilon_{jkl} A_l$ is $T_l^R = -16\pi A_l$, where A_l is the rotlet strength. The minus sign is due to the fact that the torque is exerted on body by the flow. To compute the torque from spheroidal rotlet (A10), we linearly superpose the contributions from all the contained rotlets. The torque from the flow $u_i = Q_{ij,k}^R \varepsilon_{jkl} B_l$ is therefore

$$T_l = -16\pi \int_{-c}^c d\xi (c^2 - \xi^2) B_l = -\frac{64\pi c^3}{3} B_l \equiv c_\xi B_l. \quad (\text{A18})$$

The factor c_ξ depends only on the aspect ratio of the particle (see Table III).

APPENDIX B: SPHEROIDAL INTEGRALS

In order to solve Stokes' equation and evaluating the volume integrals in the reciprocal theorem, we need to evaluate integrals on the form

$$I_m^n(|\mathbf{r}|^2, \mathbf{r} \cdot \mathbf{n}) = \int_{-c}^c d\xi \frac{\xi^n}{|\mathbf{r} - \xi \mathbf{n}|^m}. \quad (\text{B1})$$

First, when matching boundary conditions, we must evaluate the integrals with \mathbf{r} on the surface of the spheroidal particle. Second, when evaluating the reciprocal theorem, we need to integrate products of two or three I_m^n multiplied with the components of the spatial coordinate \mathbf{r} over the entire fluid volume outside the particle. Therefore, we express the functions I_m^n in a spheroidal coordinate system with symmetry axis \hat{x}' along \mathbf{n} . This is accomplished by a rotational change of variables $\mathbf{r}' = \mathbf{R}\mathbf{r}$, $\hat{x}' = \mathbf{R}\mathbf{n}$, where the latter equality defines a rotation \mathbf{R} . The absolute value (distance) between \mathbf{r} and $\xi \mathbf{n}$ is preserved by a rotation and the integral is transformed into

$$I_m^n = \int_{-c}^c d\xi \frac{\xi^n}{[(x' - \xi)^2 + (y')^2 + (z')^2]^{\frac{m}{2}}}. \quad (\text{B2})$$

This form is equivalent to the integrals $B_{m,n}$ in Chwang and Wu.²¹ Geometrically, Eq. (B1) represents a line source along the direction \mathbf{n} . The rotation \mathbf{R} places the line source along the x' -axis in an auxiliary coordinate system. The result is a function of $|\mathbf{r}|^2$ and $x' = \hat{x}' \cdot \mathbf{r}' = \mathbf{n} \cdot \mathbf{r}$.

Explicit expressions for I_m^n may be found by direct integration or by a recursion formula.²¹ Since we require only a finite number of integrals, we simply perform the direct integration once and for all and save the result in a table.

Finally, when evaluating the term corresponding to unsteady fluid inertia in the volume integral of the reciprocal theorem, we need to compute the derivatives of I_m^n with respect to the moving vector \mathbf{n} . By differentiating Eq. (B1), we derive the following formula:

$$\frac{\partial}{\partial n_i} I_m^n = m r_i I_{m+2}^{n+1} - m n_i I_{m+2}^{n+2}. \quad (\text{B3})$$

APPENDIX C: SPHEROIDAL COORDINATES

Both oblate and prolate spheroidal coordinates are extensions of a two-dimensional elliptic coordinate system (ξ_1, ξ_2) . The ξ_1 -coordinate represents concentric ellipses, while ξ_2 represents the corresponding hyperbolas. Their intersections give unique coordinates in the x - y -plane. An azimuthal angle of revolution ϕ denotes the extension into three dimensions.

1. Oblate spheroidal coordinates

Start with the x - y -plane and place an ellipse of focal distance d with its minor axis along the x -axis. Now, revolve the ellipse by 2π around the x -axis to produce an oblate spheroid. Then, ξ_1 represents concentric oblate spheroidal surfaces, ξ_2 represents the corresponding hyperbolic



surfaces, and we call ϕ the angle of revolution. The coordinate equations are

$$\begin{aligned} x &= \frac{d}{2}\xi_1\xi_2, \\ y &= \frac{d}{2}\sqrt{\xi_1^2 + 1}\sqrt{1 - \xi_2^2} \cos \phi, \\ z &= \frac{d}{2}\sqrt{\xi_1^2 + 1}\sqrt{1 - \xi_2^2} \sin \phi. \end{aligned} \quad (\text{C1})$$

The coordinate ranges are $0 \leq \xi_1 < \infty$, $-1 \leq \xi_2 \leq 1$, and $0 \leq \phi \leq 2\pi$, and the volume element $dV = \frac{1}{8}d^3(\xi_1^2 + \xi_2^2)d\xi_1d\xi_2d\phi$. In this paper, we treat oblate spheroids with dimensionless major axis length unity and minor axis length λ . These lengths determine the focal distance d as

$$d = 2\sqrt{1 - \lambda^2}, \quad (\text{C2})$$

and the particle surface is parameterised by

$$\xi_1^{(p)} = \frac{\lambda}{\sqrt{1 - \lambda^2}}. \quad (\text{C3})$$

2. Prolate spheroidal coordinates

Start with the x - y -plane and place an ellipse of focal distance d with its major axis along the x -axis. Now, revolve the ellipse by 2π around the x -axis to produce a prolate spheroid. Then, ξ_1 represents concentric prolate spheroidal surfaces, ξ_2 represents the corresponding hyperbolic surfaces, and we call ϕ the angle of revolution. The coordinate equations are

$$\begin{aligned} x &= \frac{d}{2}\xi_1\xi_2, \\ y &= \frac{d}{2}\sqrt{\xi_1^2 - 1}\sqrt{1 - \xi_2^2} \cos \phi, \\ z &= \frac{d}{2}\sqrt{\xi_1^2 - 1}\sqrt{1 - \xi_2^2} \sin \phi. \end{aligned} \quad (\text{C4})$$

The coordinate ranges are $1 \leq \xi_1 < \infty$, $-1 \leq \xi_2 \leq 1$, and $0 \leq \phi \leq 2\pi$, and the volume element $dV = \frac{1}{8}d^3(\xi_1^2 - \xi_2^2)d\xi_1d\xi_2d\phi$. In this paper, we treat prolate spheroids with dimensionless major axis length unity and minor axis length $1/\lambda$. These lengths determine the focal distance d as

$$d = 2\frac{\sqrt{\lambda^2 - 1}}{\lambda}, \quad (\text{C5})$$

and the particle surface is parameterised by

$$\xi_1^{(p)} = \frac{\lambda}{\sqrt{\lambda^2 - 1}}. \quad (\text{C6})$$

- ¹ G. B. Jeffery, "The motion of ellipsoidal particles immersed in a viscous fluid," *Proc. R. Soc. A* **102**, 161–179 (1922).
- ² G. Subramanian and D. L. Koch, "Inertial effects on fibre motion in simple shear flow," *J. Fluid Mech.* **535**, 383–414 (2005).
- ³ D. Qi and L. Luo, "Rotational and orientational behaviour of three-dimensional spheroidal particles in Couette flows," *J. Fluid Mech.* **477**, 201 (2003).
- ⁴ H. Huang, X. Yang, M. Krafczyk, and X.-Y. Lu, "Rotation of spheroidal particles in Couette flows," *J. Fluid Mech.* **692**, 369–394 (2012).
- ⁵ T. Rosén, F. Lundell, and C. K. Aidun, "Effect of fluid inertia on the dynamics and scaling of neutrally buoyant particles in shear flow," *J. Fluid Mech.* **738**, 563–590 (2014).
- ⁶ W. Mao and W. Alexeev, "Motion of spheroid particles in shear flow with inertia," *J. Fluid Mech.* **749**, 145 (2014).
- ⁷ P. G. Saffman, "On the motion of small spheroidal particles in a viscous liquid," *J. Fluid Mech.* **1**, 540 (1956).
- ⁸ F. Lundell and A. Carlsson, "Heavy ellipsoids in creeping shear flow: Transitions of the particle rotation rate and orbit shape," *Phys. Rev. E* **81**, 016323 (2010).
- ⁹ J. Einarsson, J. R. Angilella, and B. Mehligh, "Orientational dynamics of weakly inertial axisymmetric particles in steady viscous flows," *Phys. D* **278–279**, 79–85 (2014).
- ¹⁰ S. Kim and S. J. Karrila, *Microhydrodynamics: Principles and Selected Applications*, Butterworth-Heinemann Series in Chemical Engineering (Butterworth-Heinemann, Boston, 1991).
- ¹¹ J. Einarsson, F. Candelier, F. Lundell, J. Angilella, and B. Mehligh, "The effect of weak inertia upon Jeffery orbits," *Phys. Rev. E* **91**, 041002(R) (2015).



- ¹² E. Y. Harper and I.-D. Chang, "Maximum dissipation resulting from lift in a slow viscous shear flow," *J. Fluid Mech.* **33**, 209–225 (1968).
- ¹³ P. G. Saffman, "The lift on a small sphere in a slow shear flow," *J. Fluid Mech.* **22**, 385–400 (1965).
- ¹⁴ E. J. Hinch and L. G. Leal, "The effect of Brownian motion on the rheological properties of a suspension of non-spherical particles," *J. Fluid Mech.* **52**, 683–712 (1972).
- ¹⁵ C. J. Petrie, "The rheology of fibre suspensions," *J. Non-Newtonian Fluid Mech.* **87**, 369–402 (1999).
- ¹⁶ F. Lundell, D. Soderberg, and H. Alfredsson, "Fluid mechanics of papermaking," *Annu. Rev. Fluid Mech.* **43**, 195–217 (2011).
- ¹⁷ G. Subramanian and D. L. Koch, "Inertial effects on the orientation of nearly spherical particles in simple shear flow," *J. Fluid Mech.* **557**, 257–296 (2006).
- ¹⁸ Z. Yu, N. Phan-Thien, and R. Tanner, "Rotation of a spheroid in a Couette flow at moderate Reynolds numbers," *Phys. Rev. E* **76**, 026310 (2007).
- ¹⁹ H. Lorentz, "The theorem of Poynting concerning the energy in the electromagnetic field and two general propositions concerning the propagation of light," *Versl. Kon. Akad. Wetensch. Amsterdam* **4**, 176 (1896).
- ²⁰ J. Happel and H. Brenner, *Low Reynolds Number Hydrodynamics* (Kluwer Academic Publishers, 1983).
- ²¹ A. T. Chwang and T. Y.-T. Wu, "Hydromechanics of low-Reynolds-number flow. Part 2. Singularity method for Stokes flows," *J. Fluid Mech.* **67**, 787–815 (1975).
- ²² F. Candelier, J. Einarsson, F. Lundell, B. Mehlig, and J. Angilella, "The role of inertia for the rotation of a nearly spherical particle in a general linear flow," *Phys. Rev. E* **91**, 053023 (2015).



Paper D

arXiv preprint available at <http://arxiv.org/abs/1508.04976>





Numerical analysis of the angular motion of a neutrally buoyant spheroid in shear flow at small Reynolds numbers

T. Rosén,^{1,2} J. Einarsson,³ A. Nordmark,¹ C. K. Aidun,⁴ F. Lundell,^{1,2} and B. Mehlig³

¹*KTH Mechanics, Royal Institute of Technology, SE-100 44 Stockholm, Sweden*

²*Wallenberg Wood Science Center, Royal Institute of Technology, SE-100 44 Stockholm, Sweden*

³*Department of Physics, Gothenburg University, SE-41296 Gothenburg, Sweden*

⁴*George W. Woodruff School of Mechanical Engineering,
and Parker H. Petit Institute for Bioengineering and Bioscience,
801 Ferst Drive, Georgia Institute of Technology, Atlanta, GA 30332-0405*

We numerically analyse the rotation of a neutrally buoyant spheroid in a shear flow at small shear Reynolds number. Using direct numerical stability analysis of the coupled nonlinear particle-flow problem we compute the linear stability of the log-rolling orbit at small shear Reynolds number, Re_a . As $\text{Re}_a \rightarrow 0$ and as the box size of the system tends to infinity we find good agreement between the numerical results and earlier analytical predictions valid to linear order in Re_a for the case of an unbounded shear. The numerical stability analysis indicates that there are substantial finite-size corrections to the analytical results obtained for the unbounded system. We also compare the analytical results to results of lattice-Boltzmann simulations to analyse the stability of the tumbling orbit at shear Reynolds numbers of order unity. Theory for an unbounded system at infinitesimal shear Reynolds number predicts a bifurcation of the tumbling orbit at aspect ratio $\lambda_c \approx 0.137$ below which tumbling is stable (as well as log rolling). The simulation results show a bifurcation line in the $\lambda\text{-Re}_a$ plane that reaches $\lambda \approx 0.1275$ at the smallest shear Reynolds number ($\text{Re}_a = 1$) at which we could simulate with the lattice-Boltzmann code, in qualitative agreement with the analytical results.

PACS numbers: 83.10.Pp, 47.15.G-, 47.55.Kf, 47.10.-g



I. INTRODUCTION

The angular motion of a neutrally buoyant spheroid in a simple shear has recently been studied extensively and in detail at moderately large shear Reynolds numbers, by numerical stability analysis and by computer simulations using the lattice-Boltzmann method [1–7]. In particular Ding and Aidun [1] analysed rotation in the flow-shear plane and found that a saddle-node bifurcation gives rise to steady states where the symmetry axis of the particle aligns with a certain direction in the flow-shear plane. The authors of Refs. 2–7 analysed this bifurcation in detail and found a large number of additional bifurcations at intermediate and large Reynolds numbers that give rise to intricate angular dynamics.

At zero shear Reynolds number particle and fluid inertia are negligible, and the angular dynamics is determined by an infinite set of marginally stable periodic orbits, the so-called Jeffery orbits[8].

The effect of weak fluid and particle inertia on the angular motion of a neutrally buoyant spheroid in an unbounded shear was analysed recently [9–13]. In Refs. 9–12 an approximate angular equation of motion was derived for arbitrary aspect ratios of the spheroidal particle, and valid to linear order in the shear Reynolds number. Linear stability analysis of the Jeffery orbits subject to infinitesimal inertial perturbations allowed to determine the linear stability of the log-rolling orbit (where the particle symmetry axis is aligned with vorticity), and of tumbling in the flow-shear plane: log rolling was found to be unstable for prolate spheroids and stable for oblate spheroids, in agreement with the results obtained by Subramanian and Koch [13] in the slender-body limit. Refs. 9–12 predicted that tumbling in the flow-shear plane is stable for prolate spheroids. For oblate spheroids tumbling was found to be stable for flat disks, otherwise unstable. An earlier attempt to compute the stability of log rolling of nearly spherical particles arrives at conclusions that are at variance with the results stated above [14]. This fact and further literature is discussed by Einarsson *et al.* [10].

In the present paper we analyse the stability of the log-rolling orbit numerically at finite but small shear Reynolds numbers by discretising the coupled particle-flow problem directly. In the limit where the shear Reynolds number tends to zero and where the system size approaches infinity we find good agreement with the analytical results of Refs. 10–12 for the unbounded system. The numerical method allows to estimate the importance of higher-order Re_a corrections to the analytical results, and to compute the effect of confinement.

We find the bifurcations of the tumbling orbit at small shear Reynolds numbers, using lattice Boltzmann simulations. At the smallest Re_a attained with the lattice-Boltzmann code ($Re_a = 1$) the bifurcation occurs at a critical aspect ratio of $\lambda_c \approx 0.1275$ in the finite system, in qualitative agreement with the analytical results obtained for an unbounded system.

We briefly comment on the wider context of this paper. Recently there has been a surge of interest in describing the tumbling of small non-spherical particles in turbulent [15–21] and complex flows [22–24] using Jeffery's equation. Studies of the dynamics of larger non-spherical particles in turbulence [15, 20, 25] take into account particle inertia but neglect fluid inertia because it is difficult to solve the coupled particle-flow problem. For heavy particles this may be a good approximation, but the results summarised in this paper (and the results of Refs. 4, 6, 7, 10–13) show that this is approximation is likely to fail for neutrally buoyant and nearly neutrally buoyant particles.

The remainder of this paper is organised as follows. Section II describes the coupled particle-flow problem that is the subject of this paper. In Section III we summarise the analytical results of Refs. 10–12 and find the bifurcations of the angular equation of motion obtained in these references. Our numerical results are described in Section IV, and compared to the analytical results. Section V contains our conclusions.

II. FORMULATION OF THE PROBLEM

The problem has the following dimensionless parameters. The shape of the spheroid is determined by the shape factor Λ defined as $\Lambda = (\lambda^2 - 1)/(\lambda^2 + 1)$ where λ is aspect ratio of spheroid, $\lambda = a/b$ for prolate spheroids, a is the major semi-axis length of the particle, and b is the minor semi-axis length. For oblate spheroids the aspect ratio is defined as $\lambda = b/a$. The effect of fluid inertia is measured by the shear Reynolds number $Re_a = a^2 s / \nu$ where ν is the kinematic viscosity of the fluid and s is the shear rate. Particle inertia is measured by the Stokes number, $St = (\rho_p / \rho_f) Re_a$ where ρ_p and ρ_f are particle and fluid mass densities. The numerical computations described in this paper are performed in a finite system of linear size L , and $\kappa = 2a/L$ is a dimensionless measure of the system size, $2a$ is the length of the major axis of the particle.

We use dimensionless variables to formulate the problem. scale is taken to be the major semi-axis length a of the spheroid. The velocity scale is as , the pressure scale is μs , and force and torque scales are $\mu s a^2$ and $\mu s a^3$ respectively, μ is the dynamic viscosity of the fluid. In dimensionless variables the angular equations of motion read

$$\dot{\boldsymbol{n}} = \boldsymbol{\omega} \wedge \boldsymbol{n}, \quad St \dot{\boldsymbol{L}} = St (\mathbb{I}\dot{\boldsymbol{\omega}} + \dot{\mathbb{I}}\boldsymbol{\omega}) = \boldsymbol{T}. \quad (1)$$



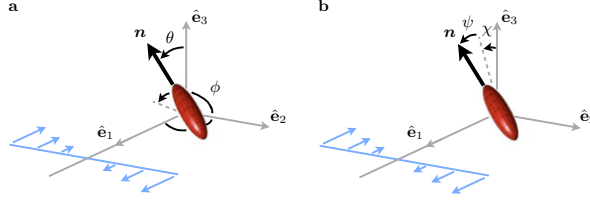


FIG. 1. Schematic illustration of spheroid in a simple shear in a coordinate system that translates with centre of mass of the particle. Vorticity points along the negative $\hat{\mathbf{e}}_3$ -axis, and $\hat{\mathbf{e}}_1$ is the flow direction. The flow-shear plane is spanned by $\hat{\mathbf{e}}_1$ and $\hat{\mathbf{e}}_2$. We use two different coordinate systems to express the orientation of the unit vector \mathbf{n} aligned with the symmetry axis of the particle. **a** Spherical coordinate system used for analysing linear stability of tumbling in the flow-shear plane, θ is the polar angle from the vorticity axis, and ϕ is the azimuthal angle in the flow-shear plane. **b** Spherical coordinate system used for analysing linear stability of log rolling, $\mathbf{n} = [0, 0, 1]$ corresponds to $\chi = \psi = 0$.

Here \mathbf{n} is the unit vector along the particle symmetry axis, dots denote time derivatives, $\mathbb{I} = A^I(\mathbb{1} - \mathbb{P}_\perp) + B^I\mathbb{P}_\perp$ is the particle-inertia matrix, \mathbb{P}_\perp is a projector onto the plane perpendicular to \mathbf{n} with elements $P_{ij} = \delta_{ij} - n_i n_j$, and A^I and B^I are moments of inertia along and orthogonal to \mathbf{n} . The particle angular velocity is $\boldsymbol{\omega}$, and \mathbf{T} is the hydrodynamic torque:

$$\mathbf{T} = \int_{\mathcal{S}} \mathbf{r} \wedge \sigma d\mathbf{s}. \quad (2)$$

The integral is over the particle surface \mathcal{S} , \mathbf{r} is the position vector, and σ is the stress tensor with elements $\sigma_{ij} = -p\delta_{ij} + 2S_{ij}$ where p is pressure, and S_{ij} are the elements of the strain-rate matrix \mathbb{S} , the symmetric part of the matrix \mathbb{A} of fluid-velocity gradients with elements $A_{ij} = \partial_j u_i$ (u_i are the components of the fluid velocity \mathbf{u}). The anti-symmetric part of \mathbb{A} is denoted by \mathbb{O} with elements O_{ij} . To determine the torque it is necessary to solve the Navier-Stokes equations for the incompressible fluid:

$$\text{Re}_a(\partial_t \mathbf{u} + (\mathbf{u} \cdot \nabla) \mathbf{u}) = -\nabla p + \Delta \mathbf{u}, \quad \nabla \cdot \mathbf{u} = 0. \quad (3)$$

For a neutrally buoyant particle $\text{Re}_a = \text{St}$.

It is assumed that the slip velocity vanishes on the particle surface \mathcal{S} , $\mathbf{u} = \boldsymbol{\omega} \wedge \mathbf{r}$ when $\mathbf{r} \in \mathcal{S}$. The perturbation calculations in Refs. 10–12 apply to a simple shear in an unbounded system, and it is assumed that the fluid velocity far from the particle is unaffected by its presence: $\mathbf{u} = \mathbf{u}^\infty$ as $|\mathbf{r}| \rightarrow \infty$. Here \mathbf{u}^∞ denotes the velocity field of the simple shear $\mathbf{u}^\infty = \mathbb{A}^\infty \mathbf{r}$ with $A_{ij}^\infty = \delta_{i1}\delta_{j2}$ (see Fig. 1 for an illustration of the geometry). The symmetric and antisymmetric parts of \mathbb{A}^∞ are denoted by \mathbb{S}^∞ and \mathbb{O}^∞ , respectively.

The numerical computations described in this paper pertain to a finite system, a cube of linear size $2\kappa^{-1}$ (in dimensionless variables). In the shear direction $u_1 = \pm\kappa^{-1}$ at $r_2 = \pm\kappa^{-1}$. In the flow and vorticity directions periodic boundary conditions are used.

III. THEORY AT SMALL Re_a .

In Refs. 10–12 an approximate angular equation of motion for a neutrally buoyant spheroid in an unbounded shear flow was derived, valid to linear order in $\text{Re}_a = \text{St}$:

$$\begin{aligned} \dot{\mathbf{n}} = & \mathbb{O}^\infty \mathbf{n} + \Lambda [\mathbb{S}^\infty \mathbf{n} - (\mathbf{n} \cdot \mathbb{S}^\infty \mathbf{n}) \mathbf{n}] + \beta_1 (\mathbf{n} \cdot \mathbb{S}^\infty \mathbf{n}) \mathbb{P}_\perp \mathbb{S}^\infty \mathbf{n} \\ & + \beta_2 (\mathbf{n} \cdot \mathbb{S}^\infty \mathbf{n}) \mathbb{O}^\infty \mathbf{n} + \beta_3 \mathbb{P}_\perp \mathbb{O}^\infty \mathbb{S}^\infty \mathbf{n} + \beta_4 \mathbb{P}_\perp \mathbb{S}^\infty \mathbb{S}^\infty \mathbf{n}. \end{aligned} \quad (4)$$

The first two terms on the r.h.s. of this equation are Jeffery's result for a neutrally buoyant spheroid in the creeping-flow limit. The remaining terms are corrections due to particle and fluid inertia. The four coefficients β_α (for $\alpha = 1, \dots, 4$) are linear in Re_a and St but non-linear functions of the particle aspect ratio λ : $\beta_\alpha = b_\alpha^{(\text{Re}_a)}(\lambda)\text{Re}_a + b_\alpha^{(\text{St})}(\lambda)\text{St}$. These functions were computed by Einarsson *et al.* [10, 11] for general values of λ , and in Ref. 12 in the nearly-spherical limit. Eq. (4) determines the effect of small inertial perturbations on the Jeffery orbits. It turns out that log rolling (\mathbf{n} aligned with the vorticity axis) and tumbling in the flow-shear plane survive small inertial perturbations. In the following two Sections we discuss the linear stabilities of these two orbits, for $\text{St} = \text{Re}_a$. We write $\beta_\alpha = \text{Re}_a b_\alpha(\lambda)$. Table I gives the asymptotes of these functions for large and small values of the aspect ratio λ . The asymptotes are obtained by expanding the results derived in Ref. 11.



TABLE I. Asymptotic behaviour of the functions $b_\alpha(\lambda) = \beta_\alpha/\text{Re}_a$ where β_α are the coefficients in Eq. (4) for $\text{St} = \text{Re}_a$. The asymptotes are found by expanding the solutions from Refs. 10, 11.

| | prolate $\lambda \rightarrow \infty$ | oblate $\lambda \rightarrow 0$ |
|-------|--|---|
| b_1 | $\frac{7}{15(2\log\lambda-3+\log 4)} + \frac{-197\log 2\lambda+92\log\lambda\log 4\lambda+106+92(\log 2)^2}{15\lambda^2(2\log\lambda-3+\log 4)^2}$ | $\frac{11}{30} + \left(\frac{176}{45\pi} - \frac{7\pi}{20}\right)\lambda + \left(-\frac{7}{3} + \frac{3968}{135\pi^2} - \frac{21\pi^2}{80}\right)\lambda^2$ |
| b_2 | $\frac{1}{5(2\log\lambda-3+\log 4)} + \frac{(\log\lambda-1+\log 2)(8\log 2\lambda-7)}{5\lambda^2(2\log\lambda-3+\log 4)^2}$ | $\frac{1}{10} + \left(\frac{8}{15\pi} - \frac{\pi}{20}\right)\lambda + \left(-\frac{1}{5} + \frac{128}{45\pi^2} - \frac{3\pi^2}{80}\right)\lambda^2$ |
| b_3 | $-\frac{4}{5\lambda^2}$ | $-\frac{1}{5} + \frac{9\pi^2-64}{60\pi}\lambda + \left(\frac{3}{5} - \frac{256}{45\pi^2} + \frac{9\pi^2}{80}\right)\lambda^2$ |
| b_4 | $\frac{4}{15\lambda^2}$ | $-\frac{1}{3} + \left(\frac{\pi}{20} - \frac{64}{45\pi}\right)\lambda + \left(\frac{5}{3} - \frac{1024}{135\pi^2} + \frac{3\pi^2}{80}\right)\lambda^2$ |

A. Linear stability analysis of log rolling

To analyse the stability of the log-rolling orbit we use the coordinate system shown in Fig. 1b. The angles χ and ψ are defined so that

$$n_1 = \sin\psi, \quad n_2 = \cos\psi\sin\chi, \quad n_3 = \cos\psi\cos\chi. \quad (5)$$

In these coordinates the equation of motion (4) takes the form:

$$\dot{\psi} = \frac{1}{8}[4(\Lambda\cos 2\psi + 1)\sec\psi\sin\chi \quad (6a)$$

$$+ (4\beta_1\cos 2\psi\sin^2\chi + (-2\beta_2 - \beta_3 + \beta_4)\cos 2\chi + 2\beta_2 + 3\beta_3 + \beta_4)\sin\psi]\cos\psi,$$

$$\dot{\chi} = \frac{1}{4}[2(\Lambda - 1)\tan\psi + ((\beta_2 - \beta_1)\cos 2\psi + \beta_1 - \beta_2 - \beta_3 + \beta_4)\sin\chi]\cos\chi. \quad (6b)$$

Log rolling along the vorticity direction $\mathbf{n} = [0, 0, 1]$ corresponds to $\chi = \psi = 0$, and this is a fixed point of Eq. (6) since $\dot{\psi} = \dot{\chi} = 0$ in this direction. The stability of this fixed point is determined by the eigenvalues of the linearisation of Eq. (6) around this fixed point. To linear order in Re_a the eigenvalues take the form

$$\gamma_{\text{LR}}^\pm = \frac{\beta_4}{4} \pm \frac{i}{2}\sqrt{1 - \Lambda^2} + o(\text{Re}_a). \quad (7)$$

The real part of this expression was derived in Refs. 10, 11 (see for example Fig. 3a in Ref. 10). The coefficient β_4 is linear in Re_a and its sign determines the stability of the log-rolling orbit at infinitesimal Re_a . The coefficient is positive for prolate spheroids (unstable log rolling) and negative for oblate spheroids (stable log rolling). The imaginary part in Eq. (7) shows that the log-rolling fixed point is a spiral at small Re_a . The imaginary part has no linear- Re_a correction.

B. Tumbling in the flow-shear plane

Under which circumstances is tumbling in the shear plane stable? In this Section we first summarise the results of analytical linear-stability calculations of Refs. [10–12] at infinitesimal Re_a . Second we discuss finite but small shear Reynolds numbers. To analyse tumbling in the flow-shear plane we use the coordinates employed in Refs. 10–12 (illustrated in Fig. 1a):

$$n_1 = \sin\theta\cos\phi, \quad n_2 = \sin\theta\sin\phi, \quad n_3 = \cos\theta. \quad (8)$$

In these coordinates the equation of motion (4) takes the form

$$\dot{\phi} = \frac{1}{2}(\Lambda\cos 2\phi - 1) + \frac{1}{8}\beta_1\sin^2\theta\sin 4\phi - \frac{1}{4}\sin 2\phi(\beta_2\sin^2\theta + \beta_3), \quad (9a)$$

$$\dot{\theta} = \Lambda\sin\theta\cos\theta\sin\phi\cos\phi + \frac{1}{4}\sin\theta\cos\theta(\beta_1\sin^2\theta\sin^2 2\phi + \beta_3\cos 2\phi + \beta_4). \quad (9b)$$



This is Eq. (42) in Ref. 10. Eq. (9b) shows that $\dot{\theta} = 0$ at $\theta = \pi/2$, in the flow-shear plane. The equation of motion for ϕ in this plane is

$$\dot{\phi} = \frac{1}{2} (\Lambda \cos 2\phi - 1) + \frac{1}{8} \beta_1 \sin 4\phi - \frac{1}{4} (\beta_2 + \beta_3) \sin 2\phi. \quad (10)$$

At infinitesimal values of Re_a there is a periodic tumbling orbit in the flow-shear plane because $\dot{\phi} < 0$. Its linear stability exponent γ_T at infinitesimal shear Reynolds numbers was calculated in Refs. 10, 11. It was found that tumbling in the flow-shear plane is stable for prolate particles in this limit, and unstable for not too thin oblate particles. For thin platelets tumbling was found to be stable. For infinitesimal shear Reynolds numbers the bifurcation occurs at the critical aspect ratio [10, 11]

$$\lambda_c \approx 0.137. \quad (11)$$

This concludes our summary of the results of Refs. [10, 11], valid at infinitesimal Re_a .

As Re_a increases we see that $\dot{\phi} \geq 0$ in Eq. (9) for some value(s) of ϕ . This implies the existence of fixed points in the flow-shear plane. This happens in Eq. (9) for any aspect ratio. But Eq. (9) is valid only to linear order in Re_a . For this reason we only look at limiting cases where Eq. (9) exhibits bifurcations at small values of Re_a . This occurs for thin rods and plates, as will be seen below.

Consider first rods. Rods of infinite aspect ratio align with the flow direction, particles with finite aspect ratio tumble at infinitesimal Re_a . At finite values of Re_a a bifurcation may cause a rod with finite aspect ratio to align. To find this bifurcation point we expand $\dot{\phi}$ to second order in $1/\lambda$ (Table I) and to second order in ϕ . A double root of the resulting quadratic equation for ϕ determines the bifurcation point:

$$\text{Re}_a^{(c1)} \sim \frac{15}{\lambda} (-3 + \log 4 + 2 \log \lambda) \quad \text{as } \lambda \rightarrow \infty. \quad (12)$$

The leading terms of this result for $\text{Re}_a^{(c1)}$ agree with Eq. (3.31) in Ref. 13 (up to a factor of 8π). Subramanian and Koch [13] derived their result using the slender-body approximation. Note that the qualitative features of the dynamics in the vicinity of $\text{Re}_a^{(c1)}$ are consistent with Eq. (12) in Ref. 1 (see also Zettner and Yoda [26]). As $\varepsilon \equiv \text{Re}_a - \text{Re}_a^{(c1)}$ tends to zero from below the period of the tumbling orbit tends to infinity as $(-\varepsilon)^{-1/2}$. Above the transition there are two fixed points, a saddle point and a stable node. It follows that the particle aligns at the angle

$$\phi_0 = \frac{1}{\lambda} + \frac{\sqrt{\varepsilon}}{15} \frac{\sqrt{30}}{\sqrt{\lambda(-3 + \log 4 + 2 \log \lambda)}} + \dots \quad \text{as } \lambda \rightarrow \infty, \quad (13)$$

for small values of ε . The form of this equation is consistent with Eqs. (3.30) and (3.31) in Ref. 13.

Now we turn to thin disks. The symmetry vector of an infinitely thin disk aligns with the shear direction, $\dot{\phi} = 0$ for $\phi = \pi/2$ when $\lambda = 0$. For non-zero values of λ the vector \mathbf{n} tumbles in the flow-shear plane in the limit of $\text{Re}_a \rightarrow 0$. At finite (but small) values of Re_a a bifurcation may cause the disk to align. To find this bifurcation point we expand $\dot{\phi}$ to second order in λ (Table I) and to second order in $\delta\phi = \phi - \pi/2$. As above a double root of the resulting quadratic equation for $\delta\phi$ determines the critical shear Reynolds number:

$$\text{Re}_a^{(c2)} \sim 15\lambda \quad \text{as } \lambda \rightarrow 0. \quad (14)$$

For $\text{Re}_a > \text{Re}_a^{(c2)}$ the symmetry vector \mathbf{n} of the disk aligns in the flow-shear plane at the angle

$$\phi_0 = \frac{\pi}{2} + \lambda + \frac{\sqrt{\varepsilon}}{15} \sqrt{30\lambda} \quad \text{as } \lambda \rightarrow 0. \quad (15)$$

In deriving this expression only the lowest orders in λ and ε were kept.

The bifurcation lines in the λ - Re_a -plane given by Eqs. (11), (12), and (14) are shown in Fig. 4. This figure also contains the results of our direct numerical simulations (DNS) which we discuss next.

IV. NUMERICAL COMPUTATIONS

We performed different types of DNS of Eqs. (1) to (3) in a finite domain with velocity boundary conditions in the shear direction, periodic boundary conditions in the other directions, and no-slip boundary conditions on the particle surface. We directly computed the linear stability of the log-rolling orbit using version 4.4 of the commercial software package Comsol Multiphysics™. As explained below this method could not be used to numerically determine the linear stability of tumbling in the flow-shear plane. Therefore we used lattice-Boltzmann simulations of the particle dynamics to determine the bifurcations of this orbit. To check the accuracy of the lattice-Boltzmann simulations we also performed steady-state DNS using version 9.06 of the commercial software package STAR-CCM+™.



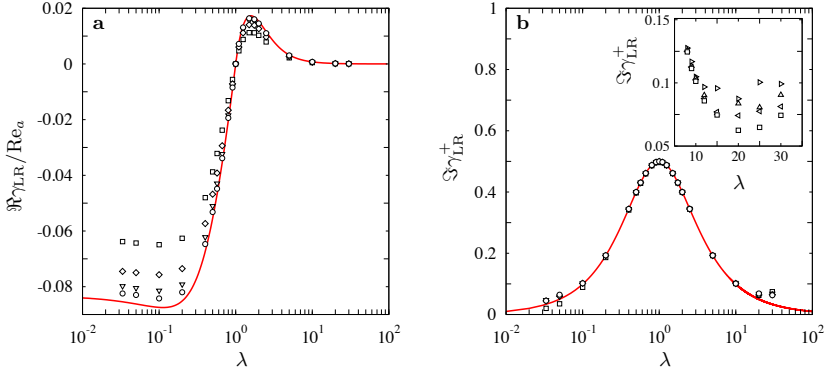


FIG. 2. **a** Comparison between the analytical result (7) for $\Re \gamma_{\text{LR}}$ (solid red line) and numerical results from direct numerical stability analysis (Section IV A). Parameters: $\text{Re}_a = 2.5 \cdot 10^{-4}$, $\kappa = 0.025$ (circles, \circ), $\kappa = 0.05$ (triangles, ∇), $\kappa = 0.1$ (diamonds, \diamond), and $\kappa = 0.2$ (squares, \square). **b** Same comparison for the imaginary part $\Im \gamma_{\text{LR}}^+$. The inset shows numerical results for $\Im \gamma_{\text{LR}}^+$ for slender prolate spheroids. Shown are results for $\kappa = 0.2$, $\text{Re}_a = 2.5 \cdot 10^{-4}$, and for different grid sizes in the vicinity of the particle: same resolution as in the main plot (squares, \square), characteristic lengths of the finite elements close to the particle larger by a factor of 1.25 (\triangleleft), 1.5 (\triangle), and 2 (\triangleright).

A. Direct numerical stability analysis of log rolling at finite values of Re_a

The eigenvalue solver in version 4.4 of the commercial finite-element software package Comsol MultiphysicsTM [27] makes it possible to analyse the stability of the log-rolling orbit as described in this Section [28]. The symmetries of the problem ensure that log rolling exists not only at infinitesimal but also at finite shear Reynolds numbers.

To determine the linear stability of this orbit it is sufficient to account for small deviations of \mathbf{n} from the log-rolling direction $\mathbf{n} = [0, 0, 1]$, and for the fact that the particle spins around its symmetry axis. Thus we avoid computationally expensive re-meshing around the particle.

The analysis proceeds in two steps. The first step is to find the steady-state solution of Eqs. (1) to (3) for a given value of Re_a , keeping \mathbf{n} fixed at $\mathbf{n} = [0, 0, 1]$. This determines the angular velocity $\boldsymbol{\omega}$ at which the particle spins around its symmetry axis. The second step is to allow for infinitesimal deviations of \mathbf{n} and $\boldsymbol{\omega}$ from this steady state. We use a so-called ‘arbitrary Lagrangian-Eulerian method’ [27] for grid refinement (deformation) close to the particle surface, linearise the resulting dynamics, and determine the eigenvalues of the linearised problem using the eigenvalue solver in Comsol, which is based on ARPACK FORTRAN routines for large eigenvalue problems [27, 29]. The eigenvalue solver provides N eigenvalues $\gamma_1, \dots, \gamma_N$ closest to the origin in the complex plane, ordered by ascending real parts, $\Re \gamma_1 > \dots > \Re \gamma_N$.

When the shear Reynolds number is small we usually find that $N-2$ eigenvalues $\gamma_3, \dots, \gamma_N$ are real (within numerical accuracy) with negative real parts. These are fluid modes that decay rapidly as the steady state is approached. In addition there is one leading pair of complex conjugate eigenvalues $\gamma_{1,2}$ with largest real part. This complex pair corresponds to the linear stability exponent γ_{LR}^\pm of the log-rolling orbit. It can have positive or negative real part, and the imaginary part determines the angular velocity of the particle. We must choose N large enough to ensure that this pair is among the N eigenvalues the solver finds. In most cases we find $N = 200$ to be sufficient. At larger values of Re_a it may happen that fluid modes have real parts that are larger than that of γ_{LR}^\pm , yet they are still real (within numerical accuracy). When this happens we verify that the complex pair describes the stability of the orientational dynamics of the particle by numerically integrating the dynamics near the steady state.

In this way we determine γ_{LR}^\pm as a function of the particle aspect ratio λ for different degrees κ of confinement, and for different values of Re_a . Fig. 2 shows real and imaginary parts of γ_{LR}^\pm as functions of the aspect ratio of the particle, for a small shear Reynolds number ($\text{Re}_a = 2.5 \cdot 10^{-4}$) and for different system sizes, $\kappa = 0.025, 0.05, 0.1$, and 0.2 . Fig. 2a compares the numerical results for the real part of γ_{LR} with the theory, Eq. (7). We observe excellent agreement for the largest system ($\kappa = 0.025$). This lends support to the analytical results of Refs. 10–12, and also to the numerical linear stability analysis. As we reduce the system size ($\kappa = 0.05, 0.1$, and 0.2) we observe increasing deviations from the theory for the unbounded system, as expected. When the system is ten times larger than the major semi-axis length of the particle there are substantial finite-size corrections. Fig. 2b compares numerical results

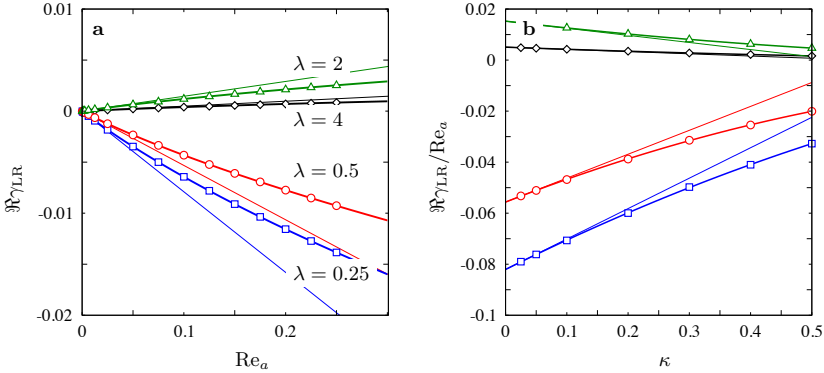


FIG. 3. **a** Shows $\Re\gamma_{LR}$ as a function of Re_a for $\kappa = 0.025$ and for four different values of λ . The thin solid lines show the limiting behaviour as $Re_a \rightarrow 0$. The thick solid lines show fits to Eq. (16). The coefficients are given in Table II. **b** Finite-size corrections to $\Re\gamma_{LR}/Re_a$ for $Re_a = 2.5 \cdot 10^{-4}$, and for the same values of λ as in panel **a**. The thick solid lines show quadratic fits to the small- κ behaviour, thin solid lines show the corresponding linear κ -dependence for small values of κ .

TABLE II. Coefficients a_1 , a_2 , and a_3 from the fit of Eq. (16) to the data in Fig. 3a, for $\kappa = 0.025$.

| λ | a_1 | a_2 | a_3 |
|-----------|---------|---------|---------|
| 1/4 | -0.0830 | 0.0652 | -0.0200 |
| 1/2 | -0.0566 | 0.0482 | -0.0183 |
| 2 | 0.0155 | -0.0125 | 0.0035 |
| 4 | 0.0051 | -0.0039 | 0.0008 |

for the imaginary part $\Im\gamma_{LR}^+$ with Eq. (7). Also for the imaginary part good agreement between the numerical results and Eq. (7) is observed for large system sizes, at least for moderate aspect ratios, $10^{-1} \leq \lambda \leq 10$. As for the real part there are finite-size corrections, but they are small relative to the $O(Re_a^0)$ -term in Eq. (7).

Now consider the deviations between the numerical results and theory that can be seen in Fig. 2b for more extreme aspect ratios. In this panel (and also in Fig. 2a) the size of the finite elements close to the particle surface is chosen as small as possible given the limited computational memory. But for very large (and also for very small) aspect ratios the resolution is insufficient. This can be seen in the inset of Fig. 2b. The inset shows data for $\Im\gamma_{LR}^+$ for $\kappa = 0.2$, and for different grid resolutions in the vicinity of the particle. For moderate aspect ratios the results converge quickly as the mesh size is reduced. But for $\lambda > 10$ we do not obtain convergence, reflecting the limitations of the numerical approach.

Fig. 3a shows finite- Re_a corrections to $\Re\gamma_{LR}$ for four different values of λ , for the smallest value of κ at which we could reliably compute, $\kappa = 0.025$. Theory [30, 31] suggests that there are $Re_a^{3/2}$ -corrections to Eq. (7) in the unbounded problem ($\kappa \rightarrow 0$). These corrections arise as follows. The leading-order inertial perturbation of the angular dynamics (linear in Re_a) is obtained in terms of the solution of the lowest-order problem, Stokes problem. At finite but small values of Re_a the Stokes solution provides an accurate description of the fluid velocity in the vicinity of the particle. But at larger distances from the particle (further away than the Ekman length $2a/Re_a^{1/2}$) the actual solutions decay more rapidly than the Stokes solution. Within the perturbative scheme used in Refs. [10–13] this gives rise to a $Re_a^{3/2}$ -correction. The next order is expected to be the quadratic order in the regular perturbation series, Re_a^2 . The prefactors of these terms are not known, they are very difficult to calculate. We have therefore compared the Re_a -dependence observed in the direct numerical simulations with a fit of the form

$$\Re\gamma_{LR} = a_1(\lambda, \kappa) Re_a + a_2(\lambda, \kappa) Re_a^{3/2} + a_3(\lambda, \kappa) Re_a^2 + \dots \quad (16)$$

The values obtained for the coefficients a_1 , a_2 , and a_3 are listed in Table II. The data shown in Fig. 3a and Table II are consistent with the existence of $Re_a^{3/2}$ -corrections when the system is large enough, $\kappa \ll Re_a^{1/2}$.

Fig. 3b shows finite-size corrections to $\Re\gamma_{LR}$ for $Re_a = 2.5 \cdot 10^{-4}$ and for four different values of λ . Also shown are

TABLE III. Coefficients c_1 , c_2 , and c_3 from the fit of Eq. (17) to the data in Fig. 3b. Also given are the numerical values of $b_4(\lambda)/4$ to which the coefficient c_1 should converge as $\kappa \rightarrow 0$ and $\text{Re}_a \rightarrow 0$. These values are taken from Ref. 10 since the aspect ratios $\lambda = 1/4, 1/2, 2, 4$ are not small (large) enough to use the asymptotic formulae given in Table I.

| λ | c_1 | $b_4(\lambda)/4$ | c_2 | c_3 |
|-----------|----------|------------------|----------|----------|
| 1/4 | -0.08205 | -0.0820 | 0.11923 | -0.04124 |
| 1/2 | -0.05564 | -0.0555 | 0.09373 | -0.04521 |
| 2 | 0.01526 | 0.0153 | -0.02784 | 0.01347 |
| 4 | 0.00510 | 0.0051 | -0.00870 | 0.00367 |

fits of the form

$$\Re\gamma_{LR}/\text{Re}_a = c_1(\lambda) + c_2(\lambda)\kappa + c_3(\lambda)\kappa^2. \quad (17)$$

The resulting coefficients are given in Table III. We see from Fig. 3b that the fits describe the numerically observed finite-size dependence accurately, but Eq. (17) is just an ansatz. Also shown are linear approximations valid at small κ . We see that the finite-size effects are to a good approximation linear in κ for the data shown for $\kappa \leq 0.1$. Table III shows that the limiting values obtained as $\kappa \rightarrow 0$ are in excellent agreement with the theoretical results for the unbounded system.

B. Time-resolved lattice-Boltzmann simulations

To analyse the bifurcations of the tumbling in the flow-shear plane we use the lattice-Boltzmann method with external boundary force [32]. To restrict the computational time, the domain size is set to a maximum of 240 lattice units. This allows us to resolve the particle with at least six fluid grid-nodes along its smallest dimension, with system size $\kappa = 0.2$. These choices limit the range of aspect ratios that can be simulated to $\lambda \in [1/8, 8]$. We take Re_a larger than or equal to unity in our simulations. This is because it is computationally very expensive to reach small values of the shear Reynolds number (as discussed by Rosén *et al.* [6, 7]).

To estimate the critical aspect ratio λ_c where tumbling changes stability for oblate particles we proceed as follows. We initialize the particle at rest, close to the tumbling orbit at $\phi = \pi/2$ and $\theta = \pi/2 - \delta\theta$ with $\delta\theta = 0.017$. We integrate the dynamics for aspect ratios $\lambda = 1/8, 1/7, 1/6, 1/5, 1/4$, and for Re_a between 1 and 10 with unit increments. We determine whether the trajectory tends to tumbling in the flow-shear plane or to the log-rolling orbit, and determine the location of the bifurcation by interpolation. At $\text{Re}_a = 1$ we run simulations for λ ranging between 0.125 and 0.160 with increments of 0.05 and determine the bifurcation point by linear interpolation. The results are illustrated in Fig. 4. We see that the results agree fairly well with Eq. (11). At the smallest value of Re_a simulated with the lattice-Boltzmann code, the transition occurs at $\lambda_c \approx 0.1275$, not too far from the analytical result (11) at infinitesimal Re_a for the unbounded system.

Using lattice-Boltzmann simulations we also obtain estimates for $\text{Re}_a^{(c1)}$ and $\text{Re}_a^{(c2)}$ (Section III). This is done by initialising the particle at rest at $\phi = \pi/4$ and $\theta = \pi/2$ for $\lambda > 1$ and at $\phi = 3\pi/4$ and $\theta = \pi/2$ for $\lambda < 1$. We then determine whether the particle tends to a steady state or continued to tumble, and determine the critical Reynolds number by linear interpolation. The results of these simulations are also shown in Fig. 4, and are compared with the analytical results for thin disks and rods given by Eqs. (12) and (14). We find that the agreement is only qualitative. This is not surprising since Eqs. (12) and (14) are based on Eq. (4) that is valid only to linear order in Re_a and cannot be expected to describe the dynamics at Reynolds numbers of order unity or larger. We also note that the lattice-Boltzmann simulations were performed for a rather small system, while the analytical results pertain to an unbounded system. Figs. 2a and 3b show that there are substantial finite-size corrections to the stability exponent of the log-rolling orbit in the finite system, for $\kappa = 0.2$. We therefore expect that there are equally important finite-size corrections to the locations of the bifurcations in Fig. 4. But at present we cannot perform lattice-Boltzmann simulations for larger systems with sufficient resolution to quantify this statement.

In order to check the accuracy of the lattice-Boltzmann simulations at $\kappa = 0.2$ we determined the critical Reynolds numbers $\text{Re}_a^{(c1)}$ and $\text{Re}_a^{(c2)}$ using an alternative approach, described in the next Section.

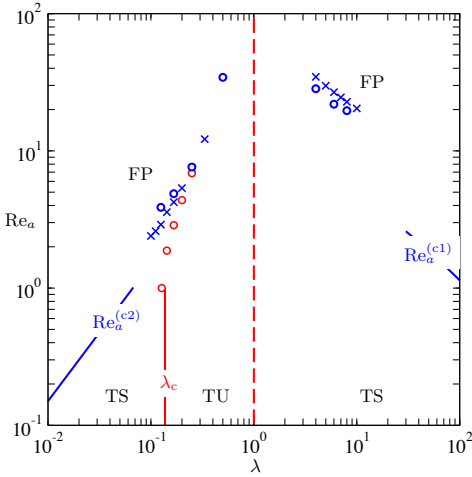


FIG. 4. Bifurcation diagram of the tumbling orbit in the flow-shear plane. Bifurcation lines derived in Section III for the unbounded system – Eqs. (12), (14), and (11) – are shown as solid lines. The label TS indicates that tumbling is stable, TU that it is unstable, and FP that the tumbling orbit has bifurcated giving rise to a fixed orientation in the flow-shear plane. The dashed line denotes the symmetry line at $\lambda = 0$ where the tumbling orbit changes stability. Numerical results for the finite system ($\kappa = 0.2$) are shown as symbols: circles (\circ) denote results from the time-resolved lattice-Boltzmann simulations described in Section IV B, crosses (\times) represent results from the steady-state simulations described in Section IV C. The bifurcations where tumbling in the flow-shear plane changes stability are shown in red, the bifurcations where stable tumbling in the flow-shear plane changes to a stable fixed point are shown in blue.

C. Steady-state simulations using STAR-CCM+TM

We compute the critical Reynolds numbers $Re_a^{(c1)}$ and $Re_a^{(c2)}$ using version 9.06 of the commercial finite-volume software package STAR-CCM+TM [33]. We choose the same system size as in the lattice-Boltzmann simulations, $\kappa = 0.2$. The particle orientation is fixed at $\theta = \pi/2$, $\phi \in [0, \pi/2]$ for prolate particles, and $\phi \in [\pi/2, \pi]$ for oblate particles. For a given particle aspect ratio λ and value of Re_a we compute the steady-state torque on the particle. If the torque vanishes, the chosen particle orientation is a fixed point for the given parameters. A fixed particle orientation makes it possible to use a very fine local grid around the particle. For different choices of ϕ we find critical Reynolds numbers where the steady-state torque vanishes. The minimum of this critical Reynolds as a function of ϕ gives $Re_a^{(c1)}$ or $Re_a^{(c2)}$, for oblate and prolate particles respectively. The corresponding results for $Re_a^{(c1)}$ and $Re_a^{(c2)}$ are also shown in Fig. 4. We conclude that the lattice-Boltzmann simulations slightly overestimate the critical value $Re_a^{(c1)}$, while they slightly underestimate $Re_a^{(c2)}$.

V. CONCLUSIONS

Using numerical linear stability analysis we computed the stability of the log-rolling orbit of a neutrally buoyant spheroid in a simple shear at small Re_a . For infinitesimally small Re_a in the unbounded system this problem was recently solved for arbitrary aspect ratios using perturbation theory in the shear Reynolds number. The fact that both calculations agree in the limits $Re_a \rightarrow 0$ and $\kappa \rightarrow 0$ (unbounded system) lends support to the analytical calculations [10–12], but also to the numerical linear stability analysis described in the present article. In the limit of large system size ($\kappa \rightarrow 0$) we found that there are corrections to the analytical result for the exponent $\Re\gamma_{LR}$ that are of order $Re_a^{3/2}$. We also investigated finite-size corrections to $\Re\gamma_{LR}$ at small Re_a , and found that they are substantial. It would be of interest to calculate both finite- Re_a and finite-size corrections to $\Re\gamma_{LR}$ by extending the method used in Refs. 10–12.

We did not investigate the stability of the tumbling orbit with numerical linear stability analysis because the required re-meshing is computationally very expensive. Instead we studied the stability of tumbling in the flow-shear plane using lattice-Boltzmann simulations. We tracked the bifurcation line between stable/unstable tumbling for thin



oblate spheroids (solid red line in Fig. 4) down to as small values of Re_a as we could reliably achieve and found that the transition occurs at $\lambda_c \approx 0.1275$ at $\text{Re}_a = 1$, in fair agreement with the theoretical prediction 0.137.

Finally we determined for which values of λ and Re_a tumbling in the flow-shear plane bifurcates to a fixed point, using lattice-Boltzmann simulations, and also by numerically computing steady-state torques using STAR-CCM+™. The two numerical procedures give results that are in fairly good agreement with each other, yet the agreement with the analytical results (12) and (14) is only qualitative.

Detailed analysis of the lattice-Boltzmann dynamics near the bifurcation at $\text{Re}_a^{(c2)}$ reveals the phase-space topology near the bifurcation at moderate Reynolds numbers ($\text{Re}_a^{(c2)} \approx 7.8$ at $\lambda = 1/4$), see Fig. 3(d),(e) in Ref. 7. For $\lambda = 1/4$ a second transition occurs at $\text{Re}_a^{(c3)} \approx 5$ where the log-rolling orbit changes from stable spiral to stable node. Eq. (4) also exhibits this transition. But since Eq. (4) is valid to linear order in Re_a the bifurcation can only be analysed in the limit $\lambda \rightarrow 0$. We find that the two transitions occur in reverse order: the tumbling \rightarrow fixed point bifurcation occurs before the spiral \rightarrow node transition as the shear Reynolds number is increased. There are several possible explanations for these subtle differences. They could be due to higher-order Re_a -corrections to Eq. (4) such as the $\text{Re}_a^{3/2}$ -corrections alluded to above. But we have also observed (not shown) in the numerical simulations of the bounded system that $\text{Re}_a^{(c3)}$ increases as κ becomes smaller. In the limit of $\kappa \rightarrow 0$ we except that the order of the transitions agrees with the prediction for the unbounded system. In summary we can conclude that the results of our numerical computations agree well with the theoretical predictions at infinitesimal Reynolds numbers: we find excellent agreement for the stability exponent of the log-rolling orbit, and the bifurcation of the tumbling orbit for thin oblate particles occurs in both theory and simulations, at similar values of λ_c . But there are a number of subtle differences between theory and simulations at larger Reynolds numbers. At present we cannot reliably perform lattice-Boltzmann simulations at much smaller Reynolds numbers than those shown in Fig. 4, and it is very difficult to perform such simulations at still smaller values of κ . Therefore it would be of great interest to extend the analytical calculations to include $\text{Re}_a^{3/2}$ -corrections, and to account for finite-size effects.

ACKNOWLEDGMENTS

JE and BM acknowledge support by Vetenskapsrådet and by the grant ‘Bottlenecks for particle growth in turbulent aerosols’ from the Knut and Alice Wallenberg Foundation, Dnr. KAW 2014.0048. TR and FL acknowledge financial support from the Wallenberg Wood Science Center (WWSC), Bengt Ingeström’s Foundation and ÅForsk (Ångpanneföreningen’s Foundation for Research and Development). The simulations were performed using resources provided by the Swedish National Infrastructure for Computing (SNIC) at the High Performance Computing Center North (HPC2N) and at the National Supercomputer Center (NSC) in Sweden. We also acknowledge the help from E. Sundström in setting up the simulations using STAR-CCM+.

-
- [1] E.-J. Ding and C. K. Aidun, “The dynamics and scaling law for particles suspended in shear flow with inertia,” *J. Fluid Mech.* **423**, 317 (2000).
 - [2] D. Qi and L. Luo, “Rotational and orientational behaviour of three-dimensional spheroidal particles in Couette flows,” *J. Fluid Mech.* **477**, 201 (2003).
 - [3] H. Huang, X. Yang, M. Krafczyk, and X.-Y. Lu, “Rotation of spheroidal particles in Couette flows,” *J. Fluid Mech.* **692**, 369–394 (2012).
 - [4] T. Rosén, F. Lundell, and C. K. Aidun, “Effect of fluid inertia on the dynamics and scaling of neutrally buoyant particles in shear flow,” *J. Fluid Mech.* **738**, 563–590 (2014).
 - [5] W. Mao and W. Alexeev, “Motion of spheroid particles in shear flow with inertia,” *J. Fluid Mech.* **749**, 145 (2014).
 - [6] T. Rosén, M. Do-Quang, C.K. Aidun, and F. Lundell, “The dynamical states of a prolate spheroidal particle suspended in shear flow as a consequence of particle and fluid inertia,” *J. Fluid Mech.* **771**, 115–158 (2015).
 - [7] T. Rosén, M. Do-Quang, C.K. Aidun, and F. Lundell, “Effect of fluid and particle inertia on the rotation of an oblate spheroidal particle suspended in linear shear flow,” *Phys. Rev. E* **91**, 053017 (2015).
 - [8] G. B. Jeffery, “The motion of ellipsoidal particles immersed in a viscous fluid,” *Proceedings of the Royal Society of London. Series A* **102**, 161–179 (1922).
 - [9] J. Einarsson, J. R. Angilella, and B. Mehlig, “Orientational dynamics of weakly inertial axisymmetric particles in steady viscous flows,” *Physica D: Nonlinear Phenomena* **278–279**, 79–85 (2014).
 - [10] J. Einarsson, F. Candelier, F. Lundell, J.R. Angilella, and B. Mehlig, “Rotation of a spheroid in a simple shear at small Reynolds number,” *Phys. Fluids* **27**, 063301 (2015).
 - [11] J. Einarsson, F. Candelier, F. Lundell, J.R. Angilella, and B. Mehlig, “Effect of weak fluid inertia upon Jeffery orbits,” *Phys. Rev. E* **91**, 041002(R) (2015).



- [12] F. Candelier, J. Einarsson, F. Lundell, B. Mehlig, and J.R. Angilella, “The role of inertia for the rotation of a nearly spherical particle in a general linear flow,” *Phys. Rev. E* **91**, 053023 (2015).
- [13] G. Subramanian and D. L. Koch, “Inertial effects on fibre motion in simple shear flow,” *Journal of Fluid Mechanics* **535**, 383–414 (2005).
- [14] P. G. Saffman, “On the motion of small spheroidal particles in a viscous liquid,” *J. Fluid Mech.* **1**, 540 (1956).
- [15] C. Marchioli, M. Fantoni, and A. Soldati, “Orientation, distribution, and deposition of elongated, inertial fibers in turbulent channel flow,” *Phys. Fluids* **22**, 033301 (2010).
- [16] S. Parsa, E. Calzavarini, F. Toschi, and G. A. Voth, “Rotation rate of rods in turbulent fluid flow,” *Phys. Rev. Lett.* **109**, 134501 (2012).
- [17] A. Pumir and M. Wilkinson, “Orientation statistics of small particles in turbulence,” *NJP* **13**, 093030 (2011).
- [18] R. Ni, N. T. Ouelette, and G. A. Voth, “Alignment of vorticity and rods with Lagrangian fluid stretching in turbulence,” *J. Fluid Mech.* **743**, R3 (2014).
- [19] L. Chevillard and C. Meneveau, “Orientation dynamics of small, triaxial-ellipsoidal particles in isotropic turbulence,” *J. Fluid Mech.* **737**, 571 (2013).
- [20] N. R. Challabotla, L. Zhao, and H. Andersson, “Orientation and rotation of inertial disk particles in wall turbulence,” *J. Fluid Mech.* **766**, R2 (2015).
- [21] M. Byron, J. Einarsson, K. Gustavsson, G. Voth, B. Mehlig, and E. Variano, “Shape-dependence of particle rotation in isotropic turbulence,” *Phys. Fluids* **27**, 035101 (2015).
- [22] M. Wilkinson, V. Bezuglyy, and B. Mehlig, “Fingerprints of random flows,” *Phys. Fluids* **21**, 043304 (2009).
- [23] V. Bezuglyy, B. Mehlig, and M. Wilkinson, “Poincaré indices of rheoscopic visualisations,” *Europhys. Lett.* **89**, 34003 (2010).
- [24] M. Wilkinson, V. Bezuglyy, and B. Mehlig, “Emergent order in rheoscopic swirls,” *J. Fluid Mech.* **667**, 158 (2011).
- [25] K. Gustavsson, J. Einarsson, and B. Mehlig, “Tumbling of small axisymmetric particles in random and turbulent flows,” *Phys. Rev. Lett.* **112**, 014501 (2014).
- [26] C. M. Zettner and M. Yoda, “Moderate-aspect-ratio elliptical cylinders in simple shear with inertia,” *J. Fluid Mech.* **442**, 241 (2001).
- [27] *Comsol MultiphysicsTM Reference Manual, version 4.4* (www.comsol.com, 2013).
- [28] T. Rosén, A. Nordmark, C. K. Aidun, and F. Lundell, “Evidence and consequences of a double zero eigenvalue for the rotational motion of a prolate spheroid in shear flow,” unpublished (2015).
- [29] <http://www.caam.rice.edu/software/ARPACK/>.
- [30] P. Lovalenti and J. Brady, “The force on a bubble, drop or particle in arbitrary time-dependent motion at small Reynolds number,” *Phys. Fluids* **5**, 2104–2116 (1993).
- [31] F. Candelier, J.-R. Angilella, and M. Souhar, “On the effect of inertia and history forces on the slow motion of a spherical solid or gaseous inclusion in a solid-body rotation flow,” *J. Fluid Mech.* **545**, 113–139 (2013).
- [32] J. Wu and C. K. Aidun, “Simulating 3D deformable particle suspensions using lattice Boltzmann method with discrete external boundary force,” *Int. J. Numer. Meth. Fl.* **62**, 765 (2010).
- [33] *STAR-CCM+ Reference Manual, version 9.06* (www.cd-adapco.com, 2014).





Paper E

arXiv preprint available at <http://arxiv.org/abs/1503.03023>





Tumbling of asymmetric microrods in a microchannel flow

J. Einarsson,^{1, a)} B. M. Mihiretie,^{1, a)} A. Laas,¹ S. Ankardal,¹ J. R. Angilella,² D. Hanstorp,¹ and B. Mehlig¹

¹⁾*Department of Physics, University of Gothenburg, 41296 Gothenburg, Sweden.*

²⁾*LUSAC, Université de Caen, Cherbourg, France.*

(Dated: 11 August 2015)

We describe results of measurements of the orientational motion of glass microrods in a microchannel flow, following the orientational motion of particles with different shapes. We determine how the orientational dynamics depends on the shape of the particle and on its initial orientation. We find that the dynamics depends so sensitively on the degree to which axisymmetry is broken that it is difficult to find particles that are sufficiently axisymmetric so that they exhibit periodic tumbling ('Jeffery orbits'). The results of our measurements confirm earlier theoretical analysis predicting sensitive dependence on particle shape and its initial orientation. Our results illustrate the different types of orientational dynamics for asymmetric particles predicted by theory.

I. INTRODUCTION

We study experimentally the orientational dynamics of neutrally buoyant non-axisymmetric particles suspended in a viscous shear flow. The rotation of axisymmetric particles in a shear flow has been studied in several experiments (we give a brief account below). The case of non-axisymmetric particles, by contrast, has received little attention experimentally. This is surprising because it is known in theory^{1,2} that the orientational dynamics can be very sensitive to small deviations from the axisymmetric limit. How sensitively the dynamics is affected by slight breaking of axisymmetry depends upon the orientational trajectory which in turn is determined by the initial orientation.

In order to verify this theoretical prediction experimentally it is necessary to use particles with well-defined shapes, to make sure that inertial effects and thermal noise are negligible, and to compare different orientational trajectories of the same particle.

In this paper we describe experimental observations of the orientational motion of micron-sized glass particles suspended in a pressure-driven micro-channel flow. The particles have different shapes: axisymmetric, slightly non-axisymmetric, and substantially non-axisymmetric (the latter are strongly triaxial particles made for the purpose of this experiment by joining two micron-sized glass rods). We verify that inertial and thermal torques have negligible effects by showing that the orientational dynamics is invariant under reversal of the pressure. An optical trap allows us to manipulate the same particle into different initial orientations, to study different orientational trajectories of the same particle. The results of our measurements confirm the predictions of Refs. 1,2, show the sensitive dependence of the orientational dynamics upon particle shape and initial orientation, and qualitatively illustrate the different types of orientational dynamics computed in Refs. 1,2. We have not attempted to quantitatively compare individual experimental particle trajectories with theory, to compare individual trajectories requires to compute the resistance tensors for the actual shape of the particles used in the experiments (the theory of Refs. 1,2 is formulated for ellipsoidal particles). This is beyond the scope of the present paper. Besides the resulting trajectories are of little general interest, they depend very sensitively on the particular shape of the particle in question.

^{a)}These authors contributed equally to this work.



The remainder of this Introduction briefly introduces the relevant theory as well as the wider context of this work. The orientational dynamics of a particle suspended in a viscous flow is determined by resistance tensors that relate the local flow velocity and its gradients to the torque acting on the particle^{3,4}. A given particle shape corresponds to a set of resistance tensors. Their elements are computed by solving Stokes' equations in appropriate geometries^{3,4}. The case of an ellipsoid in a viscous shear flow was first solved by Jeffery⁵. In this limit the equation of motion is given by the condition that the hydrodynamic torque vanishes at every instant. For particles that possess three orthogonal mirror planes⁶, particle shape enters the orientational equation of motion through two parameters, Λ and K . For an ellipsoid with half-axes a , b and c , for example, $\Lambda = (\lambda^2 - 1)/(\lambda^2 + 1)$ and $K = (\kappa^2 - 1)/(\kappa^2 + 1)$ with aspect ratios $\lambda = a/c$ and $\kappa = b/c$.

The case $K = 0$ corresponds to an axisymmetric particle. For axisymmetric particles the orientational dynamics is exactly solvable⁵. When $|\Lambda| < 1$ (so that $0 < \lambda < \infty$) there are infinitely many degenerate periodic orbits, the so-called ‘Jeffery orbits’. This is a consequence of the fact that the dynamical system has a conserved quantity: the ‘orbit constant’. The value of the orbit constant is determined by the initial orientation of the particle. The orientational motion of an axisymmetric particle in a simple shear is sometimes referred to as ‘tumbling’, the particle spends a long time aligned with the flow direction, and it periodically changes orientation by 180 degrees. Different Jeffery orbits differ in the functional form of these periodic ‘flips’. The degeneracy for $K = 0$ is particular to the simple shear flow, and it means that small perturbations can have a large effect.

Inertial forces, for example, are neglected in Jeffery’s theory. These forces induce ‘orbit drift’ into a final stable orbit. This was already suggested by Jeffery⁵, and was discussed in many experimental papers starting with Taylor⁷. See also Ref. 8. The corresponding theory is discussed by Subramanian and Koch⁹ and by Einarsson *et al.*^{10–12}.

Small particles may be affected by thermal noise so that the orbit constant performs a random walk giving rise to a statistical distribution of orientations. This mechanism forms the theoretical basis for understanding the rheology of dilute suspensions^{13,14}.

A third possibility, the topic of this work, is that the particle is not perfectly axisymmetric. This leads to a more complicated orientational equation of motion, also derived by Jeffery⁵. Some numerical examples of its solutions were reported by Gierszewski and Chaffey¹⁵ who found that the motion of a non-axisymmetric particle in a simple shear flow is qualitatively different from that of an axisymmetric particle. Hinch and Leal¹ analysed the structure of the solutions to the equation of motion. They found that for short times a nearly axisymmetric ellipsoidal particle approximately follows a Jeffery orbit, but on longer time scales the ‘orbit constant’ does not remain constant. It oscillates, giving rise to ‘doubly periodic’ tumbling: time series of the components of the unit vector aligned with the major axis of the particle show two distinct periods. Subsequently Yarin *et al.*² inferred from numerical experiments and analytical calculations that ellipsoidal particles may tumble periodically, quasi-periodically, or in a chaotic fashion – depending on the particle shape and on its initial orientation. The term ‘quasi-periodic’ refers to doubly periodic motion with incommensurable periods. Our experimental results support these theoretical predictions: our analysis demonstrates that the tumbling may indeed be periodic, doubly periodic, or possibly chaotic, depending on particle shape and initial orientation. Our results are in good qualitative agreement with theoretical predictions.

This work considers the orientational motion of small neutrally buoyant particles in a time-independent viscous shear flow. This is a special but important case. It is of theoretical interest because of its degeneracy and sensitivity to small perturbations, and it is of practical interest because it fundamentally relates to theories and experiments concerning the rheology of dilute suspensions. Theories are commonly formulated in terms of Jeffery’s equation^{13,16}. Recently there has been a surge of interest in describing the tumbling of non-spherical particles in turbulent^{17–22} and other complex flows^{23–25}. Since it is difficult to solve the coupled particle-flow problem most theoretical and numerical studies rely on Jeffery’s equation as an approximation to the orientational dynamics. Some exceptions are described in Refs. 26–28.



This article is organised as follows. In Section II we enumerate previous experimental efforts to validate Jeffery's equations. In Section III we describe the experimental setup. Section IV contains our experimental results. These results are discussed in Section V, and we conclude in Section VI.

II. PREVIOUS EXPERIMENTAL WORK

In this section we give a brief account of earlier experiments observing the orientational dynamics of single particles in shear flows.

Taylor⁷ immersed millimeter-sized aluminum spheroids in sodium silicate between two concentric rotating cylinders approximately 10 mm apart. In his brief report he asserts that the tumbling of the spheroids is in qualitative agreement with Jeffery's predictions, but that the orientational dynamics drifts after many (order of 100) particle rotations.

In a related study Eirich *et al.*²⁹ observed the orientations of glass rods and silk fibres in a Taylor-Couette device. The particles had diameters between 10 and 50 μm and aspect ratios between 5 and 100. No quantitative data on the orientational dynamics was measured, but they observed that the particles tend to align with the flow direction or with the vorticity direction.

Binder³⁰ studied fibers of many different aspect ratios suspended in glycerine. He employed a similar device with two concentric cylinders and found, as Taylor, that the orientational dynamics slowly drifts.

Mason and co-workers have studied the orientational dynamics of small particles in shear flows during two decades^{31–36}. Initially Trevelyan and Mason³¹ used a setup of two concentric cylinders rotating in opposite directions, making it possible to study a single particle over an extended period of time. The gap between the cylinders was approximately 10 mm, the suspending liquid was white corn syrup, and the particles were 9.5 μm diameter glass fibers cut to different lengths. By observing the particle orientation in a plane orthogonal to vorticity, Trevelyan and Mason³¹ found fairly good quantitative agreement of their experimental results with Jeffery's theory for one particle rotation (Fig. 7 in Ref. 31). However, for longer time series (up to 30 revolutions) their results were inconclusive: sometimes orbit drift was observed, sometimes not, and sometimes the change of orbit appeared seemingly erratic. In order to compare quantitatively with Jeffery's equations, valid for spheroidal particles, Trevelyan and Mason fitted the value of Λ to measurements of the tumbling period, yielding in their words an 'effective aspect ratio' for cylinders. Bretherton⁶ later showed that this procedure is consistent. Mason and Manley³² extended the experiment to hundreds of particle rotations (Fig. 2 in Ref. 32), but the observed orbit drift was apparently erratic. Mason and Manley mention convective currents as a possible cause for the observed drift, but no conclusions could be drawn concerning the single-particle dynamics. Bartok and Mason³³ used a similar device consisting of concentric cylinders, with a camera-equipped microscope observing along the vorticity axis, allowing to very precisely measure the tumbling behavior of high aspect ratio ($\lambda \approx 45$) acrylic ('Orlon') fibres. The experimental results were found to agree quantitatively with Jeffery's predictions for one particle rotation (Fig. 5 in Ref. 33). However, no data on the orbit drift, if any, was presented. Goldsmith and Mason³⁴ performed the first quantitative measurements of the rotations of disks. They used the same coaxial-cylinder setup described above, with silicone oil for the suspending liquid. The disks were fabricated by heating and compressing polystyrene spheres. The disk diameters were 400–850 μm , and their aspect ratios ranged from $\lambda = 1/20$ to $\lambda = 1/4$. Goldsmith and Mason showed that Jeffery's theory quantitatively predicts the orientational motion of axisymmetric disks, and that the orbit remained constant over 120 particle rotations (Table II in Ref. 34). In a sequel Goldsmith and Mason³⁵ described measurements of the motion of particles suspended in a liquid flowing through a circular tube. The tube diameters were 2–8 mm, the flow was pressure-driven by a syringe pump, and observations were recorded through a microscope traveling along the tube. Measurements were made on an assortment of particles of sizes ≈ 0.1 mm with aspect ratios ranging



from $\lambda = 1/20$ (disks) to $\lambda = 100$ (fibres). Goldsmith and Mason concluded that the dynamics along Jeffery orbits compares well with theory for short times (Fig. 5 in Ref. 35). However, they found measurable orbit drift after a single particle rotation, for both a rod and a disk, see Fig. 7 in the same paper. The drift was attributed to particle asymmetry. Anczurowski and Mason³⁶ fabricated prolate spheroidal particles by polymerising an electrostatically deformed droplet, and showed that Jeffery's theory holds quantitatively for one particle rotation given the true aspect ratio λ . They used the same concentric-cylinder device described above.

Harris *et al.*³⁷ performed experimental measurements on non-axisymmetric particles ($K \neq 0$). They used an apparatus with counter-rotating cylinders with a gap of 27 mm, which was filled with a glucose solution. The particles were machined from a composite material ('Tufnol') into cuboids of $1.75 \text{ mm} \times 1.28 \text{ mm}$ cross-section and 2.5–9.5 mm in length. They measured the unknown elements of the resistance tensors by observing simple rotations around each of the principal axes. With these numerical values of the resistance tensors they compared orientational trajectories of the cuboids to numerical solutions of Jeffery's equations and found reasonable quantitative agreement for two particle revolutions (Fig. 9 in their paper).

Stover and Cohen³⁸ investigated the effect of a wall on fibre motion using a pressure-driven flow of corn syrup through a rectangular channel. The fibres had cross-sectional diameters of $50 \mu\text{m}$ and lengths $600 \mu\text{m}$, resulting in an aspect ratio of 12. They found that the orientational dynamics are in quantitative agreement with Jeffery's theory for two particle rotations when the particle is at least one particle length away from the wall.

Kaya and Koser³⁹ observed *E. coli* bacteria advected in a microfluidic channel of rectangular cross section. They found that the orientational motion of the bacteria approximately follows Jeffery orbits.

Einarsson *et al.*²⁷ described examples of orientational trajectories of polymer microrods in a microchannel. They found that the trajectories of some particles were periodic admitting comparison to Jeffery's theory. Other trajectories were seen to be aperiodic (Fig. 8 of Ref. 27). The authors suggested that this aperiodic motion may have been caused by lack of axisymmetry of the particle in question. But it was not possible to draw definite conclusions, for several reasons. First the particles were produced by shearing polymer microspheres⁴⁰ which does not produce sufficiently well-controlled shapes. This is a problem because the shape of a given particle in the channel cannot be accurately observed. Second it could not be excluded that thermal torques affected the orientational dynamics. Third, and most importantly, the setup did not allow to record different orientational trajectories of the same particle. This motivated us to perform the experiments summarised in the following, they overcome the problems listed above.

III. METHODS

Fig. 1(a) shows a schematic drawing of the experimental setup to observe the orientational motion of small particles advected in a microchannel flow. A dilute suspension of microrods in a density-matched fluid is introduced into the microchannel. A syringe pump (a standard Harvard Apparatus infuse/withdraw model) is used to drive the flow of the particles. The system is placed under an inverted microscope equipped with a motorised translation stage. A CCD camera is used to register the orientation of a given particle. The initial orientation and position of the particle in the channel is set using an optical trap.

Fig. 1(b) shows the coordinate system that is used in this paper. The x -axis is parallel to the channel length along the flow direction. The y -axis is directed along the depth of the channel. The y -axis is also the optical axis of the microscope objective. The z -axis points along the channel width. The orientation of the particle is determined by the unit vector \mathbf{n} along the major axis of the particle.

The experiment is performed with cylindrical glass rods with diameters $3 \mu\text{m} \pm 0.01 \mu\text{m}$ (PF-30S, Nippon Electric Glass Co., Ltd). The microrods were manufactured as spacers



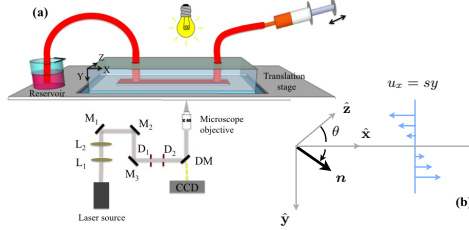


FIG. 1. (a) Schematic picture of the experimental setup, elements are not drawn to scale. $L_{1,2}$: lenses in a Keplerian telescope configuration. $M_{1,2,3}$: mirrors. $D_{1,2}$: diaphragms. DM: dichroic mirror reflecting the laser beam vertically towards the microfluidic system. The microscopic objective focuses the beam on the sample plane. Illumination is provided from the top. (b) Coordinate system in the lab frame spanned by orthogonal unit vectors \hat{x} , \hat{y} , and \hat{z} . The x -axis (flow direction) is directed along the channel length, the y -axis along the depth of the channel, and the z -axis along the channel width. The unit vector n points along the major axis of the particle. The polar angle between n and the z -axis is denoted by θ . The particles are kept roughly equally far away from the side walls of the channel. Since the channel is much wider than deep this means that the \hat{y} -direction is the shear direction, so that the local linearisation of the flow-velocity obeys $u_x = sy$ in the frame co-moving with the centre-of-mass of the particle, where s is the shear rate.

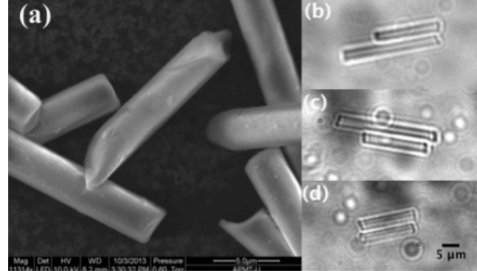


FIG. 2. (a) Electron-microscope image of the glass particles used in the experiment. Taken by Stefan Gustafsson, Chalmers. (b-d) Optical-microscope images of the double particles used in the experiments that led to (b) Fig. 5, to (c) Fig. S8, and to (d) Fig. S9. The last two figures are found in the Supplementary Online Material.

in liquid-crystal devices (PF-30S, Nippon Electric Glass Co., Ltd). This requires precise diameters. The lengths of the rods vary between approximately $10\text{ }\mu\text{m}$ and $30\text{ }\mu\text{m}$. An electron-microscope image of the particles is shown in Fig. 2(a). This Figure shows that the end surfaces of the cylindrical rods are randomly inclined and uneven, indicating that the particles were obtained by breaking longer glass rods. While this is irrelevant for the intended industrial use as spacers, it is important for our application. Random inclinations of the end surfaces break axisymmetry: sometimes only very slightly [lower left particle in Fig. 2(a)], sometimes more [c.f. particle in the centre of Fig. 2(a)]. We investigate the orientational dynamics of highly asymmetrical particles by studying aggregates of glass rods. Following Lewandowski *et al.*⁴¹ a dilute suspension of microrods is left to evaporate in order to produce double particles, Fig. 2(b)–(d). The glass particles have an index of refraction of 1.56 and a density of $\rho_p = 2.56\text{ g cm}^{-3}$.

To achieve neutral buoyancy the fluid must have the same density as the particles. To this end we mix 22.2%wt water, 4.4%wt glycerol, and 73.4%wt sodium metatungstate monohydrate (Alfa Aesar GmbH). Density matching is achieved by titration while observing



the particle under the microscope until the particle is buoyant for several minutes. But there are additional sources of error that are difficult to control. For example, when the fluid is pumped through the microchannel minute changes in temperature are expected to slightly change the fluid density. Such changes could induce small variations in the y -position of the particle that we sometimes observe during the recordings. The suspension is highly diluted in order to avoid particle-particle interactions. The mixture has a viscosity of $\mu = 25 \text{ mPa s}$ at 20°C . We estimate the shear Reynolds number $\text{Re}_s = \rho_f s a^2 / \mu$ as follows. The particle length a is of the order of $20 \mu\text{m}$. The shear rate s is determined by the flow speed u_x which is in turn given by the flow rate $8 \mu\text{l/min}$ and the cross section of the channel, $2.5 \text{ mm} \times 200 \mu\text{m}$. This results in $u \approx 0.3 \text{ mm s}^{-1}$ and a shear rate of $s \approx 3 \text{ s}^{-1}$ at $60 \mu\text{m}$ depth assuming a parabolic profile in the y -direction, and that the channel is much wider than deep. The density of the fluid ρ_f equals the particle density, $\rho_p = 2.56 \text{ g cm}^{-3}$. This gives $\text{Re}_s \approx 10^{-4}$. Inertial effects are thus negligible on the time-scale of the experiment.

The microchannel is produced using standard soft lithography. The process begins by milling a rectangular moulding form in aluminum. The surfaces of the mould are mechanically polished. A 10:1 mixture of polydimethylsiloxane (PDMS) and sylgard 184 Dow Corning (Sigma Aldrich) is poured on the moulding form and allowed to cure for several hours. The PDMS replica obtained after peeling off the mould is sealed to a glass slide (thickness 0.17 mm) by oxygen plasma bonding. This results in a rectangular channel that is 40 mm long, 2.5 mm wide, and $150 \mu\text{m}$ deep. For some measurements, a channel with a depth of $200 \mu\text{m}$ was used, see Table I. The suspension is injected into the channel using thin tubing connected to a syringe pump. PTFE tubes (Cole-Parmer) with outer diameters of 0.76 or 1.07 mm are used, the former in connection with a plastic syringe (1 ml , Terumo), the latter in connection with a glass syringe ($500 \mu\text{l}$, Hamilton).

The optical system is built around a Nikon X60 microscope objective (NA 1.0, WD 2 mm). The particle motion is recorded with a CCD video camera (Leica). The channel is mounted on a translation stage that moves the microchannel over the fixed observation microscopic objective. The stage is driven by a stepper motor that records the position of the stage. By moving the channel a given particle is kept within the field of view of the objective, despite the fact that the particle is advected by the fluid through the microchannel.

A single-beam optical trap is used to set the initial orientation and position of a given particle. The optical trap makes use of the microscope objective (Fig. 1), it provides sufficient magnification to not only visualise the particle, but also to trap it with a continuous infrared laser of wavelength 1075 nm (10 W , IPG-Laser GmbH). The most efficient way of trapping a glass rod with this setup is to direct the laser beam towards one of the two ends of the particle. Different orientations can be imposed on the particle by moving the channel sufficiently quickly to cause one end of the particle to leave the trap, yet sufficiently slowly so that the other end of the particle is kept trapped.

The experimental procedure described above ensures stable and reproducible experimental conditions. But a number of external factors were difficult to control and could still influence the experimental results to a small degree: evaporation due to the presence of unsaturated air in the reservoir, the presence of air bubbles in the channel that are difficult to get rid of, and pressure drops inside the channel due to the elasticity of the PDMS structure.

We use the image-analysis algorithm employed by Einarsson *et al.*²⁷. Images are acquired at a rate of 100 frames per second. Each frame is stored as 8-bit gray-scale bitmap with 692×520 pixels. The pixel size is $0.21 \mu\text{m}$. For a given frame the image analysis proceeds in three basic steps. First static noise is reduced by subtracting the time-averaged intensity from each frame. Then the boundary of the projection of the particle into the image plane is detected, and finally an ellipse is fitted to the boundary. Details are given in Ref. 27. The output defines the position and the orientation of the particle in the image. The centre-of-mass coordinates of the particle in the laboratory frame are determined using the output from the stepper motor recording the position of the stage.

The main sources of uncertainty in the image analysis are the limited resolution of the camera and diffraction. The latter gives rise to a diffuse particle boundary. The uncertainty



in the determination of the particle orientation is largest when the short end of the rod faces the camera, i.e. for small values of n_z (see Fig. 1).

A typical experiment starts by capturing a particle with the optical trap. The particle is brought into the desired location in the x - z -plane by moving the channel. All particles are started close to one of the inlets at approximately equal z -distances to both side walls. We verified that the z -position remains centred, with an error typically at most one particle length. This implies that the shear in the z -direction remains very small (the channel is much wider than deep). The y -coordinate thus corresponds to the shear direction, and the z -coordinate is the vorticity direction. The particle is brought to the desired initial orientation as described above and the centre-of-mass of the particle is placed at a depth of 60 mm. The precision in determining the initial depth is determined by the depth-of-field of the microscope. It is estimated to be of the order of one particle length. Then the particle is released to follow the flow in the microchannel. We then invert the pressure gradient so that the particle is advected back in the opposite x -direction. For each orientational trajectory we record both forward and backward dynamics. Since Stokes' equation is invariant under simultaneous pressure inversion and time reversal, the backward dynamics must exactly retrace the forward dynamics unless irreversible effects such as inertia or thermal noise affect the dynamics. Examples for the resulting video-microscopy recordings of the orientational dynamics in the x - z -plane are given in the Supplementary Online Material.

For a given particle this procedure is repeated many times to obtain orientational trajectories with different initial orientations. We record the length of the projection of the particle into the x - z -plane as a function of time. We estimate the particle length using the procedure described in Ref. 27. Once the particle length is known we can extract the components of the unit vector \mathbf{n} determining the orientation of the particle, as a function of time.

We plot the orientation not as a function of time but as a function of distance that the centre-of-mass of the particle has traveled through the channel, advected by the flow:

$$x(t) = \int_0^t dt' u_x(t'). \quad (1)$$

Here $u_x(t)$ is the instantaneous flow velocity at time t . This transformation simplifies the analysis because it accounts for the fact that the shear-rate is time-dependent: the flow velocity changes when the pressure is reversed, and in order to avoid inertial effects these reversals must be performed slowly. The invariance of Stokes' equation under time and pressure reversal implies $x(t) = -x(-t)$. We overlay forward and backwards dynamics by plotting the orientation as a function of centre-of-mass position.

IV. EXPERIMENTAL RESULTS

Figures 3, 4, and 5 show orientational dynamics of three different particles. For each particle five different orientational trajectories are shown, corresponding to different initial orientations [panels (b) to (f)]. In all three Figures we show trajectories of the x - and z -components of the unit vector \mathbf{n} that points along the major axis of the particle. Here n_x is the component in the flow direction, and n_z is the component in the vorticity direction. The third component of \mathbf{n} is determined by normalisation, $|\mathbf{n}| = 1$.

In panel (a) of each Figure we summarise the orientational dynamics by recording the values of n_z whenever $n_x = 0$. We denote the resulting sequence of consecutive n_z -values by $n_z^{(i)}$, $i = 1, 2, 3, \dots$. For an axisymmetric particle Jeffery's equation predicts that $n_z^{(i+1)} = n_z^{(i)}$, shown as the solid line along the diagonal in panel (a).

As mentioned above, the particle is first advected along a stream line of the pressure-driven flow in the channel. We then invert the pressure gradient so that the centre-of-mass of the particle is advected back to where it came from. For each orientational trajectory we show the ‘forward dynamics’ (blue solid line), going from right-to-left in the Figure. After the reversal follows the ‘backward dynamics’ (red dashed line). Since Stokes’ equation is



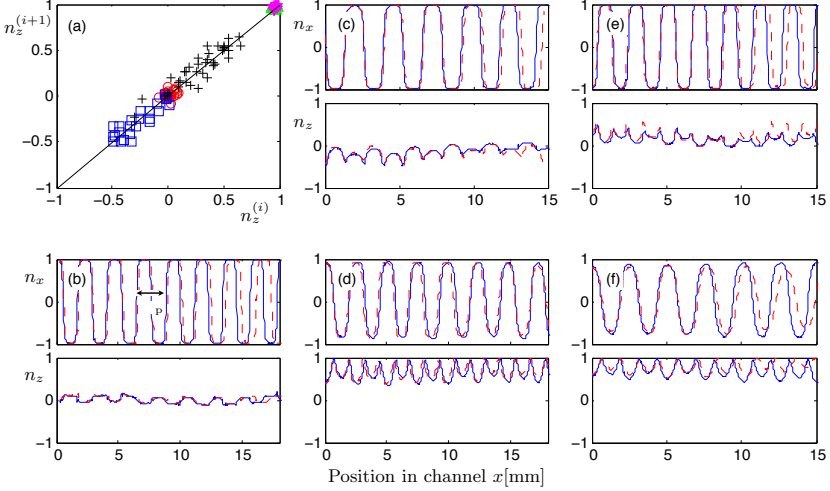


FIG. 3. Orientational dynamics of particle 1. (a) Dynamics of n_z . Here $n_z^{(i)}$ denote the values of n_z at subsequent zero crossings of n_x , $i = 1, 2, 3, \dots$. The data are taken from panels (b-f). Red \circ data from panel (b); blue \square data from (c); green \triangle data from (d); black $+$ data from (e); magenta \star data from (f). Panels (b-f) show orientational dynamics as a function of c.o.m.-position x in the channel, Eq. (1). Data in different panels correspond to different initial orientations. Solid blue and dashed red lines represent forward and backward trajectories, respectively. The flow direction is reversed at $x = 0$. The horizontal arrow in panel (b) indicates the period X_p [mm] of the trajectory.

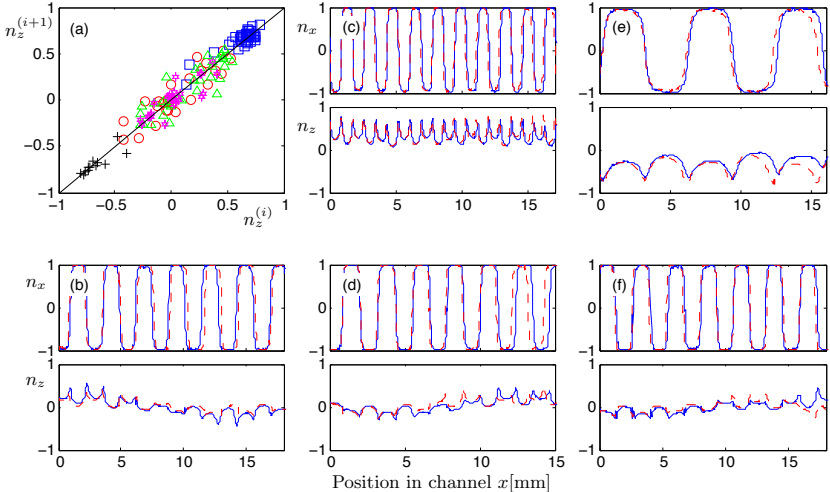


FIG. 4. Orientational dynamics of particle 2. See caption of Fig. 3 for details.



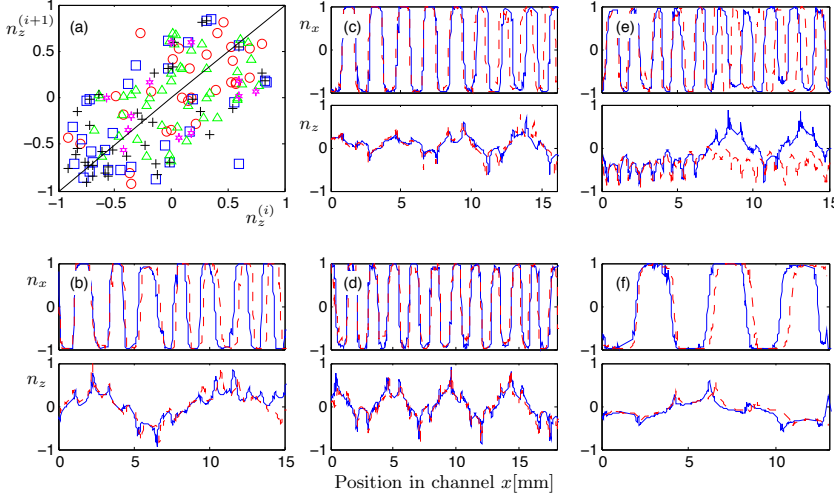


FIG. 5. Orientational dynamics of particle 3. See caption of Fig. 3 for details.

invariant under simultaneous pressure inversion and time reversal, the backward orientational dynamics must exactly retrace the forward dynamics unless irreversible effects due to inertia or thermal noise affect the dynamics noticeably on the time-scale of the experiment.

Consider first the trajectories shown in Fig. 3, corresponding to particle 1. Panels (b) to (f) show orientational trajectories of n_x and n_z for different initial orientations. In all cases the backward dynamics retraces the forward dynamics very well. This shows that neither inertial forces nor rotational diffusion affect the orientational dynamics. We attribute the small dephasing visible in each panel to a small density mismatch (discussed in Section III), causing the particle to sink (or float), changing the shear rate it experiences. Apart from this slight dephasing all orientational trajectories are fairly periodic. For a given n_x -trajectory the relative variation of the centre-of-mass distance between two consecutive $n_x=0$ -events ('half-period') is of the order of 10%. Between different panels we observe variations in the period X_p , between 2.1 mm and 2.6 mm, caused by the uncertainty in the y -position mentioned above. Panel (a) indicates that $n_z^{(i+1)}$ is approximately equal to $n_z^{(i)}$.

Fig. 4 shows the orientational dynamics of particle 2 for different initial orientations [panels (b) to (f)]. In all cases the backward dynamics retraces the forward dynamics well, at least for a few millimetres. As for particle 1 the trajectories show a slight dephasing within each panel. Different panels show quite different periods X_p , ranging between 1.7 mm and 5.9 mm. In panels (d) and (f) we see that the amplitude of n_z changes aperiodically. This is also apparent from panel (a) exhibiting a somewhat wider scatter around the diagonal than panel (a) in Fig. 3.

Fig. 5 shows the orientational dynamics of particle 3, an asymmetric double particle. For all initial orientations the backward dynamics retraces the forward dynamics fairly well, with the exception of the trajectories shown in panel (e). As for particles 1 and 2 we observe a slight dephasing within each panel. The dynamics of n_x is quite periodic, but again the periods X_p vary from panel to panel, ranging from 1.4 mm to 4 mm. In all cases n_z shows distinct aperiodicity. Panel (a) exhibits a larger scatter around the diagonal than panel (a) in Fig. 4.

The orientational dynamics of particle 1, 2, and 3 was obtained under slightly different experimental conditions. These are summarised in Table I, as well as the particle properties. Table I also gives information about other particles for which we obtained precise



| Particle number | Particle type ^a | Particle length(μm) ^b | Channel depth (μm) | Flow rate (μl/min) | Figure |
|-----------------|----------------------------|----------------------------------|--------------------|--------------------|----------------------|
| Particle 1 | single | 20.5 | 200 | 8 | Fig. 3 |
| Particle 2 | single | 24.3 | 150 | 5 | Fig. 4 |
| Particle 3 | double ^c | 28.7 | 200 | 8 | Fig. 5 |
| Particle 4 | single | 20.1 | 150 | 7.5 | Fig. S1 ^d |
| Particle 5 | single | 29.5 | 200 | 8 | Fig. S2 |
| Particle 6 | single | 17 | 150 | 5 | Fig. S3 |
| Particle 7 | single | 25 | 150 | 5 | Fig. S4 |
| Particle 8 | single | 26.5 | 150 | 5 | Fig. S5 |
| Particle 9 | single | 22.5 | 150 | 7.5 | Fig. S6 |
| Particle 10 | single | 25.5 | 150 | 5 | Fig. S7 |
| Particle 11 | double ^e | 26 | 200 | 8 | Fig. S8 |
| Particle 12 | double ^f | 17 | 200 | 8 | Fig. S9 |

TABLE I. Description of particles and other experimental parameters. ^aSingle or double particle.^bParticle length as extracted from image-analysis algorithm, see Section III. We estimate the error to be of the order of 1μm.^cThis particle is shown in Fig. 2(b). The lengths of the two glass rods are 26.4 and 17.3μm. ^dThese Figures are in the Supplementary Online Material.^eThis particle is shown in Fig. 2(c). The lengths of the two glass rods are 26 and 16.5μm. ^fThis particle is shown in Fig. 2(d). The lengths of the two glass rods are both 16μm.

orientational dynamics. The corresponding Figures are found in the Supplementary Online Material.

Video-microscopy recordings corresponding to the data shown in Figs. 3(b), (d), and 5(d) are found in the Supplementary Online Material.

V. DISCUSSION

The results summarised in Figs. 3 to 5 show the orientational dynamics of single and double glass rods. In general the particles are not perfectly axisymmetric (as seen in Fig. 2), and therefore do not follow perfect Jeffery orbits. In this section we relate our experimental results to the theoretical predictions valid for ellipsoidal particles^{1,5}. The particles in our experiment do not satisfy the mirror symmetries assumed in this theory, but it is plausible that the effects of breaking axisymmetry predicted by this theory apply at least qualitatively to our glass rods.

The equation of motion for the orientational dynamics of an ellipsoidal particle^{1,5} can be cast in the form⁴²

$$\dot{\mathbf{n}} = \mathbb{O}\mathbf{n} + \Lambda (\mathbb{S}\mathbf{n} - (\mathbf{n} \cdot \mathbb{S}\mathbf{n})\mathbf{n}) + \frac{K(1 - \Lambda^2)}{K\Lambda - 1}(\mathbf{n} \cdot \mathbb{S}\mathbf{p})\mathbf{p}, \quad (2a)$$

$$\dot{\mathbf{p}} = \mathbb{O}\mathbf{p} + K (\mathbb{S}\mathbf{p} - (\mathbf{p} \cdot \mathbb{S}\mathbf{p})\mathbf{p}) + \frac{\Lambda(1 - K^2)}{K\Lambda - 1}(\mathbf{n} \cdot \mathbb{S}\mathbf{p})\mathbf{n}. \quad (2b)$$

Following the convention outlined in Section III, \mathbf{n} is a unit vector that points along the major axis of the ellipsoidal particle. The unit vector \mathbf{p} is orthogonal to \mathbf{n} , directed along the particle axis corresponding to the length b used in the definition of the aspect ratio κ (defined in the Introduction). The geometry of the ellipsoid is characterised by the two shape parameters Λ and K that are defined in the Introduction, Section I. The matrices \mathbb{S} and \mathbb{O} are the symmetric and anti-symmetric parts of \mathbb{A} , the matrix of fluid-velocity gradients. In our case this matrix takes the form

$$\mathbb{A} = \begin{bmatrix} 0 & s & 0 \\ 0 & 0 & 0 \\ 0 & 0 & 0 \end{bmatrix}, \quad (3)$$



where s is the shear strength (Fig. 1).

Eqs. (2) are symmetric under the simultaneous exchange of \mathbf{n} and \mathbf{p} as well as Λ and K : describing the motion of the same particle using a different coordinate system within the particle must result in the same dynamics. Note also that the non-linear coupling between \mathbf{n} and \mathbf{p} involves the strain \mathbb{S} only. This coupling maintains orthogonality of the two vectors \mathbf{n} and \mathbf{p} . The anti-symmetric part \mathcal{O} just causes a solid-body rotation. For axisymmetric particles, $K = 0$, so that the tumbling of \mathbf{n} becomes independent of the dynamics of \mathbf{p} (but not vice versa). The resulting equation for \mathbf{n} has infinitely many degenerate periodic solutions, the Jeffery orbits⁵. The dynamics of \mathbf{p} describes how the particle spins around its symmetry axis.

When $K \neq 0$ (and $\Lambda \neq 0$), no general closed-form solutions of Eqs. (2) are known. It is convenient to represent the numerical solutions of Eq. (2) in terms of a Poincaré surface-of-section⁴³, recording the locations at which the dynamics intersects a surface in the phase space of Eq. (2). This section is constructed as follows. Hinch and Leal¹ have shown that the vector \mathbf{n} rotates around the vorticity at a positive angular velocity so that one can reduce the dimensionality of the problem by parametrising the orientational dynamics in terms of the corresponding angle. A suitable condition^{1,2} defining the surface-of-section is that \mathbf{n} is perpendicular to the flow direction, $n_x = 0$. Following Yarin *et al.*² we take the coordinates in the surface-of-section to be ψ and n_z , where ψ is the Euler angle parametrising the spin of the particle around the axis \mathbf{n} , and n_z is the z -component of \mathbf{n} , the cosine of the angle θ between \mathbf{n} and vorticity (Fig. 1). When $n_x = 0$ we record the coordinates (ψ, n_z) . To define the Euler angles (θ, ϕ, ψ) we use the convention of Goldstein⁴⁴ and express \mathbf{n} and \mathbf{p} as

$$\mathbf{n} = \begin{bmatrix} \sin \theta \sin \phi \\ -\sin \theta \cos \phi \\ \cos \theta \end{bmatrix}, \quad \text{and} \quad \mathbf{p} = \begin{bmatrix} -\sin \psi \cos \phi - \cos \theta \sin \phi \cos \psi \\ -\sin \psi \sin \phi + \cos \theta \cos \phi \cos \psi \\ \cos \psi \sin \theta \end{bmatrix}. \quad (4)$$

So θ is the polar angle depicted in Fig. 1. The angle ϕ is referred to as the ‘precession angle’. This angle measures the direction of the projection of \mathbf{n} into the flow-shear plane. Eqs. (2) correspond to Eqs. (2.1) and (2.2) in Ref. 2, setting $s = -1$ and defining the aspect ratios λ and κ in terms of the particle axes² as follows: $a_x = \lambda a_z$ and $a_y = \kappa a_z$.

In the experimental time series shown in Figs. 3 to 5, instances where $n_x = 0$ correspond to peaks in the oscillation in n_z . The n_z -coordinate in the surface-of-section is therefore easily read off from the experimentally observed time series. The angle ψ , by contrast, cannot be measured in our experiment because we cannot track how the particles spin around \mathbf{n} .

Four different surfaces-of-section are shown in Fig. 6, obtained by numerical integration of Eqs. (2) for a large number of different initial orientations, and plotting the sequence $[\psi^{(i)}, n_z^{(i)}]$ of (ψ, n_z) evaluated at consecutive zero crossings of n_x , labeled by $i = 1, 2, 3, \dots$. Similar sections are found in Ref. 2. The map that gives $[\psi^{(i+1)}, n_z^{(i+1)}]$ in terms of $[\psi^{(i)}, n_z^{(i)}]$ is called the Poincaré map.

Fig. 6(a) depicts the orientational dynamics of an axisymmetric particle, $K = 0$. The coordinate n_z is a conserved quantity on the surface-of-section, Jeffery orbits appear as horizontal lines in Fig. 6(a), one-parameter families parametrised by ψ . In the literature Jeffery orbits are commonly identified by their orbit constant C . It is given by the value of $\tan \theta$ at $n_x = 0$ (see for example Eq. (3) in Ref. 1). In this paper we characterise Jeffery orbits by $n_z = \cos \theta = 1/(1 + C^2)$ on the surface-of-section ($n_x = 0$). Fig. 6(a) illustrates that the orientational dynamics depends on the initial orientation, determining the value of n_z . We remark that the periods of \mathbf{n} and ψ are not in general commensurate for $K = 0$. But the tumbling of \mathbf{n} is independent of that of the angle ψ and thus periodic for axisymmetric particles.

Fig. 6(b) shows the orientational dynamics of a weakly asymmetric ellipsoidal particle ($K \approx 0.095$ and $\Lambda = 12/13$). We see that Jeffery orbits with $n_z \approx \pm 1$ remain almost unchanged. But there are substantial changes for smaller values of $|n_z|$, compared with the surface-of-section for $K = 0$. We see that n_z ceases to be a constant of motion, doubly-periodic orientational dynamics results. The most substantial changes occur near $n_z = 0$.



The $n_z = 0$ -Jeffery orbit is replaced by two fixed points at $(0, 0)$ and $(\pm\pi/2, 0)$ on the surface-of-section.

This fact and the surface-of-section patterns in the vicinity of these points follow from the time-reversal symmetry of Eqs. (2). The general principle is explained in Section 6.6 of Ref. 43. See also Ref. 45. The invariance of Stokes equation referred to in Section III implies that Eqs. (2) are invariant under

$$t \rightarrow -t, \quad n_x \rightarrow -n_x, \quad \text{and} \quad p_x \rightarrow -p_x. \quad (5)$$

The fixed point $(0, 0)$ is mapped onto itself under this transformation. It follows that the dynamics in its immediate neighbourhood can neither be expanding nor contracting. In other words the determinant describing the linearised motion in the vicinity of this fixed point,

$$\det \begin{bmatrix} \frac{\partial \psi^{(i+1)}}{\partial \psi^{(i)}} & \frac{\partial \psi^{(i+1)}}{\partial n_z^{(i)}} \\ \frac{\partial n_z^{(i+1)}}{\partial \psi^{(i)}} & \frac{\partial n_z^{(i+1)}}{\partial n_z^{(i)}} \end{bmatrix}, \quad (6)$$

must be of unit modulus despite the fact that the dynamics (2) is dissipative. We find numerically that the eigenvalues are $\exp(\pm i\sigma)$. The point $(0, 0)$ is thus an elliptic fixed point, surrounded by a one-parameter family of closed orbits that appear as concentric closed curves, much like so-called ‘tori’ in so-called ‘Hamiltonian’ systems with area-preserving phase-space dynamics⁴⁶. For near-axisymmetric particles Hinch and Leal¹ analysed the corresponding orbits by multiple-scales analysis. As these orbits rotate around the elliptic point, the value of n_z changes sign. This doubly-periodic motion may be quasi-periodic or periodic, depending on whether the two frequencies are incommensurate or not (corresponding to irrational or rational winding numbers, respectively).

The point $(\pm\pi/2, 0)$ is a hyperbolic fixed point. We find numerically that the eigenvalues are real and opposite, γ and γ^{-1} . The fact that the $n_z=0$ -orbit is destroyed upon infinitesimal perturbation and replaced by a discrete set of fixed points of alternating stability is typical for Hamiltonian systems⁴⁶. The mechanism in our dissipative system is analogous, a consequence of the symmetry (5).

For larger asymmetries chaotic orientational dynamics occurs, seen as a region with a stochastic scatter of points in Fig. 6(c). Almost all Jeffery orbits are modified, only those with n_z close to ± 1 remain. Whether the orientational dynamics is periodic, quasi-periodic, or chaotic depends upon the initial condition on the surface-of-section.

Fig. 6(d) shows the orientational dynamics for ellipsoidal particles with $K = 3/5$ and $\Lambda = 12/13$. This value of K is similar the corresponding value for the double particle 3 (Figs. 2(b) and 5), but this particle has $\Lambda \approx 40/41$. We do not seek quantitative correspondence between these parameters because the particles used in our experiment are not ellipsoidal. This prevents us from drawing quantitative conclusions, but still allows for a qualitative comparison between theory and experiment. The orientational dynamics displayed in Fig. 6(d) is either on tori or chaotic. Motion on tori can occur with large amplitudes, so that n_z changes from $n_z \approx -1$ to $n_z \approx 1$.

How are these observations reflected in the experimental time series shown in Figs. 3 to 5? Since we cannot measure the angle ψ in our experiments, we concentrate on the dynamics of n_z . Fig. 7 shows the range of changes of n_z in one iteration of the Poincaré map for particles with different degrees of asymmetry, determined by numerically recording the changes $n_z^{(i+1)} - n_z^{(i)}$ along orientational trajectories. The diagonal corresponds to symmetric particles where $n_z^{(i+1)} = n_z^{(i)}$. The larger the asymmetry, the larger is the range of $n_z^{(i+1)} - n_z^{(i)}$ that may occur, reflecting the properties of the surfaces-of-section shown in Fig. 6.

Fig. 7 can be directly compared with Figs. 3(a) to 5(a). Our experimental results show that the Poincaré map may scatter significantly around the diagonal. The above discussion explains that this is a consequence of doubly-periodic and possibly chaotic orientational dynamics of asymmetric particles. The range of scatter differs between different particles,



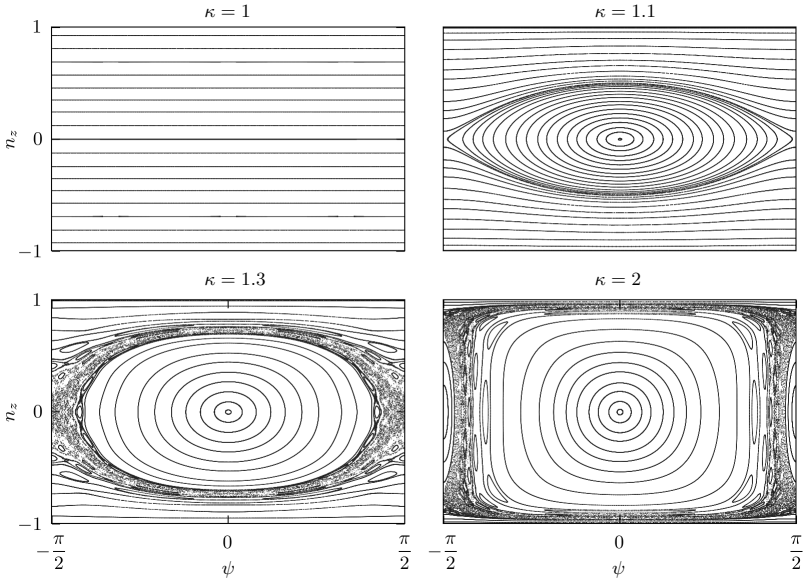


FIG. 6. Poincaré surfaces-of-section for $\Lambda = 12/13$ and different values of κ [$K = (\kappa^2 - 1)/(\kappa^2 + 1)$]. The angle ψ is defined up to $(\psi + \pi/2)\text{mod}\pi$.

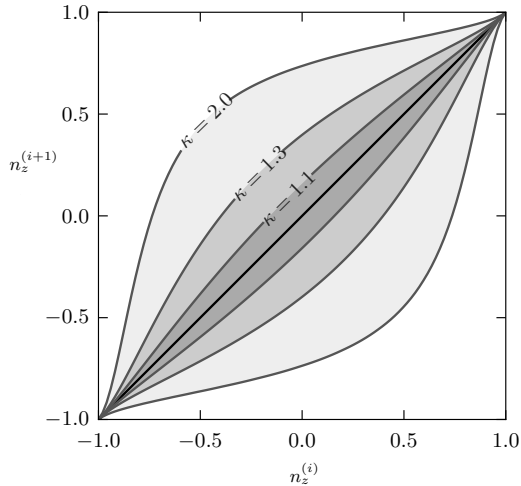


FIG. 7. Range of Poincaré map for $\Lambda = 12/13$ and different values of κ corresponding to the values used in Fig. 6, $K = (\kappa^2 - 1)/(\kappa^2 + 1)$. The data shown was obtained by iterating the Poincaré map once for randomly chosen initial conditions. The initial conditions were determined by sampling ψ uniformly over the surface-of-section for given values of n_z .



a consequence of different degrees of asymmetry. We see that the scatter is largest for the double particle 3, with $K \approx 3/5$ [Fig. 5(a)]. Particle 1, by contrast, shows only negligible scatter around the diagonal [Fig. 3(a)]. We infer that this particle is highly symmetric, K is very small. The data shown in Fig. 3 are consistent with the conclusion that particle 1 follows Jeffery orbits, n_z remains approximately constant in the surface-of-section. But we remark that the shape of the $n_z \approx 0$ -orbit does not look like a Jeffery orbit for an axisymmetric particle. We cannot exclude that this is due to possible non-ellipsoidal deviations from axisymmetry. The surface-of-section dynamics is most sensitive to such shape perturbations near $n_z = 0$. A more likely explanation is that the shape of the trajectory is a consequence of systematic (and reproducible) tracking errors due to diffraction and finite pixel size. These errors are largest for small values of n_z , as discussed in Section III.

Particle 2 is also a single glass rod, but it shows a somewhat larger range of scatter around the diagonal [Fig. 4(a)]. We attribute this to a more substantial breaking of axisymmetry at the tips of the particle [as seen for instance in Fig. 2(a)]. Particle 2 shows fairly periodic motion for $n_z \approx 1$ and distinctly doubly-periodic orientational dynamics for small values of n_z . This confirms that the initial orientation determines whether the particle tumbles periodically or aperiodically. Note also that n_z changes sign along the trajectories that remain near $n_z = 0$ [Fig. 4(b), (d), and (f)]. All of these observations are qualitatively consistent with the surfaces-of-section shown in Fig. 6(b) and 6(c).

For particle 3 the value of n_z changes sign for all orientational trajectories shown. This is consistent with the fact that the Fig. 6(d) shows predominantly this type of motion. Fig. 5(e) is consistent with chaotic orientational motion in the stochastic layer around the elliptic island. The surfaces-of-section in Fig. 6 show that there are two types of doubly-periodic motion: either n_z has the same sign, or its sign changes periodically. The trajectory in Fig. 5(e) exhibits both behaviours, indicating chaotic dynamics. Now consider the trajectory shown in Fig. 5(c). It is not periodic or doubly-periodic, but the reversal works well (at least initially). But we cannot conclude that the dynamics is consistent with surfaces-of-section discussed above. The n_z -values at $n_x = 0$ in Fig. 5(c) change from approximately 0.25 to 0.75 in modulus. Explaining this behaviour in terms of chaotic dynamics on the surfaces-of-section requires a large stochastic region, larger than the one shown in Fig. 6(d). This might mean that the trajectory shown in panel (d) is a doubly-periodic piece of a chaotic trajectory that may show different behaviours at larger times. But to determine whether these behaviours can be explained by chaotic dynamics would require to derive and numerically integrate the orientational equations of motion for the precise shape of the particle, and to experimentally record the angle ψ . Since the current experimental setup does not allow to reliably extract how the angle ψ changes, we plan to perform experiments with small triangular platelets that will allow to record the angle ψ .

The winding number of the trajectory shown in Fig. 5(d) is roughly 7 corresponding to seven $n_x = 0$ -crossings while the trajectory winds approximately once round the elliptic fixed point in the centre of the surface-of-section. The winding number of the trajectory in Fig. 6(e) is roughly 4 corresponding to four $n_x = 0$ -crossings while the surface winds once around the elliptic fixed point. These observations are in qualitative agreement with the fact that the winding numbers of tori winding around the elliptic fixed points increase as the distance from that point increases (corresponding to larger maximal values of n_z).

Additional results for seven more particles are shown in the Supplementary Online Material, Figs. S1 to S7. In general the results shown in these Figures support the observations and qualitative conclusions summarised above. But the trajectory shown in Fig. S7 is difficult to reconcile with the surfaces-of-section shown in Fig. 6. Fig. S7(c) shows an orbit near $n_z = 0$ where n_z appears not to change sign. But panels (d) and (f) in Fig. S7 show distinct sign changes, not consistent with the surfaces-of-section shown in Fig. 6.

It was pointed out in Section IV that the periods X_p observed in the orientational trajectories can differ substantially between different trajectories of the same particle. Consider for instance particle 1 (Fig. 3). For an axisymmetric ellipsoidal particle ($K = 0$) the Jeffery



period (time units) is given by⁵

$$T_p = \pi \frac{\lambda^2 + 1}{s\lambda}. \quad (7)$$

For $K = 0$ this is twice the return time to the surface-of-section. For $K \neq 0$ the return time depends upon the starting position on the surface-of-section, but for small values of K the deviations from (7) are small, of the order of K . For the nearly axisymmetric particle 1 we can use Eq. (7) to estimate the period X_p in Fig. 3. Using the parameters from Table I and assuming that the particle was located at a depth of 60 μm , Eq. (7) gives $X_p \approx 2.3 \text{ mm}$. This is consistent with the range of periods observed in Fig. 3(b) to (f), namely 2.1 mm to 2.6 mm. We infer that the precision in determining the depth at which particle 1 moves through the channel is of the order of one particle length. The variations in periods observed in Figs. 4 and 5 indicate that the actual depths vary more between different panels than in Fig. 3.

VI. CONCLUSIONS

Theory and numerical simulations predict that the orientational dynamics of small neutrally buoyant particles in a shear flow is very sensitive to breaking of axisymmetry^{1,2,15}. Axisymmetric particles tumble periodically on Jeffery orbits, but when the symmetry is broken, the Jeffery orbits are modified. Depending on the initial orientation, periodic, doubly-periodic, or chaotic tumbling may result.

In order to experimentally verify these predictions it is necessary to use particles of well-defined shape, to ensure that inertial effects and rotational diffusion are negligible, and to compare different orientational trajectories (corresponding to different initial orientations) of the same particle.

In this paper we describe measurements of the orientational motion of small glass rods suspended in a micro-channel shear flow. The measurements are precise enough to allow for a definite comparison with theory^{1,2}. First, the glass rods have highly symmetric circular cross sections. Slight imperfections at the ends break the axisymmetry weakly for some particles [Fig. 2(a)]. We also use strongly triaxial particles designed for our purpose by joining two glass rods. Second, by reverting the pressure-driven flow we observe that the orientation retraces its trajectory for many periods. This means that neither inertial effects nor rotational diffusion matter on this time scale. Third by means of an optical trap we change the orientation of the particle, making it possible to measure different orientational trajectories for the same particle.

Our results confirm the theoretical predictions^{1,2}. We observe periodic and doubly-periodic tumbling, and how the nature of the orientational dynamics depends upon the initial orientation, and on the degree to which axisymmetry is broken. Our measurements are consistent with the features of the surfaces-of-section shown in Figs. 6 and 7.

In the future we plan to experimentally map out Poincaré surfaces-of-section (Fig. 6). With the present particles this is not possible because we cannot resolve how the particle spins around its major axis. We therefore plan to perform corresponding experiments using micron-sized triangular platelets. We expect that it will be possible to resolve the tumbling and spinning dynamics of these particles using the methods described in this paper.

Finally we note that the shear flow is a special (yet important) case. It remains to be seen whether tri-axiality has significant effects on the orientational dynamics in other flows.

ACKNOWLEDGMENTS

We thank Stefan Gustafsson (Chalmers) for taking the electron-microscope image Fig. 2(a) and for granting us permission to use the image in this paper. BM gratefully acknowledges discussions with S. Östlund (University of Gothenburg) on the implications



of time-reversal symmetry for the surface-of-section dynamics shown in Fig. 6. This work was supported by grants from the Carl Trygger Foundation for Scientific Research and the Swedish Research Council.

- 1E. J. Hinch and L. G. Leal, "Rotation of small non-axisymmetric particles in a simple shear flow," *J. Fluid Mech.* **92**, 591–608 (1979).
- 2A. L. Yarin, O. Gottlieb, and I. V. Roisman, "Chaotic rotation of triaxial ellipsoids in simple shear flow," *J. Fluid Mech.* **340**, 83–100 (1997).
- 3J. R. Happel and H. Brenner, *Low Reynolds Number Hydrodynamics: With Special Applications to Particulate Media* (Springer, 1965).
- 4S. Kim and S. J. Karrila, *Microhydrodynamics: principles and selected applications*, Butterworth-Heinemann series in Chemical Engineering (Butterworth-Heinemann, Boston, 1991).
- 5G. B. Jeffery, "The Motion of Ellipsoidal Particles Immersed in a Viscous Fluid," *Proc. R. Soc. A* **102**, 161–179 (1922).
- 6F. P. Bretherton, "The motion of rigid particles in a shear flow at low Reynolds number," *J. Fluid Mech.* **14**, 284–304 (1962).
- 7G. I. Taylor, "The motion of ellipsoidal particles in a viscous fluid," *Proc. R. Soc. Lond. A* **103**, 58–61 (1923).
- 8A. Karnis, H. L. Goldsmith, and S. G. Mason, "The flow of suspensions through tubes. v. inertial effects," *J. Chem. Eng.* **44**, 181–193 (1966).
- 9G. Subramanian and D. L. Koch, "Inertial effects on fibre motion in simple shear flow," *J. Fluid Mech.* **535**, 383–414 (2005).
- 10J. Einarsson, F. Candelier, F. Lundell, J. Angilella, and B. Mehlig, "Rotation of a spheroid in a simple shear at small Reynolds number," *Phys. Fluids* **27**, 063301 (2015).
- 11J. Einarsson, F. Candelier, F. Lundell, J. Angilella, and B. Mehlig, "Effect of weak fluid inertia upon Jeffery orbits," *Phys. Rev. E* **91**, 041002(R) (2015).
- 12F. Candelier, J. Einarsson, F. Lundell, B. Mehlig, and J. Angilella, "The role of inertia for the rotation of a nearly spherical particle in a general linear flow," *Phys. Rev. E* **91**, 053023 (2015).
- 13H. Brenner, "Rheology of a dilute suspension of axisymmetric Brownian particles," *International Journal of Multiphase Flow* **1**, 195–341 (1974).
- 14E. J. Hinch and L. G. Leal, "The effect of Brownian motion on the rheological properties of a suspension of non-spherical particles," *Journal of Fluid Mechanics* **52**, 683–712 (1972).
- 15P. J. Gierszewski and C. E. Chaffey, "Rotation of an isolated triaxial ellipsoid suspended in slow viscous flow," *Can.J. Phys.* **56**, 6–11 (1978).
- 16C. J. Petrie, "The rheology of fibre suspensions," *Journal of Non-Newtonian Fluid Mechanics* **87**, 369 – 402 (1999).
- 17S. Parsa, E. Calzavarini, F. Toschi, and G. A. Voth, "Rotation rate of rods in turbulent fluid flow," *Phys. Rev. Lett.* **109**, 134501 (2012).
- 18A. Pumir and M. Wilkinson, "Orientation statistics of small particles in turbulence," *NJP* **13**, 093030 (2011).
- 19K. Gustavsson, J. Einarsson, and B. Mehlig, "Tumbling of small axisymmetric particles in random and turbulent flows," *Phys. Rev. Lett.* **112**, 014501 (2014).
- 20R. Ni, N. T. Ouelette, and G. A. Voth, "Alignment of vorticity and rods with Lagrangian fluid stretching in turbulence," *J. Fluid Mech.* **743**, R3 (2014).
- 21L. Chevillard and C. Meneveau, "Orientation dynamics of small, triaxial-ellipsoidal particles in isotropic turbulence," *J. Fluid Mech.* **737**, 571 (2013).
- 22M. Byron, J. Einarsson, K. Gustavsson, G. Voth, B. Mehlig, and E. Variano, "Shape-dependence of particle rotation in isotropic turbulence," *Phys. Fluids* **27**, 035101 (2015).
- 23M. Wilkinson, V. Bezuglyy, and B. Mehlig, "Fingerprints of random flows," *Phys. Fluids* **21**, 043304 (2009).
- 24V. Bezuglyy, B. Mehlig, and M. Wilkinson, "Poincaré indices of rheoscopic visualisations," *Europhys. Lett.* **89**, 34003 (2010).
- 25M. Wilkinson, V. Bezuglyy, and B. Mehlig, "Emergent order in rheoscopic swirls," *J. Fluid Mech.* **667**, 158 (2011).
- 26C. Marchioli, M. Fantoni, and A. Soldati, "Orientation, distribution, and deposition of elongated, inertial fibers in turbulent channel flow," *Phys. Fluids* **22**, 033301 (2010).
- 27J. Einarsson, A. Johansson, S. K. Mahato, Y. N. Mishra, J. Angilella, D. Hanstorp, and B. Mehlig, "Periodic and aperiodic tumbling of microrods advected in a microchannel flow," *Acta Mechanica* **224**, 2281–2289 (2013).
- 28N. R. Challabotla, L. Zhao, and H. Andersson, "Orientation and rotation of inertial disk particles in wall turbulence," *J. Fluid Mech.* **766**, R2 (2015).
- 29F. Eirich, H. Margaretha, and M. Bunzl, "Untersuchungen über die Viskosität von Suspensionen und Lösungen," *Kolloid-Zeitschrift* **75**, 20–37 (1936).
- 30R. C. Binder, "The motion of cylindrical particles in viscous flow," *Journal of Applied Physics* **10**, 711–713 (1939).
- 31J. Trevelyan and S. G. Mason, "Particle motion in a sheared suspensions. I. Rotations," *J. Colloid. Sci.* **6**, 354–367 (1951).



- 32S. G. Mason and R. S. J. Manley, "Particle motions in sheared suspensions: Orientations and interactions of rigid rods," Proceedings of the Royal Society of London. Series A, Mathematical and Physical Sciences **238**, 117–131 (1956).
- 33W. Bartok and S. G. Mason, "Particle motion in sheared suspensions," J. Colloid Sci. **12**, 243–262 (1957).
- 34H. L. Goldsmith and S. G. Mason, "Particle motions in sheared suspensions. XIII. The spin and rotation of disks," J. Fluid Mech. **12**, 8896 – 476 (1961).
- 35H. L. Goldsmith and S. G. Mason, "The flow of suspensions through tubes. I. Single spheres, rods, and discs," J. Colloid Sci. **17**, 448 – 476 (1962).
- 36E. Anczurowski and S. G. Mason, "Particle motions in sheared suspensions. XXIV. Rotation of rigid spheroids and cylinders," Transaction of The Society of Rheology **12**, 209–215 (1968).
- 37J. B. Harris, M. Nawaz, and J. F. T. Pittman, "Low-Reynolds-number motion of particles with two or three perpendicular planes of symmetry," Journal of Fluid Mechanics **95**, 415–429 (1979).
- 38C. A. Stover and C. Cohen, "The motion of rodlike particles in the pressure-driven flow between two flat plates," Rheol Acta **29**, 192–203 (1990).
- 39T. Kaya and H. Koser, "Characterization of hydrodynamics surface interactions of escherichia coli cell bodies in shear flow," Phys. Rev. Lett. **103**, 138103 (2009).
- 40R. Alargova, K. Bhatt, V. Paunov, and O. Velev, "Scalable synthesis of a new class of polymer microrods by a liquid? @ sliquid dispersion technique," Advanced Materials **16**, 1653–1657 (2004).
- 41E. P. Lewandowski, J. A. Bernate, P. C. Searson, and K. J. Stebe, "Rotation and alignment of anisotropic particles on nonplanar interfaces," Langmuir **24**, 9302–9307 (2008).
- 42J. Einarsson, (2013), Licentiate thesis, Department of Physics, University of Gothenburg.
- 43S. H. Strogatz, *Nonlinear dynamics and Chaos* (Westview Press, 1994).
- 44H. Goldstein, *Classical Mechanics* (Addison-Wesley, Reading, Massachusetts, 1980).
- 45A. Politi, G. L. Oppo, and R. Badii, "Coexistence of conservative and dissipative behaviour in reversible dynamical systems," Phys. Rev. A **33**, 4055 (1986).
- 46A. J. Lichtenberg and M. A. Lieberman, *Regular and stochastic motion* (Springer, New York, 1983).



Supplementaray online material

Tumbling of asymmetric microrods in a microchannel flow

J. Einarsson,^{1, a)} B. M. Mihiretie,^{1, a)} A. Laas,¹ S. Ankardal,¹ J. R. Angilella,² D. Hanstorp,¹ and B. Mehlig¹

¹⁾*Department of Physics, University of Gothenburg, 41296 Gothenburg, Sweden.*

²⁾*LUSAC, Université de Caen, Cherbourg, France.*

(Dated: 27 July 2015)

^{a)}These authors contributed equally to this work.



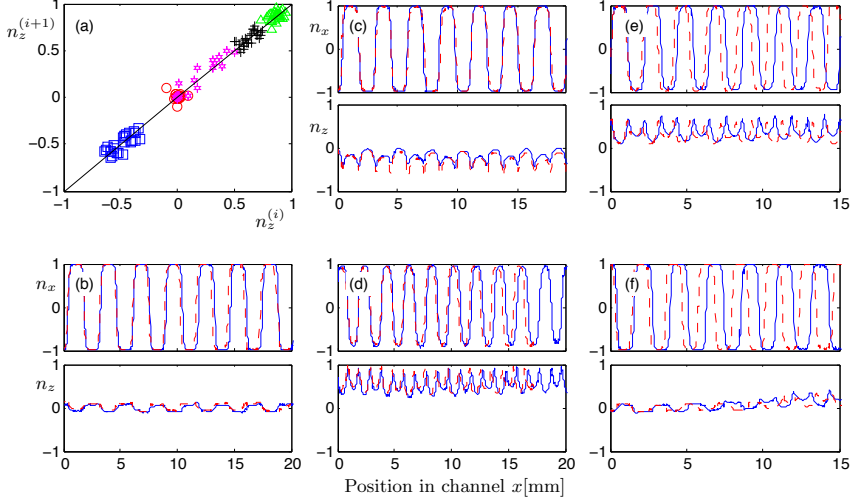


FIG. S1. Orientational dynamics of particle 4. (a) Dynamics of n_z . Here $n_z(i)$ denote the values of n_z at subsequent zero crossings of n_x , $i = 1, 2, 3, \dots$. The data are taken from panels (b-f). Red \circ data from panel (b); blue \square data from (c); green \triangle data from (d); black + data from (e); magenta \star data from (f). Panels (b-f) show orientational dynamics as a function of c.o.m.-position x in the channel, Eq. (1) in the main text. Data in different panels correspond to different initial orientations. Solid blue and dashed red lines represent forward and backward trajectories, respectively. The flow direction is reversed at $x = 0$.

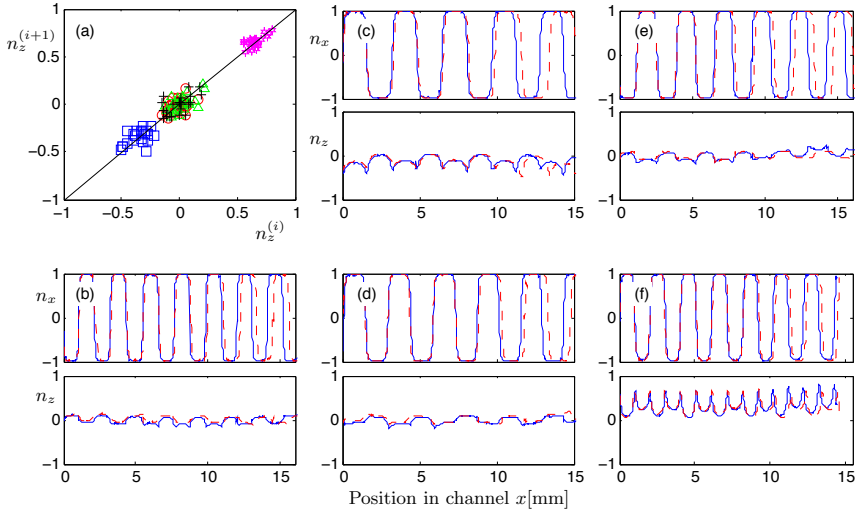


FIG. S2. Orientational dynamics of particle 5.



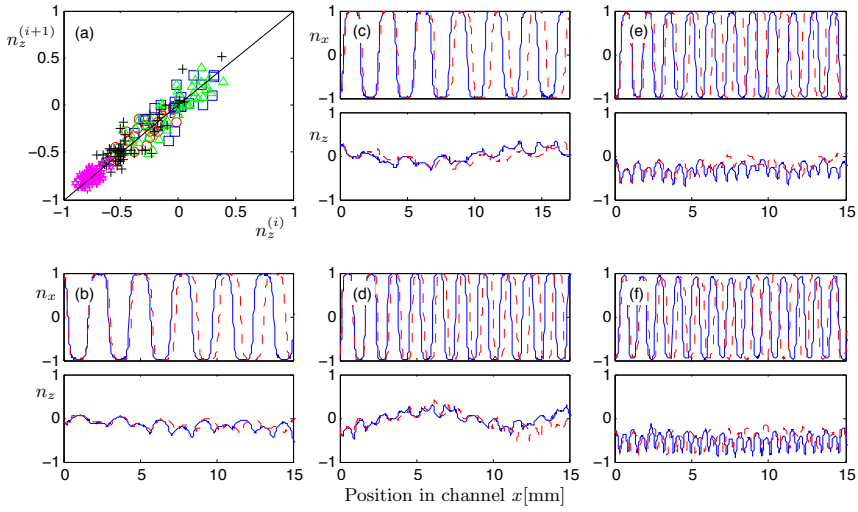


FIG. S3. Orientational dynamics of particle 6.

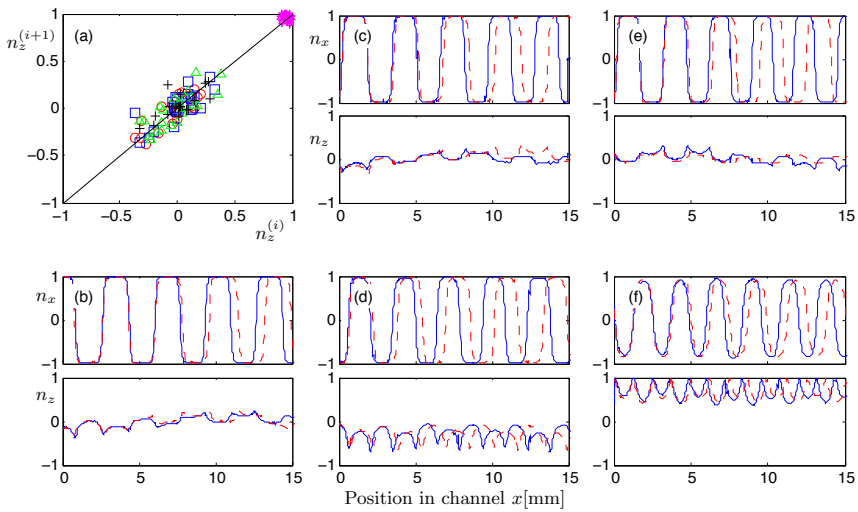


FIG. S4. Orientational dynamics of particle 7.



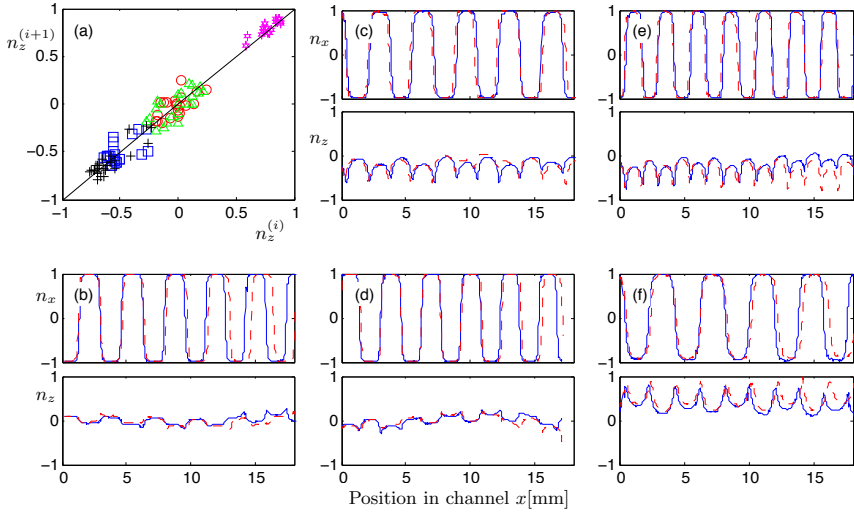


FIG. S5. Orientational dynamics of particle 8.

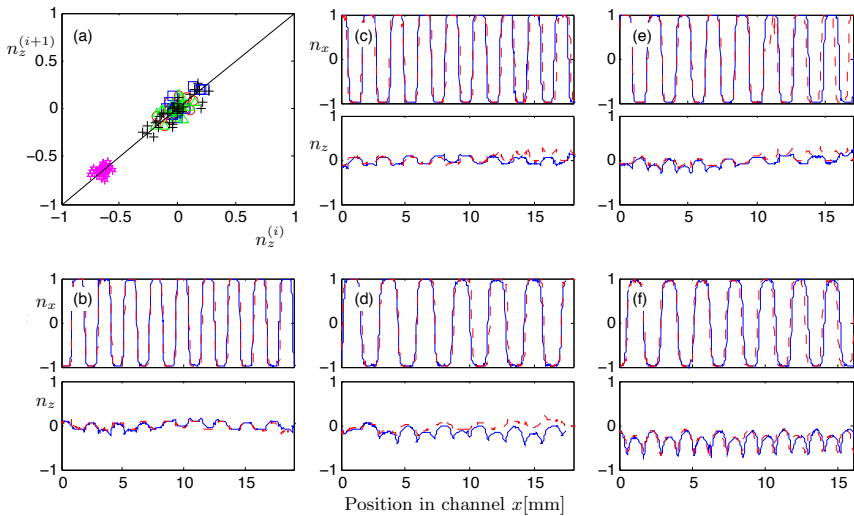


FIG. S6. Orientational dynamics of particle 9.



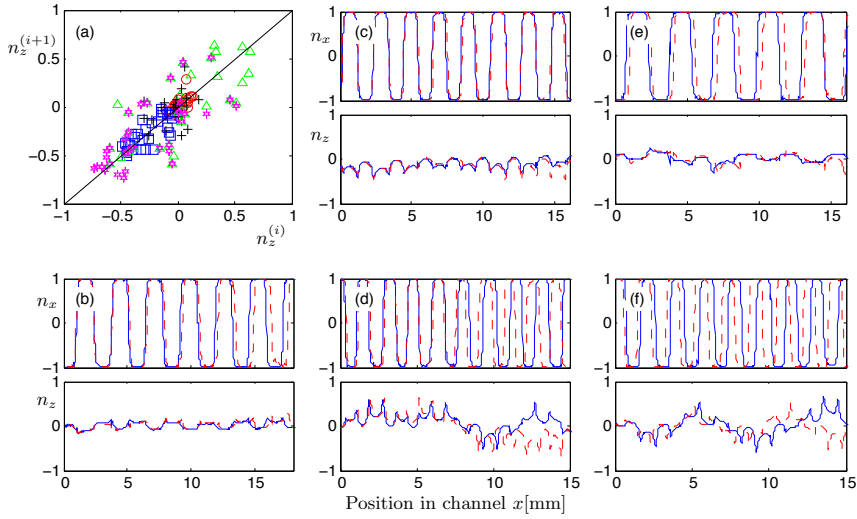


FIG. S7. Orientational dynamics of particle 10.

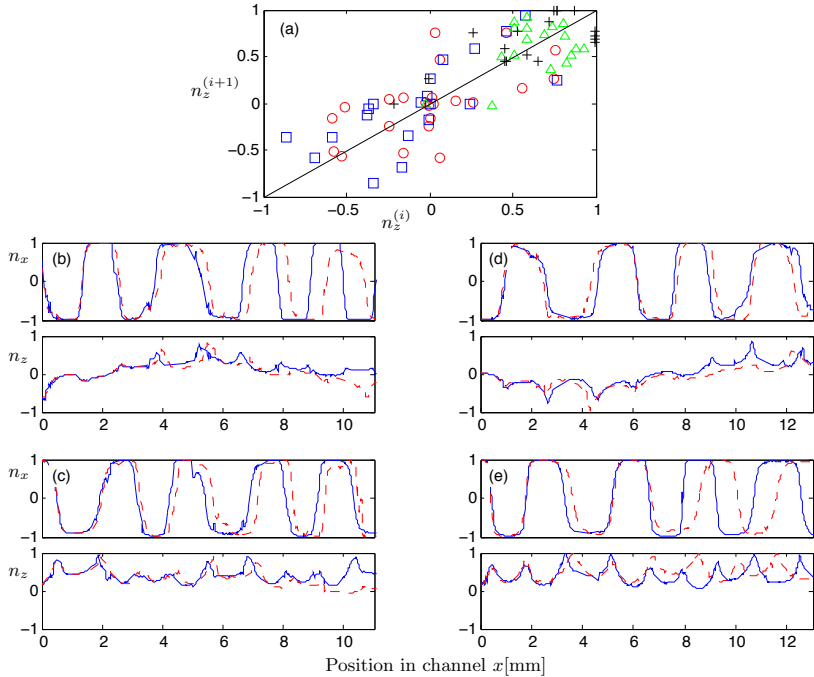


FIG. S8. Orientational dynamics of particle 11.



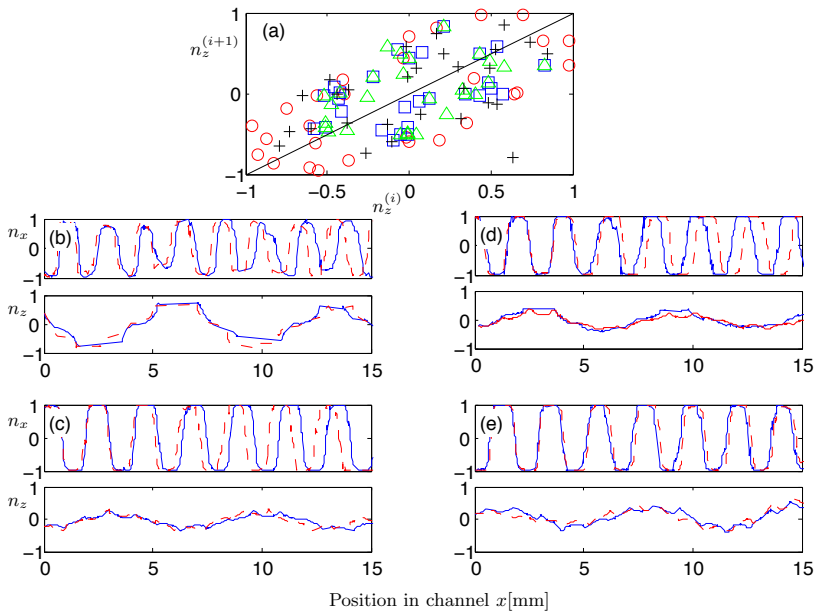


FIG. S9. Orientational dynamics of particle 12.





Paper F

arXiv preprint available at <http://arxiv.org/abs/1412.3166>





Shape-dependence of particle rotation in isotropic turbulence

M. Byron,^{1,2} J. Einarsson,^{3,2} K. Gustavsson,^{3,2} G. Voth,^{4,2} B. Mehlig,^{3,2} and E. Variano^{1,2}

¹*Civil and Environmental Engineering, University of California, Berkeley, California 94720, USA*

²*NORDITA, Roslagstullsbacken 23, 11421 Stockholm, Sweden*

³*Department of Physics, Gothenburg University, 41296 Gothenburg, Sweden*

⁴*Department of Physics, Wesleyan University, Middletown, Connecticut 06459, USA*

(Received 10 December 2014; accepted 11 February 2015; published online 2 March 2015)

We consider the rotation of neutrally buoyant axisymmetric particles suspended in isotropic turbulence. Using laboratory experiments as well as numerical and analytical calculations, we explore how particle rotation depends upon particle shape. We find that shape strongly affects orientational trajectories, but that it has negligible effect on the variance of the particle angular velocity. Previous work has shown that shape significantly affects the variance of the tumbling rate of axisymmetric particles. It follows that shape affects the spinning rate in a way that is, on average, complementary to the shape-dependence of the tumbling rate. We confirm this relationship using direct numerical simulations, showing how tumbling rate and spinning rate variances show complementary trends for rod-shaped and disk-shaped particles. We also consider a random but non-turbulent flow. This allows us to explore which of the features observed for rotation in turbulent flow are due to the effects of particle alignment in vortex tubes. © 2015 AIP Publishing LLC. [<http://dx.doi.org/10.1063/1.4913501>]

I. INTRODUCTION

Non-spherical particles moving in turbulent flows are of fundamental importance for many different scientific problems. Examples are rain initiation by ice crystals in turbulent clouds,¹ fiber suspensions,² grain dynamics in accretion disks,³ and pattern formation on the surface of turbulent and complex flows.^{4–6} Our work is motivated by the problem of describing plankton dynamics in aquatic ecosystems. The dynamics of plankton in turbulent flows are of interest because plankton occupy the lowest marine trophic level and also significantly affect the contribution of the ocean to the global carbon budget.^{7,8} These vital ecological functions are inextricably tied to the mechanical interactions between individual plankters and the complex flow environment they occupy. Rotation of planktonic organisms is critical for chemotaxis,^{9,10} and plays an important role in diffusive nutrient uptake.¹¹ The physical and biological effects of rotation continue to be a subject of inquiry, along with other kinematic factors that have clearly been shown to influence feeding, reproduction, and predator-avoidance.^{12–14}

Rotating axisymmetric particles may tumble, or spin, or both. The term tumbling denotes the orientational dynamics of the symmetry axis of the particle, while the term spinning denotes the rotation of the particle around its own symmetry axis. Tumbling of non-spherical particles has received attention recently,^{15–18} but spinning is an equally important part of rotation. For example, inertial particles do not simply sample fluid vorticity and strain, but rather extract angular momentum, transport it, and “return” it to the fluid phase. How this occurs likely depends upon how the total angular velocity of the particle is distributed between tumbling and spinning.

The rotations of small particles suspended in linear shear flows have been studied extensively, both theoretically^{19–23} and experimentally.²⁴ In this context, spinning is referred to as “log rolling.” Here, we consider particles suspended in turbulent flows and evaluate the effects of turbulence upon rotation, tumbling, and spinning.



We consider simple shapes (spheroids and cylinders) with uniform distribution of mass, and particle sizes within either the dissipative or inertial subrange of turbulence. These ranges correspond roughly to the lower and upper bounds of body size of planktonic organisms. Two representative groups of plankton, spanning this range of length scales, are diatoms (class Bacillariophyceae, 20–200 μm) and comb jellies (phylum Ctenophora, 1–15 cm). Most diatoms move only by drifting, and are usually smaller than the Kolmogorov length scale of oceanic turbulence.¹² Comb jellies locomote by a combination of active swimming and passive drifting, and their sizes typically lie within the inertial subrange of turbulence.⁵¹ Some diatoms can alter their nutrient uptake, settling velocity, or collision frequency by forming colonies with a variety of shapes. In comb jellies, different body plans are correlated with different propulsion and predation modes, and we hypothesize that shape is very important for drifting-mode locomotion as well. A beautiful diversity of shapes has been observed for diatoms, diatom colonies, and comb jellies, extending from oblate to prolate forms. Fore-aft symmetry is especially common in diatoms, and frequently found in comb jellies if we consider them in silhouette, i.e., neglecting the placement of feeding appendages. Axisymmetry is also common among diatoms and many orders of comb jellies. Herein, we focus on the basic question of passive shape-rotation interactions, upon which studies of active locomotion can build.

In this paper, we investigate the effect of shape upon the rotation of particles in turbulence, their tumbling, and their spinning. We report results of direct numerical simulations (DNS) of particles rotating in turbulent flows, statistical-model calculations, and experiments. These results enable us to characterize how the orientational dynamics of rods and disks are qualitatively very different (Sec. IV A). But we also show that, despite these significant differences, the variance of angular velocity is almost shape-independent (Sec. IV B). We show that these results are due to the inherent nature of the turbulence, by comparing the DNS results to those obtained in a random-flow model with finite correlation length and time (Sec. V). Finally, we discuss laboratory results quantifying the rotation rate of large particles in turbulence (particles whose sizes fall in the inertial range of turbulence). These results show that the angular-velocity variance of large particles at relatively low aspect ratio is shape-independent too, thus extending our results concerning the dissipative range (Sec. VI).

Before describing these results in detail, we introduce the notation and briefly mention previous work in Sec. II. Methods are discussed in Sec. III.

II. BACKGROUND

We consider cylinders and spheroids. Both shapes are characterized by an axis of symmetry (length $2c$) and two other axes of equal lengths $2a = 2b$. The aspect ratio is defined as $\alpha = c/a$. The particle orientation is defined by the unit vector \mathbf{n} that points along the axis of symmetry of the particle. The vector \mathbf{n} evolves according to

$$\dot{\mathbf{n}} = \boldsymbol{\omega} \wedge \mathbf{n}, \quad (1)$$

where $\boldsymbol{\omega}$ is the angular velocity of the particle and the dot denotes a time derivative.

The particle angular velocity $\boldsymbol{\omega}$ can be decomposed into components parallel and orthogonal to \mathbf{n} . The magnitude of the parallel component, $|\mathbf{n} \cdot \boldsymbol{\omega}|$, describes the rate at which the particle spins around its symmetry axis, the “spinning rate.” The magnitude of the orthogonal component, $|\dot{\mathbf{n}}|$, is called the “tumbling rate.” It is the combined rotation rate about the equatorial particle axes.

We consider the case of isotropic turbulence in the absence of external body forces. Thus, the steady-state statistics of the angular velocity vector $\boldsymbol{\omega}$ is isotropic. In particular, $\langle \boldsymbol{\omega} \rangle = 0$. The variance of $\boldsymbol{\omega}$ is thus simply $\langle |\boldsymbol{\omega}|^2 \rangle \equiv \langle \boldsymbol{\omega} \cdot \boldsymbol{\omega} \rangle$. Furthermore, since we consider particles with fore-aft symmetry, the averages of \mathbf{n} , $\boldsymbol{\omega} \cdot \mathbf{n}$, and $\boldsymbol{\omega} \wedge \mathbf{n}$ must also vanish because $-\mathbf{n}$ represents the same physical configuration as \mathbf{n} . Thus, the variances of the tumbling and spinning rates are simply $\langle |\dot{\mathbf{n}}|^2 \rangle$ and $\langle (\mathbf{n} \cdot \boldsymbol{\omega})^2 \rangle$.

From the above definitions, it follows that the squared rotation, tumbling and spinning rates obey a kinematic relationship: the total rotation rate squared is the sum of the squared tumbling and spinning rates, i.e.,



$$|\boldsymbol{\omega}|^2 = |\dot{\boldsymbol{n}}|^2 + |\boldsymbol{n} \cdot \boldsymbol{\omega}|^2. \quad (2)$$

It follows by averaging Eq. (2) that the same relationship holds for the variances.

The dynamics of \boldsymbol{n} have been studied by a number of authors. It has been shown that this orientation vector preferentially aligns with the strain and vorticity directions of the flow, depending on particle shape.^{16–18,25,26} The tumbling rate is readily observed in experiments,^{16,24} and its probability distribution and dependence on particle shape are known.^{16–18,26} Less is known about the spinning rate and the total angular velocity of axisymmetric particles suspended in turbulent flows. Our goals here are to qualitatively describe the dynamics and compare the distributions of these different rotation variables over a range of particle aspect ratios.

III. METHODS

A. Direct numerical simulations

DNS of the motion of anisotropic particles can be conveniently performed using velocity gradients recorded along tracer particle trajectories as long as the fluid-particle density ratio is sufficiently close to unity. We conduct one-way coupled simulations for the special case of infinitesimally small neutrally buoyant particles; in this case, the particle center-of-mass is simply advected, and $\dot{\boldsymbol{n}}$ is described by Eq. (1) using Jeffery's approximation¹⁹ for the angular velocity:

$$\dot{\boldsymbol{x}} = \boldsymbol{u}(\boldsymbol{x}_t, t), \quad (3)$$

$$\boldsymbol{\omega} = \boldsymbol{\Omega}(\boldsymbol{x}_t, t) + \Lambda \boldsymbol{n} \wedge \mathbb{S}(\boldsymbol{x}_t, t) \boldsymbol{n}. \quad (4)$$

Here, $\boldsymbol{u}(\boldsymbol{x}_t, t)$ is the fluid velocity at the particle position at time t . The vector $\boldsymbol{\Omega}$ equals half the vorticity and $\mathbb{S} = (\mathbb{A} + \mathbb{A}^T)/2$ is the strain-rate matrix, the symmetric part of the fluid–velocity–gradient matrix \mathbb{A} with elements $A_{ij} = \partial u_i / \partial x_j$. The antisymmetric part of \mathbb{A} is denoted by \mathbb{O} , and $\mathbb{O}\boldsymbol{n} = \boldsymbol{\Omega} \wedge \boldsymbol{n}$. The parameter $\Lambda = (a^2 - 1)/(a^2 + 1)$ characterizes the shape of the particle: $\Lambda = 0$ for spheres, $\Lambda = 1$ for infinitely thin rods, and $\Lambda = -1$ for infinitely thin disks. Most numerical studies that use this approach focus on rod-like particles,^{25,26} but some studies also consider oblate spheroids.^{16–18,52} Equation (4) shows that spherical particles ($\Lambda = 0$) respond only to the vorticity of the fluid, while non-spherical particles are affected by the fluid strain as well.

The results shown below were obtained using time-series for \boldsymbol{u} and \mathbb{A} downloaded from the Johns Hopkins University turbulence database.^{27,28} The database contains a DNS of forced, isotropic turbulence on a $1024 \times 1024 \times 1024$ grid at a Taylor–microscale Reynolds number of $Re_\lambda = 433$. The particles are initialized at randomly chosen positions \boldsymbol{x} and orientations \boldsymbol{n} . Given $\boldsymbol{u}(\boldsymbol{x}_t, t)$ and $\mathbb{A}(\boldsymbol{x}_t, t)$, particle position and orientation are updated according to Eqs. (1), (3), and (4) for approximately 45 Kolmogorov times τ_K . We disregard the initial transient by discarding data corresponding to the first 10 τ_K for each trajectory. Distributions of the particle angular velocity and its spinning and tumbling rates are computed from the remaining data. The DNS show that the variances of rotation, spinning, and tumbling rates rapidly approach their steady-state values, in most cases within 10 τ_K (not shown). But the results summarized in Appendix A show that differences in the rotation between prolate and oblate particles may take longer to develop for near-spherical particles.

B. Statistical-model calculations

It is instructive to compare the DNS results for particle rotation in turbulent flows with those obtained for particles rotating in an isotropic homogeneous Gaussian random velocity field with appropriate correlation length and correlation time. This comparison shows which aspects of particle spinning and tumbling are influenced by the nature of turbulence, and which aspects can be explained by a simple statistical model. An important difference between turbulence and a random Gaussian velocity field is that turbulence breaks time-reversal invariance, such that the fluid–velocity gradient matrix \mathbb{A} and its transpose \mathbb{A}^T appear with different probabilities.²⁹ In the statistical model, by contrast, \mathbb{A} and \mathbb{A}^T appear with equal probabilities. This is important for our question because the orientational dynamics of rods and disks are determined by $\mathbb{A} = \mathbb{S} + \mathbb{O}$ and $-\mathbb{A}^T = -\mathbb{S} + \mathbb{O}$, respectively.



This follows from two observations. First, the orientational equations of motion (1), (4) can be recast as $\dot{\mathbf{n}} = (\mathbb{O} + \Lambda \mathbb{S})\mathbf{n} - \Lambda(\mathbf{n} \cdot \mathbb{S}\mathbf{n})\mathbf{n}$. Second, the non-linear term on the right-hand side of this equation determines only the normalization of \mathbf{n} but not its orientation (see Appendix A).

Further differences between turbulence and random flow arise from the fact that turbulent flows exhibit much more violent vorticity fluctuations than random flows exhibit. This is important for our question because long-lived vortex structures³⁰ cause the particles to align, affecting the relation between spinning and tumbling rates.^{16–18,25,26}

Our statistical model has two dimensionless parameters, the shape factor Λ and a second parameter that is formed out of the correlation length η of the fluid velocity, its correlation time τ , and its typical speed u_0 . This parameter is referred to as the Kubo number $\text{Ku} = u_0\tau/\eta$. It is a dimensionless measure of the correlation time of the fluid velocity field. The incompressible random velocity field is represented as follows.³¹ We write $\mathbf{u} = \nabla \wedge \mathbf{A}$, where $\mathbf{A}(x, t)$ is a Gaussian random vector potential with zero mean, Gaussian spatial correlation function with correlation length η , and exponential time correlations $\langle A_i(x, t)A_j(x, 0) \rangle = \delta_{ij} \exp(-t/\tau)/6$. This stochastic model is difficult to solve in closed form because the orientational dynamics are determined by the Lagrangian correlations of the fluid-velocity gradients. The tumbling rate can be computed approximately by perturbation theory.^{18,31} This gives rise to an expansion in the Kubo number. Up to the sixth order in Ku, the tumbling rate is given by:¹⁸

$$\begin{aligned} \langle |\dot{\mathbf{n}}|^2 \rangle \tau^2 &= \text{Ku}^2(5 + 3\Lambda^2)/6 + \text{Ku}^4\Lambda^2(5 + 3\Lambda^2)/4 \\ &+ \text{Ku}^6\Lambda^2(-25 + 4668\Lambda + 45\Lambda^2 + 7236\Lambda^3 + 2484\Lambda^4)/864. \end{aligned} \quad (5)$$

The lowest-order term was obtained earlier.¹⁶ In a similar way, the variance of the particle angular velocity can be computed. We find:

$$\langle |\boldsymbol{\omega}|^2 \rangle \tau^2 = \langle (\mathbf{n} \cdot \boldsymbol{\Omega})^2 \rangle \tau^2/4 = 5\text{Ku}^2/12 + 25\text{Ku}^6\Lambda(1 + 3\Lambda)/864. \quad (6)$$

and

$$\langle (\mathbf{n} \cdot \boldsymbol{\omega})^2 \rangle \tau^2 = \langle (\mathbf{n} \cdot \boldsymbol{\Omega})^2 \rangle \tau^2/4 = 5\text{Ku}^2/12 + 25\text{Ku}^6\Lambda(1 + 3\Lambda)/864. \quad (7)$$

The terms in these perturbation expansions contain only even powers of Ku. The perturbation series (5) to (7) are asymptotically divergent, i.e., they diverge for any fixed value of Ku but every partial sum of the series approaches the correct result as $\text{Ku} \rightarrow 0$. To obtain accurate results at larger Kubo numbers requires resummation of the series. We have obtained the series expansions to order eight, making it possible to resum the series using Padé-Borel resummation.³²

C. Laboratory measurements

The methods described above assume that particles are infinitesimally small, so that their rotation is always determined by the local fluid-velocity gradients. The rotation of larger particles is influenced by their interactions with the non-linear fluid-velocity field. Furthermore, the inertia of finite-size particles feeds back to the fluid phase. For an axisymmetric particle in simple shear flow, particle and fluid inertia make substantial contributions to the orientational motion.^{20–22} But it is an open question as to what extent weakly-inertial particles in turbulence behave similarly to inertia-less ones. The effect of particle inertia upon the orientational dynamics of particles in turbulence has been calculated numerically³³ and for random flows analytically,¹⁸ neglecting the effect of fluid inertia. Two-way-coupled simulations that take into account fluid and particle inertia have been conducted for infinitesimally small particles,^{34,35} but computing the effects of inertia becomes even more difficult for finite-sized particles. Here we present, therefore, experimentally measured rotation rates of large particles in turbulence, with sizes in the inertial sub-range of ambient turbulence.

Homogeneous isotropic turbulence is created in a 3 m^3 water tank using two facing arrays of randomly firing jets.^{36,37} Turbulence in the test section has $\text{Re}_\lambda = 310$, turbulent kinetic energy $6.5 \text{ cm}^2 \text{ s}^{-2}$, integral length scale 8 cm , Kolmogorov length scale $\eta_K = 0.5 \text{ mm}$, and Kolmogorov time scale $\tau_K = 0.13 \text{ s}$. These scales were computed from Eulerian two-point velocity statistics computed with particle image velocimetry (PIV), specifically the autocovariance and second-order structure functions.³⁷



TABLE I. Dimensions of hydrogel cylinders; volume V varies no more than 20% around a mean of 0.415 cm^3 . Surface area SA varies no more than 30% around a mean of 1.72 cm^2 . Errors marked are standard error.

| Height $2c$ (mm) | Diameter $2a = 2b$ (mm) | α (=H/D) | V (cm^3) | SA (cm^2) | Λ |
|---------------------|-------------------------|-----------------|-----------------------|------------------------|-----------|
| 4.77 ± 0.11 | 10.60 ± 0.13 | 0.45 | 0.421 | 2.27 | -0.66 |
| 8.24 ± 0.18 | 8.72 ± 0.06 | 0.95 | 0.492 | 1.91 | -0.05 |
| 12.99 ± 0.14 | 6.41 ± 0.11 | 2.03 | 0.420 | 1.48 | 0.61 |
| 18.91 ± 0.06 | 4.70 ± 0.04 | 4.03 | 0.328 | 1.24 | 0.88 |

Particles are added to the turbulent flow at a volume fraction of 0.1%, for which particle–particle collisions are negligible.³⁸ Four types of particles are measured, with dimensions given in Table I. Particles are 1% denser than the ambient fluid, but stay in suspension due to the strength of the ambient turbulence. Their quiescent–flow settling velocity normalized by the turbulent velocity scale is between 0.46 and 0.72, depending on the particle type.

The particle Reynolds number in turbulent flow has several possible definitions;³⁹ here, we use the instantaneous slip velocity vector, computed by subtracting the particle center-of-mass velocity from the fluid velocity averaged over a 2D annulus surrounding the particle, exclusive of the immediate particle boundary layer. The RMS magnitude of this slip velocity is close to 1 cm/s, across all particle types and regardless of the parameters used to define the outer bound of the fluid-averaging annulus. From this, we compute a turbulent particle Reynolds number between 50 and 200, depending on the length scale that is used (a similar range is found when computing the Reynolds number based on the quiescent settling velocity). In the slip velocity, there is a small bias towards gravitational settling, with a mean value close to 2 mm/s for all particles. None of our measurements suggest that the particles are governed by Stokesian dynamics, but we can still compute a Stokesian response time as a point of reference. Using the radius of a sphere with equivalent volume to the cylinders (4.6 mm), the Stokesian time scale is 4.8 s. Computing the inertial-range time scale corresponding to a length of 4.6 mm gives a characteristic time scale $\tau_c = 0.57$ s. Comparing these two time scales suggests that particles respond slowly compared to turbulent fluctuations at their length scale.

Particles are fabricated from hydrogel, in this case 0.4% agarose by volume.⁴⁰ Because hydrogel is clear and refractive-index-matched to water, we can use PIV to track the motion of tracers (hollow glass spheres) embedded within the particles. These tracers reveal the particle's rigid-body motion. Applying stereoscopic PIV to the embedded tracers gives 3D velocity vectors on a 2D grid covering a planar slice through a particle. From these data, we compute the particle angular velocity using the equation for solid-body rotation: $\mathbf{u}_m - \mathbf{u}_n = \boldsymbol{\omega} \wedge (\mathbf{x}_m - \mathbf{x}_n)$, where \mathbf{u}_m and \mathbf{u}_n are velocity vectors at points m and n inside the particle, whose locations are \mathbf{x}_m and \mathbf{x}_n . This equation is solved using more than two vectors, to take advantage of all the data present within a particle's internal vector field. Specifically, we use an optimization scheme based on vector triplets.⁴¹

Velocity vectors are calculated with multi-pass PIV based on cross-correlation of two-dimensional image subsets, followed by stereoscopic reconstruction of $\mathbf{u}(x)$ within the measurement plane. The computations (and the supporting calibrations) are performed using the DaVis 7 software package (LaVision Inc., Göttingen, Germany). Tracers are illuminated by a 1 mm-thick laser light sheet (Quantel/Big Sky Lasers, 532 nm) passing through the flow and the particles. Two cameras (Imager PRO-X, 1600×1200 pixels, both fitted with a 105 mm Nikkor lens and a Scheimpflug/tilt adapter) focus on a subset of the light sheet of dimensions of $74.4 \text{ mm} \times 35.4 \text{ mm}$. The cameras view the test section in a stereoscopic configuration through 35° water-filled prisms mounted on the side of the tank to minimize distortion through the air-glass-water transition.³⁶

IV. SMALL RODS AND DISKS IN TURBULENCE

In this section, we use DNS results for the orientational trajectories of individual axisymmetric particles to characterize the orientational dynamics of rods and disks in turbulence. This section is



divided into two parts. We first describe the orientational motion of individual particles (Sec. IV A) and then steady-state ensemble averages over many particle paths (Sec. IV B).

A. Orientational trajectories of individual particles

Fig. 1 illustrates how alignment and rotation rates change as a function of time, along a typical particle trajectory; the tracer particle passes through a region of intense vorticity starting at $t = 30 \tau_K$. A tracer disk ($\Lambda = -1$) and a tracer rod ($\Lambda = 1$) both follow the same center-of-mass trajectory, but their orientational dynamics are very different. The blue squares represent the disk, and the red circles represent the rod.

Fig. 1(a) shows that along this trajectory, the magnitude of the angular velocity of the rod is almost identical to $|\Omega|$, half the flow vorticity (green triangle). The angular velocity of the disk, by contrast, fluctuates strongly around the fluid angular velocity. The fluctuations occur on a time scale comparable to the Kolmogorov time. This qualitative difference between the orientational motion of rods and disks in regions of strong vorticity is explained by the preferential alignment of particles to the fluid-velocity gradients.

DNS show that rods (or material lines) and vorticity in turbulence tend to align with each other. This is usually attributed to the fact that the respective equations of motion are closely related.^{25,26,42} This behavior is illustrated by Fig. 1(b), which shows how particle alignment with fluid vorticity varies as a function of time. It follows from the alignment of rods with vorticity that the spinning rate of rods ($\mathbf{n} \cdot \boldsymbol{\omega}$)² is approximately equal to the fluid rotation rate $|\Omega|^2$. In addition, rods tumble, staying closely aligned with Ω .

The orientational dynamics of a disk ($\Lambda = -1$) are expected to be very different from those of a rod ($\Lambda = 1$) because \mathbf{n}_{disk} is driven by $-\mathbb{S} + \mathbb{O}$ while \mathbf{n}_{rod} is driven by $\mathbb{S} + \mathbb{O}$. Fig. 1(b) shows that the disk aligns so that its symmetry axis is in the plane orthogonal to that of the rod. This fact is a simple consequence of the form of the equations of motion (1), (4) and the observation that the Lyapunov exponent of incompressible turbulent flow is positive. This argument is explained in detail in Appendix A. It is consistent with the intuition that the symmetry vector of a disk lies in the plane

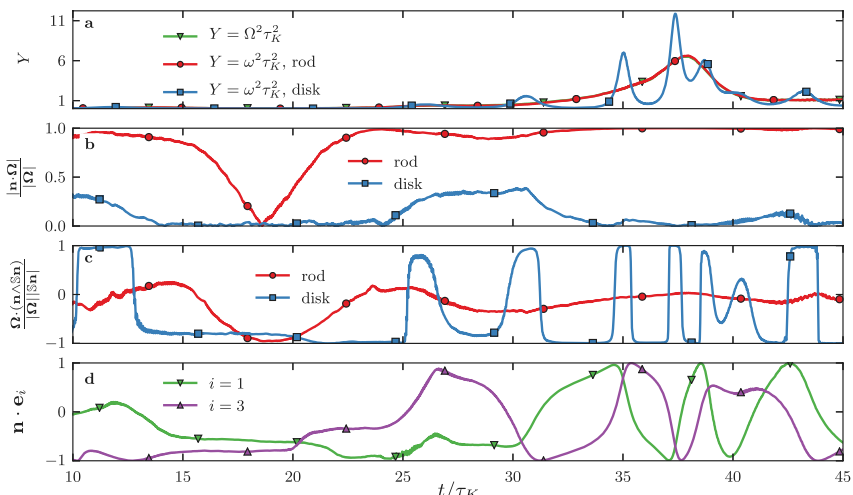


FIG. 1. DNS results for the instantaneous alignments and rotation rates for a disk and a rod as a function of time. (a) $|\Omega|^2$ (green triangles) and $|\omega|^2$ as a function of time for disks (blue squares) and rods (red circles). Note that the curves representing $|\Omega|^2$ (green triangles) and $|\omega|^2$ for rods (red circles) overlap strongly. (b) Alignment of n with Ω as a function of time for disks (blue squares) and rods (red circles), (c) alignment of $\mathbf{n} \wedge \mathbb{S}\mathbf{n}$ with Ω as a function of time for disks (blue squares) and rods (red circles), (d) alignment of \mathbf{n}_{disk} with \mathbf{e}_1 (green point-down triangles) and \mathbf{e}_3 (purple point-up triangles) as a function of time.



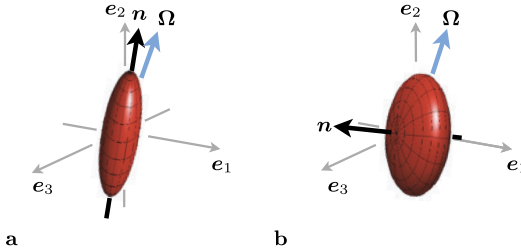


FIG. 2. Schematic of alignment between particle orientation \mathbf{n} , fluid angular velocity $\boldsymbol{\Omega}$, and eigenvectors \mathbf{e}_i of the fluid strain rate tensor \mathbb{S} in regions of high vorticity. Panel (a) illustrates rod behavior: \mathbf{n} aligns with \mathbf{e}_2 and $\boldsymbol{\Omega}$, leading to spinning. Panel (b) shows disk behavior: \mathbf{n} is orthogonal to $\boldsymbol{\Omega}$ and \mathbf{e}_2 , leading to tumbling.

orthogonal to that of a rod because a long axis of both particles is being aligned by the Lagrangian fluid stretching.⁴³

Fig. 2 shows the alignment of \mathbf{n}_{disk} , \mathbf{n}_{rod} and $\boldsymbol{\Omega}$ relative to the eigensystem of the strain rate tensor in regions of high vorticity. Because the vector \mathbf{n}_{disk} lies in the plane perpendicular to \mathbf{n}_{rod} , it follows that \mathbf{n}_{disk} tends to be found perpendicular to the vorticity direction. This behavior can be seen in Fig. 1(b) as mentioned above. This alignment leads to a vorticity-induced tumbling rate $\boldsymbol{\Omega} \wedge \mathbf{n}_{\text{disk}}$ and a correspondingly weak spinning rate. But for disks also the contribution from the strain, $\mathbf{n} \wedge \mathbb{S}\mathbf{n}$, is strong. It alternates between enhancing and opposing the rotation of \mathbf{n}_{disk} around the vorticity direction. This follows from the curious observation that material lines tend to instantaneously align with the second eigen-direction \mathbf{e}_2 of the strain-rate matrix \mathbb{S} (that is, with the smaller of the two positive eigenvalues) in regions of high vorticity.^{25,44} Since \mathbf{n}_{disk} tends to be perpendicular to \mathbf{n}_{rod} , we expect that \mathbf{n}_{disk} (and therefore also $\mathbb{S}\mathbf{n}_{\text{disk}}$) tends to lie in the plane spanned by \mathbf{e}_1 and \mathbf{e}_3 , the two strongest eigen-directions of \mathbb{S} . The resulting cross product is parallel to \mathbf{e}_2 and significant in magnitude. This alignment between $\boldsymbol{\Omega}$ and $\mathbf{n}_{\text{disk}} \wedge \mathbb{S}\mathbf{n}_{\text{disk}}$, shown in Fig. 1(c), is responsible for the fluctuations in total angular velocity of the disk.

Fig. 1(d) illustrates that the symmetry vector of a disk tumbles in the plane spanned by \mathbf{e}_1 and \mathbf{e}_3 in regions of strong vorticity. The two largest rotation events for the disks at $t = 35 \tau_K$ and $t = 37 \tau_K$ both coincide with events where \mathbf{n} becomes aligned with \mathbf{e}_1 and then rapidly rotates to become aligned with \mathbf{e}_3 . Comparing Figs. 1(a) and 1(d) shows that when the vorticity is weak, there is little or no instantaneous alignment of \mathbf{n} with the eigen-system of the strain-rate matrix²⁶ (see also Figs. 7(d) and 8(d) in Appendix A).

B. Ensemble averages

In the previous section, we showed that the angular velocities of disks and rods are very different, due to the differing alignments of their symmetry axes to the vorticity vector. Nevertheless, upon averaging over many trajectories we find that the average rotation rate $\langle |\omega|^2 \rangle$ is almost independent of shape. In Fig. 3, we show the average total rotation, spinning and tumbling rates as a function of aspect ratio α . The curves are obtained using the DNS results described above. Disks rotate on average just like spheres, while rods rotate slightly faster. However, the tumbling and spinning rates show strong dependence on shape. This indicates, from Eq. (2), that the tumbling rate and its complement, the spinning rate, must vary as a function of α in such a manner that their sum is nearly α -independent. In other words, rods spin more than they tumble, while disks tumble more than they spin. The spinning and tumbling direction are of course arbitrary for a sphere, as no principal axis can be defined; however, the mathematical construction of $\dot{\mathbf{n}}$ and $\mathbf{n} \cdot \boldsymbol{\omega}$ gives the ratio between tumbling and spinning to be two to one in this case.

The tumbling and spinning rates are especially divergent for disks, whose spinning rate is almost zero. The effect of shape on tumbling and spinning is strongest for small departures from $\alpha = 1$. Outside of the range $0.1 < \alpha < 10$, particle rotations saturate at constant values, remaining insensitive to further changes in aspect ratio.



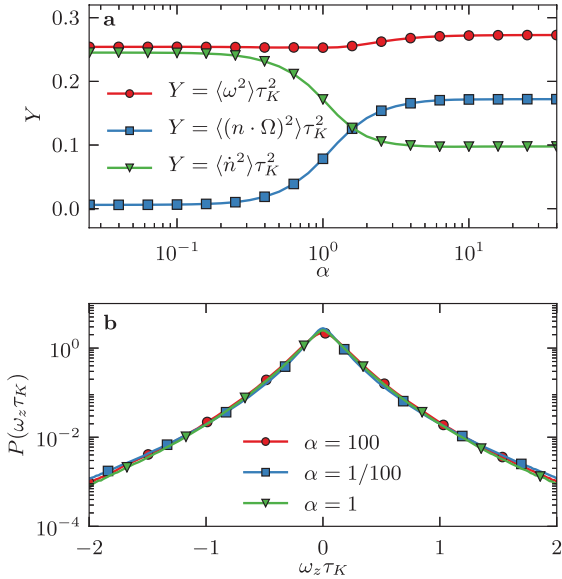


FIG. 3. (a) DNS results for the variances of the angular velocity (red circles), and the spinning (blue squares) and tumbling rates (green triangles) as a function of the particle aspect ratio α , computed for tracer spheroids in homogeneous isotropic turbulence. The data for the tumbling rate are similar to the data shown in Fig. 3 in Ref. 16 and Fig. 2 in Ref. 18. The rates are made dimensionless by rescaling with the Kolmogorov time. (b) Distribution of the z -component of the angular velocity from DNS, for different aspect ratios: rod, $\alpha = 100$ (red circles); disk, $\alpha = 1/100$ (blue square); spheres $\alpha = 1$ (green triangles). The rates are made dimensionless by rescaling with the Kolmogorov time.

Fig. 3 shows that the violent fluctuations of the rotation rate of disks around the fluid rotation rate (visible in Fig. 1(a)) average to zero, while the much smaller fluctuations of the rotation rate of rods average to a small positive contribution. The nature of these fluctuations depends crucially on the precise dynamics of rods, disks, and vorticity in relation to the local strain eigen-system.⁴² Revealing the combined dynamics of these vectors is an important goal in the study of Lagrangian turbulence and the dynamics of suspended particles. We believe that the study of disks may add to the picture of Lagrangian turbulence.

V. SMALL PARTICLES IN RANDOM FLOWS

We argue above that the observed rotation rates non-trivially arise from the specific properties of the turbulent velocity gradient tensor, as observed in a Lagrangian frame. In this section, we demonstrate this claim by analyzing the orientational dynamics in a random-flow model. The random flow we present has finite space- and time-correlations, corresponding to the Kolmogorov scales in turbulence. Solving the random flow model enables us to answer the question of which observations are *not* due to turbulence, but simply features of the equations of motion.³¹

Tumbling, spinning, and rotation variances for the statistical model are given in Eqs. (5) to (7). We have also computed the Ku^8 -contribution to these expressions (not shown). This allows us to resum the perturbation series using Padé-Borel resummation.³² The resulting rotation, spinning, and tumbling variances are shown in Fig. 4 as a function of particle shape. In comparison to the turbulence result (Fig. 3(a)), we find three notable differences. First, the average total rotation rate is shape-dependent: nearly spherical particles rotate less than non-spherical particles. Second, the shape-dependence is almost completely encoded in the tumbling rate, while the spinning rate is almost independent of particle shape. This means that preferential alignment exists but is weak in a random flow. This in turn is because vorticity and strain are not directly related, as is the case in turbulence, but only through



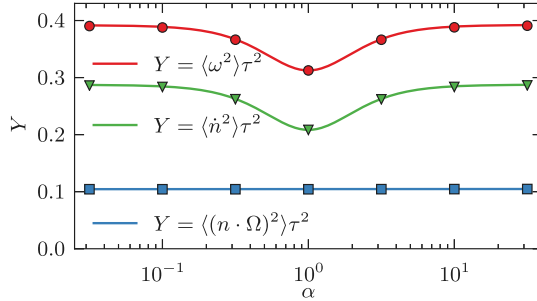


FIG. 4. Variances of the angular velocity (red circles), of the tumbling rate (green triangles), and of the spinning rate (blue squares) as a function of the particle aspect ratio α for the statistical model, computed by resumming the perturbation expansions (5) to (7), lines. Markers show results of numerical simulations of the statistical model. Parameter: $Ku = 0.5$.

preferential sampling along trajectories. Third, to a very good approximation rods and disks rotate, spin and tumble alike. This is a consequence of the fact that the statistical model is time-reversal invariant and does not allow for long-lived vortex structures.¹⁸ Finally, we note that the symmetry axes of co-located disks and rods do become perpendicular to each other also in the random flow (see Appendix A); however, neither of them significantly aligns with the vorticity direction.

VI. LARGE PARTICLES IN TURBULENCE

In the preceding sections, we considered tracer particles in turbulence and random flows. In this section, we address the question of larger particles by a laboratory experiment.

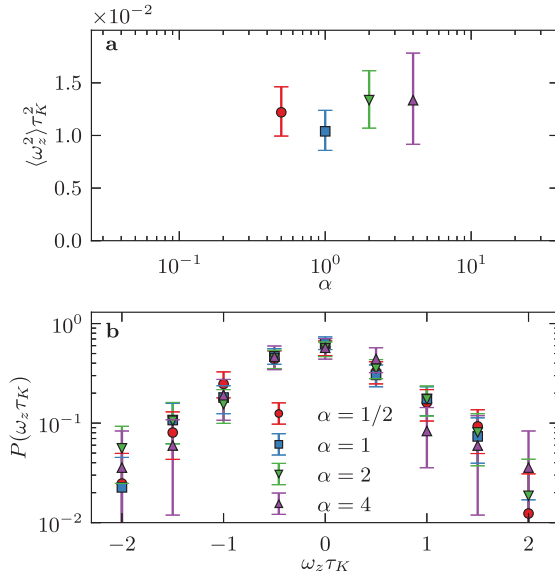


FIG. 5. (a) Variance of the z -component of the particle angular velocity (inverse seconds squared) as a function of the cylinder aspect ratio α , measured for large cylinders in laboratory turbulence. 95% confidence intervals are computed via bootstrap. (b) Distribution of z -component of the particle angular velocity for the four different cylinder aspect ratios given in Table 1; 150-400 samples are used in each of the four curves. Aspect ratio $\alpha = 1/2$ (red circles), 1 (blue squares), 2 (green point-up triangles), 4 (purple point-down triangles).



Compared to tracer particles, larger particles are affected by several additional mechanisms. First, they have particle inertia in both translational and orientational degrees of freedom. Second, the forces and torques upon larger particles include the effects of fluid inertia. Third, the finite-sized particles sample the non-linear velocity field on the scale of the particle size. All of these mechanisms potentially invalidate the arguments concerning preferential alignment, so we do not know, *a priori*, whether large particles will show shape-dependent rotation that resembles our observations for small particles.

Our results for the total rotation rate of large particles are shown in Fig. 5. Within experimental error, the shape-dependence of the average total rotation rate is consistent with our findings in Sec. IV. This remarkable fact remains to be explained. It is expected that the rotation-rate variance is smaller for large particles (because they average over fluid-velocity gradients). This is borne out by the experiment: it shows a variance that is approximately a factor of 6 smaller than the DNS variance (note that we plot ω_z^2 for the experiment and $|\omega|^2$ for the DNS, which differ by a factor of 3). Previous work⁴⁵ has successfully predicted the tumbling rate variance of high-aspect-ratio rods in the inertial subrange, showing that rod length controls the tumbling rate. However, extending this approach to low-aspect-ratio rods and disks is non-trivial. If rod rotation scaling were based on one lengthscale only, we would expect a significant difference in the angular velocity variance for the particles with $\alpha = 2$ and $\alpha = 4$, which here have $2c = 16\eta$ and $2c = 38\eta$, respectively. However, we observe no significant change in angular velocity variance. This suggests that dynamics of inertial, low-aspect-ratio rods are not accurately predicted by a single lengthscale.

VII. CONCLUSIONS

In this paper, we have analyzed the rotation of axisymmetric particles in turbulence by experiments, direct numerical simulations, and random-flow model calculations. We have found that disks rotate very differently from rods in regions of intense vorticity in turbulence. While the symmetry axis of a rod follows closely the second strain eigenvector e_2 and vorticity, the symmetry axis of the disk tumbles in the plane spanned by e_1 and e_3 , the strain eigenvectors corresponding to the largest extensional and largest compressional eigenvalues (illustrated in Fig. 2). Rods spin around their own symmetry axis at a rate of half the vorticity, while fluid vorticity and strain act to make disks tumble. In other words, because of their different alignment with respect to fluid vorticity, rods tend to spin more than they tumble, while disks tend to tumble more than they spin.

This has important implications for the instantaneous rotation dynamics in turbulence. The strain makes only a small contribution to the rotation of rods, while for disks it makes a large contribution: it tends to rotate the symmetry vector of disks around the vorticity vector, sometimes decelerating, sometimes accelerating the rotation. The orientational dynamics of disks lend interesting optical properties to flow visualization devices, such as Kalliroscopes; in regions of strong vorticity, disks exhibit rapid tumbling. This may affect the visual signal in these regions. In Refs. 4–6, it was suggested that tumbling affects the orientational patterns of rod-like particles floating on randomly stirred two-dimensional flows. It would be of interest to analyze the resulting singularities by light-reflection measurements.

Despite this qualitative difference, the variance of the total rotation rate is almost independent of shape. In fact, the rotation rate variance of a disk is neither more nor less than that of a sphere. This exact equivalence is unexpected. Also, prolate particles rotate with nearly the same angular velocity variance as disks and spheres. This is borne out by both DNS and experiments, for small and large particles, respectively.

We also demonstrated by a random-flow calculation that our observations in turbulence are not a feature of the equations of motion, but depend on the distinguishing statistical features of turbulence in a Lagrangian frame. In the random-flow model, the rotation rate variance depends on shape, and the preferential alignment between fluid vorticity and the symmetry axes of particles is very weak.

Several aspects of particle rotation in turbulence remain to be understood. An important open question concerns the alignment of disks, rods, and vorticity with the eigen-system $e_j(t)$ of the strain-rate matrix, $j = 1, 2, 3$. The time-delayed correlations $\langle \Omega(t) \cdot e_1(0) \rangle$ shed some light on the vorticity dynamics,⁴⁶ but is there a corresponding “pirouette effect” for disks? A second important question



is to understand the effect of finite particle sizes. Our results from DNS and the statistical model pertain to tracer particles. Finite-size corrections and the effects of particle and fluid inertia on the particle-rotation rate remain to be understood. A third question to consider is the implication of our results concerning the rotation and alignment of less symmetric particles such as ellipsoids with three distinct moments of inertia or non-ellipsoidal particles.

A motivation for this investigation is the effect of shape upon the dynamics of planktonic organisms. The relationships between the shape of a planktonic organism, its kinematics in flow, and its biological success are quite complex, but our results can contribute a few facts to this ongoing investigation. First, shape does not control how much angular velocity an organism inherits from the ambient turbulence on average, but it does control how this angular velocity is distributed about the organism's principal axes. This may impact swimming behavior according to the directionality of the propulsive system employed (directional, as in copepods, or omnidirectional, as in cydippid ctenophores). Second, it is tempting to label planktonic species as either "spinners" or "tumblers" based on their shape, but this nomenclature cannot be taken too literally; our results indicate that shape can only *emphasize* spinning or tumbling, it cannot select one exclusively. In other words, even the most extreme tumblers show a fair bit of spinning, and vice versa. Potential reasons for an organism to emphasize tumbling over spinning may include mass transfer, swimming, or gyrotaxis.^{47,48} Third, if an organism or colony were to emphasize spinning or tumbling by changing its shape, the greatest marginal return occurs when aspect ratio is near unity. Once an organism departs significantly (by a factor of 10) from this ratio, further shape changes have no effect on rotation. Spheroidal body plans with aspect ratios near unity ($1 < \alpha < 2$) are commonly observed in cydippid ctenophores, which places them in the range for which small changes in shape will greatly influence rotation. This is suggestive that shape may play a major role in their behavior and locomotion. Of course, continued cross-disciplinary study is needed to elucidate the full impact of body shape on plankton biology in complex flows. Here, we have described some of the passive physical mechanisms involved, and future work may build upon this foundation, investigating how and whether aquatic organisms take advantage of these mechanisms.

ACKNOWLEDGMENTS

We thank NORDITA in Stockholm for hospitality during the workshop Particles in Flows - Fundamentals and Applications where this manuscript was begun. This material is based upon work supported by the National Science Foundation under Grant Nos. DGE-1106400 (M.B.), OCE-1334788 (E.V.), and DMR-1208990 (G.V.) and by Vetenskapsrådet, and the Göran Gustafsson Foundation for Research in the Natural Sciences and Medicine (J.E., K.G., B.M.).

APPENDIX A: RELATION BETWEEN THE ALIGNMENT OF DISKS AND RODS

Consider the time evolution of the vector \mathbf{n}_{rod} for a rod with shape factor Λ and the corresponding vector \mathbf{n}_{disk} for a disk with shape factor $-\Lambda$. Assume that the center-of-mass of the rod and the disk take the same paths through the turbulent flow. How do the symmetry vectors of the rod and the disk align with respect to each other? Recall the equations of motion (1) and (4). They can be rewritten as

$$\dot{\mathbf{n}} = \boldsymbol{\Omega} \wedge \mathbf{n} + \Lambda \mathbb{S} \mathbf{n} - \Lambda (\mathbf{n} \cdot \mathbb{S} \mathbf{n}) \mathbf{n}. \quad (\text{A1})$$

It follows that the cosine of the angle between the two vectors \mathbf{n}_{rod} and \mathbf{n}_{disk} for rods and disks with shape factors Λ and $-\Lambda$ evolves according to

$$\frac{d}{dt} [\mathbf{n}_{\text{rod}} \cdot \mathbf{n}_{\text{disk}}] = \dot{\mathbf{n}}_{\text{rod}} \cdot \mathbf{n}_{\text{disk}} + \mathbf{n}_{\text{rod}} \cdot \dot{\mathbf{n}}_{\text{disk}} = -\Lambda \mathbf{n}_{\text{rod}} \cdot \mathbf{n}_{\text{disk}} (\mathbf{n}_{\text{rod}} \cdot \mathbb{S} \mathbf{n}_{\text{rod}} - \mathbf{n}_{\text{disk}} \cdot \mathbb{S} \mathbf{n}_{\text{disk}}) \quad (\text{A2})$$

provided that the centers of mass of both particles follow the same path through the fluid. Put differently,

$$\frac{d}{dt} \log |\mathbf{n}_{\text{rod}} \cdot \mathbf{n}_{\text{disk}}| = -(\Lambda \mathbf{n}_{\text{rod}} \cdot \mathbb{S} \mathbf{n}_{\text{rod}} - \Lambda \mathbf{n}_{\text{disk}} \cdot \mathbb{S} \mathbf{n}_{\text{disk}}). \quad (\text{A3})$$

The right-hand side of this equation, evaluated along particle trajectories, tends to be negative because of the way the symmetry vectors of rods and disks align with the eigensystem of the strain \mathbb{S} . This



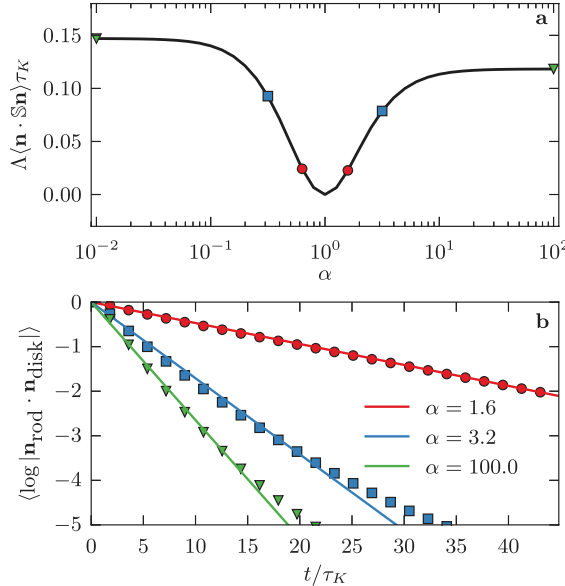


FIG. 6. (a) DNS results for $\Lambda \langle \mathbf{n} \cdot \mathbb{S}\mathbf{n} \rangle$ as a function of the particle-shape parameter α , solid line. The symbols indicate the values used to compute the solid lines in the lower panel of this figure. (b) Alignment of \mathbf{n}_{rod} and \mathbf{n}_{disk} , which tends to zero as time increases. At $t = 0$, \mathbf{n}_{rod} and \mathbf{n}_{disk} are parallel along $\hat{\mathbf{z}}$. DNS results (symbols) compared to expectation (exponential growth rates taken from panel (a), lines). Parameters $\alpha = 100$ and $1/100$ (green triangles), $\alpha = 3.2$ and $1/3.2$ (blue squares), and $\alpha = 1.6$ and $1/1.6$ (red circles).

is why we cannot discuss \mathbf{n} and \mathbb{O} only. The steady-state average of the right-hand side is negative; DNS results confirm this (Fig. 6(a)). It follows that the angle between \mathbf{n}_{rod} and \mathbf{n}_{disk} must decrease as a function of time. This is demonstrated by the DNS results shown in Fig. 6(b).

We note that the quantity $\Lambda \langle \mathbf{n} \cdot \mathbb{S}\mathbf{n} \rangle$ (shown in Fig. 5(a)) is the exponential growth rate (Lyapunov exponent) of a vector \mathbf{q} evolving according to

$$\dot{\mathbf{q}} = (\mathbb{O} + \Lambda \mathbb{S})\mathbf{q}, \quad \mathbf{n} = \mathbf{q}/|\mathbf{q}|. \quad (\text{A4})$$

The vector \mathbf{q} points in the same direction as \mathbf{n} but it is not normalised,^{4,49} $\mathbf{n} = \mathbf{q}/|\mathbf{q}|$. In order to compute the orientational dynamics, it is sufficient to consider the vector \mathbf{q} that obeys the linear equation of motion (A4). In the limit of $\alpha \rightarrow \infty$ (rods or material lines, $\Lambda \rightarrow 1$) this Lyapunov exponent was computed in earlier direct numerical simulations.⁵⁰ These simulations at smaller Reynolds numbers ($\text{Re}_\lambda = 38, 63$, and 90) obtained a Lyapunov exponent of 0.13 in units of τ_K which is in fairly good agreement with our data in Fig. 5(a) for large aspect ratio.

If the Lyapunov exponents of \mathbf{q}_\pm with shape factors $\pm\Lambda$ sum to a positive number for a given flow, the symmetry vectors of rods and disks must become orthogonal to each other. As Fig. 5(a) shows, this is the case for isotropic turbulence and this is consistent with the arguments summarized in the previous paragraph.

It is also the case for the random-flow model discussed in Sec. V, where to $O(\text{Ku}^4)$

$$\Lambda \langle \mathbf{n} \cdot \mathbb{S}\mathbf{n} \rangle \tau = 2\text{Ku}^2 \Lambda^2 - \text{Ku}^4 \Lambda^2 (9\Lambda^2 + 16)/3 + \dots \quad (\text{A5})$$

APPENDIX B: SUPPLEMENTARY FIGURES

This appendix contains further examples of orientational trajectories of disks and rods in turbulence obtained from the DNS described in the main text. The rapid oscillations seen in Figs. 7 and 8 are due to artifacts in numerically determining the fluid-velocity gradients. That such oscillations are weaker in Fig. 1 is a coincidence.



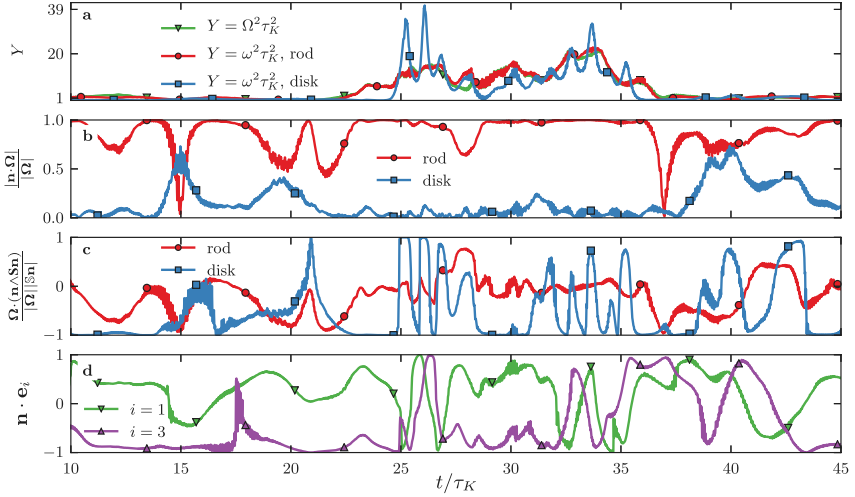


FIG. 7. DNS results for the instantaneous alignments and rotation rates of a disk and a rod as a function of time. (a) Fluid angular velocity variance $|\Omega|^2$ (green triangles) and particle angular velocity variance $|\omega|^2$ as a function of time for disk (blue squares) and rod (red circles). Note that the curves representing $|\Omega|^2$ (green triangles) and $|\omega|^2$ for rods (red circles) overlap strongly. (b) Alignment of \mathbf{n} with Ω as a function of time for disk (blue squares) and rod (red circles), (c) alignment of $\mathbf{n} \wedge \mathbb{S}\mathbf{n}$ with Ω as a function of time for disk (blue squares) and rod (red circles), (d) alignment of \mathbf{n}_{disk} with \mathbf{e}_1 (green point-down triangles) and \mathbf{e}_3 (purple point-up triangles) as a function of time.

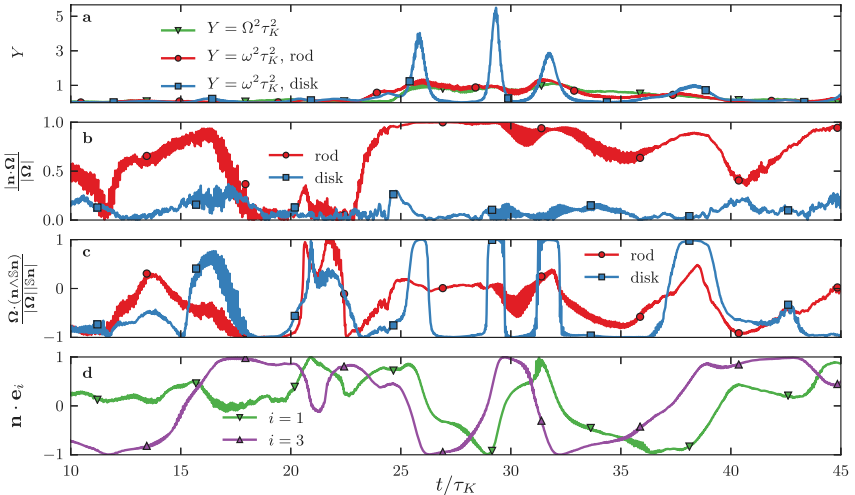


FIG. 8. DNS results for the instantaneous alignments and rotation rates for a disk and a rod as a function of time. (a) $|\Omega|^2$ (green triangles) and $|\omega|^2$ as a function of time for disks (blue squares) and rods (red circles). Note that the curves representing $|\Omega|^2$ (green triangles) and $|\omega|^2$ for rods (red circles) overlap strongly. (b) alignment of \mathbf{n} with Ω as a function of time for disks (blue squares) and rods (red circles), (c) alignment of $\mathbf{n} \wedge \mathbb{S}\mathbf{n}$ with Ω as a function of time for disks (blue squares) and rods (red circles), (d) alignment of \mathbf{n}_{disk} with \mathbf{e}_1 (green point-down triangles) and \mathbf{e}_3 (purple point-up triangles) as a function of time.



- ¹ H. R. Pruppacher and J. D. Klett, *Microphysics of Clouds and Precipitation*, 2nd ed. (Kluwer Academic Publishers, Dordrecht, The Nederlands, 1997), p. 954.
- ² F. Lundell, D. Söderberg, and H. Alfredsson, "Fluid mechanics of papermaking," *Annu. Rev. Fluid Mech.* **43**, 195–217 (2011).
- ³ M. Wilkinson, B. Mehlig, and V. Uski, "Stokes trapping and planet formation," *Astrophys. J., Suppl. Ser.* **176**, 484 (2008).
- ⁴ M. Wilkinson, V. Bezuglyy, and B. Mehlig, "Fingerprints of random flows," *Phys. Fluids* **21**, 043304 (2009).
- ⁵ V. Bezuglyy, B. Mehlig, and M. Wilkinson, "Poincaré indices of rheoscopic visualisations," *Europhys. Lett.* **89**, 34003 (2010).
- ⁶ M. Wilkinson, V. Bezuglyy, and B. Mehlig, "Emergent order in rheoscopic swirls," *J. Fluid Mech.* **667**, 158 (2011).
- ⁷ D. M. Sigman and E. A. Boyle, "Glacial/interglacial variations in atmospheric carbon dioxide," *Nature* **407**, 859 (2000).
- ⁸ N. Jiao, G. J. Herndl, D. A. Hansell, R. Benner, G. Kattner, S. W. Wilhelm, D. L. Kirchman, M. G. Weinbauer, T. Luo, F. Chen, and F. Azam, "Microbial production of recalcitrant dissolved organic matter: Long-term carbon storage in the global ocean," *Nat. Rev. Microbiol.* **8**, 593–599 (2010).
- ⁹ R. M. Macnab and D. E. Koshland, "The gradient-sensing mechanism in bacterial chemotaxis," *Proc. Natl. Acad. Sci. U.S.A.* **69**, 2509–2512 (1972).
- ¹⁰ A. Ishihara, J. E. Segall, S. M. Block, and H. C. Berg, "Coordination of flagella on filamentous cells of escherichia coli," *J. Bacteriol.* **155**, 228–237 (1983).
- ¹¹ H. Nguyen, L. Karp-Boss, P. A. Jumars, and L. Fauci, "Hydrodynamic effects of spines: A different spin," *Limnol. Oceanogr.: Fluids Environ.* **1**, 110–119 (2011).
- ¹² T. Kiørboe, *A Mechanistic Approach to Plankton Ecology* (Princeton University, Princeton, USA, 2008).
- ¹³ K. L. Denman and A. E. Gargett, "Biological-physical interactions in the upper ocean: The role of vertical and small scale transport processes," *Annu. Rev. Fluid Mech.* **27**, 225 (1995).
- ¹⁴ M. W. Denny and B. Gaylord, "Marine ecomechanics," *Annu. Rev. Mar. Sci.* **2**, 89 (2010).
- ¹⁵ M. Shin and D. L. Koch, "Rotational and translational dispersion of fibres in isotropic turbulent flows," *J. Fluid Mech.* **540**, 143 (2005).
- ¹⁶ S. Parsa, E. Calzavarini, F. Toschi, and G. A. Voth, "Rotation rate of rods in turbulent fluid flow," *Phys. Rev. Lett.* **109**, 134501 (2012).
- ¹⁷ L. Chevillard and C. Meneveau, "Orientation dynamics of small, triaxial-ellipsoidal particles in isotropic turbulence," *J. Fluid Mech.* **737**, 571 (2013).
- ¹⁸ K. Gustavsson, J. Einarsson, and B. Mehlig, "Tumbling of small axisymmetric particles in random and turbulent flows," *Phys. Rev. Lett.* **112**, 014501 (2014).
- ¹⁹ G. B. Jeffery, "The motion of ellipsoidal particles immersed in a viscous fluid," *Proc. R. Soc. A* **102**, 161 (1922).
- ²⁰ G. Subramanian and D. L. Koch, "Inertial effects on fibre motion in simple shear flow," *J. Fluid Mech.* **535**, 383 (2005).
- ²¹ G. Subramanian and D. L. Koch, "Inertial effects on the orientation of nearly spherical particles in simple shear flow," *J. Fluid Mech.* **557**, 257 (2006).
- ²² J. Einarsson, J. R. Angilella, and B. Mehlig, "Orientational dynamics of weakly inertial axisymmetric particles in steady viscous flows," *Physica D* **278**, 79 (2014).
- ²³ F. Lundell and A. Carlsson, "Heavy ellipsoids in creeping shear flow: Transitions of the particle rotation rate and orbit shape," *Phys. Rev. E* **81**, 016323 (2010).
- ²⁴ J. Einarsson, A. Johansson, S. K. Mahato, Y. Mishra, J. R. Angilella, D. Hanstorp, and B. Mehlig, "Periodic and aperiodic tumbling of microrods advected in a microchannel flow," *Acta Mech.* **224**, 2281 (2013).
- ²⁵ A. Pumir and M. Wilkinson, "Orientation statistics of small particles in turbulence," *New J. Phys.* **13**, 093030 (2011).
- ²⁶ R. Ni, N. T. Ouelette, and G. A. Voth, "Alignment of vorticity and rods with Lagrangian fluid stretching in turbulence," *J. Fluid Mech.* **743**, R3 (2014).
- ²⁷ Y. Li, E. Perlman, M. Wan, Y. Yang, C. Meneveau, R. Burns, S. Chen, A. Szalay, and G. Eyink, "A public turbulence database cluster and applications to study Lagrangian evolution of velocity increments in turbulence," *J. Turbul.* **9**, 31 (2008).
- ²⁸ H. Yu, K. Kanov, E. Perlman, J. Graham, E. Frederix, R. Burns, A. Szalay, G. G. Eyink, and C. Meneveau, "Studying Lagrangian dynamics of turbulence using on-demand fluid particle tracking in a public turbulence database," *J. Turbul.* **13**, 1–29 (2012).
- ²⁹ M. Chertkov, A. Pumir, and B. Shraiman, "Lagrangian tetrad dynamics and phenommenology of turbulence," *Phys. Fluids* **11**, 2394 (1999).
- ³⁰ Z. S. She, E. Jackson, and S. A. Orszag, "Intermittent vortex structures in homogeneous isotropic turbulence," *Nature* **344**, 226 (1990).
- ³¹ K. Gustavsson and B. Mehlig, "Statistical models for spatial patterns of inertial particles in turbulence," e-print [arXiv:1412.4374](https://arxiv.org/abs/1412.4374) (unpublished).
- ³² K. Gustavsson and B. Mehlig, "Lyapunov exponents for particles advected in compressible random velocity fields at small and large Kubo numbers," *J. Stat. Phys.* **153**, 813–827 (2013).
- ³³ C. Marchioli, M. Fantoni, and A. Soldati, "Orientation, distribution, and deposition of elongated, inertial fibers in turbulent channel flow," *Phys. Fluids* **22**, 033301 (2010).
- ³⁴ F. Zhao and B. G. M. van Wachem, "Direct numerical simulation of ellipsoidal particles in turbulent channel flow," *Acta Mech.* **224**, 2331–2358 (2013).
- ³⁵ H. I. Andersson, L. Zhao, and M. Barri, "Torque-coupling and particle-turbulence interactions," *J. Fluid Mech.* **696**, 319–329 (2012).
- ³⁶ G. Bellani and E. A. Variano, "Homogeneity and isotropy in a laboratory turbulent flow," *Exp. Fluids* **55**, 1 (2014).
- ³⁷ G. Bellani, M. A. Nole, and E. A. Variano, "Turbulence modulation by large ellipsoidal particles: Concentration effects," *Acta Mech.* **224**, 2291 (2013).
- ³⁸ S. E. Elgobashi, "On predicting particle-laden turbulent flows," *Appl. Sci. Res.* **52**, 309–329 (1994).
- ³⁹ G. Bellani and E. A. Variano, "Slip velocity of large neutrally buoyant particles in turbulent flows," *New J. Phys.* **14**, 125009 (2012).



- ⁴⁰ M. L. Byron and E. A. Variano, "Refractive-index-matched hydrogel materials for measuring flow–structure interactions," *Exp. Fluids* **54**, 1 (2013).
- ⁴¹ G. Bellani, M. L. Byron, A. G. Collignon, C. R. Meyer, and E. A. Variano, "Shape effects on turbulent modulation by large nearly neutrally buoyant particles," *J. Fluid Mech.* **712**, 41 (2012).
- ⁴² E. Dresselhaus and M. Tabor, "The kinematics of stretching and alignment of material elements in general flow fields," *J. Fluid Mech.* **236**, 415–444 (1992).
- ⁴³ G. G. Marcus, S. Parsa, S. Kramel, R. Ni, and G. A. Voth, "Measurements of the solid-body rotation of anisotropic particles in 3D turbulence," *New J. Phys.* **16**, 102001 (2014).
- ⁴⁴ W. T. Ashurst, A. R. Kerstein, R. M. Kerr, and C. H. Gibson, "Alignment of vorticity and scalar gradient with strain rate in simulated Navier–Stokes turbulence," *Phys. Fluids (1958–1988)* **30**, 2343–2353 (1987).
- ⁴⁵ S. Parsa and G. Voth, "Inertial range scaling in rotations of long rods in turbulence," *Phys. Rev. Lett.* **112**, 024501 (2014).
- ⁴⁶ H. Xu, A. Pumir, and E. Bodenschatz, "The pirouette effect in turbulent flows," *Nat. Phys.* **7**, 709–712 (2011).
- ⁴⁷ F. De Lillo, M. Cencini, W. M. Durham, M. Barry, R. Stocker, E. Climent, and G. Boffetta, "Turbulent fluid acceleration generates clusters of gyrotaotic microorganisms," *Phys. Rev. Lett.* **112**, 044502 (2014).
- ⁴⁸ N. A. Hill and D.-P. Hader, "A biased random walk model for the trajectories of swimming micro-organisms," *J. Theor. Biol.* **186**, 503–526 (1997).
- ⁴⁹ F. P. Bretherton, "The motion of rigid particles in a shear flow at low Reynolds number," *J. Fluid Mech.* **14**, 284 (2012).
- ⁵⁰ S. S. Girimaji and S. B. Pope, "Material-element deformation in isotropic turbulence," *J. Fluid Mech.* **220**, 427–458 (1990).
- ⁵¹ M. Hutchins and D. Olendorf, *Grzimek's Animal Life Encyclopedia: Lower Metazoans and Lesser Deuterostomes*, Vol. 1. (Gale/Cengage Learning, 2004).
- ⁵² N. R. Challabotla, L. Zhao, and H. I. Andersson, "Orientation and rotation of inertial disk particles in wall turbulence," *J. Fluid Mech.* **766**, R2 (published online 2015).



